Spring 2009

Multidisciplinary Design Optimization for Sonic Boom Mitigation

Isik A. Ozcer
Old Dominion University

MULTIDISCIPLINARY DESIGN OPTIMIZATION FOR SONIC BOOM MITIGATION

Isik A. Ozcer

B. S., June 2003, Istanbul Technical University
M. S., December 2005, Old Dominion University

A Dissertation Submitted to the Faculty of
Old Dominion University in Partial Fulfillment of the
Requirement for the Degree of

DOCTOR OF PHILOSOPHY
AEROSPACE ENGINEERING
OLD DOMINION UNIVERSITY
May 2009

Approved by:

Osama A. Kandil (Director)

Oktay Baysal (Member)

Robert L. Ash (Member)

Duc T. Nguyen (Member)

ABSTRACT

MULTIDISCIPLINARY DESIGN OPTIMIZATION FOR SONIC BOOM MITIGATION

Isik A. Ozcer
Old Dominion University, 2009
Director: Dr. Osama A. Kandil

Automated, parallelized, time-efficient surface definition and grid generation and flow simulation methods are developed for sharp and accurate sonic boom signal computation in three dimensions in the near and mid-field of an aircraft using Euler / Full-Potential unstructured / structured computational fluid dynamics. The full-potential mid-field sonic boom prediction code is an accurate and efficient solver featuring automated grid generation, grid adaptation and shock fitting, and parallel processing. This program quickly marches the solution using a single non-linear equation for large distances that cannot be covered with Euler solvers due to large memory and long computational time requirements. The solver takes into account variations in temperature and pressure with altitude. The far-field signal prediction is handled using the classical linear Thomas Waveform Parameter Method where the switching altitude from the non-linear to linear prediction is determined by convergence of the ground signal pressure impulse value. This altitude is determined as $r/L \approx 10$ from the source for a simple lifting wing, and $r/L \approx 40$ for a real complex aircraft. Unstructured grid adaptation and shock fitting methodology developed for the near-field analysis employs an Hessian based anisotropic grid adaptation based on error equidistribution. A special field scalar is formulated to be used in the computation of the Hessian based error metric which enhances significantly the adaptation scheme for shocks. The entire cross-flow of a complex aircraft is resolved with high fidelity using only 500,000 grid nodes after only about 10 solution/adaptation cycles. Shock fitting is accomplished using Roe's Flux-Difference Splitting scheme which is an approximate Riemann type solver and by proper alignment of the cell faces with respect to shock surfaces. Simple to complex real aircraft geometries are handled with no user-interference required making the simulation methods suitable tools for product design. The simulation tools are used to optimize three geometries for sonic boom mitigation. The first is a simple axisymmetric shape to be used as a generic nose

component, the second is a delta wing with lift, and the third is a real aircraft with nose and wing optimization. The objectives are to minimize the pressure impulse or the peak pressure in the sonic boom signal, while keeping the drag penalty under feasible limits. The design parameters for the meridian profile of the nose shape are the lengths and the half-cone angles of the linear segments that make up the profile. The design parameters for the lifting wing are the dihedral angle, angle of attack, non-linear span-wise twist and camber distribution. The test-bed aircraft is the modified F-5E aircraft built by Northrop Grumman, designated the Shaped Sonic Boom Demonstrator. This aircraft is fitted with an optimized axisymmetric nose, and the wings are optimized to demonstrate optimization for sonic boom mitigation for a real aircraft. The final results predict 42% reduction in bow shock strength, 17% reduction in peak Δp, 22% reduction in pressure impulse, 10% reduction in foot print size, 24% reduction in inviscid drag, and no loss in lift for the optimized aircraft. Optimization is carried out using response surface methodology, and the design matrices are determined using standard DoE techniques for quadratic response modeling.

ACKNOWLEDGEMENTS

I would like to take this opportunity express my gratitude towards everyone whose support and contribution made it possible to complete this dissertation.

First and foremost, I would like to thank my advisor Dr. Osama A. Kandil for his trust, continuous support, constant attention, and valuable input throughout my studies at Old Dominion University. This dissertation would not be possible without his guidance. I am most thankful for the funding he made available for attending prestigious international conferences and giving me the opportunity to give technical presentations in public.

I wish to extend my gratitude towards my committee members, Dr. Oktay Baysal, Dr. Robert Ash, and Dr. Duc Nguyen, for serving on my dissertation committee and their valuable feedback.

Thanks are extended to Dr. Mujeeb Malik at the Simulation and Computational Dynamics Branch at NASA LaRC for his partial support during this research work.

I would like to thank Dr. Osama A. Kandil, Dr. Oktay Baysal, and Dr. Colin Britcher for taking the time and resources for making the necessary software and hardware available for completing this dissertation. Thanks are extended to Dr. Drew Landman for his course on response surface methodology and optimization, and his continued feedback on my research.

Thanks to Newmerical Technologies Int. for their technical support in using OptiGRID, and extra licenses provided free of charge that made it possible to compute a very large number of design simulations in a relatively shorter period of time.

I am most thankful to my friends Dr. Bayram Celik and Can Sabuncu for taking the time to help me with the final stages of the dissertation submission procedure.

I would like to express my love, gratitude and appreciation to my parents and family members for their emotional and financial support throughout my educational life. I would also like to thank all my friends who patiently tolerated the busy schedule of a graduate student, and made Norfolk a better place. Special thanks go to my friend Hector Garcia for providing a three-dimensional print of my final optimized aircraft design that was most effective during the oral defense.

Finally, I would like to thank my fiancée Pinar for all her love and support during this study. Thanks for all the joy and the colors that you brought into my life that I had long forgotten. I would have never finished this dissertation in a timely manner if it weren't for you and for your most appreciated help with fixing the defense presentation and correction of the text.

TABLE OF CONTENTS

Section Page

LIST OF FIGURES

Figure Page

Figure Page

Figure Page

Figure Page

LIST OF TABLES

Table Page

Table Page

LIST OF SYMBOLS

a	Speed of sound
AC_x	Aerodynamic center axial location
α	Angle of attack
α_T	wing tip twist angle
α_i	wing incidence angle with respect to aircraft centerline
α_w	wing angle of attack = $\alpha + \alpha_i$
$\alpha(y)$	wing span-wise twist profile
β	$\sqrt{M^2 - 1}$, semi vertex angle of the delta wing
β_i, β_{ii}	Response model coefficients
b	vector for response model coefficient estimates
C_1, C_2, C_3	Grid adaptation parameters
C_L	Lift coefficient
C_p	Coefficient of pressure
C_R	Root chord length
δ_{ij}	Kronecker Delta
Δp	Over-pressure
e	Total energy per unit mass
$e(x)$	Approximate error in grid for adaptation
E	Total energy per unit volume $E = \rho e$
f_S	Shock detector function
$F(y)$	Whitham's F-function
$\mathbf{F}_i$	Euler inviscid flux vectors
F	vector of coded design factor settings

g_M	Scalar for grid adaptation
g^{mn}	Contravariant metric tensor
g_{mn}	Covariant metric tensor
γ	Ratio of specific heats, 1.4 for air
h	static enthalpy, unstructured grid cell height
H	Total enthalpy
I	pressure impulse, $\int_{\Delta p>0} \Delta p dt$
J	Jacobian of coordinate transformation
k	Grid adaptation parameter
L	Reference body length
L_{peak}	Peak loudness at ground level, dB
λ	Eigenvalue, wing trailing edge sweep angle
M	Mach number
Mn	Mach number normal across a shock
N_α	power of non-linear twist profile
p	Static pressure
p_0	Total pressure
ϕ	Velocity potential
$\vec{q}$	Vector of primitive variables
Q	Vector of conservative flow variables
r	Radial distance
$R(x)$	Radius of the body
R_B	Base radius of the body
ρ	Density

$S(x)$	Cross-sectional area
t	Time, dummy variable in ϕ integral
t_c	camber at mid-chord
$t_c(y)$	camber at mid-chord span-wise distribution
T	Static temperature
T_0	Total temperature
θ	Azimuthal angle, wedge angle, meridian profile ramp angle
θ_D	dihedral angle
u_i, u, v, w	Cartesian velocity components
U_m	Contravariant velocity components
V	Total velocity
$\mathbf{V}$	Velocity vector
x_i	design factor levels in response surface modeling
x_i, x, y, z	Cartesian coordinates
X_i	axisymmetric meridian profile ramp lengths
y	Characteristic value in the linear solution to ϕ, wing span
ξ^i, ξ,η,ζ	Curvilinear coordinates

LIST OF ABBREVIATIONS

ANOVA	Analysis of Variance
ASCII	American Standard Code for Information Interchange – text files
BBD	Box – Behnken Design
CAD	Computer Aided Design
CCD	Central Composite Design
CFL3D	Computational Fluids Laboratory Three Dimensional – flow solver
DARPA	Defense Advanced Research Projects Agency
DoD	Department of Defense
DoE	Design of Experiments
FAA	Federal Aviation Administration
FCD	Face Centered Defense
FPM3D	Full Potential Marching Three Dimensional
FUN3D	Fully Unstructured Navier-Stokes Three Dimensional
GCC	General Curvilinear Coordinates
HPC	High Performance Computing
HSR	High Speed Research
LEX	Leading Edge Extension
LoF	Lack of Fit
MPI	Massage Passing Interface
NASA	National Aeronautics and Space Administration
PDE	Partial Differential Equation
QSP	Quiet Supersonic Platform
RHS	Right Hand Side
RSM	Response Surface Methodology
SFGA	Shock Fitting and Grid Adaptation
SSBD	Shaped Sonic Boom Demonstrator
VIF	Variance Influence Factor

1. INTRODUCTION

Supersonic flight over land is banned in most countries today due to the detrimental effects of sonic boom on general public and structures. The "Quiet Supersonic Platform" initiated by the Defense Advanced Research Projects Agency (DARPA) in 2000 set the current target for maximum sonic boom pressure at ground level for safe supersonic operation as 0.3 pounds per square foot [1][1]. Current supersonic aircraft produce much stronger N-wave type signals with bow shocks exceeding 1.0 psf. Pain threshold level for noise is 120 dB in general. For impulsive noise, the peak pressure level in psf can be converted to peak noise level in dB by [2]

$$L_{\text{peak}} = 127.6 + 20 Log_{10}\left(\Delta p_{\text{peak}}\right) \tag{1}$$

where L_{peak} and Δp_{peak} are the peak loudness and peak over-pressure. A more accurate representation of the perceived noise for N-wave type sonic booms, that takes the wave duration into account in addition to the peak pressure, can be given as C-weighted sound exposure level (CSEL) defined by [3]

$$CSEL = L_{\text{peak}} - 26 \tag{2}$$

Using these equations, a 0.3 psf limit translates to L_{peak} = 117 dB, and CSEL = 91 dB. For comparison, Table 1 shows ground level peak pressure and noise levels of sonic booms from several aircraft. The noise levels are well above the limits even for very low supersonic Mach numbers. The noise will be noticeably higher for aircraft flying at anticipated ideal supersonic travel cruise Mach numbers between 1.6 and 2.0.

Market studies for over a 10 to 20 year period have shown a demand for 250-450 small supersonic aircraft that cruise at Mach 1.8 in the \$50 - \$100 million price range [4]. Although this market is dominated by business jets, such capable aircraft can also be used as medical transport in life saving emergency missions. To enable supersonic flight over land, the sonic boom noise should be mitigated to make it safe for the environment.

---

[1] Model journal for reference style is *AIAA Journal.*

Table 1: Example supersonic aircraft ground sonic boom noise levels [5, 6]

Aircraft	Length, ft	Flight Alt., ft	Mach	Wave length, milli-seconds	Ground Δp_{peak}, psf	L_{peak}, dB	CSEL, dB
F-5E	47	32,000	1.40	90	1.46	130.9	104.9
F-18	56	30,000	1.20	140	1.6	131.7	105.7
SR-71	107	30,000	1.25	170	3	137.5	111.5

Since the 1950s, substantial research has shown that the sonic boom signal can be shaped and mitigated using various techniques ranging from aerodynamic geometry modification to using plasma injection towards free stream flow [1, 4, 7-41]. The noise limits set by FAA are so challenging, however, that no commercial supersonic aircraft in service can fly at Mach 2 with an acceptable sonic boom signature. The design process is challenging both in experimental and computational terms. The experiments cannot fully be carried out in wind tunnels since the sonic boom signal must be measured at hundreds of body lengths from the aircraft. Actual size prototypes need to be built and tested under flight conditions. Such experimentation is very costly and time consuming since it involves aircraft manufacture, flight testing, in-flight ground and airborne data acquisition covering several miles in axial and lateral directions. The atmospheric conditions also limit when the test flights can be conducted since atmospheric turbulence and non-standard random local temperature, pressure, and wind variations produce non-repeatable data. Two famous examples of such experimentation are the SR-71 test in 1995 [5] and the Shaped Sonic Boom Experiment in 2004 [1]. Computationally the hardship occurs when the designer is not satisfied with the classical linear sonic boom prediction methodology. The available linear theory assumes that the flow is axisymmetric and utilizes linear small disturbance equations to relate the geometry to the pressure signal. Aircraft designs optimized using the linear prediction methods tend to have slender fuselages and blunt noses for sonic boom mitigation. Using three dimensional non-linear methods, it is possible to investigate less conventional, even asymmetric, geometries and the cross-flow shock structure influence on the under-track signal. However, non-linear analysis requires high order computational fluid dynamics (CFD) solutions on carefully adapted grids for proper shock capturing in the near-field and mid-field. Such solutions can be computationally very expensive and can retard the design process.

The work presented in this dissertation outlines a time efficient computational multivariable design optimization framework for sonic boom mitigation using high order solution methods. The framework features automated parametric surface definition generation, structured and unstructured grid adaptation for near-field solution, full-potential marching with shock fitting

and grid adaptation for the mid-field solution, and Design of Experiments (DoE) / Response Surface Methodology (RSM) for multi-response modeling and optimization. Parallel processing is utilized at all flow simulation and grid adaptation stages of the framework, with efficient scalability and load balancing. Optimization studies are carried out on simple aircraft components (nose and wing) and the Shaped Sonic Boom Demonstrator to demonstrate the power of the automated user-friendly non-linear sonic boom prediction technology developed herein. This work demonstrates that high-order CFD solutions for near and mid-field sonic boom prediction are no longer a prohibitively expensive practice in aircraft design optimization for sonic boom mitigation.

1.1 Background

When supersonic flight became common in the 1950's, researchers were surprised to find that shock waves could reach the ground with sufficient strength to be a public annoyance. After about ten years of supersonic operation, DoD, NASA, and FAA released the "Commercial Supersonic Aircraft Report" outlining the requirements for feasible supersonic aircraft designs, and providing guidance for overall sonic boom research [42]. With this initiative, researchers developed methods to predict sonic boom at ground level [43, 44], and to relate aircraft aerodynamics to the generated sonic boom signal [19]. After spending approximately one billion dollars on sonic boom research through 1972, the supersonic transport program was halted due to increasing public complaints and environmental concerns such as ozone depletion. Eventually all types of supersonic flight over the continental US were banned (Sec. 91.817 – civil aircraft sonic boom). These developments retarded sonic boom research funding considerably over the next ten years, and eventually it was completely dropped.

In the late 1980's, sonic boom research was revived in the High Speed Research Program following two national reports stating that the US should have research programs on supersonic transportation [42]. The research focused on methods to decrease the boom noise level by modifying the shape of the sonic boom signature by changing the aerodynamics of the aircraft. The idea of "shaped sonic boom" was introduced where the typical "N-wave" pressure signature was replaced by targeted, "flat-top" and "ramp" type signatures. These signatures are illustrated in Figure 1. Note that this illustration is only conceptual to show the different signal shapes in the leading (positive) lobe of the wave. Changes in the positive lobe will cause changes in the

negative lobe in actuality due to the fact that when lift addition is taken out, both sides of the signal have to balance.

The design Mach numbers considered for these supersonic concepts ranged between 2 and 3. To obtain more accurate near-field results than those provided by the linear theory, CFD was incorporated in sonic boom research. The linear F-function theory is limited to axisymmetric flows where the geometry of the body is connected to the pressure signal via the "F-function", which is a function of the cross-sectional area distribution of the body [45]. In case of lifting bodies, the lift is converted to an equivalent area distribution and added to the cross-sectional area distribution of the body. This way the effect of the lifting body is approximated by an axisymmetric body having the "equivalent" area distribution. CFD is necessary to provide the axial lift distribution included in this computation.

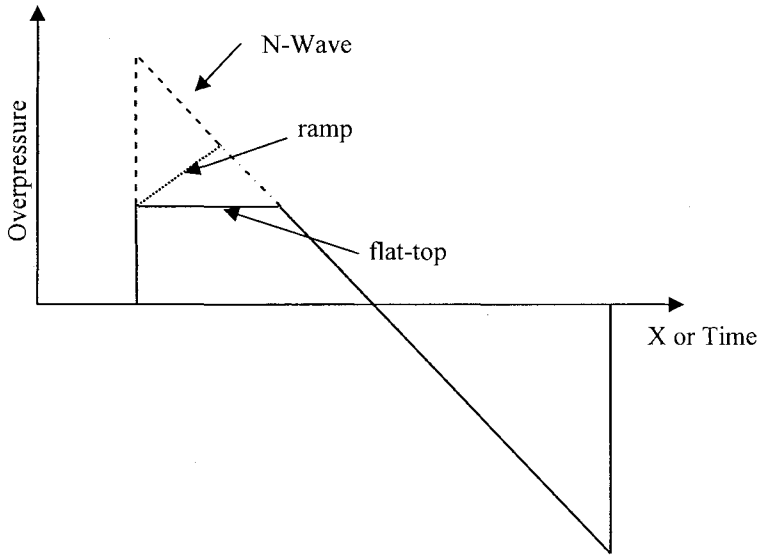

Figure 1: Illustrated comparison of some possible sonic boom shapes.

Shaped sonic boom signatures can lower the "loudness" of the boom significantly, which is the main source of annoyance to the public. By careful shaping of the aircraft, it is possible to generate desirable shaped signatures that maintain their form all the way to the ground [46]. By the end of the High Speed Research (HSR) program, tests with a modified SR-71 showed that a shaped boom could be sustained all the way to the ground, but with the penalty of significant volume addition to the airplane [1].

In 2000, a new program by DARPA, called the Quiet Supersonic Platform (QSP), was initiated. The goal is to come up with a feasible commercial aircraft design that produces a sonic boom initial over-pressure of about 0.3 psf. A breakthrough achievement by Northrop – Grumman was their "Shaped Sonic Boom Demonstrator" (SSBD) aircraft, which is a modified version of the F-5E fighter aircraft, designed as a part of this research program. This aircraft generates ground level shaped sonic booms that are nearly a flat-top with the bow shock strength 25% lower than the original configuration. [47]. The flight tests were completed in January 2004. The flight altitude was near 32,000 ft and Mach number was 1.4. Near-field signal was recorded by an F-15 flying about 90 ft below the SSBD. Pawlowski and Graham [1] state that this is the first validation of the sonic boom mitigation theory as developed by Seebass and George [19], for actual flight conditions employing a test aircraft.

In 2002 Kandil *et al.* developed a full-potential equation (FPE) method and a computer code that marches the sonic boom signal through stratified three-dimensional atmosphere from the near-field to ground level [48]. Unlike the classical sonic boom prediction tools that use linear geometric acoustics to predict the signature, this code used three-dimensional non-linear FPE and a conical shock fitted and adapted grid to march the solution in space. The methodology is based entirely on CFD, where near field results are obtained solving the Euler equations using an approximate Riemann solver like Roe's Flux-Difference Splitting (FDS) scheme, and with shock fitted and adapted grids to satisfy the Rankine-Hugoniot shock jump criteria. The work was initially supported by Eagle Aeronautics through a contract from Lockheed Martin. Preliminary results of the FPE approach were given for a delta wing configuration for uniform and stratified atmospheres. The code handles atmospheric changes by sub-blocking the domain in the vertical coordinate z, and applying a different free stream speed of sound and pressure setting at each sub-block. Shock fitting and grid adaptation are essential to ensure accuracy, sharpness, and high fidelity of the predicted signal all the way to the ground. Using the FPE method, sonic boom mitigation using dihedral is shown to produce up to 14% reduction on the ground level bow shock strength in Ref. [30] in 2003. In a report submitted to NASA Langley and Eagle Aeronautics in August 2004, Kandil and Yang [49] give FPE results for the Baize-Coen High Speed Commercial Transport (HSCT) configuration [50] with shaped ground sonic boom. In the same document, excellent agreement between computational and experimental mid-field data was shown for the Susan Cliff wing-body configuration [51]. In January 2005, Kandil *et al* presented the FPE-computed ground level sonic boom signal of the SSBD where exceptional agreement of computational and experimental signal shape and pressure levels were obtained [52]. In December 2005, a detailed explanation of the Euler/FPE sonic boom prediction

methodology was included in Ozcer's M.S. thesis, along with the results for the SSBD and a double cone configuration [53]. Also in 2005 Kandil and Zheng showed computational results for sonic boom focusing using several schemes to solve the non-linear Tricomi equation [54, 55]. This is a very important problem since the shock waves can coalesce and focus on what is called the "caustic line" and easily amplify the signal strength by more than a factor of two. Any structure, airborne vehicle, or human that resides on the caustic line can be damaged or injured. In January 2006, Kandil and Ozcer presented sonic boom computations for the double cone using CFL3D, FUN3D, and full-potential codes, where the geometry is a cone-cylinder-cone found in Ref. [7]. Kandil and Khasdeo [56] set forth a parametric investigation of the superboom problem using the codes developed in Ref. [55]. A sonic boom mitigation study using 2-level factorial RSM and the steepest descent approach was given by Kandil *et al* [57] where wing camber, thickness, and nose angle of a delta wing configuration were examined. In January 2007, Ozcer and Kandil presented a nose optimization study using axisymmetric configurations with linear segmented meridian profiles and applied the optimum profile to a delta wing configuration as a nose attachment for sonic boom mitigation [58]. Dihedral angle was added as a fourth parameter in the multivariable design analysis of a delta wing for sonic boom mitigation by Kandil *et al* [59]. In January 2008, Ozcer and Kandil developed a very efficient automated iterative unstructured grid adaptation methodology for near-field sonic boom prediction [60]. The methodology is used to predict high fidelity shocks using only half a million grid nodes in the complete near-field (above and below) of the SSBD aircraft. Results with 10 solution/adaptation cycles were obtained in less than an hour using 16 AMD Opteron 2.0GHz CPUs on a UNIX HPC Cluster, with no user interference. The grid adaptation formulation is designed such that a fixed set of adjustable parameters work equally well for the simplest (double cone) and the most complex (SSBD – real aircraft) geometries. The level of automation reached with this methodology made it possible to test hundreds of geometries in a timely manner for this dissertation without requiring any user time for grid generation or intricate case dependent adjustments of solver and grid adaptation parameter settings. The grid is no longer a problem in sonic boom near-field computations, but is a part of the solution.

1.2 Present Work

The work presented here is a multivariable multi-response design optimization study for sonic boom mitigation, using advanced flow simulation methods. The emphasis is on the development of automated, user-friendly, high order sonic boom prediction tools based on CFD, including parametric watertight (non-manifold) surface and grid generation. The power and efficiency of these tools are demonstrated in design optimization loops with non-linear response modeling. Analytical linear sonic boom prediction and mitigation methods are valuable in providing necessary insight to the problem but are not necessarily sufficient to reach the 0.3 psf criteria. There is significant nonlinearity in relationships between the geometric parameters and responses such as sonic boom pressure, impulse, lift, drag, etc. Therefore, it is essential to use non-linear prediction and optimization tools in general for sonic boom mitigation [24]. The solution methods used in this work include structured/unstructured CFD with grid adaptation and shock fitting for near field, FPE marching for mid-field, and linear ray-tracing for far-field analyses. Design variables are geometric parameters defining the aerodynamic bodies under investigation. Responses include ground level peak pressures, mid-field and far-field pressure impulses, and lift and drag coefficients. Constraints are applied on the length, thickness, and volume of the bodies, as well as aerodynamic centers and center of gravity. Optimization is based on DoE and RSM. Three sets of optimization applications are presented in the current study. The first is for an axisymmetric body, the second is for a delta wing, and the third is for the SSBD aircraft with nose and wing modifications.

In section 2, the literature is surveyed covering sonic boom prediction, shock fitting and grid adaptation, and sonic boom mitigation topics. In section 3, the formulation for equations governing the physics of the problem is presented briefly. Boundary conditions and atmospheric pressure and temperature variation in the full potential code are included. In section 4, methodology is explained. Solution methods for near, mid, and far-field are discussed. Shock fitting and grid adaptation techniques are explained. The unstructured grid adaptation technique is presented in detail. The Hessian based grid error estimation used in the grid adaptation software OptiGRID is discussed, and the formulation of the special scalar that enhances the presence of shocks in coarse grid solutions is given with examples. Details on the optimization procedures are given for the studied aerodynamic geometries. The framework of solution / optimization is discussed here with explanations for software coupling and parallel processing. Finally the regression model equation and some statistical terms used in the response modeling

and optimization are presented in brief. In section 5, comparative assessment and validation of the sonic boom prediction tools are given using a double cone, a delta wing, and the SSBD geometries for testing. Linear and non-linear propagation results are compared. A discussion on when to switch from the non-linear to linear propagation is given. Section 6 covers the optimization studies for sonic boom mitigation carried out using non-linear solution tools and response surface modeling. The first sub-section here presents the optimization of the axisymmetric meridian profile which is to be used as a generic aircraft nose component. The second sub-section presents parametric shape optimization of a lifting delta wing for sonic boom mitigation where the volume and the lift are conserved. The general parameters investigated are wing camber, dihedral, angle of attack and twist. Span-wise non-linear camber and twist distributions are also included in the optimization. The final sub-section presents results of the optimization study carried out on the original SSBD aircraft geometry where the optimum axisymmetric shape found in the first section is attached to the aircraft as a nose extension, and the wing is replaced with a delta wing optimized for sonic boom mitigation. Due to the existence of interference lift and the need to match the aerodynamic center of the original wing, the new wing for the SSBD is optimized while it is attached to the fuselage. Therefore, a second wing optimization study similar to the one in the second section is carried out in this final section. Finally, section 7 lists conclusions and recommended future work.

2. LITERATURE SURVEY

This section reviews the literature related and referred to in the current dissertation. The material is collected under three sub-headings. In section 2.1, literature on sonic boom prediction methods is reviewed. In section 2.2, grid adaptation and shock fitting techniques for sonic boom prediction are discussed. A review of sonic boom mitigation and shape optimization research is given in section 2.3. In the final section, 2.4, a summary is provided orienting what this dissertation's contribution is to the current literature. Sonic boom prediction and mitigation research spans at least fifty years, and there is a plethora of material published on the matter. This section is limited to literature that is widely known and to literature that is utilized in the text.

2.1 Sonic Boom Prediction

The first major work in sonic boom analysis was published by Gerald Beresford Whitham [45] in 1952, where he introduced the "F-function" that relates the body geometry to the sonic boom signature through a linearized axisymmetric velocity potential function. This function encompasses the source distribution that appears in the solution of the linearized potential equation. The linear axisymmetric potential equation is

$$\phi_{rr} + \frac{1}{r}\phi_r - \beta^2 \phi_{xx} = 0 \tag{3}$$

which is a form of Laplace's equation. The solution for a finite length body in supersonic flow is given as

$$\phi = -\int_0^{x-\beta r} \frac{f'(t)dt}{\sqrt{(x-t)^2 - \beta^2 r^2}} \tag{4}$$

This solution is basically the superposition of solutions to infinitesimally spaced point sources representing the body. Superposition of solutions is possible due to the linearity of the partial

differential equation. This solution cannot be used directly in sonic boom analysis because it does not allow shock formation. Shocks are formed by intersecting characteristic surfaces. When they intersect, a multi-valued front called a "shock" forms. The characteristic rays for the above solution are straight and parallel lines due to the linear approach whereas in reality they intersect and curve at different rates. In two dimensional and linear axisymmetric flow, characteristic values are constants. In real flow, however, these characteristic values are variable themselves as well [61]. What Whitham did at this point was to keep the characteristic values constant as in linear flow but modify the paths of the characteristic lines to allow shock formation in the solution. The correct slopes of characteristic lines are taken directly from the exact speed of sound variation through Bernoulli's equation. The constant linear characteristic value for Eq. (4) is

$$\nu(x,r) = const. = x - \beta r \tag{5}$$

which is a family of straight lines with slope β. Whitham substituted Eq. (5) into Eq. (4). After the non-linear slope modification, Eq. (5) becomes

$$\nu(x,r) = const. = x - \beta r + c(\nu,r) \tag{6}$$

Function $c(\nu,r)$ is a very complicated integral given fully in Ref. [45]. Whitham then defined the F-function using Eqs. (4) and (6) as

$$F(\nu) = \int_0^{\nu} \frac{f'(t)dt}{\sqrt{\nu - t}} \tag{7}$$

Applying a linearized tangency boundary condition for smooth slender bodies of revolution gives [45, 62]

$$f(t) = \frac{S'(x)}{2\pi} \tag{8}$$

where $S(x)$ is the cross-sectional area of the body. Using Eq. (8) in Eq. (7), the F-function becomes

$$F(\nu) = \frac{1}{2\pi} \int_0^{\nu} \frac{S''(t)dt}{\sqrt{\nu - t}} \tag{9}$$

This is the standard form of the function for smooth meridian profiles. This version is widely used in classical sonic boom analysis because of ease in integration. For cornered profiles, a more involved formulation was suggested by M. J. Lighthill through the use of Bessel functions and Heaviside mathematics [63]. Gottlieb and Ritzel [64] provided a simpler alternative to the Lighthill formulation for cornered shapes that is easily programmable. This alternative is called the "Modified F-function", which is a blend of the Whitham and the Lighthill formulations.

Whitham related the far-field ($\beta r/y >> 1$) pressure signal to this F-function by

$$\frac{\Delta p}{p_\infty} = \frac{\gamma M^2}{\sqrt{2\beta r}} F(y) \tag{10}$$

and the far-field bow shock strength by

$$\Delta p = 2^{1/4}\gamma(\gamma+1)^{-1/2}\left(M^2-1\right)^{1/8}\left\{\int_0^{y_0} F(y)dy\right\}^{1/2} r^{-3/4} \tag{11}$$

where $F(y_0) = 0$. The characteristic "y_0" is called the dividing characteristic that separates the characteristics that form the leading and the trailing shocks. This characteristic line is linear unlike the other disturbances, and does not coalesce with the others. For a three-shock signal, there are two dividing characteristics and so on. However, Whitham stated all signals eventually assume the N-wave shape at great distances, and only one dividing characteristic will remain. Due to this dividing property of the y_0 characteristic, the bow shock pressure computation involves the integral of F(y) only up to $y = y_0$. The terms preceding the radial distance term in Eq. (11) are all constants, meaning that the far-field bow shock strength is represented by a constant, determined by the geometry, and the free stream Mach number, and varies inversely with the 3/4th power of distance from the aircraft. Note that through Eq. (10) $\Delta p = 0$ when $y = y_0$. The above expressions constitute the backbone of the classical sonic boom theory. Whitham showed that any intermediate (inner) shocks in the signal attenuate faster than the bow shock at a rate of $r^{3/2}$. He also shows that the wave drag is related to the F-function by

$$Drag = \pi\rho_\infty V_\infty^2 \int_0^\infty F^2(y)dy \tag{12}$$

The ARAP sonic boom prediction code developed by Hayes *et al*[43] uses the F-function as the starting solution for far-field sonic boom prediction. For complex geometries with lift, an equivalent area distribution based on the supersonic area rule and lift distribution is used to provide $S(x)$ for Eq. (9). The idea of an equivalent body of revolution that substitutes for a non-axisymmetric lifting body in the far-field was first introduced by Walkden in 1958 [65]. According to Hayes the non-linearities in sonic boom propagation are very weak and the use of linear geometric acoustics is a valid approach for tracing the signal along rays. Linear geometric acoustics is an asymptotic approach where the solution to start the signal propagation is required to be at an asymptotic state with negligible local non-linearities. The F-function is based on linearized supersonic flow and is already an asymptotic state. However, Hayes claimed that the range of the problem is large, and the cumulative effect of these locally negligible non-linearities on the ground level sonic boom signal become important. To account for this global non-linearity, Hayes used an "aging factor" calculated from the atmospheric conditions which distorted the signal as it propagated through the atmosphere. The distortion of the signal is based on the changes in the wave propagation speed as the signal travels through a stratified medium. The distortions are identified as shock coalescence, new shock formations, and the changes in distances between shocks. Hayes stated that the aging variable approach does not substitute for all the non-linear effects. He noted that the approach is not valid for Mach numbers above 2 where the non-linear effects are amplified significantly.

A similar sonic boom prediction method was developed by Thomas [44] using linear geometric acoustics and ray-tracing, known as the Thomas Waveform Parameter Method. Instead of using the F-function as the starting solution for propagation, Thomas used the near or mid-field pressure signal shape. Thomas defined the signal shape (the waveform) with geometric parameters defining heights and slopes in the waveform, and he used ordinary differential equations to compute the evolution of these parameters over the propagation distance. The Thomas method eliminates the use of an aging variable to account for cumulative global non-linearities. Instead, such effects are handled using the variation of speed of sound with the altitude in the underlying computations. Using the pressure signal initialization allows near-field experimental or computational pressure data to be used for sonic boom propagation. This is convenient when the near-field pressure data are available and the F-function is difficult to calculate. However, since the method uses linear geometric acoustics for propagation, asymptotic starting pressure data is required. In other words, the pressure data has to be sufficiently far from the aircraft to neglect local non-linearities. This critical distance is aircraft geometry dependent, and can be as low as one body length in the case of simple axisymmetric geometries, and as high

as fifty body lengths in the case of a complex realistic aircraft with non N-wave sonic boom shapes. This is discussed in detail in section 5.4.

PCBoom3 software developed by Plotkin [66] is based on the Thomas Waveform Parameter Method, and addresses sonic boom focusing. Here the initial starting data can be given either as the F-function or the pressure signature. The program has a graphical user interface and is widely used in industry for ground level sonic boom predictions. A variant of this program called MDBOOM provides F-function generation based on the supersonic area rule and equivalent area distributions including lift. MDBOOM addresses the azimuthal variations in the signal using a cross-flow multipole representation of the F-function based on George's formulation [9]. George extended the linear axisymmetric formulation in Eq. (3) to accommodate azimuthal changes by

$$\phi_{rr} + \frac{1}{r}\phi_r - \beta^2 \phi_{xx} + \frac{1}{r^2}\phi_{\theta\theta} = 0 \tag{13}$$

A simplified version of the F-function to be used with Eq. (13) is given by Page and Plotkin [67] as

$$F(\nu,\theta) = \sum_{n=0}^{\infty} F_n(\nu)\cos(n\theta) \tag{14}$$

which is a Fourier representation with the sine terms eliminated due to lateral symmetry. Here "n" is the order of the multipole where n = 0 is a simple source, n = 1 is a dipole, n = 2 is a quadrupole, etc. An axisymmetric geometry requires n = 0, a simple delta wing requires n = 1, and an X-wing configuration requires n = 2 as shown in Ref. [9]. For complex realistic aircraft, much higher multipole orders can be included for high fidelity representations of the cross-flow. This is still a linear approach with propagation based on geometric acoustics, and the starting solution set has to be at an asymptotic state. Page and Plotkin incorporated a CFD matching technique in order to use a high order non-linear CFD solution to derive the F-functions for asymptotic propagation. The CFD pressure data is interpolated onto a cylinder with its axis passing through the nose of the aircraft and aligned with the flight path. The pressure was then converted to an F-function approximation using a matching algorithm based on Eq. (10). For a simple wing body configuration at Mach 2 and 5^0 angle of attack, pressure data on a cylinder with

a 0.5 body length radius was reported to be sufficient for the matching procedure. For complex realistic aircraft however, Page and Plotkin determined that the matching radius should be much larger because the full effect of lift was not captured, resulting in underprediction of the far-field sonic boom pressure levels.

Siclari and Darden [68] developed an Euler code for sonic boom propagation using central differencing in the cross-flow and upwind differencing in the marching direction. The solutions were provided only up to eight body lengths. Atmospheric variations in temperature and pressure were not accounted for in the code, since they would be negligible over such short propagation distances. Grid adaptation was provided based on approximate grid error equidistribution, and focused on stronger shocks. Shock fitting was not provided and the computed shocks were somewhat dissipated although they agreed perfectly with experimental data.

Kandil *et al* [48] provided ground level sonic boom CFD solutions based on the full potential equation. The solver program non-linearly marches the complete three dimensional cross-flow field along the flight path, until the under-track signal reaches ground altitude. This full potential sonic boom propagation code was the first published CFD code to march the complete three dimensional sonic boom signal all the way to the ground in a stratified atmosphere. The computational grid was constructed around the region enclosing the shocks, forming a hollow cone that covered the entire distance from the aircraft to the ground. Atmospheric variations in temperature and pressure were accounted for by multi-blocking the domain in the axial (main-blocks) and vertical (sub-blocks) directions, and assigning each sub-block a different free stream temperature and pressure condition. A near-field Euler solution was used as the initial boundary condition. Unlike the cylindrical cut employed by Page and Plotkin, this code used a vertical slice downstream from the aircraft, and positioned normal to the flight direction. The distance of the Euler - full potential interface from the aircraft was dependent on the size of the wake, and the separation distance of the trailing shock from the wake boundary. A distance of 0.5 body lengths downstream of the tail was generally sufficient. Due to the irrotationality of the FPE, the wake was excluded from the computations. This is achieved by using a toroidal cross-flow grid with the outer radius larger than the bow shock radius, and the inner radius between the trailing shock and the wake boundary. Unlike the linear propagation codes, the FPE propagation code does not depend on the location of the starting solution. This is because FPE includes the non-linearities and performs the computations in three dimensions. Reference [30] presents a study on the sensitivity of FPE and ray-tracing methods to the starting solution location. Shock fitting and grid adaptation are essential elements in the code to ensure

that high fidelity shocks are computed all the way to the ground. Otherwise shocks are lost to numerical dissipation and marching cannot continue. Shock fitting is based on aligning the grid with the leading and trailing shocks. The alignment procedure is based on minimizing the error on the shock jump conditions across the grid surfaces representing the shocks, by checking on mass, momentum, and energy conservation in the normal direction across the grid surface elements. Shock fitting is used also in the near-field Euler computations where the solver and adaptation code work iteratively until convergence via shock jump errors is attained.

Kandil and Yang [49] presented solutions for the Baize-Coen HSCT configuration and Susan Cliff wing-body design using the FPE marching program. The Baize-Coen configuration is a conceptual supersonic passenger aircraft predicted to produce a shaped sonic boom on the ground, having a weak bow shock strength of 0.78 psf, followed by a ramp type pressure rise. FPE computations exhibit a stepped shock structure in the near-field that coalesces to form a signal that resembles the ramp shape at ground altitude. Comparison with the experimental data available in the Susan Cliff wing-body case shows excellent agreement with the FPE computations in the mid-field at $r/L = 3.6$. The FPE was able to capture details in the shock structure that were missing in the experimental data, specifically the shock emanating from the junction of the model and the sting.

Using the Euler/FPE method, Kandil *et al* [52] provided computational solutions for the ground level sonic boom signal of the SSBD, a modified F-5E aircraft built by Northrop Grumman for shaped sonic boom demonstrations. The near-field Euler solution was provided by Northrop Grumman, using 17 million grid points on a structured multiblock domain. Excellent agreement with the ground experimental signature was obtained, accurately predicting the non-linear flat top like signal shape.

Ozcer further developed the Euler/FPE framework [53]. An updated shock fitting and grid adaptation scheme named SFGA was developed and implemented both in the near-field Euler and the far-field full-potential computations. Instead of using the Rankine-Hugoniot shock jump criteria to determine the orientation of the grid surface elements that align with the shock surfaces, a Mach and density gradient based search algorithm was developed to identify shock points in the solution. The algorithm identified shock locations between two grid points, similar to a floating shock fitting approach, instead of snapping on available grid points or orienting available grid surfaces. These shock points were then used in a least-square surface fitting routine to generate the shock aligned grid surface. A data filtering algorithm was used in the shock detection routine to eliminate "bad" points that were incorrectly detected, and considered to be outliers in the least square fitting process. Such points degraded the quality of geometric

shock fitting when included. Using the SFGA algorithm, fitting for the interior shocks was also included, naturally suppressing the dissipation and dispersion errors for these shocks, thus eliminating the need for artificial dissipation in the full potential propagation code. The sub-block interface boundary condition was changed from velocity matching to averaging of the velocity potential from two adjacent blocks, improving the continuity of the solution across sub-block interfaces. Parallel processing was introduced via Message Passing Interface (MPI) by distributing the sub-blocks among multiple processors. In addition to reducing the computational time from several days to a few hours, parallelization also allowed for more sub-blocks to be solved. With more sub-blocks spanning the cross-flow, the jump in atmospheric conditions across sub-block interfaces was reduced and solution continuity and stability were improved. Automated shock detection and adaptation, automated sub-block addition with increasing cross-flow radius, and elimination of user defined artificial dissipation coefficients allowed fully automatic operation of the FPE marching code, making it an ideal design tool. Ozcer [53] provided near-field and mid-field Euler solutions for an axisymmetric double cone configuration taken from Ref. [7], covering a distance of 25 body lengths (L) from the object's centerline. Initial grid was generated without prior knowledge of the shock structure. To accommodate the merging shocks in a shock aligned structured grid topology, the computational domain covering 25L was divided into several stratified blocks in the vertical direction. At each block the number of cells between shocks was readjusted automatically using a fixed average cell width criterion to avoid cells coalescing into a singularity. A total of seven solution/adaptation cycles were run before the process terminated upon convergence of the shock jump criteria across shocks. Excellent agreement with experimental data from Carlson [7] was obtained at r/L = 6, 10, and 18. The two interior shocks were captured distinctly prior to merger, and the solution was free of oscillations, overshoots, or dissipation errors all the way to the outer boundary at r/L = 25.

Ozcer and Kandil [60] provided an unstructured grid adaptation method for near-field sonic boom computations. The grid adaptation software OptiGRID from Newmerical Technologies was used in this work with a custom-developed shock adaptation metric. The adaptation metric was a scalar computed from the flow field variables that distinctly identified shocks regardless of their strength. It was based on the normal Mach number across the shock. The idea of using the normal Mach number stemmed from Ref. [69]. This scalar enabled adaptation of the grid only around the shocks, ignoring any other high gradient flow features like wake vorticity, expansions, etc. The level of coarsening for non-shock flow phenomena was controlled by a user-specified parameter, in order to retain other essential flow features as shocks were refined. The shock detection metric also accounted for the shock weakening with distance

from the source, equalizing the density of adaptation close to and far from the source. This unstructured near-field sonic boom prediction method was a breakthrough because it insured high fidelity shock capture over the entire cross-flow using an economical grid size, starting from a coarse initial grid that was created without prior knowledge of shock locations and strengths. The surface definition and initial grid generation could easily be automated thus eliminating user time spent on grid generation. In CFD applications, 90% of user effort is spent generally on grid generation. With the method introduced in this paper this effort becomes trivial. The final adapted grid evolves as a part of the solution, where the solver and OptiGRID work iteratively until the signal shape on a desired data cut location has converged. Ozcer and Kandil presented the solution for SSBD using the unstructured grid methodology with an initial grid of only 270,000 nodes, requiring only eleven solution/adaptation cycles to reach the final solution. The final grid had only 500,000 grid points and the computational time required was about one hour using 16 CPUs. The predicted signal shape matched perfectly with the available experimental and computational results at 1.82 body lengths underneath the aircraft. A fixed set of adaptation parameters were determined for all geometries ranging from simple axisymmetric to complex and realistic 3D aircraft, making the methodology user friendly and automated for use in aircraft design.

Kandil and Zheng [54, 55] provided numerical solutions for sonic boom focusing, also known as the super-boom. The software they developed solved the non-linear non-conservative Tricomi equation using the frequency-domain scheme, a time-domain scheme, and a time-domain with overlapping grid scheme. A conservative form of the nonlinear Tricomi equation has been developed and solved as well, using a time-domain scheme. The four schemes have been applied to several incoming waves which include an N-wave, a Concorde aircraft wave, symmetric and asymmetric flat-top and ramp-top waves. In Ref. [56] a parametric study was carried out to investigate the effects of several software parameters on the sonic-boom focusing results obtained from the above listed solvers.

2.2 Shock Fitting and Grid Adaptation for Sonic Boom Prediction

Ground level sonic boom is caused by the near-field shock structure from a supersonic aircraft that propagates through the atmosphere. "Shock- fitting" is essential to obtain high fidelity CFD solutions of those shock structures. Shock fitting basically means to satisfy the proper physical Rankine-Hugoniot jump conditions across the discontinuity. Due to the approximate nature of CFD solvers and discritization errors, these conditions are not satisfied unless proper measures are taken. The classical method for shock fitting is to treat the shock front separately during computations by taking it as a grid boundary or a separate embedded data entity across which the shock jump conditions are enforced manually. This method is difficult to automate for a wide variety of realistic aircraft geometries with complicated shock structures where interacting, merging, and incomplete shocks occur. An alternative is aligning the grid element faces with the shock surfaces. Trepanier *et al*[70] presented a conservative shock fitting method of this type. They stated that when the solution was obtained using an "upwind approximate Riemann solver" where a one dimensional Riemann problem was solved across a cell face, grid-shock alignment produced the correct shock jump conditions. Roe's Flux-Difference Splitting is a suitable scheme in this case. Using an unstructured grid, shock jump conditions were shown to have been satisfied exactly when the triangular element edges were aligned with the shock from a two dimensional wedge. Comparisons with experimental data were also provided. In section 4, the same wedge problem is examined using the codes in the current study to validate the shock fitting capability.

Chung, Choi, Alonso, and Weide [71-73] demonstrated the use of "h-refinement" for grid adaptation, which refines the grid by dividing the available cells into smaller cells, using the Mach number in the pressure gradient direction to drive the adaptation mechanism. Near-field grids in these studies employed 3 to 7 million grid points clustered mostly underneath the aircraft for under-track signal extraction at up to $r/L = 1.125$. The solution method was based on a central-differencing scheme with artificial dissipation for shock capturing. Shock fitting was not maintained since the element faces are not necessarily aligned with the shock surfaces, and the solver was not an approximate Riemann solver. To adequately resolve the shocks underneath the aircraft, a high number of grid nodes were employed and grid adaptation was constrained to this region. The near-field signal captured here was not sharp, even with such a dense grid. The dissipation in the results and the high grid density could be due to lack of shock fitting.

Park [74] described a grid adaptation method using unstructured grids. The h-refinement method was used where the cells with error indices greater than a preset criterion were divided into smaller parts by node insertion. The adaptation was based on the intensity of errors in adjoint and flow variables. An adjoint variable could be selected as any particular response like lift or drag, and it was tied to the grid using an adjoint formulation. The error was computed as the difference between the linear and the non-linear interpolated values on an embedded mesh. Feature-based adaptation refers to adapting to high-gradient regions of a flow variable in the domain. For certain responses, adaptation on all high-gradient regions may not be necessary. Using the adjoint method, adaptation could be tailored to improve the accuracy of that specific global response without wasting additional grid points to adapt for all local high gradient regions in the flow field. Park demonstrated the adjoint based grid adaptation capability on isotropic grids for three dimensional transonic, subsonic, and incompressible flows, and extended the methodology to anisotropic adaptation for turbulent flows [75].

Gnoffo [76] reported that the use unstructured grid shortens the initial grid generation process from weeks to hours compared to structured grid generation. Concepts like multiblocking, overlapped blocking, and topological decisions to effect the blocking are immaterial in unstructured grid generation. Gnoffo stated that to provide a quality adaptation using structured grids, the initial grid topology needed to be designed carefully, taking into consideration where the shocks were expected. This clearly requires prior knowledge of shock locations. Comparing feature-based and adjoint based adaptation for drag prediction for an airfoil in supersonic flow, Gnoffo showed that the adjoint based adaptation required one tenth as many nodes to reach the accuracy of the feature-based adaptation. Gnoffo and White [77] emphasized the importance of aligning grid element faces with the shock fronts to avoid abrupt entropy fluctuations along the streamlines that pass through the shocks. They provided this alignment by feature-based adaptation.

Bibb *et al* [78] presented an anisotropic feature-based grid adaptation for the refinement of shocks using sample applications at Mach 2, 6, and 10. A Spring-analogy method was used to provide node movement to high gradient regions like shocks, where the forcing function used was the temperature gradient. Node movement provided a much more efficient grid compared to those adapted using h-refinement alone, where the available nodes were clustered towards shocks to increase the shock accuracy. No new nodes were inserted and the problem size was maintained. Refinement and coarsening based on the gradient magnitude was also used in case the node movement was insufficient to resolve the shocks to the desired level. H-refinement and coarsening was applied in this case. Grid anisotropy was provided by node movement, where the

cells could be stretched along the shocks. Anisotropy was determined by the Hessian of Mach number. Stretched cells helped to maintain a small grid size. Node movement also provided grid smoothing to fix badly shaped cells that could degrade convergence of the flow solution. Edge swapping was provided to increase the quality of the cells. Grid adaptation parameters controlled the number of solution / adaptation cycles, grid modification relaxation factor, mesh size, the level of anisotropy, maximum cell aspect ratio, and maximum/minimum edge length. No stopping criterion was provided for terminating the solution / adaptation procedure. For the Mach 6 case with full gradient based adaptation, a total of six solution/adaptation cycles were used. The total number of solver iterations was about 12,000. The density gradient was used as the adaptation feature. Maximum allowable cell aspect ratio was set at five. Initial grid for this case had 105,000 points and the final grid had 610,000 points. For the Apollo capsule case in Mach 10 flow, three solution/adaptation cycles were used with density gradient as the adaptation feature. The maximum allowable cell aspect ratio was 10. The initial grid had 630,000 points and the final grid had 5 million points. The adaptation mechanics used in the current dissertation and in this reference are very similar with the exception of the choice of the adaptation feature. Thus the numbers listed above are useful benchmark data for performance comparison.

Jones *et al* [79] provided solutions up to 20 body lengths for the double cone configuration mentioned earlier, using unstructured CFD and adjoint-based grid adaptation. The results of this study are used here as reference computational data for comparison in section 5.1. Similar to Ozcer's [53] approach, the axisymmetric grid was created as a wedge covering only a meridian slice in the full three dimensional domain. The adjoint variable was the integral of over-pressure on a cylindrical surface with radius equal to the target signature distance. For Mach 1.26, the cylinder radius was r/L = 18, and for Mach 1.41, it was r/L = 20. These locations corresponded to experimental data locations in Ref. [7]. The adjoint-based grid adaptation was done via the h-refinement method described above. While h-refinement increases the grid density about the shocks, it does not provide alignment of element faces with the shock surfaces unlike Hessian-based node movement and anisotropy. Jones stated that feature-based adaptation required a fine initial grid to capture the shocks to some extent, so that the adaptation features become available. Generation of such a fine initial grid imposes several user difficulties, and more often than not requires prior knowledge of the shock locations. This was considered as a major drawback of feature-based adaptation and interrupts automation. Jones emphasized that with the adjoint-based adaptation there is no need for a fine initial grid or any prior knowledge of the shock structure. The results of the current dissertation show that feature-based adaptation can actually work for coarse initial grids without any prior knowledge of shock structure. Besides,

the cell stretching along the shocks, cell/shock alignment, and the resultant shock fitting is provided only by the Hessian-based adaptation. For the double cone, the initial grid used in Ref. [79] had 4400 nodes. Twenty solution / adaptation cycles were used in the Mach 1.26 case with a final grid of 400,000 nodes, and twenty-two cycles were used in the Mach 1.41 case with a final grid of 742,000 nodes. The two distinct shocks captured by Ozcer [53] that do not appear to have merged at r/L = 10 are computed as a single dissipated shock in Ref. [79]. The overshoots in the computed signals were reported to be due to the lack of flux-limiters in the flow computations.

An efficient Hessian-based unstructured grid adaptation strategy with signal pre-processing for shock enhancement was outlined by Remaki *et al* [80]. The methodology was demonstrated on coarse initial grids created without prior knowledge of the shock locations. The grid adaptation scheme rapidly generated shock adapted grids providing high fidelity shocks under ten solution / adaptation cycles. The adaptation methods outlined in this paper were implemented in OptiGRID unstructured grid adaptation software developed by Newmerical Technologies, Montreal, Canada. The adaptation mechanics included node movement, edge refinement and coarsening, and edge swapping. The adaptation was driven by equi-distributing the approximate error based on the Hessian of a scalar. The Hessian matrix is composed of the second derivatives of the scalar, which are proportional to the leading term in the truncation error of most numerical flow solvers using first order approximations. Thus it provided a reasonable index to measure the error due to grid placement. Hessian based error also provided directional adaptation where the eigenvectors provided the direction and the eigenvalues the distance for node movement. This allowed formation of anisotropic cells and helped to keep the grid size small. Signal preprocessing using deconvolution sharpened the weak shocks to improve their presence in the solution. Solution smoothing by convolution was used before and after the deconvolution process to clean the possible noise in the solution such as overshoots and oscillations. Signal pre-processing cut down the total number of solution / adaptation cycles by enhancing the shock presence and making them detectable even though they are not obvious in the original solution. A metric modification technique that influences the node movement in the velocity gradient direction around the vicinity of the discontinuities accelerated the node clustering towards the shocks. Signal pre-processing and metric enhancement together allowed feature-based adaptation to start and rapidly progress using coarse initial grids.

Ozcer and Kandil [60] provided near-field adapted unstructured grid solutions for the double cone, a delta wing, and the F-5E aircraft modified with the Shaped Sonic Boom Demonstrator using OptiGRID. A flow field scalar originated in this paper was used with OptiGRID to provide control on how much to adapt for the non-shock flow phenomena. The

shocks away from the body are considerably weaker compared to the non-shock flow features in the immediate vicinity of the body. While trying to adapt for the shocks at a distance from the source, an unnecessary level of adaptation usually takes place near the aircraft, increasing computational costs. This is one of the major drawbacks of feature-based adaptation, as mentioned earlier. The metric developed in Ref. [60] controlled the level of adaptation for the unshocked regions allowing the nodes to be used primarily for the shocks. This provided notable savings in the grid sizes and computational time and resources. The metric also provided rapid progression of adaptation towards the coarser regions where the shocks are yet unresolved, completely alleviating the problems associated with coarse initial grids and feature-based adaptation. Shocks were evenly adapted for regardless of their strength or distance from the source. Again, this provided savings in the grid size by avoiding excessive adaptation for strong shocks while resolving the weaker ones. For the double cone cases, Ozcer and Kandil used only eleven solution / adaptation cycles to reach a final grid of 500,000 nodes covering a domain up to r/L = 21. For the SSBD case, only eleven cycles and 500,000 nodes were used to obtain a crisp detailed shock signal in the entire cross-flow (above and below the aircraft) up to 1.5 body lengths form the aircraft. The parameters controlling the adaptation were set such that the method worked for the simplest axisymmetric configuration and the complex SSBD aircraft without case dependent software "tweaking". This in turn facilitated automation and made the methodology an ideal design tool for sonic boom mitigation research. The studies in this paper are fundamental to the current dissertation, and are explained in detail in sections 4 and 5.

2.3 Sonic Boom Mitigation

Carlson [7] provided experimental and theoretical results for eight different axisymmetric models, all with same length and base radius, to compare them in the context of sonic boom mitigation. Using single cone-cylinder configurations, he investigated the parametric effect of the conic section length and the half cone angle on the sonic boom signal. Using a power law type meridian body profile where the geometry was defined by

$$R(x) = R_B\left(\frac{x}{L}\right)^N \tag{15}$$

Carlson looked into the effect of nose bluntness on the pressure signal. The eighth geometry used was the double cone configuration, formed by two cones connected by a cylinder in the middle. This geometry is referenced repeatedly throughout the current dissertation, and is used for validations in several other references [53, 60, 79, 81, 82]. Carlson showed that the blunt nose has higher near-field pressures and drag, but lower far-field pressure impulse. Pressure impulse is the integral of over-pressure in the leading part of the sonic boom signal where $\Delta p > 0$. He stated that since the theory of sonic boom prediction is linear and axisymmetric, sonic boom mitigation efforts are limited to and constrained by these assumptions.

Busemann [8] suggested the use of quadrupoles for sonic boom mitigation. The multipole representation for sonic boom computation could be used to manipulate the flow field to produce negative pressure effects underneath the aircraft. Lift is usually generated as one-half pressure towards the ground and half suction towards the sky. To represent this behavior, at least a dipole system with a source below and a sink above the body is required. "The sonic boom signal heard on the ground is nature's way of reflecting the lift force exerted by the air". The dipole configuration could be extended to a quadrupole by having two sources side by side on the flight path axis, one sink below, and one sink above the flight path. This way the sink strengths can be adjusted to provide more suction towards the sky and less pressure towards the ground, while preserving the net lift force. Busemann stated that it was essential to have a "sound idea of the multipoles and their effect on lift and sonic boom" before attempting optimization studies for sonic boom mitigation.

George [9] presented the idea of lateral distribution for sonic boom minimization. The idea was to excite multipoles on the sides of the aircraft that could produce negative effects underneath. He showed an example quadrupole configuration using X-shaped delta wings with opposing lift surfaces. George stated that the boom strength due to lift was not be reduced in this way, but the volume generated boom was reduced. He mentioned that addition of higher order multipole contributions increased the wave-drag, and concluded that sonic boom mitigation would inevitably increase drag. This is similar to the findings of Carlson for the axisymmetric case. Hence drag increase should be expected in the optimization of both axisymmetric and three dimensional wing-like shapes for sonic boom mitigation. Last but not least, George stated that the multipole approach cannot relate the far-field signal to a unique geometry, meaning that many solutions can be found giving the same far-field signal with different aerodynamic shapes and multipole configurations.

Howes [10] pointed out that a sine-wave like signal would be the best for the auditory response of humans. However, the sonic boom signal almost always ends up in an N-wave with two shocks. Thus the best signal would be a sine-wave cycle bounded by shocks. Such a signal can be approximated by a shock wave for the bow shock, a ramp type increase, a linear expansion, a second ramp type increase and a trailing shock.

Koegler [11] suggested that since the intermediate shocks attenuate with $r^{3/2}$ in contrast to the bow shock attenuation factor of $r^{3/4}$, the bow shock could be segmented to place some of its energy in the intermediate shocks. With a faster rate of attenuation, the intermediate shocks could help increase the rate of mitigation of the whole sonic boom signal with the distance from the source. Koegler also pointed out that in his mitigation efforts some drag increase was observed. However, he stated that since the leading shock strength was ultimately tied to the area under the F-function up to $y = y_0$ (Eq. (11)) and the drag is tied to the area under the F^2 curve (Eq. (12)), it could be possible to avoid drag increase by careful adjustment of the F-function.

Resler [12] briefly explained the sonic boom mitigation and lift generation properties of a biplane with the lower wing parallel to the flow direction, and the upper wing placed at an angle of attack. The upper wing was supposed to provide the lift while the lower wing would cancel the shocks generated by it. Resler showed that while the geometry creates no sonic boom at zero angle of attack, it also fails to generate lift. The positive first order lift created by the inclination of the upper wing was canceled by a second order negative lift caused by the shock cancellation process. This indirectly showed that a lifting boomless configuration was unlikely.

Barger and Jordan [13] presented a method to design axisymmetric bodies by continuously increasing their volume without affecting the peak overpressure or the pressure impulse. They achieved this by inserting a zero overpressure segment in the sonic boom signal separating the positive (leading) and the negative (trailing) sections of a generic N-wave. To generate such a signal, multiple pairs of balancing positive and negative lobes were inserted into the original F-function. From the F-function, Barger and Jordan used an inverse method to compute the geometry that would create the additional lobes. The length of the axisymmetric shape could be extended this way by adding as many lobe pairs as needed to reach the required volume. The method could be extended to infinity, however, practical limitations on the slenderness apply in reality. If the volume could be increased without increasing the pressure levels, a geometry that already meets the sonic boom limitations could be modified to increase its volume sufficiently for a feasible passenger aircraft.

Ferri [14] presented bi-plane conceptual configurations for transport aircraft that are 300 ft. in length and predicted to generate boom levels as low as 0.5 psf on ground. He stated that

sonic boom is inevitable since lift has to be generated, but it could be reduced to meet certain criteria. With the bi-plane configuration suggested, the wing area is distributed to two sets of wings. Two sets of wings at different vertical stations increased the effective length of the lift distribution. The upper wing acted like a tandem wing placed downstream at the same level as the lower wing, traversed along the Mach lines. The wings were to be connected by rigid end-planes, creating a box like structure. The rigidity eliminated the need for structural enhancement that would increase the empty weight of the aircraft. The wings were staggered in the axial direction to avoid interaction and choking of the flow at transonic speeds. With such a configuration, Ferri claimed that a 300 ft. aircraft weighing 460,000 pounds and flying at 60,000 ft. at Mach 2.7 produces only 0.5 psf sonic boom pressure at ground level. The analysis was based on the equivalent area distribution and Whitham's linear, axisymmetric F-function method. With lighter aircraft to fly short-range missions, the pressure levels can be reduced further to meet the 0.3 psf criterion. Ferri also suggested that a low-lift flight profile could be followed over a city by first pulling up to a higher altitude and following a descent path until the city was cleared.

Hague and Jones [15] optimized the power-body shapes defined by Eq. (15), using various search algorithms. Of the nine search algorithms they tested, the steepest descent method was one of the most inefficient, where the solution usually ended up oscillating about the ridges of the response surface. This remark is taken into consideration in the current dissertation to avoid relying on steepest descent searches. Instead, high order non-linear models are used as a part of response surface methodology. Hague and Jones used the usual linear F-function theory for the prediction of the sonic boom signals produced by the bodies they optimized. The response being minimized was the peak over-pressure in the overall signal. Constraints were applied on the length and base radius as $L = 4$ and $R_B = 0.25$ for all shapes tested. In the near-field the $N = \frac{3}{4}$ power-body was the optimum design, whereas in the far-field the optimum was with $N = \frac{1}{4}$. N is the power in Eq. (15). $N = 0.79$ produced a true flat top signal at $r/L = 10$. A CFD solution using structured grid without shock fitting is provided in Ref. [83] for the $N = 0.79$ body, which shows the same flat-top signal predicted by non-linear calculations.

The most widely cited sonic boom minimization theory was set forth by Seebass and George [19]. The methodology was based on minimizing selected features of the F-function, depending on the minimization scenario. Scenarios could be listed as a signal with no shocks, with a flat-top, and with minimum over-pressure and/or impulse. Seebass and George stated that since F(y) has to be positive somewhere in the signal, best pressure reduction is obtained by making F(y) as large as possible as early as possible, then reducing it down to minimal levels. Such a signal would correspond to a strong bow shock with high wave drag coming from a blunt

nose. Reductions in over-pressure levels achieved with this method were said to increase the pressure impulse. If the impulse is unimportant, significant reductions in pressure levels could be achieved using the sonic boom minimization methodology of Seebass and George. Northrop Grumman's SSBD was designed using this theory to mitigate the bow shock of the original F-5E configuration and produce a flat-top signature at ground level [1]. Darden [20] extended the work of George and Seebass to include nose-bluntness relaxation. This allowed the theory to have control over the portion of the F-function defining the nose shape to provide a compromise between low sonic boom and low drag.

Crow and Bergmeier [21] looked into active sonic boom control using an unsteady approach, where the velocity and the lift distribution of the aircraft were changed periodically. The velocity change attenuated the boom significantly by forming it into a prolonged series of weak reverberations, however, the amplitude of the accelerations required were reported to be impractical. Periodic changes in lift distribution, while keeping the mean lift center fixed changed the signal shape significantly, but did not reduce the peak over-pressure levels.

Use of genetic algorithms is becoming more popular for aircraft design optimization to reduce sonic boom [33, 71, 73, 84-86]. The parameters defining the geometry are used as genes during crossover breeding for new generations. F-function sonic boom prediction was used in all of these studies, where the objective was to minimize the ground level peak pressures while keeping the drag within a feasible limit. Genetic algorithms are helpful in avoiding local minima traps unlike the gradient based methods; however, tens of thousands of function evaluations may be necessary as the number of generations increase. Such a requirement for a high number of runs prohibits the use of computationally expansive CFD based non-linear sonic boom prediction tools. Furthermore, genetic algorithms do not necessarily give the user a detailed opinion on how and to what level a factor affects the responses, since no models relating the response to the changes in design variables are produced. This can rule out the benefits of engineering intuition and aerodynamic design experience in the optimization process.

Examples using response surface methodology for design optimization can be found in references [26, 31, 37]. These studies look into the effects of a large variety of geometric parameters defining a complete aircraft geometry. The parameters include engine placement settings, wing sweep, aspect ratio, twist, thickness, etc. The methodology followed in general is to start off with a "good" candidate design before performing parametric modifications. Similar to many other sonic boom optimization methods, the F-function and equivalent area method was used for ground level sonic boom signal prediction. The experimental design was a central composite design with 35 factors in a 3-level configuration with a total of 1025 runs. The starting

baseline configuration has a maximum over-pressure of 1.3 psf whereas the optimum solution was 1.0 psf.

Unique designs for sonic boom mitigating concepts were proposed by numerous researchers. Karr *et al*[33] proposed a keel type structure attached underneath the nose of the aircraft that looks like a protruding fin. This structure would alter the flow field such that the effect of having a long nose spike (phantom spike) would be simulated. The keel component was considered structurally superior to an equivalent long and thin spike. Having a spike-like structure basically extends the aircraft length, smoothes out the area distribution, weakens and pushes the bow shock upstream. Gulfstream Aerospace [4, 38, 40] proposed and patented the "Quiet Spike" which is an extendable boom placed at the nose of an aircraft for sonic boom mitigation. When the spike is fully extended in supersonic cruise, the leading bow shock was divided into a series of weaker shocks. Since the intermediate shocks attenuate more rapidly, this method helped increase the mitigation rate with distance from the aircraft. The design and analysis of the spike configuration had been done using an axisymmetric method of characteristics for the near-field, and the Thomas waveform method for the far-field. The sonic boom mitigation capability of the spike was demonstrated using Euler CFD with 10 million grid points for a spike / wing / body configuration. The spike component extended 30% of the entire aircraft length [87]. It was tilted down towards the flight path to reduce its local angle of attack and help delay the coalescence of multiple shocks. With the addition of Quiet Spike, the signal of the original baseline aircraft configuration of Gulfstream with 0.4 psf bow shock and 0.6 psf peak pressure was modified to one with 0.15 psf bow shock followed by several shocks reaching a maximum at 0.5 psf peak pressure. Lyman and Morgenstern [39] looked into bending the wing surfaces behind the nacelle shock to create expansion waves that would interact and cancel the inlet shocks. In their analysis they used Euler CFD with grid adaptation for near-field solution which was interfaced with the Thomas waveform propagation method through the use of multipoles as explained in Ref. [67]. The proposed design providing shock cancellation would decrease the predicted initial shock strength from 1.4 psf to 0.5 psf. This design was featured as Lockheed Martin's supersonic business jet proposal. Tam *et al*[22] proposed a new concept called Artificially Blunted Leading Edge (ABLE). This design had a slit or channel at the tip of the nose or the leading edge of a wing to remove the stagnant flow by allowing it to pass through. This would allow sustaining the detached bow shock with favored sonic boom mitigation properties, while eliminating to a great extent the pressure drag rise. Wintzer *et al*[88] looked into an oblique wing configuration where the wings were placed asymmetrically across the $y = 0$ plane. They stated that this is superior to the swing wing concept in a number of ways. The

oblique wing does not require such heavy machinery as the swing wing. It also maintains the same center of gravity and aerodynamic center as the sweep is modified, avoiding excessive trimming that could add to the sonic boom signal. It would be structurally more stable compared to highly swept wings, and would provide drag reduction by extending the longitudinal lift distribution. The design optimization process utilized Krigging and RSM. No sonic boom information is given in the paper to relate to the mitigation performance of such a wing configuration.

The most basic use of CFD in sonic boom mitigation design optimization in the current literature is for computing the axial lift distribution which is necessary to build the equivalent area distribution and the F-function. Examples have been presented in references [89-91]. The objective in these studies was to minimize the leading shock pressure strength. References [24, 72, 73, 85, 92] took it a step further and used CFD for near-field signal computations to provide detailed pressure signatures with three dimensional effects included, to be used subsequently in a Thomas waveform propagation method. Grid adaptation was essential in this case to provide a strong signal at the target distance from the aircraft. Even with grid adaptation however, the number of nodes used was usually on the order of 3 to 7 millions. Such a large grid size can be impractical for rapid design optimization. Moreover, the adaptation was provided only for the under-track portion of the signal. This would weaken the three dimensional cross-flow effects of the whole aircraft that influence the under-track signal.

Recent publications from Kandil's group [30, 57, 58, 93] focused on nose and wing optimizations using an axisymmetric nose shape with a meridian profile formed using linear segments (ramps), and a delta wing with 30° semi-vertex angle and a biconvex symmetric airfoil profile with 5% thickness-to-chord-ratio. The studies were carried out for Mach 2.0 flow. The effects of dihedral, camber, thickness, and nose angle were investigated using a 2-level factorial analysis, and an optimum configuration was reported in the light of steepest descent search. Meridian profile ramp length and angle effects on the interior shock location and strength were investigated. The emphasis here was to find a way to keep the nose short while providing effective sonic boom mitigation. Therefore the base diameter and the length of the nose shapes were constrained to fixed values. It was shown that the interior shock location and strength can be controlled via the ramp angles and lengths. The coalescence of shocks could be avoided by proper control of these parameters. The sonic boom signals were obtained using non-linear CFD with shock fitting and grid adaptation in general, using the in-house developed Euler/FPE sonic boom prediction methodology.

2.4 Summary

This dissertation addresses the cost of three-dimensional near-field sonic boom prediction for complex bodies first. In the current literature grids up to 7 million nodes have been used to resolve the shocks only underneath the aircraft. Still the shocks appear to be rounded off due to the dissipative nature of unstructured grids. No matter how fine the unstructured mesh, some dissipation is bound to occur when the mesh is refined by just adding more elements near the shocks. What should really be done is that cells should be aligned almost perfectly and stretched along the shock surfaces to minimize or alleviate dissipation errors. This is more of an adaptation effort compared to mesh refinement. Mesh refinement should be of second priority so that first the available grid node locations are optimized by moving the nodes and stretching the cells along the shocks. In this way, excessive increases in grid size can be avoided. The near-field of an aircraft does not consist only of the under-track region. The under-track signal is influenced greatly by off-centerline features such as the wings, nacelles, etc. To predict the correct contribution to the signal from these components, the cross-flow should also be accurately resolved. This immediately means that the grid size will be increased at least by one order. Clearly, solving a 70 million node grid for each design point is not going to be in the best interest of a designer. This is why CFD is not used to resolve the near-field shocks, but only for the lift computation in the current sonic boom mitigation literature. This dissertation proposes that a complete near-field shock structure for a complex aircraft geometry can be computed with only half a million grid nodes. CFD can then be included in the design sequence for near-field shock structure prediction for every design point.

Creating the appropriate grid to resolve the complete three dimensional cross-flow of a complex aircraft using only half a million grid nodes is a challenge. The grid adaptation methods in the current literature cannot provide this. The problem is extremely cumbersome especially if total automation in initial grid generation and grid adaptation is desired. The feature-based adaptation techniques in the literature require that the initial grid be dense to resolve the features to some extent before adapting. This is counter-productive since initial grids will be expensive to generate and will most probably be created with significant user effort. In addition to this, feature-based adaptation does not necessarily minimize the number of grid points used in the final solution. To resolve shocks towards the exit boundaries, the error thresholds will have to be reduced and excessive refinement will take place near the aircraft and for features that are of no interest. These problems associated with feature-based adaptation are mostly overcome by using

adjoint based adaptation where the error of an integral variable is tied to the grid and minimized. However, the complete three dimensional near-field shock structure from a complex aircraft cannot be lumped into a single integral variable without losing the signal details. The wave shapes are very complex and sensitive to local changes in the grid. The shocks are features of the flow, and to resolve them, a grid optimization methodology that is designed for adapting to flow features should be used. This dissertation proposes a feature-based adaptation technique that alleviates the problems associated with feature-based adaptation by using a specially formulated adaptation metric to detect shocks and isolate them from the rest of the flow features. Adaptation can start from a very coarse grid created with no prior shock location information, and it requires a maximum of ten solution / adaptation cycles to reach an optimum grid of about half a million nodes resolving the entire cross flow of a complex aircraft. In short, cost of CFD computations for complete near-field shock structure is greatly reduced, to a level that can be acceptable in industrial design loops. The particular addition to the literature here would be the formulation of the adaptation scalar metric used to achieve this.

Sonic boom prediction should be a 3-stage analysis where the signal propagation is divided into near-field, mid-field, and far-field. This is already the accepted approach in the literature, where the near-field is computed by Euler or Navier-Stokes equations, and the mid- and far-fields are computed either using full potential equations or the waveform propagation method. The ideal way is to go from Euler or Navier-Stokes to full potential, then from full-potential to linear propagation as the final stage. Currently there is no automatic way established to decide when to switch from one field to the other for any aircraft shape. This dissertation presents a case-independent strategy to decide when to switch from the non-linear to linear propagation methodology, by checking on the convergence of the ground undertrack signal shape as the nonlinear to linear switching distance from the aircraft is increased. The method is implemented in a computer program and applied to a delta wing and the SSBD cases for demonstration.

Using an affordable near-field CFD sonic boom prediction methodology and a 3-stage ground signal prediction methodology enables realistic shape optimization to be carried out using non-linear sonic boom prediction. The current literature refrains from using CFD to get design points, simply because of the aforementioned costs. This dissertation demonstrates the use of CFD for near and mid-field prediction inside design loops for shape optimization and sonic boom mitigation. Optimized shapes include an axisymmetric nose, a delta wing, and the SSBD aircraft modified with the optimized nose and a new set of wings optimized for minimum ground level sonic boom. The total number of the cases solved is on the order of a thousand, all obtained

using CFD for complete near-field analysis. The goal here is to demonstrate that CFD is no longer a prohibitively expensive tool to use in sonic boom mitigation design loops. For the three dimensional cases, one design point is obtained in less than an hour, and for the axisymmetric cases it is obtained in under 10 minutes. All stages including initial grid generation, surface definition generation, grid adaptation / solution coupling are automated and case independent, meaning that these design point computations can be done on a nightly basis. User time is allocated only for the analysis of the results that are acquired in a batch mode execution during off-user time.

Drag increase is inevitable with sonic boom mitigation, but the trade-off could be optimized. For axisymmetric shapes, the bluntness relaxation method attempts to achieve just this. This method is restricted with the limitations imposed on linear prediction methods however, and non-linear computations may provide better trade-off designs. The optimized axisymmetric nose shapes obtained in the current dissertation produce both reduced drag and lower ground level sonic boom strength than some classical solutions obtained in the literature for similar shapes. The particular addition to the literature in this case is the setting of the slope of the nose at the tip to the critical shock detachment angle at a given Mach number. By keeping the shock attached, the excessive drag penalty arising from the stagnant flow upstream of a blunt nose is avoided.

The parameters for wing shape optimization in the current literature are limited. In the current dissertation, non-linear span-wise camber and twist distribution are introduced as design parameters. Optimizing such distributions can be very expansive since several span-wise sections need to be optimized, and the design variables immediately increase at least by one order. An affordable way of optimizing these distributions is proposed and demonstrated, without necessarily increasing the number of design variables. Especially the non-linear span wise camber distribution proves to be very effective in minimizing sonic boom.

3. FORMULATION

The equations defining the flow physics used in the current dissertation are listed below. Euler equations are used in the near-field, and the full-potential equation is used in the mid-field. Formulations related to far-field linear propagation and the Thomas Waveform Method are not repeated here since the emphasis is on the use of CFD for sonic boom prediction. Readers may refer to references [43-45, 64] for detailed information on the linear methods. Some insight is given in section 2.1 via listing a summarized formulation of Whitham. Formulations for the unstructured grid adaptation scheme and optimization based on response surface methodology are included in the methodology listed in section 4. Symbols (x_1,x_2,x_3) and (x,y,z), and (ξ^1,ξ^2,ξ^3) and (ξ,η,ζ) are used interchangeably below, where equations are expanded.

3.1 Euler Equations

Near field computations are carried out using non-dimensionalized three-dimensional Euler Equations in General Curvilinear Coordinates (GCC). Starting in Cartesian coordinates (x_1, x_2, x_3), the conservative form of the non-dimensional, unsteady, compressible Euler equations is given by

$$\frac{\partial \mathbf{Q}}{\partial t} + \frac{\partial \mathbf{F}_1}{x_1} + \frac{\partial \mathbf{F}_2}{x_2} + \frac{\partial \mathbf{F}_3}{x_3} = 0 \tag{16}$$

where **Q** is the vector of conservative variables in Cartesian coordinates

$$\mathbf{Q} = \left[\rho, \rho u_1, \rho u_2, \rho u_3, \rho e\right]^T \tag{17}$$

and $\mathbf{F}_i$ are the inviscid flux vectors in Cartesian coordinates

$$\mathbf{F}_i = \left[\rho u_i, \rho u_1 u_i + \delta_{i2} p, \rho u_2 u_i + \delta_{i2} p, \rho u_3 u_i + \delta_{i3} p, \rho u_i \left(e + \frac{p}{\rho} \right) \right]^T \tag{18}$$

Here δ_{ij} is the Kronecker delta function, $\delta_{ij} = \begin{Bmatrix} 1 & i = j \\ 0 & i \neq j \end{Bmatrix}$. Pressure is related to the flow variables through the gas equation

$$p = (\gamma - 1)\rho \left(e - \frac{u_1^2 + u_2^2 + u_3^2}{2} \right) \tag{19}$$

The computational grids used in this study are shock and body oriented rather than a Cartesian system, hence the formulation needs to be extended to general curvilinear coordinates. The conservative form of the above equations is then given by

$$\frac{\partial \hat{\mathbf{Q}}}{\partial t} + \frac{\partial \hat{\mathbf{F}}_1}{\xi^1} + \frac{\partial \hat{\mathbf{F}}_2}{\xi^2} + \frac{\partial \hat{\mathbf{F}}_3}{\xi^3} = 0 \tag{20}$$

where

$$\hat{\mathbf{Q}} = \frac{\mathbf{Q}}{J} = \frac{1}{J} \left[\rho, \rho u_1, \rho u_2, \rho u_3, \rho e \right]^t \tag{21}$$

and

$$\hat{\mathbf{F}}_i = \frac{1}{J} \left[\frac{\partial \xi^i}{\partial x_1} \mathbf{F}_1 + \frac{\partial \xi^i}{\partial x_2} \mathbf{F}_2 + \frac{\partial \xi^i}{\partial x_3} \mathbf{F}_3 \right] \tag{22}$$

In terms of flow variables

$$\hat{\mathbf{F}}_i = \frac{1}{J} \left\{ \rho U_i, \rho u_1 U_i + \frac{\partial \xi^i}{\partial x_1} p, \rho u_2 U_i + \frac{\partial \xi^i}{\partial x_2} p, \rho u_3 U_i + \frac{\partial \xi^i}{\partial x_3} p, \rho U_i \left(e + \frac{p}{\rho} \right) \right\}^t \tag{23}$$

Here U_i is the contravariant component of velocity which is defined by

$$U_i = \frac{\partial \xi^i}{\partial x_1} u_1 + \frac{\partial \xi^i}{\partial x_2} u_2 + \frac{\partial \xi^i}{\partial x_3} u_3 \tag{24}$$

and $1/J = J^*$ is the Jacobian of the coordinate transformation. For a stationary mesh,

$$J^* = \begin{vmatrix} x_\xi & x_\eta & x_\zeta \\ y_\xi & y_\eta & y_\zeta \\ z_\xi & z_\eta & z_\zeta \end{vmatrix} = x_\xi \left(y_\eta z_\zeta - y_\zeta z_\eta \right) - x_\eta \left(y_\xi z_\zeta - y_\zeta z_\xi \right) + x_\zeta \left(y_\xi z_\eta - y_\eta z_\xi \right) \tag{25}$$

The dimensionless variables of the Euler equations are defined as

$$\rho = \frac{\tilde{\rho}}{\tilde{\rho}_\infty}, \quad a = \frac{\tilde{a}}{\tilde{a}_\infty}, \quad u_i = \frac{\tilde{u}_i}{\tilde{a}_\infty}, \quad p = \frac{\tilde{p}}{\tilde{\rho}_\infty \tilde{a}_\infty^2}, \quad \rho e = E = \frac{\tilde{E}}{\tilde{\rho}_\infty \tilde{a}_\infty^2} \tag{26}$$

where "~" stands for dimensional values. With these non-dimensionalizations, the free stream values become

$$a_\infty = 1, \quad \rho_\infty = 1, \quad p_\infty = \frac{\rho_\infty a_\infty^2}{\gamma} = \frac{1}{\gamma}, \quad E_\infty = \frac{p_\infty}{\rho_\infty (\gamma - 1)} + \frac{V_\infty^2}{2} = \frac{1}{\gamma(\gamma - 1)} + \frac{M_\infty^2}{2} \tag{27}$$

Euler equations in GCC are solved using Roe's FDS scheme. This scheme ensures that all the fluxes are upwinded, by checking on eigenvalues of the Jacobian matrices. These eigenvalues are actually the slopes of the characteristics of the compatibility equations for Euler flow. A positive eigenvalue is the positive slope of a characteristic direction which is called right running and is to be backward differenced. On the other hand, a negative eigenvalue is for a left running characteristic and it should be forward differenced. Such an upwinding procedure is very robust for all subsonic, transonic, and supersonic flows. Such a procedure has implicit artificial dissipation due to the one sided difference operators and it dampens the oscillations that appear near discontinuities like shocks. No external user input is necessary to control this numerical dissipation. The details and the derivation of the scheme used in CFL3D and FUN3D can be found in Ref. [94].

3.2 Full-Potential Formulation

The conservative form of the steady compressible full potential equation in Cartesian coordinates is given by [95]

$$\frac{\partial(\rho u_1)}{\partial x_1}+\frac{\partial(\rho u_2)}{\partial x_2}+\frac{\partial(\rho u_3)}{\partial x_3}=0 \tag{28}$$

where

$$u_1=\phi_x \quad u_2=\phi_y \quad u_3=\phi_z \tag{29}$$

and density is given by the isentropic relation

$$\rho=\left[1-\frac{\gamma-1}{2}M_\infty^2\left(\left(u_1\right)^2+\left(u_2\right)^2+\left(u_3\right)^2-1\right)\right]^{1/\gamma-1} \tag{30}$$

where M_∞ is the free stream Mach number. When density is normalized by the free stream value, speed of sound is given by

$$a^2=\frac{\rho^{\gamma-1}}{M_\infty^2} \tag{31}$$

In generalized curvilinear coordinates, the conservative form of the compressible FPE takes the form [48, 49]

$$\left(\frac{\rho U_1}{J}\right)_\xi+\left(\frac{\rho U_2}{J}\right)_\eta+\left(\frac{\rho U_3}{J}\right)_\zeta=0 \tag{32}$$

U_m are the contravariant velocity components defined by

$$U_m=g^{m1}\phi_\xi+g^{m2}\phi_\eta+g^{m3}\phi_\zeta \tag{33}$$

The elements of the symmetric contravariant metric tensor, g^{mn}, are given by

$$g^{mn} = \frac{\partial \xi^m}{\partial x_1}\frac{\partial \xi^n}{\partial x_1} + \frac{\partial \xi^m}{\partial x_2}\frac{\partial \xi^n}{\partial x_2} + \frac{\partial \xi^m}{\partial x_3}\frac{\partial \xi^n}{\partial x_3} \tag{34}$$

Finally, the density is redefined in the curvilinear system by

$$\rho = \left[1 - \left(\frac{\gamma - 1}{2}\right) M_\infty^2 \left(U_1\phi_\xi + U_2\phi_\eta + U_3\phi_\zeta - 1\right)\right] \tag{35}$$

In the full potential propagation code FPM3D, the ξ (axial) coordinate is aligned with the flight path which is also parallel to the x-axis. This is the marching direction, and the first term in Eq. (32) is approximated by second order backward differencing. The other two terms represent the cross-flow and they are central differenced. The upwinding is provided by performing the density computation in the direction of local characteristics. As mentioned earlier, this procedure produces the correct implicit numerical dissipation term equivalent to that of one sided differencing to suppress the dispersion errors which cause oscillatory behavior of the solution about the shocks. The density biasing is type-differenced, meaning that biasing is applied when the equation behavior is hyperbolic and not applied when it is elliptic. Although the flow in the cross-flow directions (y,z) is purely subsonic when a Cartesian system is used, it is of mixed type with shock aligned curvilinear coordinates. In FPM3D, $\xi^2 = constant$ surfaces are aligned with shocks, and the contravariant velocity component, U_2 *becomes* normal to the shock. Since the flow switches from supersonic to subsonic in the normal direction across a shock, it switches from hyperbolic to elliptic in nature along the ξ^2 coordinate line. The details of the computational scheme can be found in Refs. [48, 49, 95-97]. Ozcer [53] provides details of the derivations omitted in those references to provide an in depth analysis of the scheme.

3.3 Euler/Full-Potential Interface

The Euler velocity components are converted into the velocity potential using a simple computational scheme on an interface cut taken downstream of the aircraft. The interface cut is a toroidal domain excluding the wake with its strong vorticity. This is necessary for the full-potential iterations to converge since this equation assumes the flow is irrotational. Figure 2 shows an example interface cut used in SSBD computations. The left pane shows the vorticity magnitude whereas the right pane shows the shocks using a simulated Schlieren view created by taking the natural log of density gradient magnitude. The dark bands are shocks. Weaker shocks are not visible in this plot due to the adjustment of the color map to clarify the strong leading and trailing shocks. The strong vorticity caused by the jet flow is confined to a small radius downstream the tail of the aircraft. If the case was solved using viscous flow, entrainment would have caused the strong vortical region to be larger. The inner boundary of the toroidal interface grid is conveniently placed between the trailing shock and the strong vorticity. Outer boundary radius is kept larger than that of the leading shock with a reasonable clearance. The vorticity is not zero on the rest of the interface plane, but is approximately 0.1 in average which is at least one order smaller than the free stream velocity magnitude. Hence the irrotationality assumption for this region is reasonable [48, 49].

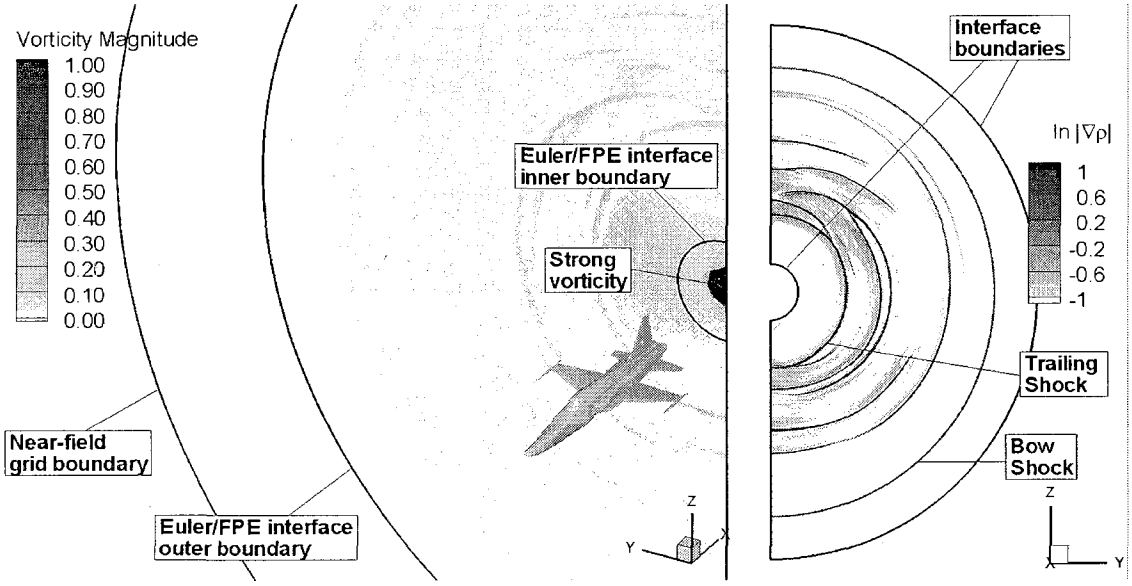

Figure 2: Vorticity magnitude (left), the shocks (right), and the toroidal interface cut at x/L = 1.5.

The interface cut is normal to the flight path, and has three cross-flow planes (i-planes). The computation of the velocity potential from the Euler velocities is done by rewriting the FPE (Eq. (32)) in terms of ϕ_η and ϕ_ζ as unknowns, and using the remaining terms as source terms on the right hand side [48, 49]

$$\frac{\partial}{\partial\eta}\left[\frac{\rho}{J}\left(g^{22}\phi_\eta + g^{23}\phi_\zeta\right)\right] + \frac{\partial}{\partial\zeta}\left[\frac{\rho}{J}\left(g^{32}\phi_\eta + g^{33}\phi_\zeta\right)\right] = RHS \tag{36}$$

where

$$RHS = -\frac{\partial}{\partial\xi}\left[\frac{\rho}{J}\left(g^{11}\phi_\xi + g^{12}\phi_\eta + g^{13}\phi_\zeta\right)\right] - \frac{\partial}{\partial\eta}\left[\frac{\rho}{J}\left(g^{21}\phi_\xi\right)\right] - \frac{\partial}{\partial\zeta}\left[\frac{\rho}{J}\left(g^{31}\phi_\xi\right)\right],$$

and RHS is calculated by deriving $\phi_\xi, \phi_\eta, \phi_\zeta$ from u_1, u_2, u_3 through

$$\begin{Bmatrix}\phi_\xi\\ \phi_\eta\\ \phi_\zeta\end{Bmatrix} = \begin{bmatrix}x_\xi & y_\xi & z_\xi\\ x_\eta & y_\eta & z_\eta\\ x_\zeta & y_\zeta & z_\zeta\end{bmatrix}\begin{Bmatrix}u_1\\ u_2\\ u_3\end{Bmatrix} \tag{37}$$

The derivatives with respect to η and ζ on the left hand side of Eq. (36) are central differenced, and ξ derivatives are first order backward differenced. After finding ϕ on the third plane, it is found on the 2nd and first planes by,

$$\phi_i = \phi_{i+1} - \phi_\xi \tag{38}$$

When the conversion process is completed, results are verified by recalculating velocity components from the newly computed velocity potential, and comparing them to the original Euler solution. The error of conversion is computed at each grid point on the interface by

$$\%Error = \left(\frac{\left|u_{Euler} - u_{FPE}\right|}{u_{Euler}}\right)\cdot 100 \tag{39}$$

This error is largest near the inner boundary of the toroidal interface where some wake effects remain. FPE smears out the vorticity in this region due to its irrotational nature, creating a difference with the original Euler solution. This error is immaterial for the sonic boom problem and is therefore ignored.

3.4 Boundary Conditions in Full-Potential Marching

The outer conical boundary is the given free stream conditions since it is upstream of any disturbance. The inner conical boundary is not far enough from the trailing shock to assign free stream conditions, thus an extrapolation boundary condition is applied here. The $y = 0$ boundaries are given symmetry condition. No boundary conditions are applied at the downstream end of a main-block in the marching direction since the flow is supersonic. The downstream boundary of a preceding main-block is used as the upstream boundary condition of the succeeding main-block by overlapping them to share three cross-flow planes. At this point the free stream atmospheric conditions are modified since the altitudes of the center points of the sub-blocks have changed. To reflect the effect of the atmospheric condition change on the velocity potential data that resides on the overlapped main-block interface planes, the *dimensional* over-pressure is matched by [49]

$$\dot{p}_A^* - \dot{p}_{A\infty}^* = \dot{p}_B^* - \dot{p}_{B\infty}^* \tag{40}$$

where A and B refer to sub-blocks upstream and downstream of the main-block interface, respectively. Using the isentropic relation

$$\frac{p}{p_\infty} = \left[1 + \frac{\gamma - 1}{2} M_\infty^2 \left(1 - \phi_x^2 - \phi_y^2 - \phi_z^2\right)\right]^{\frac{\gamma}{\gamma - 1}} \tag{41}$$

Eq. (40) is rewritten as

$$\dot{p}_{A\infty}^* \left\{\left[1 - \frac{\gamma - 1}{2} M_{A\infty}^2 \left(V_{T,A}^2 - 1\right)\right]^{\frac{\gamma}{\gamma - 1}} - 1\right\} = \dot{p}_{B\infty}^* \left\{\left[1 - \frac{\gamma - 1}{2} M_{B\infty}^2 \left(V_{T,B}^2 - 1\right)\right]^{\frac{\gamma}{\gamma - 1}} - 1\right\} \tag{42}$$

where $p^*_{A\infty}$ and $p^*_{B\infty}$ are the dimensional free stream pressures at sub-blocks A and B; and $V_{T,A}$ and $V_{T,B}$ are the non-dimensional total velocities. The only unknown here is $V_{T,B}$. The first step of matching is setting $\phi_A = \phi_B$ on the third plane of the interface. This is acceptable since ϕ is always defined in terms of a constant. Then the following is true on the third plane, using the definition for contravariant velocities in Eq. (33)

$$\left(U_{mB} - U_{mA}\right) = g^{m1}\left(\phi_{B\xi} - \phi_{A\xi}\right) \tag{43}$$

Then by using $V_T^2 = U_1\phi_\xi + U_2\phi_\eta + U_3\phi_\zeta$ the following is written.

$$V_{T,B}^2 - V_{T,A}^2 = U_{1B}\phi_{B\xi} - U_{1A}\phi_{A\xi} + g^{21}\phi_\eta\left(\phi_{B\xi} - \phi_{A\xi}\right) + g^{31}\phi_\zeta\left(\phi_{B\xi} - \phi_{A\xi}\right) \tag{44}$$

Letting $\Delta\phi_\xi = \left(\phi_{B\xi} - \phi_{A\xi}\right)$, Eq. (43) becomes

$$g^{11}\Delta\phi_\xi^2 + 2U_{1A}\Delta\phi_\xi + \left(V_{T,B}^2 - V_{T,A}^2\right) = 0 \tag{45}$$

Solving Eq. (45) for $\Delta\phi_\xi$ and considering $\phi_{B\xi} = \phi_{B3} - \phi_{B2}$ and $\phi_{A\xi} = \phi_{A3} - \phi_{A2}$, one can obtain $\phi_{B2} = \phi_{A2} - \Delta\phi_\xi$ where under-scripts 2 and 3 represent the 2nd and 3rd interface planes. ϕ_{B1} is obtained similarly.

4. METHODOLOGY

Fully three-dimensional and non-linear CFD solutions are generally avoided in sonic boom mitigation research due to their prohibitive costs in user time spent for complex grid generation and computational time spent on excessively large grids refined rather inefficiently to better capture the shocks. In the current literature the near-field solutions use millions of grid nodes only to capture the under-track portion of the sonic boom signal of a full aircraft at a few body lengths. The signal obtained as such is not fully developed for complex 3D lifting bodies since the lift contribution from off-centerline components like the wings, and cross-flow diffraction effects in general are not resolved. The final solution at ground level is bound to (1) underpredict the over-pressure levels, (2) inaccurately represent the signal shape, and (3) mislead the designer in the optimization process. Therefore it is crucial to start with a sharp and accurate near-field shock solution that covers most of the cross-flow domain in order not to overlook flow features that significantly influence the undertrack signal. Proper grid adaptation and shock fitting are vital in obtaining such a solution in an economic way. The Euler/Full-Potential CFD methodology originally developed in Refs. [48, 49, 52, 53, 81] is extended here with an unstructured grid adaptation and shock fitting technique for the near-field computations, to provide an automatic solution/adaptation process based on coarse initial grids to minimize/eliminate user time for grid generation. Full 3D flow around complex aircraft are finely resolved using only around 500,000 nodes for the near-field (up to about 2 body lengths). Coupled with the parallel full-potential, space-marching code, the 3D non-linear solution is rapidly extended to very large distances ($r/L >> 1$) where the signal evolution is asymptotic and can be switched to linear geometric acoustics (Thomas Waveform Parameter Program [44]). The applicability of this CFD-based methodology in sonic boom mitigation studies is demonstrated through shape optimization for an axisymmetric nose, a delta-wing, and a real complex aircraft to minimize their ground level sonic boom signal parameters.

Nose geometry near-field calculations are carried out using structured grids to make use of the already available CFD solution and shock fitting and grid adaptation (SFGA) scheme developed in prior work [53, 58, 81, 82]. CFL3D is used as the structured solver in this case. SFGA code is updated and Unix scripts are developed to allow automatic coupling of user-interference-free operations that cover meridian profile and grid generation, grid adaptation and shock fitting, far-field signal propagation, and post processing, all in one pass. Mid- and far-field sonic boom prediction for the axisymmetric nose shapes are carried out using the linear

propagation method. Tests have been run to show that full potential and linear propagation give exactly the same results when the linear extrapolation is started after one body length for axisymmetric cases. The operations listed previously are coupled in an automated framework for Linux HPC machines where parallel computations take place. Input and output to the framework are tabulated design factors and responses formatted in a generic form applicable for standard DoE/RSM interfaces.

Unstructured CFD is used for the three-dimensional cases involving the delta wing and the SSBD aircraft. Unstructured grid generation for complex shapes is extremely easy since it virtually eliminates the need for multi-blocking the 3D volume and the water-tight surface geometry. It can easily be automated to minimize or eliminate user time for grid generation. Initial grid prior to solution/adaptation cycles is generated using GRIDGEN, making use of journal scripts to allow batch mode automatic execution without the graphical user interface. Parameterized aircraft surface definitions are automatically used with preset grid constants to generate the grids for case studies, completely eliminating user time spent on grid generation. The FUN3D unstructured solver is used for the flow computation and OptiGRID is used for Hessian based grid adaptation. The full potential sonic boom propagation code now labeled FPM3D is used for mid-field propagation of the sonic boom signals from complex 3D aircraft. Far-field computations are completed using the linear waveform parameter method. A study on when to switch from the non-linear full potential solution to a linear solution is carried out. A convergence criterion for the ground signal shape is determined to test the switch-over altitude. Similar to the nose geometry analysis, surface definition and grid generation, near-field computations with iterative solution/adaptation cycles, and signal post processing are coupled through an automated framework to eliminate a user interference requirement during case studies. A batch of cases is listed in a text input file containing flow conditions and tabulated geometry parameters. Computations are carried out using parallel processing during flow solution and grid adaptation processes. To make the most out of the nodes on a high performance Linux cluster, local I/O is performed on computational nodes before collecting the results back to the working directory by the completion of a run.

Optimization strategy follows the DoE/RSM approach, a method that reduces significantly the number of runs required. RSM gives a clear idea on how each factor influences the responses, and which factors (design variables) are significant. This is valuable information for an aerodynamicist designing aircraft to help make decisions on future sets of runs and new design factors that can be looked at. The design factors are geometric parameters defining the nose and the delta wing shapes. The responses are: maximum overpressure in the far-field,

pressure impulse in the mid- and far-field, drag, and lift. For the SSBD aircraft case, special attention is paid to the center of lift and gravity to eliminate additional trimming that would otherwise be necessary to sustain level flight. For the delta-wing and the SSBD cases, the volume of the wing is kept equal to the original baseline configuration to make sure no airborne mass is reduced while optimizing. The ultimate goal is to fly the same amount of material at the same speed with a lower sonic boom. Wing volume change can be allowed if a complete aircraft geometry and mission parameters are being optimized, where the volume removed from the wing can be added somewhere else on the fuselage, or the mission range can be decreased since the fuel tank volume would decrease. The current study focuses on individual aircraft component optimization rather than such a comprehensive flight mission optimization, and the volume constraint is strictly applied. Since the volume is kept constant, the lift is also required to remain constant. The volume constraint is easily applied during surface generation, but the lift equality constraint needs to be matched via multi-response optimization analysis.

4.1 Near-Field Analysis

Near-field analyses for all cases are done using Euler computations with Roe's FDS scheme and the min-mod limiter. To capture sharp and accurate shocks, shock fitting is provided via having the grid cell faces align with shock surfaces. When used with an approximate Riemann type flow solver, grid-shock alignment renders the problem into 1D Riemann problem in the computational domain and provides the exact shock jump conditions [70]. This is a conservative method since the scheme is not interrupted across the shock to manually enforce Rankine-Hugoniot shock jump conditions, as is done in conventional shock fitting methods like floating shock fitting [98].

For the axisymmetric nose cases, structured grids are used with CFL3D. Grid adaptation and shock fitting is done using the SFGA code, iteratively coupled with CFL3D, where SFGA takes a computed solution and generates a better fitted grid using the shocks detected in this solution. The shock detection procedure involves checking on the magnitude of the density and Mach gradients along the stream-wise grid coordinates. The details of the SFGA scheme can be found in Ref. [81] and Section 3.4 of Ref. [53]. In short, along each stream-wise coordinate a chain of grid points with Mach gradient larger than a user prescribed threshold are detected as a group of possible shock points. For each shock the stream-wise coordinate passes through, there

is a distinct group of points. The point with the strongest density gradient in a group is selected as the point to represent that particular shock on that particular stream-wise coordinate. The shock points form chains in the radial direction representing the shock fronts. These chains are smoothed using curve fitting to generate proper radial grid lines. Once these grid lines are ready, the sections in between are filled with cells to complete to grid. The shock detection routine first counts the number of shocks, then sets up the grid topology accordingly. Because the distances between shocks vary as they move away from the source, the number of grid cells in between need to be modified at certain radial intervals. To create this discontinuous change of grid topology, the domain is multiblocked in the radial direction. The SFGA code handles the multiblocking and the change in number of shocks from one block to the next. Such topological issues are the drawbacks of structured grids. The updated SFGA code also handles meridian profile and initial grid generation. The code reads in an input file with geometric parameters defining the meridian profile of the axisymmetric shape, shock detection criteria, and grid point distribution information. The initial grid is created with radial lines tilted in the Mach line directions. A CFL3D input deck is automatically prepared in the SFGA code to accommodate the newly created grid. The grid and the input file are partitioned for parallel processing using the Splitter tool of CFL3D, prior to starting the flow computations.

For the fully 3D cases FUN3D is used in inviscid mode. Unstructured near-field CFD is crucial in design optimization since the grid generation for complex geometries becomes trivial once a watertight surface definition is provided. The ad-hoc, case dependent method of multiblocking to partially refine select regions in the structured grid topology or to conform to twists, turns, and grooves in the surface definitions becomes obsolete here, saving significant user time spent on grid topology planning. Multiblocking of the grid also requires the grid adaptation code to be multiblocked, further complicating the whole process. User-interference free operations in this case are hard to set up and almost impossible to generalize for arbitrary geometry and flow conditions. With unstructured grids, local enrichment of the grid can be done without having to add unnecessary grid lines in the rest of the block to maintain grid index continuity as in the case of structured grids. This greatly reduces computer resource requirements. Hence unstructured grid generation is extremely easy to automate and can be included in design optimization loops without requiring user interference. Fully automatic parametric case studies can be carried out, preferably over-night, and user time can be reallocated to engineering and design efforts instead of being consumed by grid generation.

Unstructured grids are known for their dissipative effects on sharp gradients like shocks. This is primarily due to the chaotic alignment of the cell faces in the automatically triangulated

flow domain where no particular attention is paid to the flow conditions, Mach lines, etc. In general the gradients are resolved with greatest fidelity if the finite difference computations are executed along the gradient direction. This can be done by having cell faces aligned normal to the gradient direction. One common method of grid adaptation for unstructured grids is called h-refinement, where a node is inserted in a cell with large gradients to divide the cell into four smaller cells. The process is repeated until enough smaller cells are added to resolve the gradient to a desired degree. This method does not provide gradient direction alignment with the cell face normal, and causes unnecessary refinement in the directions where the gradient is not strong. The latter is usually avoided in structured grid adaptation where the grid density is increased only in the gradient direction, e.g. boundary layer computations. To resolve the shocks to a good degree, h-refinement increases the grid size to prohibitively large levels. Even with such excessive refinement, shocks captured about one body length away from the source can still be dissipated. References [24, 72, 73, 85] present sonic boom prediction studies carried out using the h-refinement method, where 3 to 7 million nodes have been used only to resolve the under-track portion of the flow domain. Resolving the entire 3D cross-flow to the same degree would require a grid size several orders larger.

To create a computationally efficient unstructured grid for sonic boom prediction, the available nodes must migrate towards the shocks instead of dividing cells and increasing the grid size, and the cell faces must be aligned with shocks as a result of node movement. Anisotropic adaptation is a directional adaptation technique, similar to increasing grid density along one coordinate in structured grids. Node movement and anisotropy can be created using Hessian based adaptation, where the Hessian of a chosen flow field scalar is tied to the discritization error associated with the grid. The adaptation can be done to minimize and equidistribute the Hessian based error metric throughout the domain. Eigenvectors of the Hessian give the direction for the node movement, and eigenvalues give the relative normalized distances for node movement, thus creating anisotropy [80]. The nodes of a cell face that are closest to the shock end up having the same stand-off distance from the shock surface due to the equidistribution of the error process. This orients that particular face parallel to the shock surface, providing the necessary condition for shock fitting. The Hessian based adaptation is the preferred technique in the current work due to its advantages in shock fitting, anisotropic grid generation, and maintaining a low grid density.

Hessian based grid adaptation works with the available flow features and adapts the grid for them. This is problematic since generally a fine grid is needed at the start to capture the traces of these features to a good extent. Obviously this makes the initial grid generation process very inefficient and can require significant user time. Another notable problem is that feature based

adaptation provides strong adaptation in the vicinity of the source, and weak adaptation away from the source where the signal is weaker. If a solution is required, say at r/L = 10, adaptation and error thresholds must be reduced sufficiently to let the code handle the weak signal at this location. This usually causes excessive refinement near the aircraft, significantly increasing computational costs. Third, feature-based adaptation works on all high gradient regions, some of which are not of interest. Expansion waves, strong vortical flows, sheer layers, etc. are also adapted as one tries to adapt for shocks. Again this results in inefficient use of grid nodes and increased computational costs. Finally, feature based adaptation usually refines the grid in all regions where the shocks are present. It is common in sonic boom prediction research that the signal above the aircraft is of little interest. An increasingly popular grid adaptation method called adjoint based adaptation eliminates the above listed four major problems associated with feature based adaptation to a good extent, promoting computational efficiency and automation. The adjoint problem formulation minimizes the uncertainty in the adjoint integral variables like lift, drag, etc., by refining and adapting the grid. Applications using the adjoint adaptation method can be found in Refs. [74, 75, 79, 99]. Reference [79] in particular applies the adjoint based adaptation to sonic boom problems, where the adjoint variable is the integral of the overpressure extracted on a cylinder with its axis aligned with the flight path of the aircraft and radius at some target signal distance. Mesh adaptation is done through an h-refinement process. Although adjoint based optimization has advantages in terms of automation and reduced user time, it does not necessarily provide the cell face/shock surface alignment that is essential for shock fitting. Moreover, the adjoint variable is a global integral value which can represent an infinite number of shock shapes, given that all of them have the same area under the pressure curve. Finally, an h-refinement strategy used with adjoint based adaptation does not take advantage of grid anisotropy and stretched cells. A sonic boom signal is a distinct feature in the flow field unlike integral values like lift, drag, thrust, etc., and it should be computed using an adaptation scheme following the shock features in the domain. The Hessian based adaptation method introduced in this dissertation takes advantage of the anisotropic grid and grid/shock alignment, but eliminates the above listed problems associated with feature based adaptation. In other words, it is a feature based adaptation method with the level of automation and efficiency of adjoint based adaptation.

4.2 Hessian Based Unstructured Grid Adaptation

Hessian based adaptation for unstructured grids is carried out using OptiGRID software developed by Newmerical Technologies, Inc., Montreal, Canada. The program first computes an approximate grid-based error of the solution using the Hessian matrix of a user defined scalar. This scalar can be any user provided formula, or one of the readily available values like Mach number, density, pressure, etc. Next, the software moves the available nodes, and adds or subtracts nodes to bring the error on all nodes to the same level (equidistribution). The target error level can be either specified by the user, or automatically computed depending on the desired target number of nodes or elements. The software performs edge swapping and grid smoothing by the end of the adaptation process to improve grid quality and avoid possible badly shaped cells after node movement. Limits on maximum and minimum edge sizes, total number of nodes and elements, and iteration steps are applied to maintain the grid size, grid quality, and computational time requirements. The optimum error threshold specification can be case dependent, and having to adjust it for each new case or solution/adaptation cycle is counterproductive. To remedy this, OptiGRID has the option for the user to specify a target number of grid nodes or elements, where it automatically computes the required error threshold value to reach that target. This allows the user to plan ahead for the available computational resources and timing issues. OptiGRID has unique options for shock adaptation that are not available in other adaptation codes, and this is the primary reason why it was chosen for this dissertation study. The first option for shock adaptation is signal preprocessing, where the noise in the solution is cleaned using convolution, and the weak shocks are augmented using deconvolution. The second option is the error metric correction for shocks, which accelerates node movement toward shocks by projecting the error on the gradient direction of the scalar. The details of these procedures can be found in Ref. [80]. Signal preprocessing and metric correction helps the software to start the adaptation on a coarse initial grid, and reach the final grid in less solution/adaptation cycles.

The error driving the adaptation mechanisms is computed locally for each grid point as the difference between the numerical and real solution of the PDE. Of course the real solution is not known, but, the error at least can be computed approximately. Full details of error computation and minimization performed in OptiGRID can be found in Refs. [80, 100]. A brief excerpt from these resources is given below. The error is defined as

$$e(x) = \left| g^*(x) - g(x) \right| \tag{46}$$

where g*(x) is the real solution of the PDE and g(x) is the numerical solution. Since g*(x) is not known in general, this error is approximated using Taylor expansion approximations. For a cell of height "h", the error is computed as

$$e = \frac{h^2}{8} \left| g''(0) \right| \tag{47}$$

In three dimensions, the second derivative in the above equation is replaced with the Hessian. The error for an edge element is then given by

$$e = \frac{h^2}{8} \left| \vec{V}^T H \vec{V} \right| \tag{48}$$

where h is now the length of the edge, $\vec{V}$ is the unit vector of the edge direction, and H is the Hessian of the scalar chosen for adaptation. As mentioned earlier, the eigenvectors of the Hessian determine the node movement direction and the associated eigenvalues determine the magnitude of the movement needed to decrease the error, resulting in anisotropic cells stretched along strong discontinuities like shocks.

Unstructured Grid Adaptation and Shock Fitting for a 2D Wedge

The following example shows the level of accuracy in shock fitting obtained by Hessian-based unstructured grid adaptation for a 10° wedge in 2D Mach 2.0 flow. The wedge extends from x = 0 to x = 1, followed by a flat after-body to x = 2, where the exit boundary is located. The case is the same as the first problem solved in Ref. [70] to demonstrate the conservative shock fitting idea using shock aligned cell edges and Roe's FDS scheme. Figure 3 shows the initial and final grids with density contours after five solution/adaptation cycles. The figure is enlarged at the tip of the wedge to show clearly the grid elements. The adapted grid domain from x = 0 to x = 2 is shown in the box on the right figure. The first thing to note here is the sharpness of the contour gradients in the adapted solution, compared with the smeared unadapted cells in

the initial solution. Second, the change in the grid after adaptation is noted, where the nodes are clustered towards the shock and the grid is coarsened away from the shock. The grid elements are stretched along the shock, creating an anisotropic distribution, owing to the Hessian based error formulation and node movement mechanism. The figure in the box showing the complete domain clearly shows the adaptation for the oblique shock. The grid is only concentrated on the sharp gradients in a very clean fashion. The initial grid is coarse and created without consideration for the shock locations. Instead of increasing the number of nodes, OptiGRID actually reduced the grid size from 3304 to 1909 nodes. The final grid size in OptiGRID is strongly dependent on two user settings, the minimum edge and target error density. For all problems where the geometry is of unit length, these settings are kept as 0.01 and 0.1, respectively. Minimum edge = 0.01 setting is referred to as "coarse adaptation" in the current work, which is explained more clearly in the following sections.

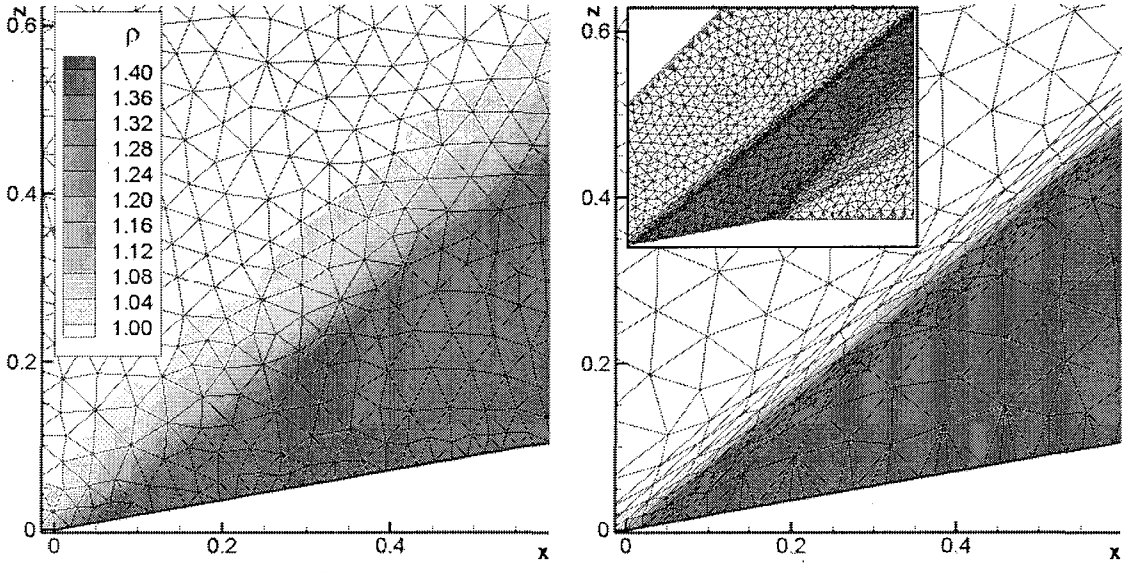

Figure 3: Initial (left) and adapted (right) grid and density contours for a 10° wedge in 2D Mach 2.0 flow.

The analytical solution for pressure ratio on both sides of the oblique shock is $(p/p_0)_1 = 0.1278$ and $(p/p_0)_2 = 0.2215$. The shock angle, β, is 39.3140°, and the Mach number downstream of the shock is 1.6405. These values are computed using the following set of equations [62]

$$\frac{p}{p_0}=\left(1+\frac{\gamma-1}{2}M^2\right)^{\frac{\gamma}{1-\gamma}},$$

$$\tan\theta=2\cot\beta\frac{M_1^2\sin^2\beta-1}{M_1^2\left(\gamma+\cos 2\beta\right)+2},\quad M_2=\frac{1}{\sin\left(\beta-\theta\right)}\sqrt{\frac{1+\frac{\gamma-1}{2}M_1^2\sin^2\beta}{\gamma M_1^2\sin^2\beta-\frac{\gamma-1}{2}}} \tag{49}$$

where p_0 is the stagnation pressure, θ is the wedge angle, M_1 and M_2 are the Mach numbers upstream and downstream of the shock. Figure 4 shows the pressure jump on initial and adapted grids on a level cut at z = 1. The solution of the initial grid is dissipated whereas the adapted solutions have sharp shocks. The solution at one body length is already greatly improved by the first adaptation cycle, despite the use of a coarse initial grid and feature based adaptation. The values obtained at cycle 5 for the pressure ratios upstream and downstream of the shock are $\left(p/p_0\right)_1=0.1278$ and $\left(p/p_0\right)_2=0.2214$. These values are virtually equivalent to the analytical solution. A single "fine adaptation" cycle is run following the coarse cycles where the minimum edge setting in OptiGRID is changed from 0.01 to 0.001. This results in a much finer adaptation at the shock with the grid size increased to 5153 nodes. The plot on the right in Figure 4 shows the pressure jump obtained after fine adaptation. Now the shock is perfectly crisp and clean, matching the analytical solution exactly.

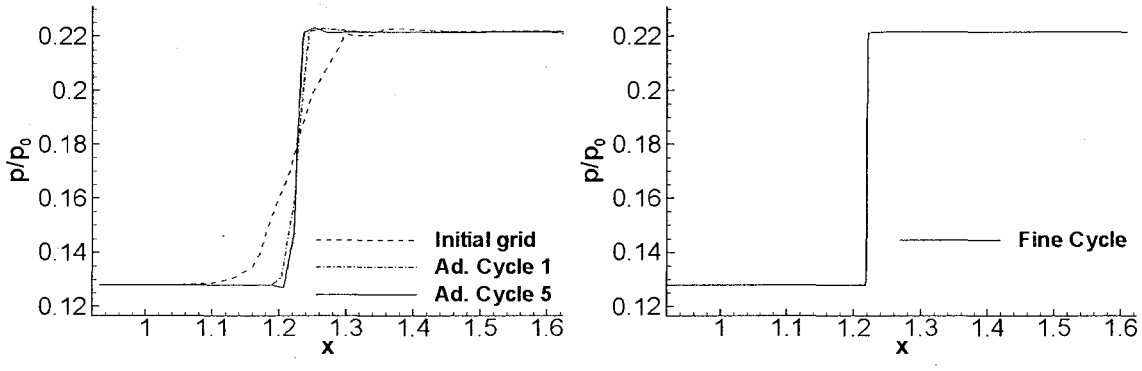

Figure 4: Pressure jump at z = 1 for the 10° wedge in 2D Mach 2.0 flow on initial and adapted grids.

Next, conservation conditions across the shock are tested. These conditions state that mass, momentum, and energy across the shock should be conserved. The Rankine-Hugoniot shock jump conditions are derived from the one-dimensional canonical conservation laws,

$$\begin{aligned} (\rho V_n)_1 &= (\rho V_n)_2 && \textit{mass} \\ (p+\rho V_n^2)_1 &= (p+\rho V_n^2)_2 && \textit{momentum} \\ (h+\tfrac{1}{2}V_n^2)_1 &= (h+\tfrac{1}{2}V_n^2)_2 && \textit{energy} \end{aligned} \tag{50}$$

where subscripts 1 and 2 refer to the upstream and downstream locations relative to the shock, V_n is the normal component of the velocity across the shock, and h is static enthalpy given by

$$h = \frac{\gamma p}{\rho(\gamma - 1)} \tag{51}$$

The values upstream of the shock are 1.2671 for mass, 2.3199 for momentum, and 3.3028 for energy. Using these values as reference, a percentage error for each quantity is computed similar to Eq. (39). The error distributions in the normal direction across the shock are shown in Figure 5 for the initial grid, 5th coarse cycle, and the final fine cycle. The normal data cut passes through the shock at x = 1. These data cuts are taken from upstream to downstream, where the shock point is at 0. The length scale is the same as the original grid length scale. The figure clearly shows how the errors in conserved quantities diminish as the grid adaptation takes place. With the fine cycle, the error is confined tightly at the shock point. The conclusion is that proper shock fitting is achieved by using OptiGRID and FUN3D, which perform Hessian based adaptation providing cell face/shock surface alignment and flow solution using Roe's FDS scheme.

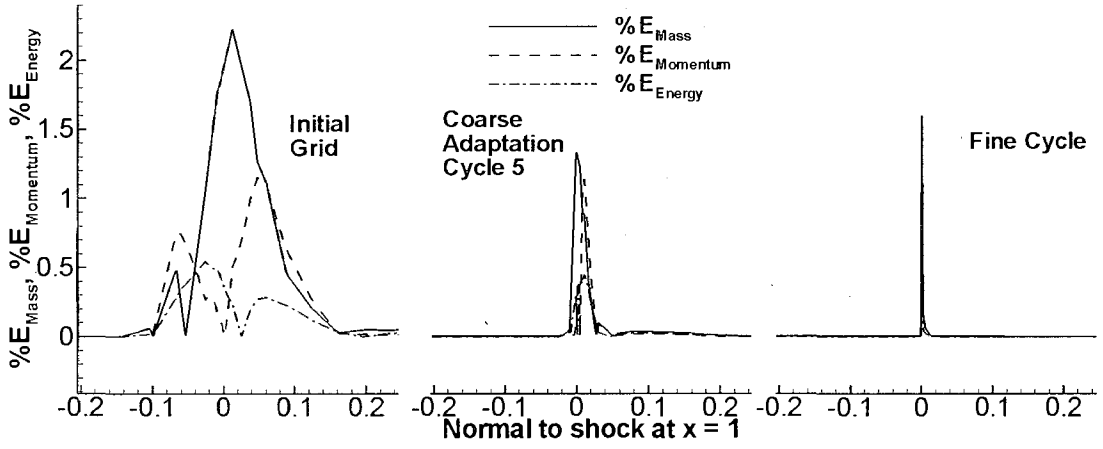

Figure 5: Percentage error distribution in conserved quantities on a data cut passing normal through the shock at x = 1.

4.3 Adaptation Scalar Formulation

The quality and efficiency of the adaptation is dependent on the choice of the scalar. The recommended scalar for shock adaptation is the Mach number which is used in the above example. Although this scalar is very good for simple geometries with simple shock structures, it does not help much with weak shocks at a distance and it does not necessarily focus on shocks alone. Density and pressure fields behave similarly. OptiGRID is quite effective for automating the error threshold setting and initializing from a coarse grid created with no prior knowledge of the shock structure, however it is still subject to three of the four problems associated with feature-based adaptation mentioned earlier. Adaptation is done everywhere in the domain where there are shocks, excessive refinement occurs close to the aircraft when attempting to adapt for weak or distant shocks, and non-shock phenomena is adapted for as well. A special user defined scalar is formulated in this work to address these problems, which is computed externally and provided to OptiGRID in the input solution file. Details on the formulation of the scalar are as follows:

The first step is to find a way to clearly identify the shocks, and use this information to reduce the presence of the disturbance in the non-shock flow regions. In that way, excessive adaptation can be avoided in the regions of no interest like the wake, expansions, strong gradients close to the surface of the aircraft, etc. The normal Mach number across the shock is used as a marker for shocks in the current study. The normal Mach number across any shock has to go from supersonic to subsonic, thus becoming 1.0 right on the shock. This is a common shock visualization method found in some flow visualization software like Plot3D. Reference [69] gives examples of shock visualization using this technique. To compute normal Mach number across a shock, the direction of the normal needs to be known. However, the location of the shocks are unknown at the start of the shock detection algorithm, thus it is not possible to compute the normal directly. Reference [69] suggests that the direction of the density gradient can be used in this case, since all gradients have to be normal to the shock on the shock surface. Based on this approach, a scalar Mn to represent the normal Mach number is computed by

$$Mn = \frac{\mathbf{V}}{a} \cdot \frac{\nabla \rho}{|\nabla \rho| + \varepsilon} \tag{52}$$

where $\vec{V}$ is the total velocity vector, a is the local speed of sound, and $\varepsilon << 1$ is a small number utilized to avoid divide-by-zero problems or erratic directional variations where the density gradient is very close to zero in the numerical solution. In the current work ε = constant = 1e-7 is used. Mn is referred to as the "normal Mach number", however, it is only normal to the shock surface on the shock surface. In any other region, it is just the Mach number in the gradient direction. For shock detection and adaptation purposes, $Mn \approx 1$ is of interest. A second scalar is formulated which reaches a peak value of unity only when $Mn = 1$, and asymptotes to zero otherwise. It is computed by

$$f_S(Mn) = e^{-C_1(Mn-1)^2} \tag{53}$$

which is a very simple exponential function. The term in the parentheses translates the vertical asymptote to $Mn = 1$. Squaring the parenthetical expression creates a smooth continuous peak in place of the vertical asymptote. This function conveniently peaks at 1, making it useful for applications where a unit or step function is needed. The coefficient C_1 controls the steepness and the thickness of the peak as shown in Figure 6. A lower value of C_1 identifies a broader (thicker) region as the shock, and vice versa. Such a scalar can be used as a shock indicator, allowing the user to control the strength of non-shock features in the domain. For example, f_S can be multiplied with the Mach number in the whole domain to zero it out on all non-shock points while allowing it to keep its original value at shock points. The Hessian based error, given in Eq. (48), will be negligible at non-shock regions when (Mf_S) is used as the adaptation scalar, forcing OptiGRID to focus only on shocks. However, multiplying Mach number and f_S at the outset does not leave any degrees of freedom to control the level of adaptation on non-shock phenomena or provide an even level of adaptation on both strong and weak shocks. Further development is needed.

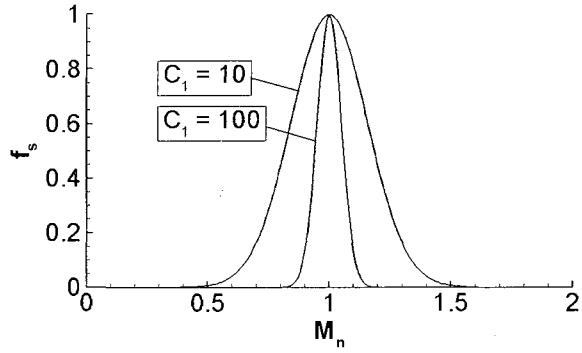

Figure 6: Shock indicator function f_S (Eq. (53)) at two different C_1 settings.

Before including the shock indicator scalar f_S in the computation of the final form of the adaptation scalar, a distance based signal strength control mechanism is formulated. This allows the signal to be amplified with distance in order to remove the weakening effect of the signal distance from the aircraft. Furthermore the signal can be turned off in regions where no adaptation is needed. Let

$$\Delta M^* = \left(\frac{M - M_\infty}{M_\infty}\right)\left(1 + C_2\left(\frac{r}{L}\right)^k\right) \tag{54}$$

where the first parentheses is the disturbance in Mach number normalized by its free stream value, and the second parentheses is the amplification factor as a function of the radial distance from the aircraft centerline. C_2 and k are user defined parameters to adjust the amplification rate. Their default choices will be explained subsequently. A constant 1 is added to the amplification factor to avoid having zero disturbance at r = 0. To bound the physical domain of adaptation, ΔM^* is multiplied by

$$f_p = \begin{cases} 1 & (x,y,z,r)_{low} < (x,y,z,r) < (x,y,z,r)_{high} \\ 0 & otherwise \end{cases} \tag{55}$$

Adaptation does not take place where the disturbance is zeroed. The adaptation can be enclosed in a domain with any shape. The above method works only to provide some limits in the x, y, z directions, and the radial direction. This is sufficient for the current analysis. Alternative formulations for f_p can be used depending on the particular needs of the user.

To reduce the presence of the non-shock phenomena in the signal, scalar f_S given in Eq. (53) is used to further amplify the signal at the shock locations. The final form of the adaptation scalar is given by

$$g_M = f_p\left[\Delta M^* + C_3 f_S sign\left(\Delta M^*\right)\right] \tag{56}$$

where C_3 is a user defined constant, controlling the level of augmentation of shocks in the signal. The scalar f_S equals to unity no matter how strong or weak the shock is. Augmenting the shocks in the signal with this scalar increases the shock strength equally for all shocks, reducing significantly the difference in the level of adaptation between weak and strong shocks. This helps

to resolve the weak shocks as effectively as strong shocks while avoiding excessive adaptation for stronger shocks. Ultimately this provides huge savings in grid size requirements. It is necessary to multiply the shock unitary indicator function, f_S, by the sign of the disturbance in order to augment the signal in the correct direction.

The values of the parameters C_1, C_2, C_3, and k are determined by trial and error to find the best settings for a variety of cases. In the current work, the tests are done using a double cone as a simple axisymmetric shape, delta wing as a simple 3D lifting surface, and the SSBD as a real complex aircraft. The recommended settings that were appropriate for all the cases keeping the maximum solution/adaptation cycles around 10 were

$$C_1 = 10 \quad C_2 = 3 \quad C_3 = 0.1 \quad k = 1.5 \tag{57}$$

Increasing C_2 speeds up the propagation of adaptation towards the exit boundary. For large domains though, high C_2 settings create chaotic adaptation at large distances. Increasing C_3 increases the presence of shocks relative to the rest of the signal. However, the remaining pressure signal is also important for the whole flow field to be resolved at a satisfactory level of accuracy. Increasing C_3 too much initially causes excessive coarsening in the non-shock regions, which in turn distorts the shocks themselves and the grid simply disintegrates. From first order linear theory, shock strength decreases with $(r/L)^{1/2}$ in the near-field and $(r/L)^{3/4}$ in the far-field. However, k = 1 appears to be more effective than any of these values in general, possibly because in close proximity of the aircraft the linear assumptions are not valid. The following is achieved by using OptiGRID with the just defined scalar:

- Coarse initial grids can be used with no prior knowledge of shock structure
- Hessian based error is higher in coarse regions where the gradients are weak or nonexistent, providing rapid extension of grid adaptation toward the exit boundaries.
- The level of adaptation for the strong non-shock flow features near the aircraft is controlled, avoiding excessive adaptation for features of no interest.
- All shocks are treated the same, regardless of strength, by using a shock detection scheme prior to the generation of the scalar.
- The signal is amplified with the distance from the source to eliminate the shock strength differential close and far from the aircraft.

- The adaptation region is limited in the domain using binary switches that disable the signal in regions where adaptation is not wanted, e.g. above the aircraft.
- The grid density is kept similar on all shocks, weak and strong, near and far from the aircraft.
- A predetermined constant set of OptiGRID software and the scalar formulation parameters are used for all geometries, regardless of complexity, eliminating the user requirement for case dependent software adjustment.
- Similar level (density) of adaptation is provided at all altitudes.
- Full cross-flow of a real airplane up to 1.5 body lengths downstream of the nose is resolved with high fidelity and accuracy using only 500,000 nodes.
- About 10 solution/adaptation cycles are needed to complete a run.
- Termination of adaptation cycles is based on checking the convergence of the signal shape point by point at a target signal cut location.
- For all geometries being tested, fully automatic case independent operations are carried out performing surface definition and initial grid generation, flow solution and grid adaptation, and termination of the cycles followed by post processing and data reporting (signal extraction, peak Δp and impulse calculation, lift and drag listing, etc.).

Figure 7 compares the Mach based and g_M (Eq. (56)) based adaptation on the symmetry plane of the SSBD grid. Both grids are final adapted grids after 10 solution/adaptation cycles, created with the target number of nodes equal to the 500,000 criterion in OptiGRID. Adaptation based simply on Mach number clusters most of the nodes close to the aircraft surface rather than using them on the shocks. The weak shocks emanating from the fore-body downstream of the bow shock are ignored completely. The newly developed adaptation scalar g_M however provides even adaptation for all the shocks no matter how strong or weak they are, making very efficient use of the limited number of nodes. This is achieved mainly by the shock detector function, f_S, and the $C_3 = 0.1$ setting. Figure 8 shows the Mach number, g_M, and f_S distributions on the target signal cut location at x/L = 1.5 (vertical signal cut) at both grids displayed in Figure 7. The Mach number plot shows that the leading shock is much weaker than the trailing shock since it is farther away from the aircraft centerline on the vertical cut. The weak shocks that appear as small bumps downstream of the leading shock have absolutely no influence on the grid adaptation when Mach number is used as the adaptation scalar. With g_M however, the distance-based signal amplification and the effect of the shock detection function f_S brings the leading and trailing

shocks to a similar strength level, and enhances significantly the presence of the weak shocks. This in turn results in the adapted grid on the right side of Figure 7. The function f_S peaks at 1.0 at each shock regardless of its strength, and remains 0 otherwise.

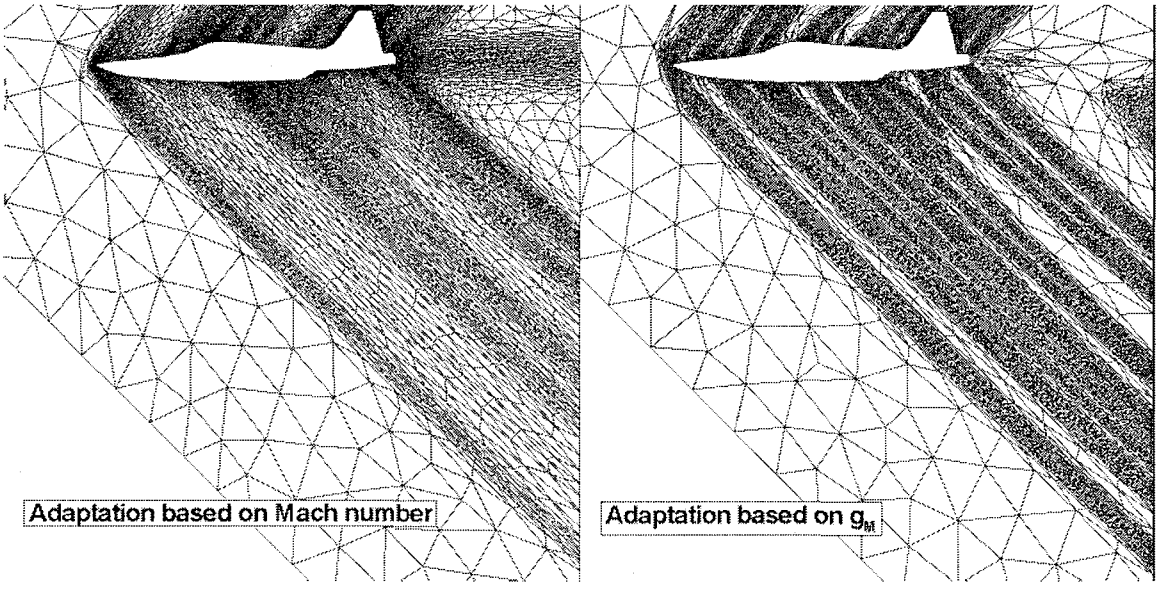

Figure 7: Comparing grid adaptation on the symmetry plane using Mach number, and the adaptation scalar formulated in the current study. Both grids have 500,000 nodes in the whole 3D domain.

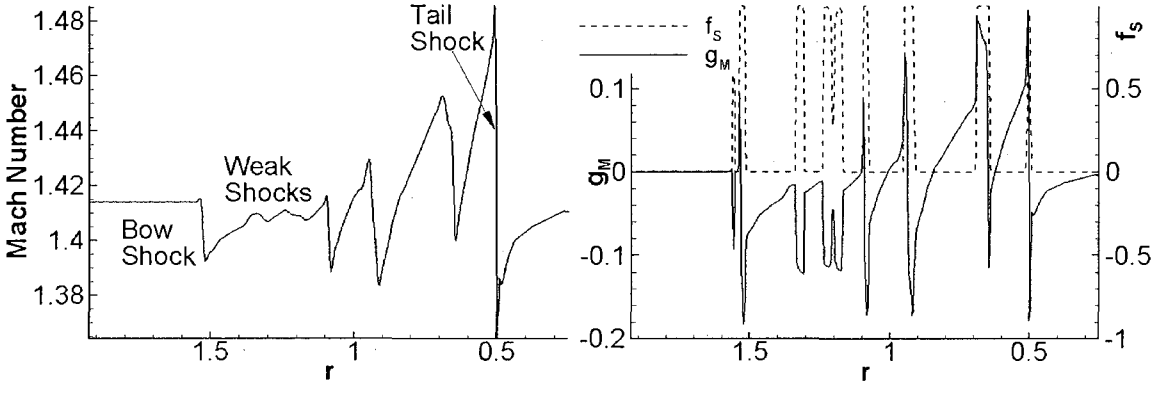

Figure 8: The Mach number, g_M, and f_S distribution on the vertical cut at x/L = 1.5 in the final solution. The adaptation constants for g_M are $C_2 = 3$, $C_3 = 0.1$, and $k = 1$.

4.4 Software Coupling Framework

The robustness of the grid adaptation and shock fitting method described above makes it possible to function as part of a fully automated near-field shock fitted solution procedure. Since grid generation is no longer a user effort, a software-coupling framework that automatically takes care of surface definition generation, initial grid generation, solution/adaptation cycles, and post processing is developed. This is extremely handy for solving a large set of design points for optimization studies. User time is reallocated from grid generation, adaptation, solution adjustment, and post processing of results to optimization efforts. For the delta wing and SSBD wing shape optimization studies, the complete analysis framework is set up in the following way.

- A case list file is prepared with the actual values of the design factors defining the wing geometry tabulated by the user. This list can be created in the DoE software or in Excel.
- Initialization scripts generate numbered case subdirectories with the input files and additional scripts needed by the framework.
- Once cases are ready to be started, they are added to a global batch job file which is read by agent master jobs that loop through list. The master jobs are submitted to the job queue of the cluster by the user. Once a master job starts, it reads the first line in the job batch file which has the path to a case. It rewrites the file with the first line omitted, and goes to that case directory to start the job. Once that particular case is completed, the master job goes back to the job batch file and reads the path of the next case to be solved. The master job quits the queue when there are no more cases listed in the job batch file.
- More than one master job can be submitted to the cluster queue, all processing the same job batch file to finish the listed cases quicker. Each case is solved using parallel processing for grid adaptation and flow solution. Master jobs can be submitted for any number of CPUs, depending on the availability. FUN3D and OptiGRID both process the case in a parallel load-balanced manner. Most frequently used combination in the current work is five master jobs each with 16 CPUs working on the same job batch file.
- Surface definition is the first step in the case processing. A simple F95 code generates the surface of the delta wing using the geometric parameters tabulated for that particular case.
- Next, GRIDGEN is launched in batch mode using a template *glyph* script which performs the following steps:

- Surface file and a template grid file with inflow and outflow boundaries are read.
- In the case of SSBD with wing modification, a series of automatic prerecorded CAD operations take place where the wing surface is scaled and translated to the proper location relative to the aircraft, intersection lines with the SSBD surface are extracted, and a watertight fairing is created connecting the wing and the fuselage. The CAD operations are not wing specific and the same journal file works with all wing geometries to be tested on SSBD.
- Predetermined constant grid spacing parameters like max/min edge, angular deviation, etc., are applied prior to surface triangulation.
- The wing surface mesh is created using "create domains on database entities" option.
- The symmetry plane is created at y = 0. (z is up)
- Unstructured block is generated with tetrahedral cells.
- Boundary condition tags are applied to the domains to differentiate walls, symmetry plane, and inflow/outflow surfaces in the grid file.
- Grid file is exported in FieldView ASCII format. The initial grids are very coarse and the ASCII files are about 15MB for the delta wing cases and 35MB for the SSBD cases.

- FUN3D solves the flow on the initial grid, writes the FAST formatted grid and solution files. Post processing scripts extract certain zones and signal cuts and prepares them in Tecplot format.
- OptiTRANS, the in-house developed tool for interfacing FUN3D and OptiGRID reads the FAST grid and solution files to generate OptiGRID input and solution files. The scalar to be used for Hessian based adaptation is computed by OptiTRANS during the translation from FAST to OptiGRID format.
- OptiGeo, the CAD preprocessor for OptiGRID reads in the OptiGRID type input grid file to extract the surface and create a connectivity file to be used in successive adaptation cycles.
- The solution adaptation loop starts. The first step is the adaptation where OptiGRID starts working on the initial solution. Once OptiGRID quits, OptiTRANS converts the adapted grid file to FAST format that is used by FUN3D. The solution is also interpolated on the adapted grid and is converted to FUN3D ".flow" restart file.

- *Party*, the grid partitioning tool of FUN3D reads the FAST formatted grid, creates the ".part" grid file, and repartitions the ".part" and ".flow" files into number of available CPUs.
- FUN3D resumes the solution on the adapted grid
- Upon the completion of FUN3D run, OptiTRANS converts the files to allow the next cycle to start, and post processing tools extracts desired zones and sonic boom signal cuts.
- Sonic boom signals from the previous and current cycles are compared at a user defined data cut. The solution/adaptation loop quits when the signals are converged.
- Upon the completion of FUN3D/OptiGRID loop, Tecplot formatted output files with signal cuts and zones of interest are arranged for further post processing.
- Once a case is complete, the master job moves on to the next available case in job batch file.
- When all the cases are complete, final post processing scripts gathers the signal cuts from all cases into one Tecplot file for comparative viewing. Peak pressure, pressure impulse, lift, drag, and moment center of each case is tabulated in a single file along with the design factor settings that can be readily input to the RSM software for response modeling.

Local I/O is performed in the majority of the processes where the input grid and solution files of each node are made available on its own hard-drive. This way having 80 nodes accessing the same hard-drive (where the working directory is located) is avoided, which would slow down the entire system considerably and may cause jobs to hang. OptiGRID requires each node to read in the same global grid and solution file. These files can be on the order of a few hundred MB. The OptiGRID input files are distributed to all nodes working on the problem using an "MPI-copy" tool written in F95 with MPI, where the head node reads in the files and broadcasts the data using the MPI_BCAST call to all the nodes. This allows the data to be branched out among the nodes instead of using only the head node to sequentially distribute the file to each node at one time. Upon completion of a case, only the required files are moved back to the original working directory.

4.5 Mid and Far-field Calculations

Mid-field is considered to be the region where the cross-flow effects are negligible, and the non-linearities in the signal are weak. The signal is not necessarily asymptotic in this region, and contains multiple interior shocks that are still in the process of merging. Far-field is where the signal is asymptotic and its shape is "frozen" [43]. The decrease of the shock strengths and signal levels follow Whitham's approximations [45] in the far-field, where the signal is an N-wave in general. According to Whitham, all signals eventually become an N-wave at some point. Shaped sonic booms are more of a mid-field concept. Related works in the literature frequently discuss the idea that quiet supersonic aircraft should fly at low altitudes so that their ground signal is actually in the mid-field range. A shaped sonic boom may have higher frequency content with a series of weaker shocks that are yet to coalesce, making it less loud and destructive than the N-wave at ground level. The range and boundaries of near-, mid-, and far-fields are different for different types of aircraft. For a simple axisymmetric shape the far-field can start as soon as one body length from its centerline, whereas for a conceptual quiet supersonic jet the ground level at 300 body lengths may still be in the mid-field. For this reason, the non-linear full 3D cross-flow analysis needs to be extended to $r/L >> 1$ for low sonic boom designs. If this is not done, non-axisymmetric geometry and lift effects on the under-track signal will not be fully captured and the ground signal pressure levels will be underpredicted [67]. This in turn will cause the designer to believe that their optimum meets the FAA requirements whereas in reality it would still produce much stronger signals, violating the noise criteria. If the optimized design based on linear prediction methods reaches the costly experimental prototype building stage, the funding is jeopardized. Therefore it is imperative that the non-linear analysis is extended to a distance where linear propagation methods are accurate.

Non-linear mid-field sonic boom propagation is accomplished using the full-potential equation. The full-potential sonic boom propagation code has been under development in the ODU Aerospace Engineering Department under the supervision of Dr. Kandil. The first results using the prototype code were presented in Ref. [48]. The code has gone through a major overhaul during 2005 [53], and through the first half of 2006. The updates and improvements on the code can be listed as:

- Universal source code development allowing the code to run error free on Unix systems as well as Windows.

- Parallelization of shock detection, shock fitting, grid generation, and flow solution via MPI.
- Large numbers of sub-blocks can now be solved using many CPUs to improve the continuity of the solution across sub-block interfaces where there is a jump in stratified atmospheric conditions.
- Automatic increase of sub-blocks by checking on the average aspect ratio of the cells in the cross-flow plane. This eliminates the need for the user to stop execution and prepare new input files every time the sub-block number is desired to increase.
- The shock detection (physical fitting) scheme is renewed using density and Mach gradients with a normalized threshold system. Signal filtering is performed to avoid involving erroneously detected shock points in geometric fitting.
- Geometric fitting using least-square based surface fitting both in the axial and radial directions instead of cubic spline fit in radial direction only.
- Shock detection and fitting for interior shocks between the leading and the trailing shocks.
- Elimination of the artificial dissipation routine which was used to reduce oscillations and overshoots for interior shocks. Now with interior shock fitting available, the interior shocks do not need artificial dissipation.
- Adjustment of the user defined artificial dissipation coefficient as altitude changes is eliminated to promote automatic operation with a single input file.
- Velocity potential is averaged at sub-block interfaces instead of velocity matching which improves the solution continuity in the vertical direction when stratified atmosphere is simulated.
- Double pass on every main block to provide two iterations of shock fitting and grid adaptation before advancing to the next block. This improves accuracy and stability of the run.
- Rich set of error reports and data outputs for user-friendly maintenance and debugging in case a problem occurs.
- The same code is tested for a set of geometries that vary in complexity of the cross-flow shock structure. Case dependency of the program is eliminated.
- Restart file and solution file formats are optimized to minimize disk space requirements and post processing time.

As of January 2008, the full potential sonic boom propagation code of Professor Kandil's team is called "Full Potential Marching Three-Dimensional", or FPM3D. The solution scheme is based on Refs. [48, 49] and [97], where backward differencing is used on the marching coordinate aligned with the flight path, and an upwind biased central differencing scheme is applied on the cross-flow coordinates. Upwinding is provided here by biasing the density computation in the direction of the characteristic rays. This approach maintains the tridiagonality of the matrix operations while providing the same truncation error leading term found in one sided differencing. Tridiagonal matrices can be solved without needing to invert them to save computational time. The particular truncation error leading term provided with this upwind biasing creates the necessary numerical dissipation to stabilize the solution. The details of the solver can be found in Refs. [48, 49, 53, 95-97]. Since upwinding is done in the direction of the characteristics, grid/shock alignment produces shock fitting satisfying RH shock jump conditions

The near-field Euler solution is used as the initial condition for the full-potential marching. An interface code converts the Euler velocity components into the velocity potential on a cross-flow slice taken downstream of the aircraft normal to the flight path. The Euler domain is rotated (both grid and velocity components), if there is an angle of attack in order to make the free stream velocity parallel to the x-axis. This simplifies grid generation, atmospheric condition application, and data post processing, simplifying the coding. Having the x-coordinate parallel to the flight path anchors the cross-flow planes on a constant x-value, reducing memory and disk space requirements by having a single real number instead of a whole 2D array to store the x coordinate values. The interface cut is a toroidal domain enclosing only the leading and the trailing shock and the area between them, but excluding the wake. The wake is not involved in the marching process since the full-potential equation is irrotational. It is not needed anyway since it is outside the important part of the sonic boom signal. The distance of the interface from the aircraft nose does not make a change on the final ground prediction. In general enough space should be given to provide reasonable spacing between the wake boundary and the trailing shock. Keeping a large distance between the aircraft and the interface plane promotes automation where a care-free setting of the inner boundary stand-off distance can be applied. Otherwise user time is required for careful determination of a proper interface location to make sure the trailing shock is kept inside the domain at all azimuths while the wake is avoided. With low boom designs, the shock formation can be delayed (i.e. isentropic compression on the surface) for several body lengths from the aircraft. In case there are no apparent shocks, the shock detection and grid generation mechanism in FPM3D cannot work. For such cases either the near-field Euler solution is extended to 2 to 3 body lengths, or FPM3D is run without shock fitting (since there are

no shocks yet) with a grid aligned with the Mach cones until the shocks are clearly available. In depth explanation of the Euler/Full-potential methodology can be found in Refs. [48, 49] and in Ref. [53].

Far-field computations are carried out using the Thomas Waveform Parameter Method. This is a ray tracing method based on linear geometric acoustics. It is the most commonly used sonic boom prediction method in the industry. Compared to Hayes' propagation method that uses the F-function as the input data, Thomas' method requires only the pressure signal shape as input which can easily be obtained from experimental or computational data. The details can be found in Ref. [44]. The original code is written in FORTRAN. The input signal shape is parameterized as segments connecting corner data points. The code extrapolates the signal by modifying the signal shape parameters using the principles of geometric acoustics. A simple N-wave input signal can be represented by four input data points. A signal with a single interior shock can be defined using six points, etc. In the current work, the CFD solution is extracted on a line parallel to the flight path on the symmetry plane at a desired altitude. The extracted data set is composed of a large set of interpolated points. The standard procedure to use a CFD or experimental solution with this code is to approximate the curved signal features with straight shock lines and ramps to end up with a discrete looking signal shape. This is neither an accurate nor a user-friendly approach. However, when the source code of Thomas is used, a continuous data signal with hundreds of points often results in floating point errors like "NaN" and "Infinity". The code has been debugged for the current dissertation to avoid these errors and to allow a fully detailed CFD extracted signal to be used without any user-based parameterization. The code input and output functionalities are also modified to allow reading in signal data in Tecplot format. The output is modified to print the signal at desired intervals down to the target distance, instead of listing all the output altitudes separately. The outputs are also written in Tecplot format. Thomas code takes a fraction of a second to complete the operation.

The predicted ground signal strengths and footprint sizes are strongly dependent on the input signal distance from the aircraft using the linear method. Reference [30] presents a brief set of results for a delta wing signal to show this. This variation is due to the non-linearities and the cross-flow effects still being strong in the near-field. The input signal to the Thomas code needs to be in the asymptotic state for distance dependence to cease. The point where the signal reaches this asymptotic state is different for each aerodynamic configuration, and there is no closed form or approximate expression that can give an estimate of this location. In the current dissertation, this point is determined in a crude fashion by using the Thomas code ground results for comparison, which are initiated at different altitudes. The signal is extracted on the symmetry

plane at every body length interval as the full-potential computation continues to march to a solution. Thomas code is called to extrapolate the extracted signal to ground level. FPM3D terminates the computations when the pressure impulse of the linearly extrapolated ground signal converges. A more scientific way to determine the full-potential/linear propagation switching location would be to check on the magnitudes of the cross-flow derivatives and non-linear terms in the full-potential equation as the solution propagates downstream. However, this is practically no different than checking on just another parameter like the ground level signal pressure. After all, the ground signal is the final expected result from the run.

4.6 Aerodynamic Shape Optimization

Optimization is accomplished via a Design of Experiments and Response Surface Methodology approach. The responses of interest like sonic boom signal levels, lift, etc. are modeled for a selected design space using actual computational solutions at systematically chosen design points. Once a response surface is obtained for the available data, a global optimum is sought that satisfies the constraints via a gradient based search technique implemented in the response surface analysis software. Since an optimum is an extremum where the surface "dips", the response models must be at least second order to capture such stationary points. Linear models are insufficient in this case. The software used for creating the design run matrix and generate the least-square based models is "Design-Expert" from Stat-Ease. The software is complementary to the textbooks used in ODU's DoE and RSM courses [101, 102]. This is a graphical software, allowing the user to visualize the models and statistical diagnostics. ANOVA tables are given for detailed quantitative statistical significance assessment of the experimental setup and the response models. The included optimization tool locates a set of optimal design points through a gradient based search method. The search algorithm starts from several initial random points since there can be local minima in the design space. Multi-response optimization is accomplished by combining the optimization criteria in a weighted desirability function. The search algorithm then finds points with maximum desirability. This allows the user to minimize one response while maximizing another and keeping a third at a target value, etc.

Designs such as Box-Behnken (BBD) and Central Composite (CCD) are mostly used for non-linear modeling of the responses in the current work. These are efficient small run designs that provide enough degrees of freedom for quadratic modeling and lack of fit. Depending on the

case, CCD is used as face centered, or quadratic orthogonal. Since CFD is a deterministic solution method, the primary diagnostics of interest are the model R-squared value and the variance inflation factors (VIF). VIFs show how the variance of the model term is influenced by lack of orthogonality in the design matrix. Orthogonality of the design provides decoupling of the model terms (regression coefficients) to make them uncorrelated. This is desired in RSM since the analyst would like to see the pure effect of linear and non-linear terms on the response. Ideal VIF = 1 for all terms.

Although linear modeling and steepest descent search prior to non-linear modeling is a standard procedure in DoE/RSM, it is skipped in this dissertation work. The main reason for this is that the cost of runs is cheap and running three times the cases using an automated computational framework is more efficient than performing steepest descent searches and deciding on new design space limits. The latter is a user-intensive approach. Moreover, starting with a linear model covering the whole design space may be misleading in terms of evaluating the strength of the effect of a factor on a response. Imagine a situation where the response has similar values at -1 and +1 (factorial) settings of a factor, but is quite different at 0 (center). Factorial analysis would show this factor to be of low importance where it is not. Therefore at least a 3-level analysis is crucial in general. With the automated framework for grid generation/solution/adaptation coupling developed in the current study, hundreds of cases can be run over night without user interference. Therefore carrying out a non-linear analysis is more efficient than spending user time pursuing the steepest descent direction with several linear designs.

A sequential optimization strategy is followed both in the axisymmetric nose shape and delta wing optimization, where the complexity of the designs is increased progressively. For example, the axisymmetric nose meridian profile that is composed of linear ramps is optimized using 2-ramp, 3-ramp, 4-ramp, and 5-ramp configurations. A measure of the rate of improvement of designs can be determined as the number of design variables is incremented. Starting with basic designs has the advantage of recognizing the significance and effect of each new design factor. This knowledge comes in handy when the number of runs increases with increasing numbers of factors. Insignificant factors and inefficient factor levels can be eliminated from the design matrix to reduce the total number of runs needed for complex configurations. The delta wing study starts by looking into the effects first of camber and angle of attack, then dihedral and angle of attack. Once the optimums with these 2 factor combinations are found, the analysis is extended to 3 factors where the combined effects of camber, dihedral, and angle of attack are analyzed. Finally twist is added as the last parameter to carry out a 4-factor optimization. This

approach is helpful in understanding the individual effects of each parameter, and planning for the inclusion of new factors that could be beneficial. The details of the optimization strategy followed for each problem are given in the respective results and discussion sections.

The model equation used for the responses is a multivariable polynomial where the variables are the levels of design factors. The polynomial coefficients are determined using the least squares method. The multivariate linear regression model equation is given by

$$y = \beta_0 + \sum_{i=1}^{k} x_i \beta_i + \sum_{i=1}^{k} x_i^2 \beta_{ii} + \sum_{i=1}^{k} \sum_{\substack{j=1 \\ i \neq j}}^{k} x_i x_j \beta_{ij} + \varepsilon \tag{58}$$

where y is the actual data value obtained from experimental or computational analysis, $x_1, x_2, \ldots, x_k$ are design variables representing k factors, β's are the polynomial coefficients, and ε is the error between the model prediction and the actual value of the response at that point. Values of y and x's are known, but β's and ε are unknown. β_0 is the mean, $x_i \beta_i$ are the linear regression terms also called main effects (ME), $x_i x_j \beta_{ij}$ are the 2-factor-interactions (2FI), and $x_i^2 \beta_{ii}$ are the full quadratic terms. In the least squares method, the error term, ε, is assumed to have zero mean and distributed normally over all observations. The least squares method minimizes the sum of ε^2 from each data point with respect to the model coefficients by

$$\frac{\partial \left(\sum_{i=1}^{n} \varepsilon_i^2 \right)}{\partial \beta_j} = 0, \quad j = 0, 1, 2, \ldots, p-1 \tag{59}$$

where n is the number of observations. For a model with p terms including the mean, Eq. (59) provides a set of p number of linear algebraic equations in terms of β's. The square of the error ε^2 in Eq. (59) can be eliminated by rewriting and squaring Eq. (58). In matrix form, Eq. (59) can be arranged to reveal the coefficients on the left hand side as

$$\mathbf{b} = \left(\mathbf{X}'\mathbf{X} \right)^{-1} \mathbf{X}'\mathbf{y} \tag{60}$$

where $\mathbf{b}$ is a vector with size p containing the least square estimates of β's, $\mathbf{y}$ is a vector of size n equal to the number of input data points (observations), and $\mathbf{X}$ is an n by p matrix containing the

terms x_i, x_i^2, $x_i x_j$, etc., for all observations. The derivation of Eq. (60) is straight forward and can be found in any source explaining the least squares method, e.g. Ref. [102].

Since CFD analysis is a deterministic method and repeat runs do not show variation, the "pure error" is zero or absent in the model analysis. Pure error is the difference in the response between two runs at the same point. Without pure error, many of the statistical tests in RSM are not required. One useful statistic regarding the accuracy of the model is the Adjusted R-squared (R^2_{Adj}) value. This value simply shows how close the model predicted values are to the actual observations. The following is a short derivation of this statistic.

$$\mathbf{e} = \mathbf{y} - \hat{\mathbf{y}}, \quad SS_E = \mathbf{e}'\mathbf{e} \tag{61}$$

where $\hat{\mathbf{y}}$ is the vector of model estimates of the response, $\mathbf{e}$ is the error vector, and SS_E is the error sum of squares.

$$SS_R = \mathbf{b}'\mathbf{X}'\mathbf{y} - \frac{\left(\sum_{i=1}^{n} y_i\right)^2}{n}, \quad SS_T = SS_R + SS_E \tag{62}$$

where SS_R is the regression (model) sum of squares and SS_T is the total sum of squares.

$$R^2 = \frac{SS_R}{SS_T}, \quad R^2_{adj} = 1 - \frac{n-1}{n-p}\left(1 - R^2\right) \tag{63}$$

R^2 shows how much of the total sum of squares is made up by the model. $R^2 = 0.95$ is the accepted norm in general for a good model. It is possible to increase R^2 by adding more terms in the model without necessarily improving the model fit. Basically SS_E can stay the same but SS_R and SS_T increase, increasing R^2. Therefore, R^2_{adj} is a better figure of merit for judging the accuracy of the model where the increase in R^2 is countered by the denominator $n-p$ which decreases as number of terms (p) is increased. However, in deterministic studies where pure error is zero, a saturated model $(n = p)$ will always produce a perfect fit, and both R^2 and R^2_{adj} will be unity. The models in the current study are never saturated, and sufficient degrees of freedom are left for the Lack-of-Fit (LoF) test. A saturated model will mask outliers which can point out distinct changes in the behavior of the response between two adjacent design sub-spaces.

Outliers can be due to true sudden changes in the response, or incorrect computations due to user error or some computational problem that is overlooked during flow simulations or post processing. Since the cases are run in a batch automated fashion in the current study, it is possible to overlook certain problems associated with the automation, solution method, or simply typing a faulty line in the case listing file. The outliers detected during response modeling help identify such erroneous cases.

The test design matrices are kept mostly orthogonal in the current study. An orthogonal experimental design means a variance-optimal design, where the variances of estimated model coefficients are minimal and the covariences are zero. This means that model terms are uncorrelated and do not influence each other. This is a desirable feature for the analyst to judge the influence of main effects, 2 factor interactions, and the pure quadratic terms independently. If orthogonality is not satisfied, the problem of "multicollinearity" among the regressor model terms occurs. Multicollinearity can have serious adverse effects on the applicability of the model. For an orthogonal design, the off-diagonal elements of the matrix $\mathbf{X}'\mathbf{X}$ in Eq. (60) are zero. The Variance Inflation Factor (VIF) is the measure of the correlation between regression coefficients. It is computed by first standardizing the factor levels and scaling them such that all diagonal elements of $\mathbf{X}'\mathbf{X}$ become 1 with the method outlined in Appendix 2 of Ref. [102]. Then the VIF's for regression coefficients are given by

$$VIF(b_j) = C_{jj}, \quad \mathbf{C} = \left(\mathbf{X}'\mathbf{X}\right)^{-1} \tag{64}$$

If the off-diagonals of $\mathbf{X}'\mathbf{X}$ are non-zero, VIF > 1 indicating that some coefficients are correlated. VIF > 10 is unacceptable. In this case either the term should be removed, or the experimental design matrix should be adjusted.

Multi-response optimization is accomplished using the "desirability" approach, where the responses are gathered in a single unitary function ranging from 0 to 1, which is to be maximized. Each response y is individually scaled over the whole domain to give d where

$$0 \le d \le 1 \tag{65}$$

For m responses, a single desirability function is written as

$$D = \left(d_1 d_2 \ldots d_m\right)^{1/m} \tag{66}$$

If a response is being minimized, the desirability function is set up as

$$d=\begin{Bmatrix} 1 & y<T \\ \left(\frac{U-y}{U-T}\right)^{r} & T\le y\le U \\ 0 & y>U \end{Bmatrix} \tag{67}$$

where T is the desired minimum bound to be reached, U is the upper limit of the response, and r is a weighting parameter. When r = 1, the desirability increases linearly from 0 to 1. When $r>1$, the desirability is further reduced where $y>T$. This increases the importance of being closer to the target. In case of multiple responses, the weights can be used to increase or decrease the influence of a response on the optimization. If a response is being minimized,

$$d=\begin{Bmatrix} 0 & y<L \\ \left(\frac{y-L}{T-L}\right)^{r} & L\le y\le T \\ 1 & y>T \end{Bmatrix} \tag{68}$$

Desirability is 1 at and beyond the target values in Eqs. (67) and (68). If the user sets T under the absolute maximum or above the absolute minimum, this global stationary point will not be reached. Therefore setting T beyond the anticipated value of the extremum may be required to trick the scheme to settle on the global extremum. If a target value of the response is required (i.e. lift), then the desirability is formulated as

$$d=\begin{Bmatrix} 0 & y<L \\ \left(\frac{y-L}{T-L}\right)^{r_1} & L\le y\le T \\ \left(\frac{U-y}{U-T}\right)^{r_2} & T\le y\le U \\ 0 & y>U \end{Bmatrix} \tag{69}$$

5. VALIDATION OF SONIC BOOM PREDICTION METHODOLOGY

This chapter presents a series of results to show the accuracy of conservative shock fitting using shock aligned grid cells, and the efficiency of the Hessian based adaptation technique developed in the current study. Computational and experimental results from the literature are used for comparison with the current test results. First, results up to r/L = 20 with unstructured grids are given for the double cone at three different speeds, Mach 1.26, 1.41 and 2.01. Next, the case of a delta wing is solved for Mach 2.0 and angle of attack of 2.24°. Third, the unstructured grid adaptation is applied to the baseline SSBD aircraft, flying at Mach 1.414 with an angle of attack of 1.922°. Finally, far-field signal propagations for the three aircraft are given with non-linear and linear propagation coupling. The results given in this chapter are to validate the sonic boom prediction methodology before proceeding any further with the optimization studies.

5.1 Axisymmetric Double Cone

In this axisymmetric test case, unstructured grid adaptation is carried out for a domain that radially stretches 25 body lengths from the centerline of the object, a double cone configuration. The target signal locations are r/L = 18 and 20. The results are validated with reference experimental and computational results. The efficiency of the solution method is discussed by comparing the small number of solution/adaptation cycles needed to complete the run to the reference computational solution using adjoint based grid adaptation [79]. The two-step grid adaptation strategy with a primary set of coarse cycles and a final fine cycle is developed. The stopping criterion for grid adaptation cycles is set as the convergence of the pressure signal shape at the target altitude. An error index is formulated to test the signal shape convergence. The double cone is the simplest geometry tested in the current work with axisymmetric flow.

The double cone is an axisymmetric configuration originally used in Ref. [7] for experimentation with the meridian profile given by

$$
\begin{aligned}
R(x) &= x\sqrt{\frac{0.08}{\pi}} && (0 \le x/L \le 0.25) \\
R(x) &= \frac{L}{2}\sqrt{\frac{0.02}{\pi}} && (0.25 \le x/L \le 0.75) \\
R(x) &= \frac{L}{2+\sqrt{2}}\sqrt{\frac{0.04}{\pi}}\left(2\frac{x}{L}-\frac{2-\sqrt{2}}{2}\right) && (0.75 \le x/L \le 1.00) \\
R(x) &= \frac{L}{2+\sqrt{2}}\sqrt{\frac{0.04}{\pi}}\left(2-\frac{2-\sqrt{2}}{2}\right) && (x/L \ge 1.00)
\end{aligned}
\tag{70}
$$

where L is taken as unity. The fourth segment is the cylindrical sting used during the wind tunnel experiments. Figure 9 shows the geometry in three dimensional view. Double cone is the simplest geometry used to test the current unstructured grid adaptation methodology for the near-field computations. Properly adapting an unstructured grid up to and beyond 20 body lengths to produce a sharp and accurate shock with absolutely no dissipation or oscillations is a challenging goal. This is a very large distance for near field computations, and feature based grid adaptation starting with a coarse initial grid would normally have a hard time getting a solution at that distance. However, in the current study adaptation all the way to the exit boundary is completed in less than 10 solution / adaptation cycles. The computations are carried out at three Mach number settings, 1.26, 1.41, and 2.01, to match the experiments. The grid is a meridian slice spanning 4° about the x-axis. The upstream boundary is set at an angle to the x-axis equal to the Mach angle for Mach 1.26, and the downstream boundary is set similarly for Mach 2.01. The top boundary is set at r/L = 25. The initial grid is coarse with only 65914 nodes.

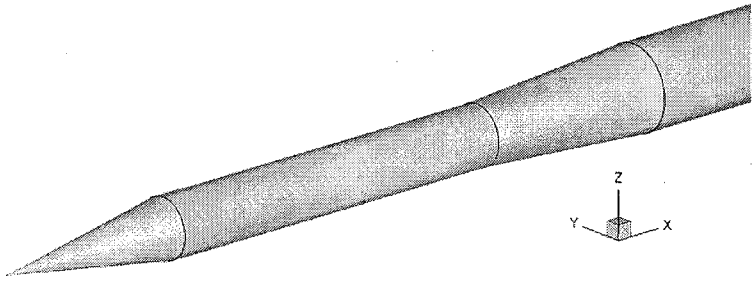

Figure 9: The double cone geometry in three dimensional view.

The adaptation is done in two steps, the coarse adaptation and the fine adaptation. In coarse adaptation, the grid adaptation starting from a coarse initial grid is allowed to propagate towards the exit boundary to "grow the shocks". At this step, the requirement is to have a fairly strong signal at the target distance using the least amount of grid points and solution/adaptation cycles necessary. The parameter controlling the grid density is the minimum edge setting in this case, which is set as 0.01L. By the end of coarse adaptation phase, the signal is strong but not sharp. Only one additional cycle is performed for fine adaptation, this time with minimum edge setting = 0.001L. Doing so in general increases the grid size ten fold. To avoid such a large grid size, the adaptation strategy is switched to a "target number of nodes" in OptiGRID, where the error density is now computed automatically to make the grid settle at the target grid size. This method requires more internal iterations to be run in OptiGRID. The target number of nodes is set at 500,000. By the end of fine adaptation cycle, the signal is very sharp and free of oscillations. The stopping criterion for coarse adaptation cycles is the convergence of the signal shape which is determined by

$$\%E_{Signal} = 100 \cdot \frac{\sum_{i=1}^{m} \left| \Delta p_i^n - \Delta p_i^{n-1} \right| / m}{\sum_{i=1}^{m} \left| \Delta p_i^n \right| / m} \tag{71}$$

where m is the number of points on the signal extraction data cut, and n is the cycle number. Eq. (71) computes the difference in the signal at each point. The absolute values are necessary to present positive errors canceling out negative errors. The average of the errors at all data points is divided by the average signal amplitude which is just a reasonable reference value of the same order. This error definition ensures that the signal shape is being tested point by point rather than global integral values which could be the same for two completely different shaped signals. The coarse adaptation phase is terminated when $\%E_{Signal} < 5$. Maximum number of coarse cycles are set at 10.

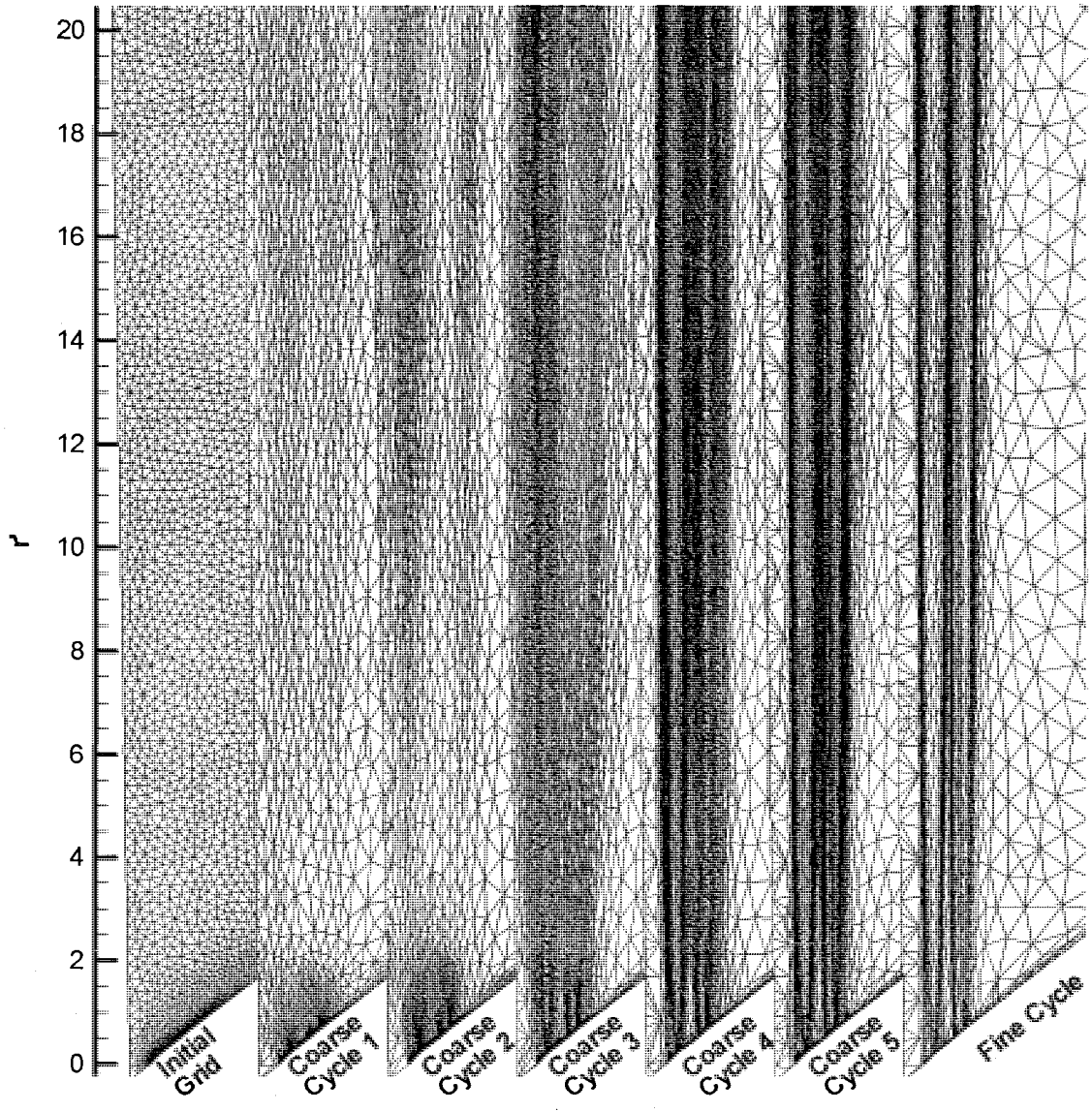

Figure 10: Grid adaptation history for the double cone in Mach 1.26 flow.

Figure 10 shows the grid adaptation history for the double cone in Mach 1.26 flow. The grid is rotated counter-clockwise 90°-β to save plot space by positioning the shocks vertically. The vertical coordinate is $r' = -x\sin(\beta - 90) + r\cos(\beta - 90)$. The figure shows that shocks all the way up to r = 20 are quickly adapted for starting by the first coarse cycle even though the initial grid is coarse. This is the result of signal scaling and amplification used in the adaptation scalar. By coarse cycle 6, there are about 400,000 nodes in the domain. The fine cycle targets 500,000 nodes. Even though there are 25% more nodes in the fine cycle than in coarse cycle 6, the adaptation looks clearly more focused on shocks. This is the effect of the reduced minimum

edge length constraint which is $1/10^{th}$ of the value used in coarse cycles. The solution of the fine cycle is sharper and cleaner (no oscillations or dissipated shocks) compared to the coarse cycle. The coarse cycles are essential to prepare the solution for the fine cycle. Rapid development of the shocks in the entire domain does not take place with a similar set of fine cycles. Therefore the fine cycle can only follow the coarse runs. The increase in grid size is plotted in Figure 11 where it starts to asymptote to a constant towards the end of the cycles. With the coarse cycles the grid size converges as well as the signal shape at target altitude. The convergence of the grid size shows that additional coarse cycles are not going to improve the solution. Figure 12 shows the grid detail at the target signal location at the final coarse cycle and the fine cycle. The adaptation is cut-off at r/L = 20.5 for the fine cycle to avoid wasting grid points. The coarse cycle creates a more wide-spread dense grid which helps to promote shock formation in the coarse regions. Like a precision instrument, the fine cycle focuses on the shocks made obvious by the coarse adaptation phase. The reduced minimum edge constraint causes thinner cells to be formed along the shock surfaces to capture sharper shocks. The node clustering by the shocks and the stretched anisotropic cells are clearly visible. For all cells including the ones away from the shocks, at least one face is aligned parallel to the shock surfaces to provide accurate shock fitting. This can only be obtained by Hessian based node movement. Omitting the coarse phase does not work since the fine cycle has no basis for adaptation. Using a smaller minimum edge constraint in the coarse phase (it would not be called coarse anymore) results in excessive adaptation and the grid size quickly becomes unmanageable. Therefore the two-phased grid adaptation is the ideal and most efficient strategy.

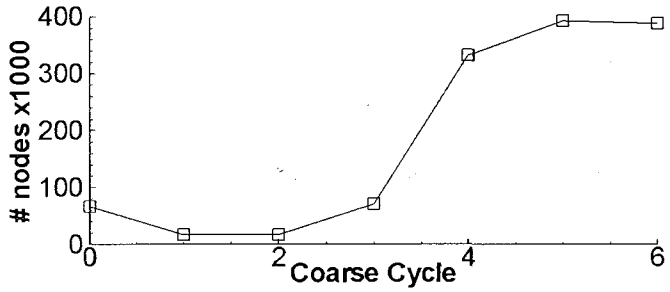

Figure 11: Grid size increase with adaptation cycles for the double cone in Mach 1.26 flow.

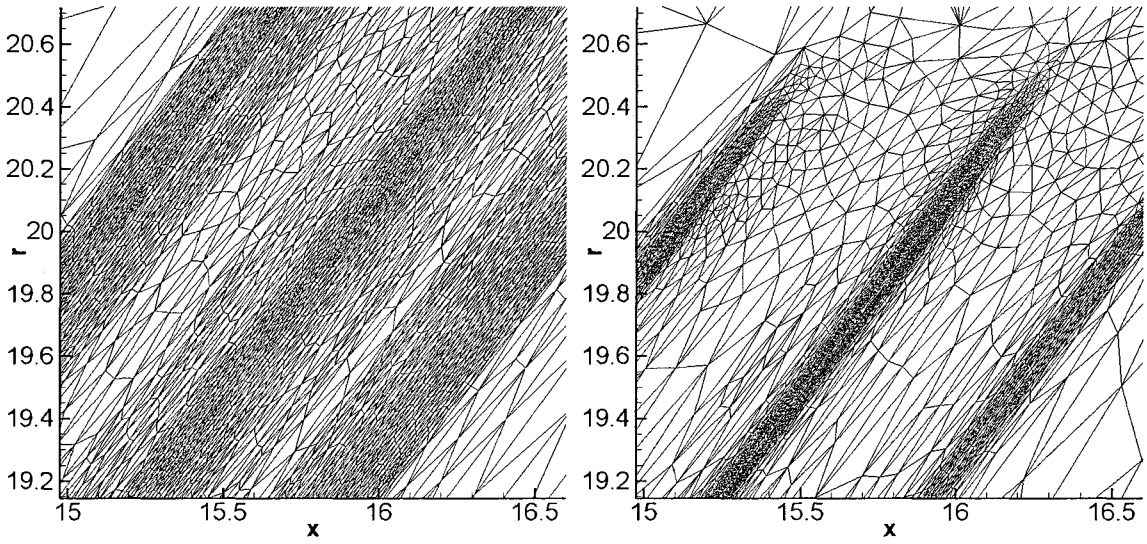

Figure 12: Grid detail for double cone Mach 1.26 case at coarse cycle 6 (left) and fine cycle (right).

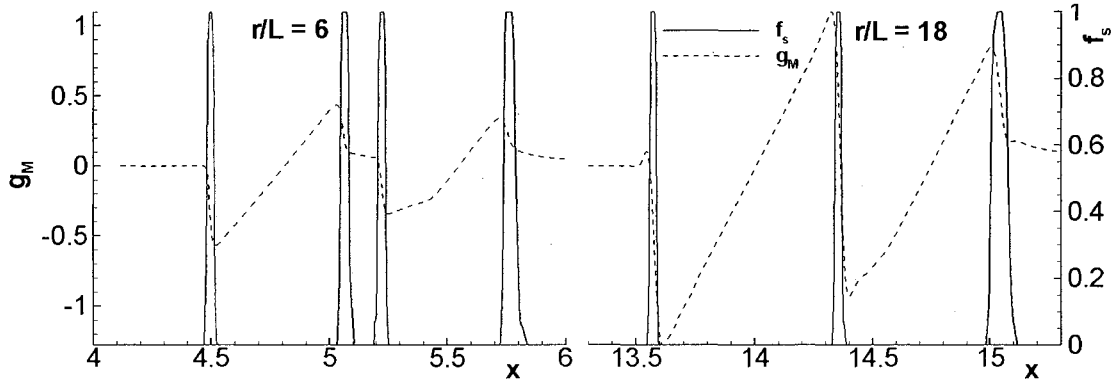

Figure 13: The shock detection function f_S and the adaptation scalar g_M at two different altitudes in the double cone Mach 1.26 case coarse cycle 6.

In Figure 13, the shock detection metric, f_S, and the adaptation scalar, g_M, is displayed at two different altitudes. Although the signal gets weaker with increasing distance from the source, g_M increases with the distance. This is the ideal behavior required in the coarse adaptation phase to promote rapid growth of shocks far from the source. The parameter setting $k = 1.5$ is mainly responsible for this amplification. Higher k reduces the number of coarse cycles, but also results in excessive adaptation at high r. Setting k between 1 and 1.5 will result in satisfactory adaptation in general for large domains like this one. Setting k = 0.75 more or less equalizes the signal strength at all altitudes as the linear theory suggests, but this is not enough to promote grid adaptation in the coarse regions. Shock detection metric, f_S, nicely peaks to 1 where there are

shocks, weak or strong, and remains 0 otherwise. It is a very practical function for shock visualization and grid generation with respect to shocks.

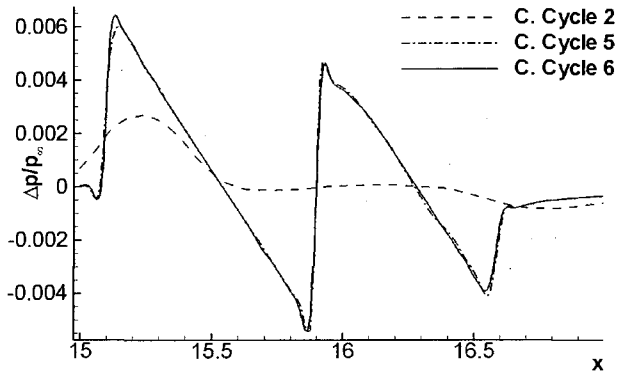

Figure 14: Double Cone pressure signals at target altitude r/L=20 at different stages of adaptation.

Figure 14 shows the double cone signal for the Mach 1.26 case at r / L = 20 at three different coarse cycles. By coarse cycle 2 there is already some disturbance at such a large distance. The signals at coarse cycles 5 and 6 show the convergence of the signal with 4.12% error computed using Eq. (71). The signals look practically the same and thus the 5% error criterion is a reasonable one. Finally, the fine cycle signals at three different altitudes for all Mach settings are shown in Figure 15 along with reference experimental and computational results for comparison. The results show excellent agreement with the experimental data. The signals are crisp without any overshoots, in contrast to the reference computational data taken from Ref. [79], which uses FUN3D with adjoint based adaptation. In the reference computations the number of solution/adaptation cycles and the final grid size is 20 and 400,000 for the Mach 1.26 case, and 22 and 742,000 for the Mach 1.41. In the current study these numbers are 6 and 500,000 for the Mach 1.26 case, and 7 and 500,000 for the Mach 1.41. It may be possible to improve the efficiency of the adjoint based adaptation and reduce the number of cycles needed by careful formulation of the adjoint variable just as was done in the current study for the scalar field used in Hessian based scalar. However, node movement to provide shock/cell face alignment is a feature-based problem and can only be dealt with feature-based adaptation. Shock/cell face alignment is essential to provide shock fitting and accurate shock jump conditions.

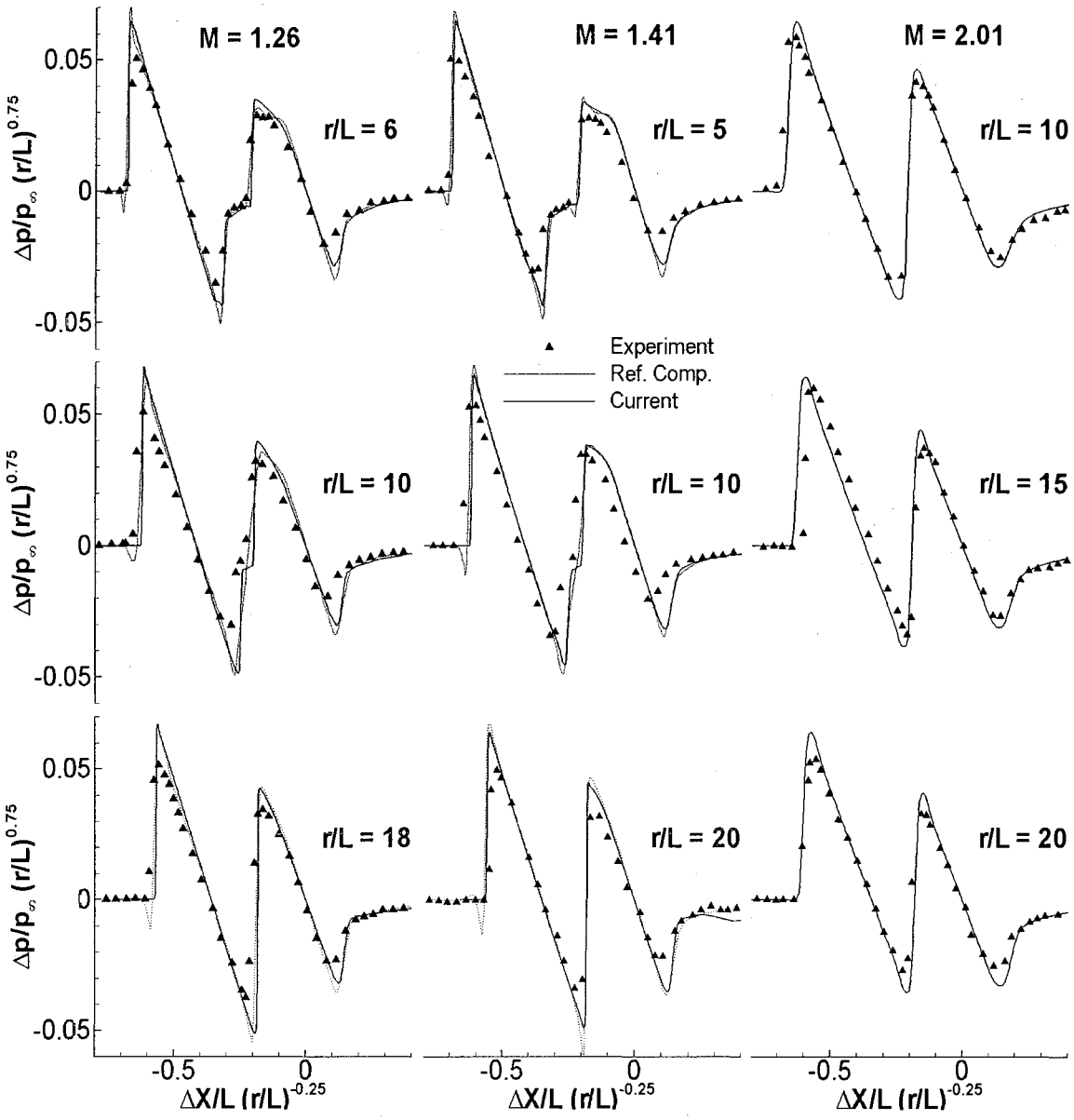

Figure 15: Double Cone solution comparison showing pressure signals at 3 different altitudes for each Mach number setting.

5.2 Delta Wing

The delta wing is the simplest geometry yet it is an interesting case to test the three dimensional effects of the cross-flow on sonic booms. The bow shock from the delta wing is conical but the trailing shock starts out as two separate planes emanating from the trailing edge. The trailing shock planes start to curl further downstream from the aircraft. These planes eventually connect and form a continuous conical shock in the far-field. The delta wing test case is essential for the optimization study in the section 6.2.

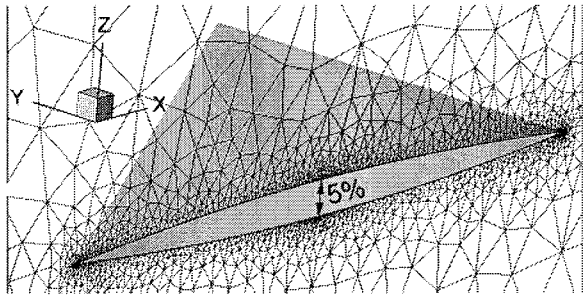

Figure 16: The delta wing in three dimensional view with the y = 0 symmetry plane grid.

The delta wing is displayed in Figure 16 along with the y = 0 symmetry plane initial grid. The airfoil is symmetric biconvex with 5% thickness- to-chord ratio. The semi-vertex angle is 30° which matches the Mach angle for Mach 2.0 flow. The airfoil profile is similar over the whole span. The initial grid has 31711 nodes. The flow conditions are Mach 2.0 and $\alpha = 2.24°$. These parameters are selected to be consistent with the data of prior work [48, 49, 58] for comparison. With these flow conditions the delta wing generates $C_L = 0.0765$ and $C_D = 0.0102$ (based on the planform area). The target signal location is set as x/L = 3.5 where a vertical cut on the symmetry plane is taken below the aircraft. Signal convergence criterion is again set as $\%E_{Signal} < 5$. The signal is checked on a vertical cut since the full-potential propagation code interfaces with the Euler solution this way. The target distance of x/L = 3.5 is chosen intentionally here since the wing optimization study in section 6 requires the Euler/FPE interface to be no closer than this distance. The reason for this is explained in detail in section 6.2.1.

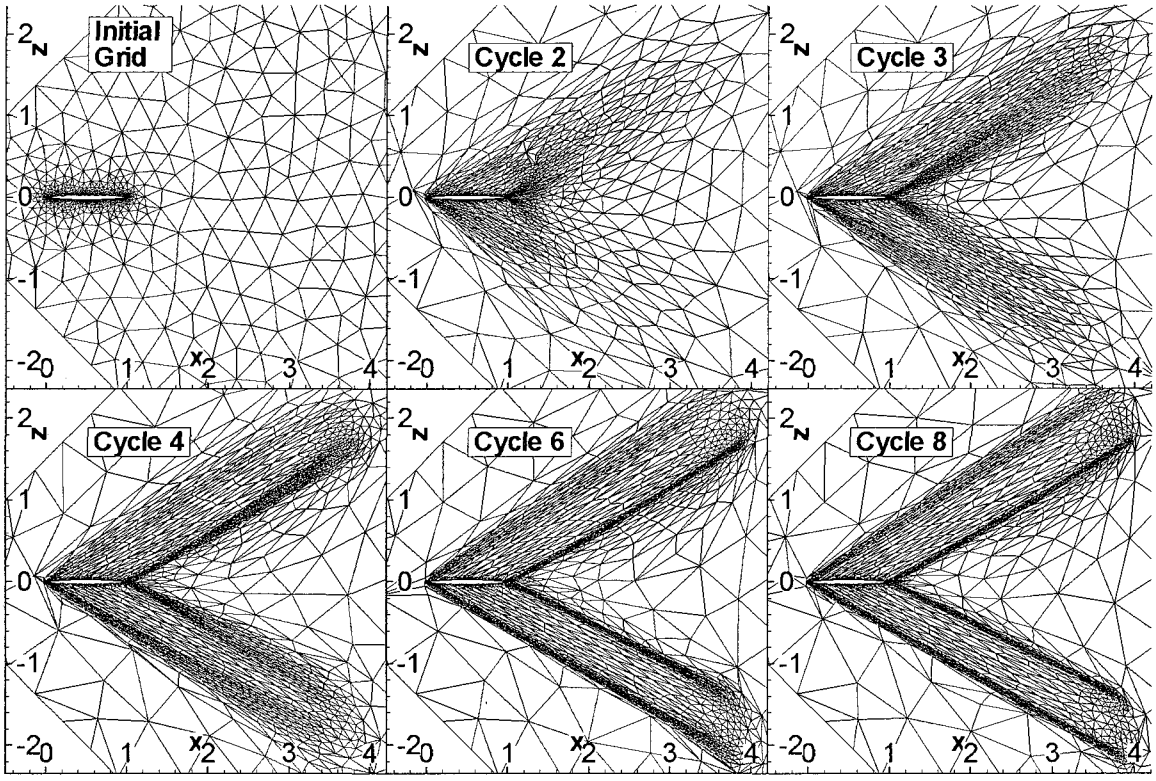

Figure 17: Delta wing y = 0 symmetry plane change through coarse cycles in Case 1.

Adaptation history for case 1 is displayed in Figure 17 using the y = 0 symmetry planes. Again, the coarse initial grid created with no prior knowledge of the shocks poses no problem for the rapid completion of shock adaptation with feature based adaptation. The cells are nicely clustered and aligned with respect to the shocks in an orderly fashion. Adaptation is cut off by x = 4 to avoid wasting grid nodes. The effect of the adaptation in cross-flow is shown in Figure 18 using evenly spaced non-dimensional density contour lines covering the whole range of the variable. There are no signs of the shocks in the initial solution displayed on the left. On the right however, the leading and trailing shocks are clear all the way down to the target signal location in the entire cross flow. The contour lines are clean and the shocks are sharp. Note that the trailing shock is not a continuous cone and starts as oblique planes which gradually curve as x gets larger. Such incomplete shock surfaces are hard to deal with in structured grid adaptation where the grid surface matching the shocks needs to be a complete cone. For this very reason the need of prior knowledge of the shock structure is generally inescapable in structured grid adaptation for shocks. Finally, Figure 19 shows the signal comparison using the current and reference solutions at x / L = 2.4. The reference solution is obtained using CFL3D with the structured grid adaptation scheme SFGA used in prior work. This solution is only available up to

x/L = 2.4 in the structured grid case. The pressure signal is scaled with the vertical distance, using the scaling suggested by the linear theory, to display the leading and trailing shocks at similar strengths. Otherwise the trailing shock appears much stronger since it is closer to the centerline of the body due to the vertical data cutting. The reference and current solutions are in excellent agreement. Feature based unstructured grid adaptation is successfully performed for a three dimensional case with lift covering up to x/L = 3.5 using less than 100,000 nodes for the entire cross-flow with only eight solution/adaptation cycles.

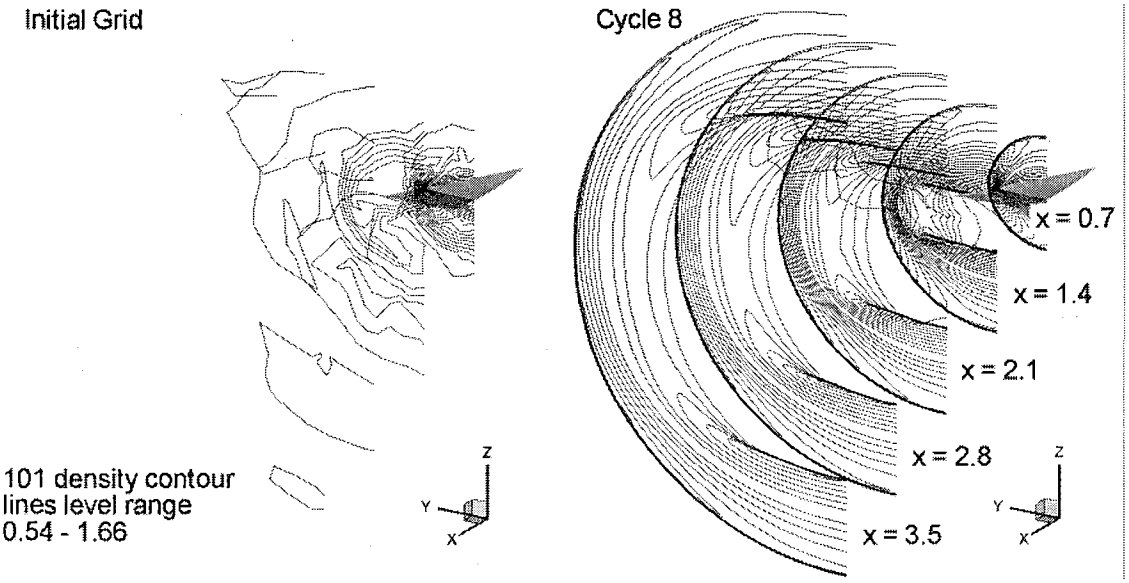

Figure 18: Delta wing density contour lines at 5 equidistant cross-flow planes for the initial and final adapted cycles.

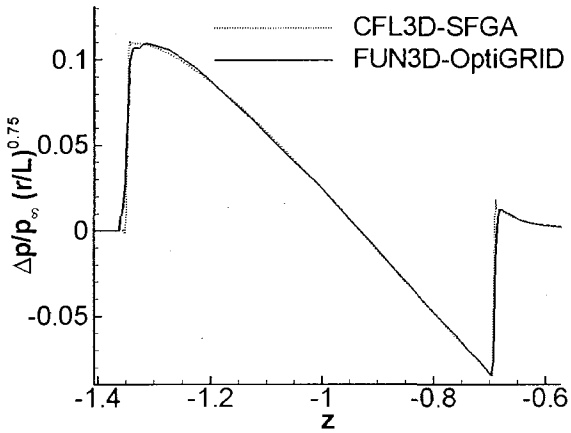

Figure 19: Delta wing signals at x/L = 2.4 (vertical cut), comparing current and reference computations.

5.3 SSBD, Modified F-5E

In this section the unstructured CFD solution is computed for the SSBD aircraft that was built and flight tested by Northrop Grumman for the QSP program. This is a real aircraft modeling and simulation case with complex features like engine inlet and outlets, a boundary layer bleed port between the nacelle and the fuselage, wings, and the tail. Complex flow interactions occur due to this geometry and the shock structure in the cross-flow is anything but ordinary. The flight conditions are Mach 1.414, $\alpha = 1.922°$, and the altitude is 32,140 ft. These conditions correspond to the experimental near field signature recording 6 during flight 30 [6]. The actual lift based on the wing area is reported as $C_L = 0.0936$. The length of the aircraft is L =50 ft, and the wing area is 186 ft^2.

The surface mesh and the geometry details about the inlet and exhaust models are shown in Figure 20. The surface mesh contains 35687 nodes. The mesh is generated using the surface definition extracted from the structured grid and solution file acquired from Northrop Grumman in November 2004 for the testing of the Euler/FPE method with results published in Ref. [52]. The original surface found in this resource has the inlet modeled all the way up to the compressor intake with transonic flow conditions inside the inlet channel. Due to the unavailability of inlet/exhaust type boundary conditions in the FUN3D version 10.4.1 used in the current study, detailed modeling of the flow at the compressor intake is not carried out. Instead, the inlet opening is covered with a surface as shown in Figure 20, and the exit back pressure boundary condition is applied here. This is a valid approach since the external flow inlet can be treated as a pressure source deflecting the flow. This boundary condition is a modified version of the far field boundary condition where a constant pressure is exerted on the flow leaving through the applied surface. The constant back pressure to be applied on the inlet surface is determined by running several test cases attempting to match the inlet shock strength at a target distance to that found in the structured solution provided by Northrop Grumman. Since the flow details inside the inlet are unimportant to the sonic boom propagation problem, this inlet model suffices. The initial guess for the back pressure is calculated by interpolating the data from the reference solution onto the inlet surface, then computing the average. The initial value is found to be $p/p_\infty = 2.08$, producing a stronger inlet shock at x/L = 1.5 than that found in the reference solution.

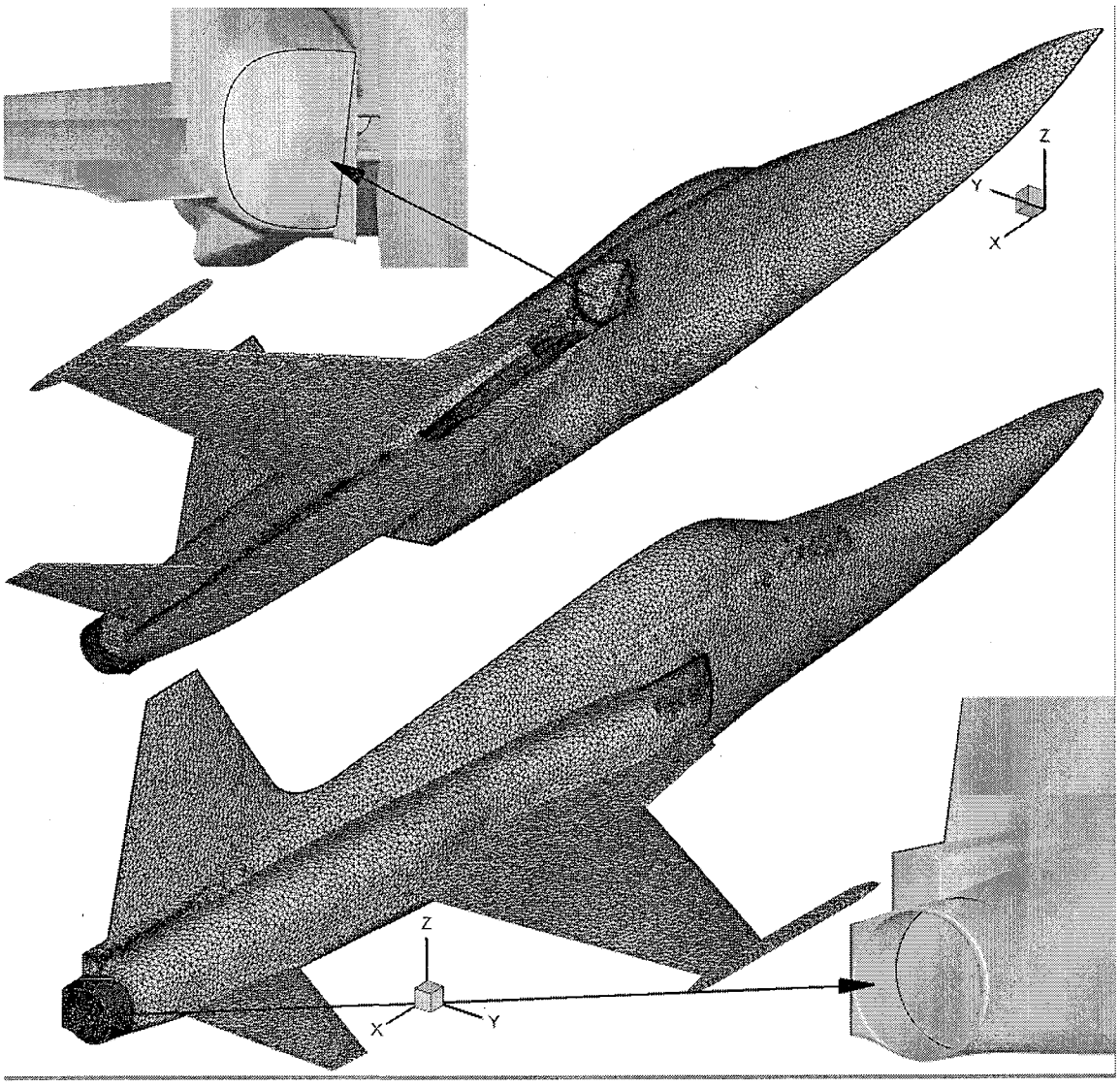

Figure 20: Surface grid and geometry details about the inlet and the exhaust of the SSBD.

Additional test cases show that $p/p_\infty = 1.91$ is the best approximation, which is rather close to the initial guess based on data interpolation. The bleed port is modeled similarly using the far field boundary condition. The exhaust flow is simulated using the subsonic tunnel inflow boundary condition. The exhaust of the F-5 is a simple converging nozzle where the flow accelerates from subsonic to sonic conditions at the exit throat, and continues to accelerate to supersonic speeds once it leaves the nozzle. The subsonic tunnel inflow boundary condition requires the total pressure and total temperature in order to specify the reservoir conditions of the tunnel flow. Although the flow is not at rest at the plane where this boundary condition is applied, it is still subsonic and this particular boundary condition works perfectly. Again the

average values of p_0/p_∞ and T_0/T_∞ are extracted from the reference solution since these values were not available to this author. These values are $p_0/p_\infty = 4.358$ and $T_0/T_\infty = 8.39$. The boundary condition is applied at a plane inside the nozzle, located at x/L = 0.975. Here the resultant average Mach number is 0.707, non-dimensional velocity is 1.952, and the non-dimensional density is 0.409. These values are almost identical to those in the reference solution which are 0.709, 1.958, and 0.404, respectively. At the sonic throat located at x/L = 1.0 the newly computed average Mach number, velocity magnitude, and density are 1.05, 2.74, and 0.314, respectively. In the reference solution these values are 1.03, 2.70, and 0.321, respectively. In conclusion, the reference and current computations at the exhaust are in very good agreement, meaning that the current exhaust boundary condition approximation is valid. Last but not least, FUN3D reports the lift coefficient as 0.0935, which is virtually equal to the in-flight measured value mentioned above.

The pressure signal of the SSBD contains several weak shocks as well as the strong leading and trailing shocks, and the $C_3 = 0.1$ setting is essential in capturing the weak shocks. This is not a problem in the double cone and the delta wing cases where all shocks are strong. Figure 21 shows the grid adaptation history for the SSBD using the symmetry and the exit planes. Again 500,000 target node specification is used in the fine cycle which follows coarse cycle 10. The figure shows the coarse initial grid created irrespective of the shock locations. Only in 10 solution/adaptation cycles the entire three dimensional domain is adapted using less than half a million grid points. With the fine cycle, the adaptation is clearly focused on the shocks. Figure 22 shows the increase in grid size with the coarse cycles. Again the grid size is converging towards an asymptotic value. Perhaps one of the most important figures in this work is Figure 4.5, given in the methodology in section 4, where the adaptation based on a standard flow scalar like Mach number is compared to the current method. The superiority of the adaptation scalar developed in this work against the Mach number is clear. Figure 23 shows the Hessian-based error distributed over the percentage of the edges in the grid. The target error in the coarse phase is set as 0.1 by default. The plot shows that while the initial grid has a greater percentage of edges with error higher than 0.1, the coarse cycle 10 grid brings most of the points to and below the target error.

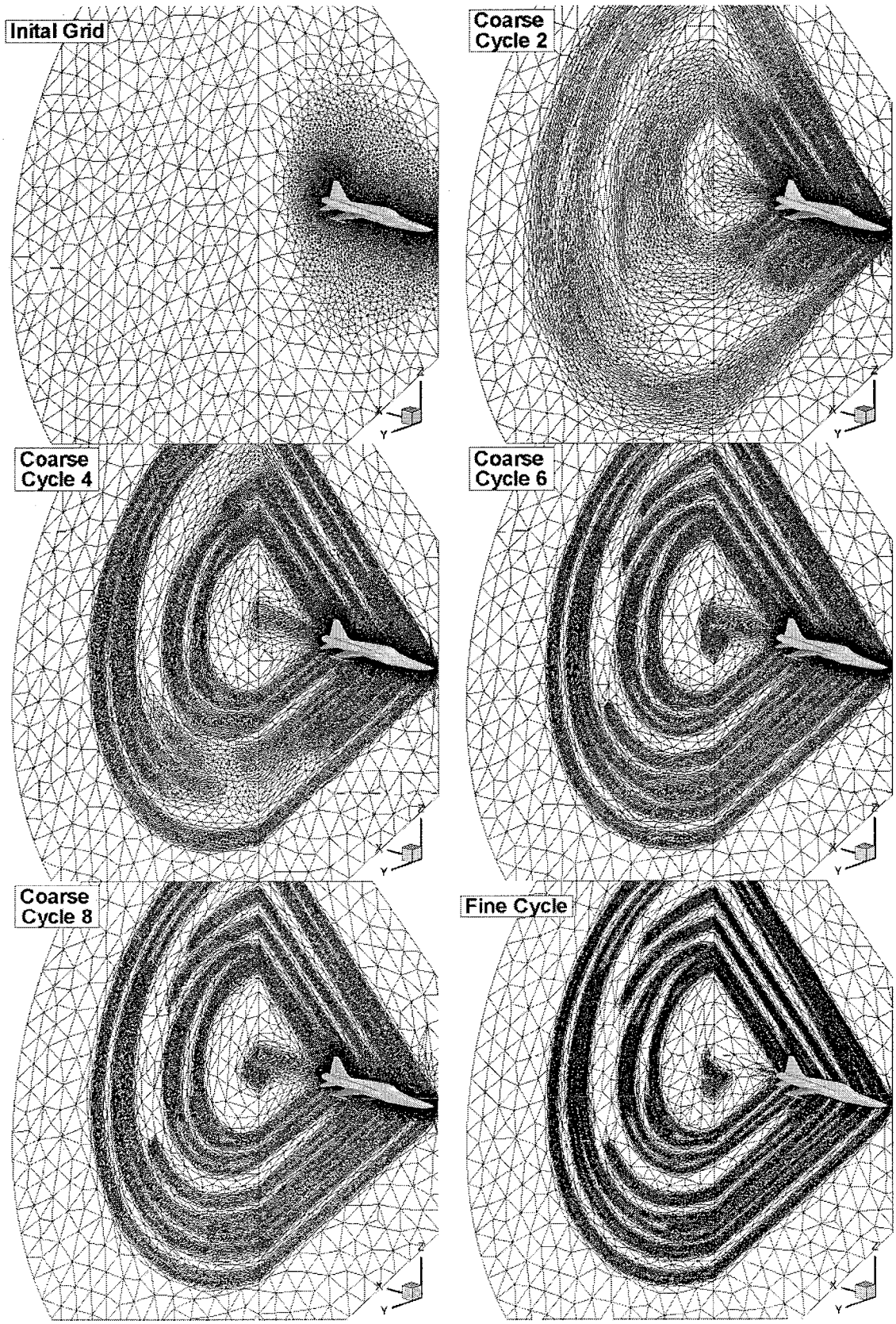

Figure 21: Grid adaptation history for the SSBD

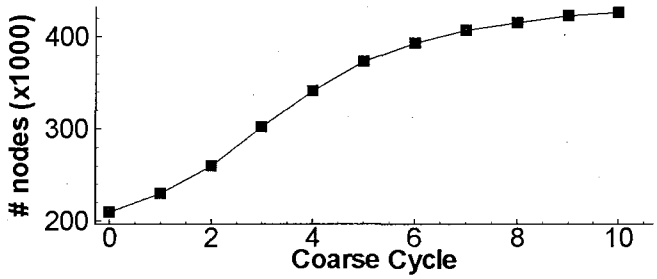

Figure 22: Change in SSBD near field grid size with adaptation cycles.

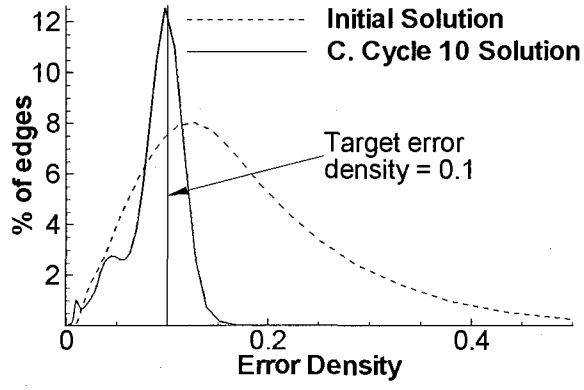

Figure 23: Error distribution at the initial and final cycles of the coarse adaptation phase in SSBD computations.

The cross-flow shock structure of the SSBD is quite complicated and interesting. Using f_S for shock visualization, the cross-flow is plotted at four different x stations in Figure 24. This is a very clean and detailed shock visualization method made possible by the particular formulation of f_S. The dark bands are where $f_S = 1$. There are incomplete, merging, and intersecting shocks in the solution. The numbering of the shocks underneath the aircraft on the x/L = 1.5 plane matches the numbering shown in Figure 25 which displays the current and reference computational pressure signals at the same location. The weak shocks numbered 2, 3, and 4 are clearly visible in the cross flow plane. These shocks are important for the far-field propagation where they form a saw-tooth structure which eventually becomes the flat-top shape. Using the plain Mach number for grid adaptation ignores these weak shocks and results in an incorrect computation of the signal shape at ground level, affecting the noise characteristics. A comparison of the pressure signals in Figure 25 shows the current solution using half a million nodes and a single block grid, is just as good as the 17.1 million-node 24-block structured grid in the reference solution. The computational time and grid generation user time required for such a

structured grid with overlapped zones is quite significant compared to the requirements for a single block unstructured grid. Moreover, the reference grid is fine only at the under-track portion of the cross-flow whereas the current grid is adapted in the entire cross-flow. The figure shows that a one million-node unstructured, adapted grid produces practically the same pressure signal as the half-million-node grid. Thus the 500,000 nodes is quite adequate for accurate sonic boom computations for a real aircraft, up to x/L = 1.5.

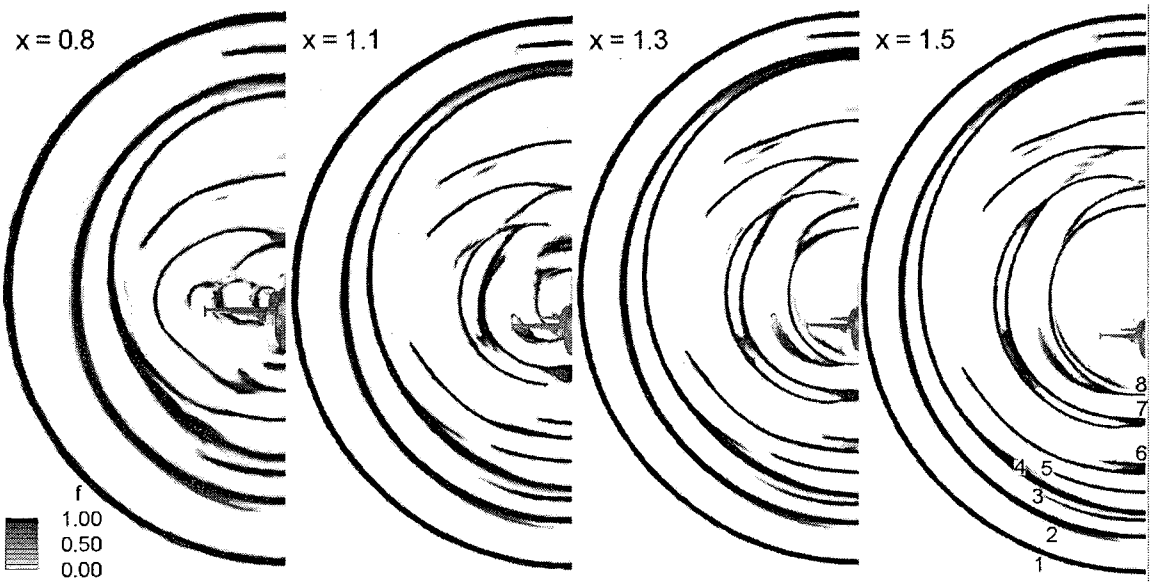

Figure 24: SSBD cross-flow shock patterns on the final converged solution.

Figure 26 shows a comparison of the computed and experimental pressure signatures 91 ft below the aircraft. This is a horizontal data cut parallel to the flight path at r/L = 1.82. The signal is marched using the full-potential equation starting from x/L =1.5, until a complete signal is obtained at r/L = 1.82. The current computational result is in very good agreement with the experimental and reference computational solutions. The only problem is that both computations are missing the shock between the inlet and wing shocks located approximately 27 ft downstream of the bow shock. This is most likely related to the surface definition used in both solutions.

The "min-mod" flux limiter is used in all cases where its value is limited after 150 iterations. The CFL number is allowed to increase from 1 to 200 in 500 steps. The convergence criterion is given as 1e-11. Figure 27 shows the convergence of SSBD Euler computations with FUN3D. The case converges in less than 300 iterations.

To conclude the last three sections covering the double cone, delta wing, and the SSBD unstructured grid adaptation, the most general adaptation parameter settings (for all the cases) are determined to be $C_1 = 10$, $C_2 = 3$, $C_3 = 0.1$, and $\kappa = 1.5$. The best combination of these parameters will be case dependent if the efficiency is to be maximized for each individual problem, however, these parameter settings are a safe conservative set for any case and constitute a reliable starting point.

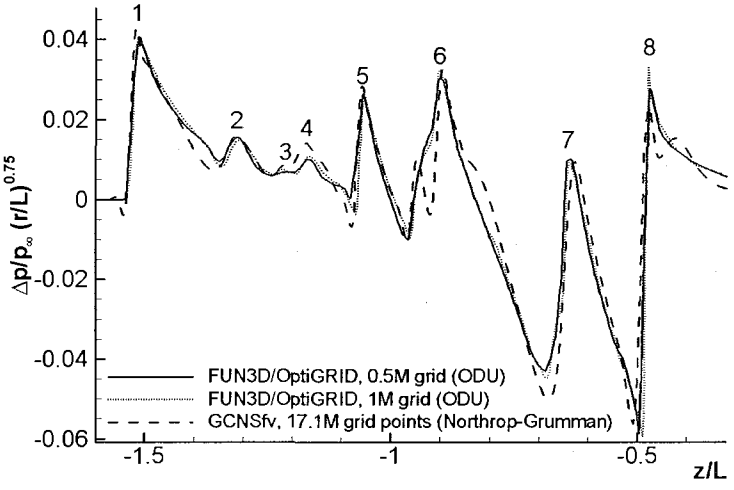

Figure 25: SSBD pressure signal at x/L = 1.5 from reference and current computations.

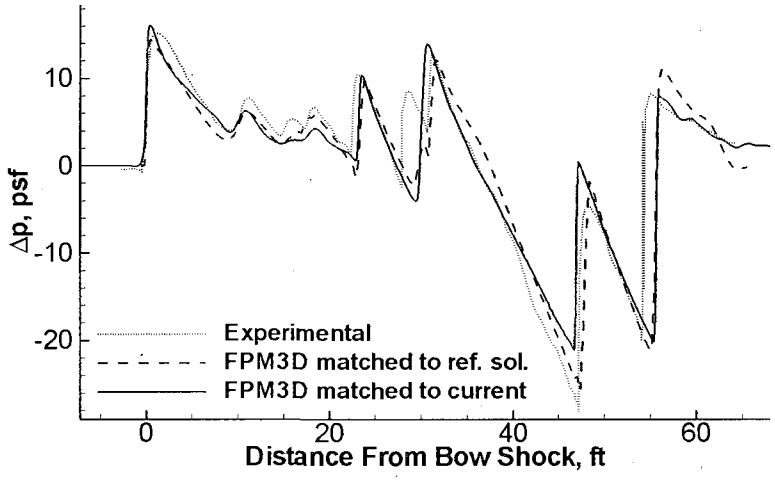

Figure 26: SSBD pressure signal at r/L = 1.82, 91 ft below the aircraft.

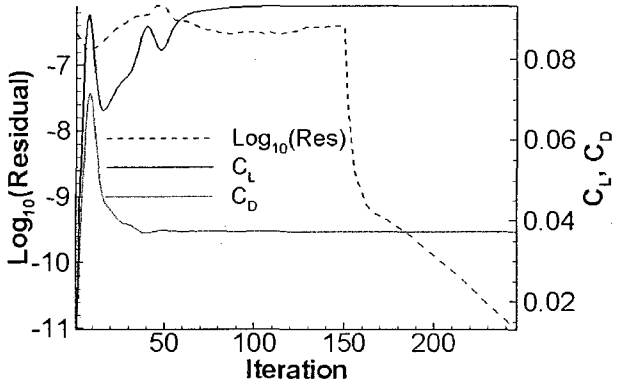

Figure 27: SSBD Euler computations convergence.

5.4 Non-Linear and Linear Propagation Coupling

Three-dimensional, non-linear propagation produces the most accurate sonic boom predictions at ground level since it maintains the non-linear effects, cross-flow diffraction effects, and the lift effects produced by off-centerline components like the wings. If these effects are neglected in the signal propagation as in linear methods, the ground level pressure levels will be underpredicted. This can have serious consequences in aircraft design procedure where a proposed prototype predicted to meet the noise requirements can fail by a significant margin in actual flight tests. The cost of designing, building, and flight testing a prototype is high. Therefore it is crucial to provide the strongest ground level signal level predictions during the initial design phase in order to reduce financial and time resource requirements. Three dimensional non-linear signal propagation has an associated computational cost since it is a CFD method with a very large solution domain where a very small disturbance is computed. The maximum disturbance in terms of $\Delta p/p_\infty$ quickly drops below the order of 10^{-4} as the signal propagates away from the source, and the distance to be covered exceeds several hundred body lengths from the aircraft to the ground. Therefore the marching step size is kept on the order of 10^{-3} L, at most, to provide numerical accuracy at least to the order of 10^{-6}. This requirement results in billions of grid points to be marched by FPM3D (56 billion in the SSBD case) to cover the whole atmosphere on one side of the symmetry plane above and below the aircraft. FPM3D running in parallel mode reduces the computational time required to complete the run from the aircraft to the ground from several days to several hours, butthis is still not fast enough from the design point of view. Surely there has to be a cut-off altitude where the non-linear and cross-flow

diffraction effects are negligible such that linear propagation will suffice. Linear propagation software takes only a split second to run. Therefore stopping the full-potential propagation at a reasonable altitude and completing the computations with the linear code can provide significant savings in computational time requirements with little or no loss in accuracy. In this section the effect of the linear/non-linear propagation changeover distance on the ground level signal is investigated, and an automated method to stop the full-potential marching in order to continue with linear propagation is devised. Tests using the double cone, the delta wing, and the SSBD are reported. Double cone and delta wing cases are solved in a uniform atmosphere mode since there is no in-flight ground signal data available for comparison using these geometries. The atmospheric data used is specific to the SSBD flight conditions in January 2004 over Edward AFB, CA, and is only used to propagate the SSBD signal in a stratified atmosphere.

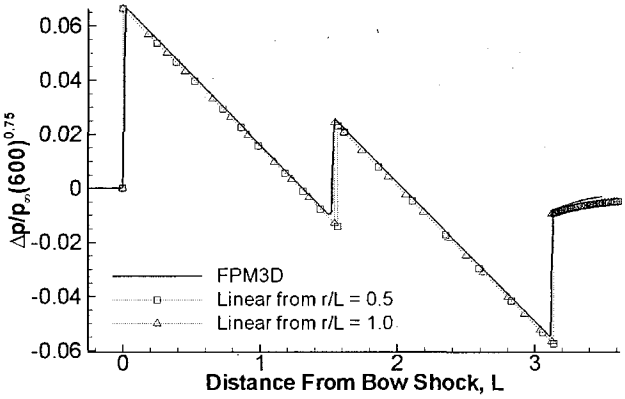

Figure 28: Pressure signature at r/L = 600 for the double cone in Mach 2.01 flow, computed using non-linear (FPM3D) and linear propagation.

The switching distance from non-linear to linear propagation is strongly case dependent. For a simple axisymmetric configuration like the double cone, this distance is as small as one body length from the centerline of the body, and for a complex real aircraft like the SSBD it is over 30 body lengths. Figure 28 shows the pressure signature of the double cone at Mach 2.01 for an axisymmetric flow at r/L = 600. This distance is roughly equal to the ground level for the SSBD flights, and is assumed to be ground level for all cases studied in the current work. The pressure is adjusted with the scaling factor of $(r/L)^{0.75}$ as suggested by the linear theory to make the pressure levels comparable to the data in Figure 15. The figure shows the signal propagated using FPM3D for non-linear propagation all the way to r/L = 600, and linear propagations

starting from r/L = 0.5 and r/L = 1.0. All curves reasonably close, where especially the linearly propagated signal from r/L = 1 is almost a perfect match to the fully non-linear solution. Obviously non-linear propagation after r/L = 1 is not needed for the double cone case. This is because the double cone is axisymmetric, the flow is axisymmetric, the geometry is very simple with linear surface features with no curvature, and there is no lift generated. The body is slender with an attached bow shock. All these simplifications satisfy the assumptions for the linear theory at a very close distance from the centerline. The picture is different for the delta wing case however, where there are three dimensional diffraction effects along with a lift contribution. Figure 29 shows the variation in the ground pressure impulse prediction with the linear propagation starting distance from the delta wing. The pressure impulse is a useful and appropriate way of representing the ground signal using only one scalar value. It is computed as the integral of the pressure in the leading part of the signal where $\Delta p>0$. The leading shock strength is proportional to the pressure impulse in the far-field as suggested by Whitham's theory. This can be seen by observing Eqs. (10) and (11), and the fact that $\Delta p(F(\gamma_0))=0$. The predicted ground signal pressure levels and the foot print size increase towards asymptotic values as the non-linear propagation is extended further downstream. Since the pressure impulse is tied both to the signal amplitude and the foot print size (specifically to the duration of the $\Delta p>0$ lobe) and is proportional to the leading shock strength, it collectively represents all the important features of the signal. Thus it is chosen as the scalar variable to check for convergence of the ground signal prediction as the starting distance for linear propagation is increased. The idea is implemented as follows. As the full-potential code marches the signal downstream, a horizontal signal cut at constant r/L is taken at every Δ(r/L) = 1 interval. The signal cuts are used with the Thomas waveform method to predict ground signals. As input signal r/L increases, the value of the pressure impulse computed from the predicted ground signals converge. The non-linear propagation is terminated when the convergence reaches a user defined threshold. A non-dimensional error index is computed as

$$E_1 = \frac{\left| I_{r/L} - I_{r/L-N} \right| / N}{I_{r/L}} \tag{72}$$

where $I_{r/L}$ is the pressure impulse of the linearly predicted ground signal based on the input data at r/L, and N is a user defined integer, setting the range of the signal convergence check. Larger N compares linear propagations based on input signals further apart. The problem here is that the real ground signal is not known and there is no way of checking against a constant number as

done in CFD computations where the residual is checked against zero. Simply put, the user does not know what the signal is converging to at the start of computations. A small N setting like N = 1 may be misleading since a small variation over one body length can still accumulate a large error over 600 body lengths if it persists. Therefore it is important to check on input signals further apart. In light of current computational results for the delta wing and the SSBD, N = 5 is determined as a satisfactory setting. The dotted curve in Figure 29 shows the error index E_I in the delta wing case. By r/L = 10 the error is 0.012, and by r/L = 30 it is 0.0000924. The ground signal linear prediction comparison up to r/L = 10 input altitude is given in Figure 30 for the delta wing. The figure shows that pressure levels and the foot print size are increasing as the linear propagation starting distance increases. By r/L = 10, the linearly predicted signal is indistinguishable from the non-linear (FPM3D) prediction. This could mean that $E_I = 0.01$ is a reasonable threshold to stop the non-linear computations. However, the results from the SSBD analysis also need to be considered before determining a final value for this threshold.

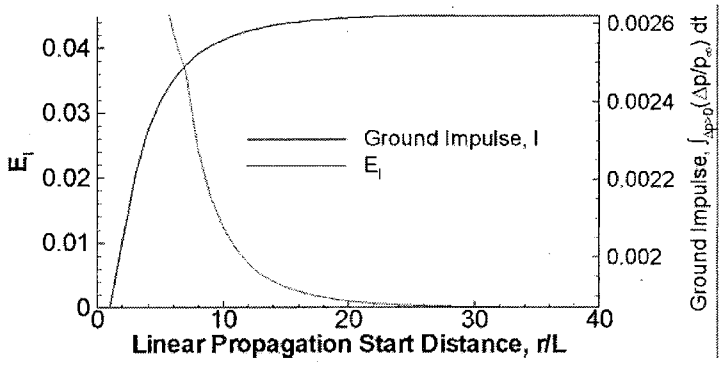

Figure 29: Variation in ground signal pressure impulse level prediction with linear propagation starting distance from the delta wing at Mach 2.0 flow with $\alpha = 2.24°$

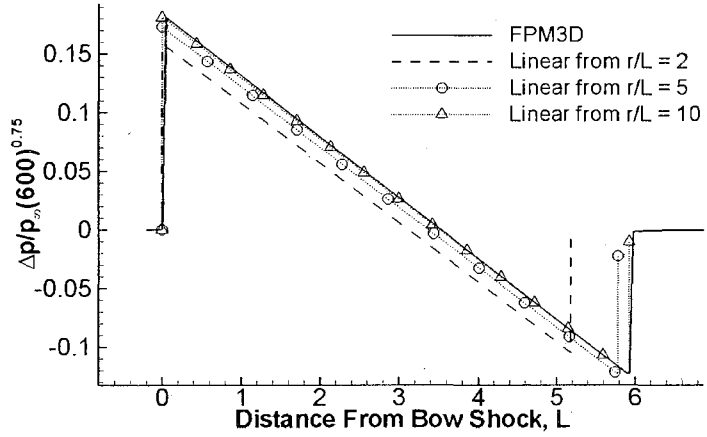

Figure 30: Signature at r/L = 600 (ground level) for the delta wing in Mach 2.0 flow with $\alpha = 2.24°$.

The SSBD ground signal pressure impulse convergence is shown in Figure 31, and the ground signal linear predictions starting from various altitudes are given in Figure 32 along with the experimental data for comparison. The reflection factor used in the computational data is 1.9. Again the convergence of the ground pressure impulse is observed after input altitude r/L = 30 for the SSBD. The ground impulse variation curve is not as smooth as in the delta wing case because of the more complicated shape of the sonic boom signal and the occurrence of shock merging in the cross-flow. The presence of several intermediate shocks makes this case quite different than the delta wing case with a simple N-wave. This time the linearly predicted ground signal shape is also one of the variables, in addition to the pressure impulse, foot print size, and the leading shock strength. This variation in the shape is clear in Figure 32. Fortunately the shape also converges along with the other parameters as the linear propagation input signal distance is increased. The variation in signal shape is due to the difference in intermediate shock merging patterns at different altitudes. The roughness of the ground impulse variation curve in the particular case of SSBD is due to the wing and the inlet shocks on ground appearing merged (which is the real case) after input r/L $\approx$ 26. This change is the reason for the kinks in the curves in Figure 31 around r/L = 26. The error index E_I falls below 0.01 as early as r/L = 8 for the SSBD case. Based on Figure 5.24 this clearly is not good enough since there is still a noticeable difference between signals based on input at r/L = 10 and r/L = 36. The change in ground signals based on input at r/L = 36 and 50 on the other hand is negligible, and E_I falls below 0.0001 by input at r/L = 36. This means that $E_I < 0.0001$ can be used safely as a conservative threshold for complex three-dimensional, lift-producing aircraft geometries. Running FPM3D only up to r/L = 36 instead of r/L = 600, provides about a 16-fold savings in computational time. The comparison with the experimental data shows good agreement in terms of the signal shape and pressure levels. The experimental data is from flight 15, recorded at Edwards AFB, CA, in January 2004 [103].

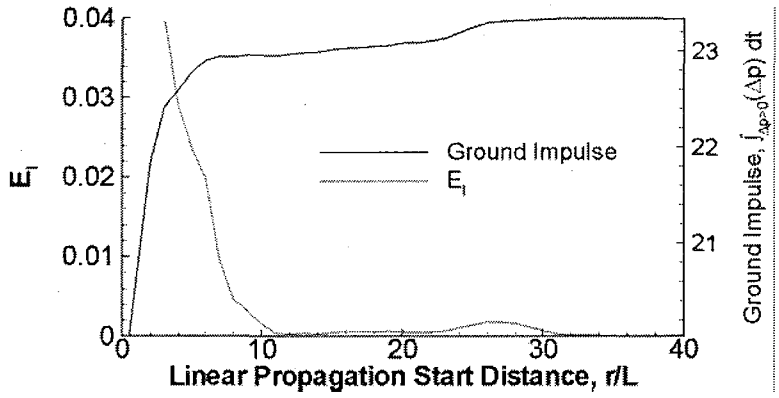

Figure 31: Variation in ground signal pressure impulse level prediction with linear propagation starting distance from the SSBD at Mach 1.414 flow with $\alpha = 1.922°$.

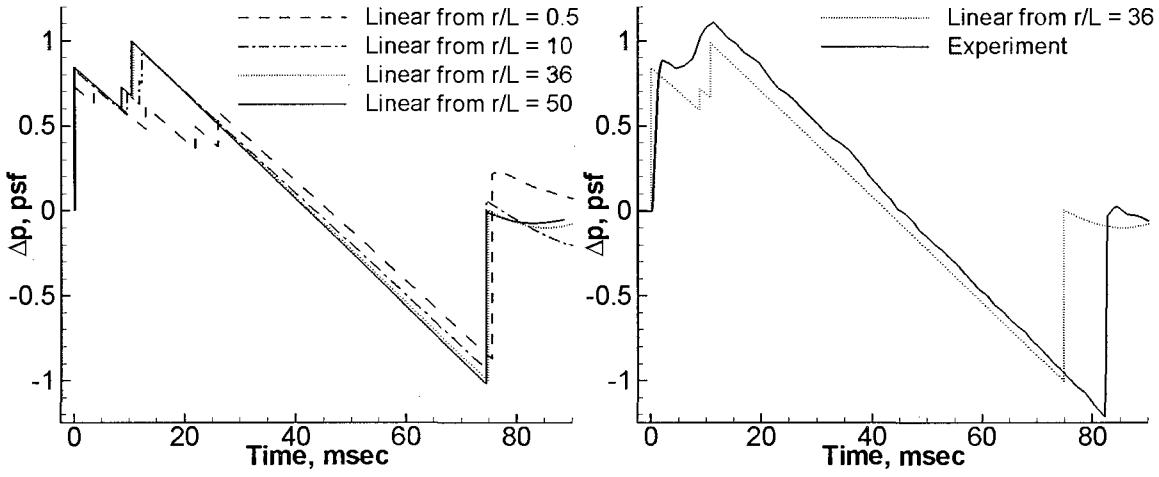

Figure 32: Ground level pressure signature comparisons for the SSBD, computed using non-linear/linear propagation coupling.

5.5 Summary

The Hessian based grid adaptation technique using a special adaptation scalar emphasizing the presence of shocks regardless of their strength is shown to be successful in capturing sharp and accurate shock signatures. Grid adaptation cycles are started with a coarse initial grid created with no prior knowledge of the shock locations. A maximum of 10 solution/adaptation cycles and 500,000 final number of grid nodes are needed to complete runs in general. The grid adaptation methodology is developed with special care to make sure one set of software settings apply to all problems, ranging from the simplest axisymmetric case to the most

complex realistic three-dimensional cases. In this way, the methodology can be implemented in an automated fashion in geometric design optimization for sonic boom mitigation. The fundamental problems associated with feature based adaptation are alleviated, which are: the necessity for a fine initial grid to partially resolve the features; a high number of solution/adaptation cycles; excessive refinement for stronger features; and unwanted refinement for features of no interest. Rankine-Hugoniot shock jump conditions are shown to be satisfied with the current methodology, which is provided by shock fitting, resulting from Roe's FDS formulation and shock aligned cell surfaces. Excellent agreement with reference experimental and computational data is obtained for all geometries tested. Via the unstructured methodology, huge savings in user and computational time are provided for initial grid generation and flow solution/grid adaptation processes.

The coupling of non-linear full-potential and linear geometric acoustics propagation methods is performed to reduce significantly computational time requirements for ground level sonic boom prediction. An error index is formulated to check on the convergence of the ground signal with the increase in input data distance from the aircraft for the linear propagation. The studies indicate that while an axisymmetric case requires the non-linear solution only up to one body length, complex three dimensional geometries with lift and shaped sonic booms need up to 40 body lengths. The cut-off distance for non-linear propagations can be automatically determined by the error index given in Eq. (72). The Thomas waveform parameter code is utilized when the signal is available at a new r/L integer value below the aircraft to compute the ground signal, from which the pressure impulse is computed. For axisymmetric cases, the required non-linear solution distance can easily be covered using Euler computations.

The current sonic boom prediction methodology formally divides the problem into near-field, mid-field, and far-field propagation using Euler, full-potential, and linear computations, respectively. Using this method, ground level sonic boom prediction for the SSBD shows very good agreement with the available experimental data, closely matching the pressure levels and the signal shape. The method is considered accurate and computationally efficient, and the optimization studies given in the following chapter are based on the pressure signal responses obtained using this methodology.

6. SHAPE OPTIMIZATION FOR SONIC BOOM MITIGATION

This section presents optimization studies using the sonic boom prediction methodologies demonstrated in section 5. The accuracy and efficiency of the non-linear prediction steps, automated parametric surface definition and grid generation, grid adaptation and shock fitting, and the parallel processing via MPI makes the available computer programs and coupling scripts an ideal framework for use in aerodynamic design optimization for sonic boom mitigation. Similar to the layout of the previous chapter, an axisymmetric shape, a delta wing, and the SSBD aircraft airframe are used as baseline configurations for optimization. The responses targeted for minimization are the ground level sonic boom signal features like bow shock strength, peak Δp, and impulse. The optimized axisymmetric shape is used as a nose attachment to the SSBD aircraft to reduce its bow shock strength. Unlike Gulfstream's approach of dividing the original bow shock into smaller shocks in series, this study is aimed at lowering the bow shock strength directly. This shortens the nose attachment length significantly since there is no need for long cylindrical sections to provide the necessary separation between shocks in order to avoid coalescence. The second optimization study with a delta wing is performed using dihedral, camber, angle of attack, and wing twist as primary design factors. Span-wise non-linear camber and twist distribution are introduced as design factors as well, which significantly increases the complexity of the analysis. Volume and lift of the delta wing are conserved. In the final part, the SSBD aircraft is equipped with the optimized nose attachment and a new wing that matches the lift, volume, and aerodynamic center of the original wing. The new wing is designed as a delta wing and optimized similarly. The optimum delta wing found in the second part cannot be used directly on the SSBD, primarily due to the existence of interference lift between the wing and the fuselage. Interference lift cannot be estimated unless the wing and fuselage are attached. Therefore the delta wing optimization is repeated for the SSBD application with wing parameters like volume, aerodynamic center, root thickness and chord length set specifically for this aircraft.

6.1 Axisymmetric Nose Optimization

The axisymmetric nose optimization study is carried out to design a low boom, low drag shape that can be used as the nose or an extension to the original nose of an aircraft to reduce its bow shock strength on the ground. Literature shows that low boom designs generate high drag, and vice versa [7]. The sonic boom minimization theory of Seebass and George [19] points to a high drag axisymmetric shape where the F(y) function is strongest at the tip and minimal thereafter. The nose bluntness relaxation method developed by Darden [20] as an add-on to Seebass and George minimization theory adds new parameters to the F-function definition which can be adjusted to control drag as well, allowing the user to compromise between low boom and low drag. In general the minimization studies based on linear prediction theory results in high drag designs for low sonic boom. The axisymmetric shape optimization for the low sonic boom problem is re-examined here using non-linear near-field analysis based on CFD, to see if optimization based on non-linear solutions can efficiently lead to designs with low sonic boom as well as low wave drag. The final result is compared to the axisymmetric optimization study outcome of Hague and Jones [15] which is based on linear prediction methods and similar geometric constraints.

The parameterization of the meridian profile of the axisymmetric nose shape is done using a series of linear ramps connecting the tip to the base perimeter. The parameters of optimization are the ramp lengths ($X_1, X_2, X_3, \ldots$), and half-cone angles ($\theta_1, \theta_2, \theta_3, \ldots$). Up to 5 ramp elements are used in the present work. The configuration is illustrated in Figure 33 using 3 ramps for simplicity. The choice of defining the meridian profile with ramps stems from Ref. [58] where a set of 2-ramp configurations creating one intermediate shock was tested for bow shock strength and the position of the intermediate shock with respect to the bow shock. This study shows that a convex meridian profile with $\theta_2 < \theta_1$ produces weaker sonic boom signals with an intermediate shock. A set of 2-ramp convex and concave meridian profiles and their respective pressure signals at r/L = 14.9 are shown in Figure 34. The flow is axisymmetric at Mach 2.0. The signal altitude r/L = 14.9 is well into the linear far-field for the axisymmetric shapes, as pointed out in the previous chapter. The pressure impulse and the peak pressure levels of convex profiles are significantly lower than concave profiles. Convex profiles divide the bow shock into two smaller shocks, reducing the overall peak pressure. Since the intermediate shocks dissipate faster than the bow shock in the far-field, convex profiles will produce weaker sonic booms at ground level compared to concave profiles. The C_1 discontinuity of the meridian profile

is responsible for the second shock, and the convexity keeps it from coalescing with the bow shock. Smooth convex meridian profiles do not create intermediate shocks, which is why the study here is carried out using a series of linear ramps with different angles rather than a smooth convex curve.

Perturbations on the 2nd ramp angle, over a short range, modify the position of the intermediate shock with respect to the bow shock [58]. Similarly, short range perturbations on the 2nd ramp length control the intermediate shock strength. The effects of the 2nd ramp angle (θ_2) and length (X_2) on the pressure signal are displayed in Figure 35. The figure shows that the ramp angle only modifies the position, and the ramp length only modifies the strength of the intermediate shock. However, stronger intermediate shocks move faster upstream toward the bow shock, due to the increased local pressure, temperature, and speed of sound, and the above statement is valid only over a short range of ramp length modifications. In short, by using a series of ramps defining the meridian profile, it is possible to determine a particular setting of ramp angles and lengths to obtain a desired signal shape. The study in this section builds on the findings of Ref. [58] and extends the investigation to 3-, 4-, and 5-ramp configurations. Increasing the number of ramps exponentially complicate the investigation as interactions of design parameters occur and make it impractical to come up with expressions relating each design parameter (ramp angle, length, for each ramp) to a particular feature in the far field signal. Geometric constraints that have to be applied for a feasible design further complicate the analysis. Therefore the study is carried out as a multivariable design optimization study based on response surface methodology to minimize the peak delta pressure, pressure impulse, and drag at ground altitude.

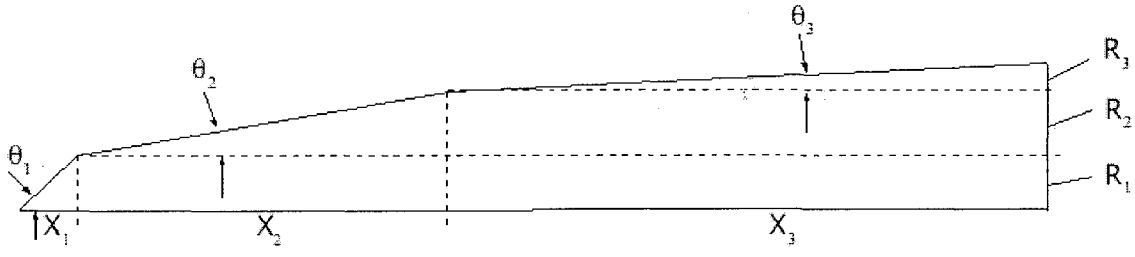

Figure 33: Meridian profile for 3-ramp configuration

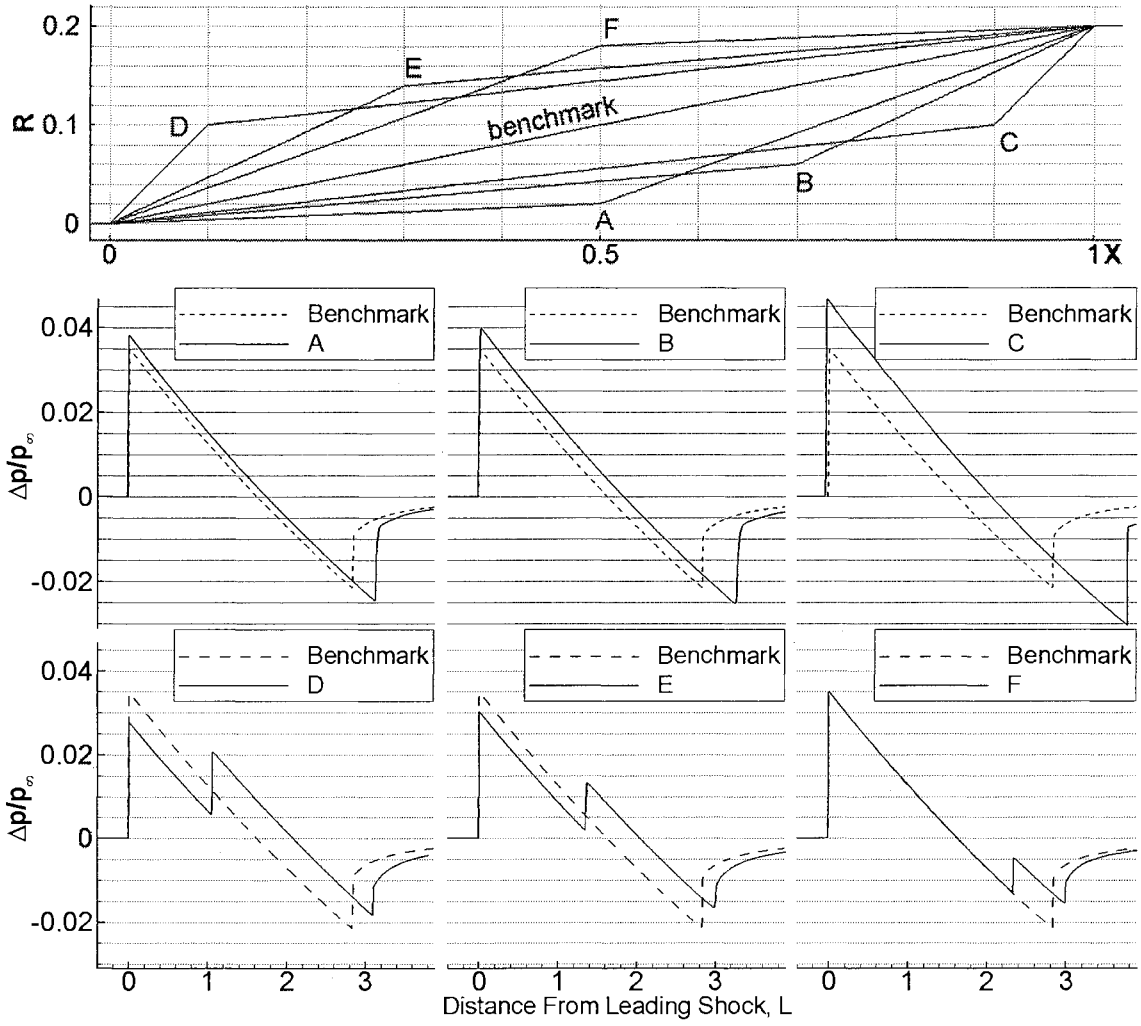

Figure 34: Convex and concave 2-ramp meridian profiles (above) and their pressure signals (below) at r/L = 14.9 in Mach 2.0 axisymmetric flow [58].

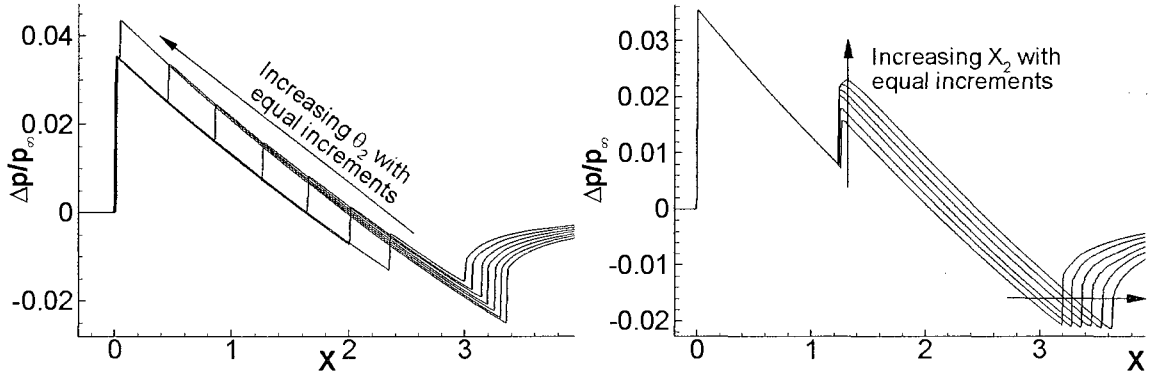

Figure 35: Effects of 2nd ramp angle (left) and length (right) on the intermediate shock position and strength at signal altitude r/L = 14.9.

6.1.1 Geometric Constraints and Profile Parameterization

The literature shows that the more slender the axisymmetric shape gets, the lower the far-field sonic boom levels are. Since it is not feasible to fly an infinitely long aircraft with a finite maximum cross sectional area, the length of the axisymmetric nose shape under investigation needs to be limited. Long extensions to the nose of an aircraft are likely to compromise the structural integrity and pitch/yaw controls due to the increased moment arm. Such tests on controls and structural vibrations are outside the scope of the current study. The length and base diameter constraints used in the current study are determined rather arbitrarily with some insight to the problem gained from Gulfstream's Quiet Spike™ development, where the attached nose spike was 30% of the entire aircraft length, and the base diameter was about half the maximum fuselage diameter [87]. The concerns associated with this design are: weight and aeroelastic stability. The length constraint in the current study is set as $\mathcal{L}_{NOSE} = 0.2\mathcal{L}_{SSBD}$, where $\mathcal{L}_{SSBD}$ is the length of the original SSBD aircraft configuration on which the optimized axisymmetric nose shape will be attached. When the nose geometry is attached at the tip (x = 0) location, it constitutes 16.7% of the total length ($\mathcal{L}_{NOSE} + \mathcal{L}_{SSBD}$) of the new configuration. This is almost half the length of the Quiet Spike™ already flight tested, and is a conservatively safe and competitive constraint. The base radius is kept similar to the Gulfstream setting of about half the maximum fuselage radius. The maximum cross-sectional area of the SSBD fuselage (computed using the CAD data) is $0.00924\mathcal{L}_{SSBD}^2$. Treating this as a circular area the maximum radius would be $0.054\mathcal{L}_{SSBD}$. The base radius in the current study is set to $R_B = 0.025\mathcal{L}_{SSBD}$ which is a reasonable rounded number and is about half the maximum fuselage radius. Neither the length nor the base radius are considered to be design variables since the larger the length, the weaker the ground boom, and the smaller base radius reduces the stiffness of the geometry. Optimization of these parameters should be done in a structural/aeroelastic framework which is beyond the scope of the current study. The current study focuses on finding the best meridian profile with given axial length and base diameter that minimizes ground level sonic boom intensity and drag.

In addition to the constant total length and base diameter constraints, individual ramp lengths and angles are also constrained. The optimum condition is to have intermediate shocks in the signal which requires a convex meridian profile as discussed above. Therefore the half-cone angle of each ramp is constrained to be positive and smaller than the preceding one. Figure 34 shows that the steeper the first ramp angle, the lower the maximum signal pressure levels. This is no news since it has been shown in the literature that blunt shapes produce lower booms, but also

very high wave drag due to the detached bow shock. To keep the shock attached while minimizing the boom levels, the 1st ramp angle is set just as large as the critical shock separation angle. This is the key setting to keep the drag low while minimizing boom. Again, looking at Figure 34 one can see that keeping the 2nd ramp length longer than the 1st ramp produces lower maximum pressure levels. This is because more of the bow shock strength is transferred to the intermediate shock, and both shocks end up at similar pressure levels. Hence the final constraint is to have each ramp longer than the preceding one. The ramp angles are measured as half-cone angles with respect to the centerline, and the ramp lengths are measured as the axial length of the segment.

The nose geometry optimization is carried out at Mach 1.414, the cruise speed of the SSBD. Referring to Figure 33, the first ramp angle, θ_1, is set equal to the critical angle for detached shock formation determined by the use of Taylor-Maccoll equation for supersonic conical flow [61]. For Mach 1.414, $\theta_1 = 28^o$. In mathematical form, the physical constraints are given by

$$X_1 < X_2 < X_3 ... < X_{N_{RAMP}} \tag{73}$$

$$\sum_{i=1}^{N_{RAMP}} X_i = L_{NOSE} \tag{74}$$

$$\theta_1 > \theta_2 > \theta_3 > ... > \theta_{N_{RAMP}} \tag{75}$$

$$\sum_{i=1}^{N_{RAMP}} R_i = R_B \tag{76}$$

where N_{RAMP} is the number of ramps, and

$$R_i = X_i \tan\theta_i \tag{77}$$

Equations (74) and (76) eliminate one factor each. Presetting θ_1 eliminates one more factor, bringing the total number of design factors to $2(N_{RAMP}) - 3$. The constraints listed above put tight restrictions on the parametric physical values. The applicable range for one factor depends strongly on the parameter settings of the preceding ramps. This makes it difficult to set up an experimental design matrix with a global set of maximum and minimum settings for each factor. When done so, factorial design points which are either at a global max or a global min setting of a parameter will not be realizable. Using factorial points is an easy way of setting up an

orthogonal design matrix which is important to generate a reliable model with uncorrelated model terms. It is possible to generate a near-orthogonal experimental matrix without factorial points using computer generated optimal designs, however, the resulting factor levels are usually not well rounded numbers, and are difficult to work with. Moreover, the constraints are non-linear due to Eq. (77). The DoE/RSM software Design-Expert used in this study does not support non-linear constraints, and the design space cannot be defined. There are two ways to work around these problems. One is to provide a rich list of user created candidate points with simple numeric values which can be input to DE, then letting the software pick the best combination without declaring any constraints. The second way is to redefine the factors as percentages of the allowable range of each design parameter, where these ranges change as the parameters controlling the previous ramp element geometry changes. The constraints on the ramp angles are partially shown in Figure 36 for the 3-ramp configuration. Keeping the same X_2, ramp 2 can be segment "d" with $\theta_2 = \max$, or segment "e" with $\theta_2 = \min$. As X_2 gets smaller, the maximum allowable value of θ_2 increases up to θ_1. Segment "a" is another limiting case for the 2nd ramp where θ_2 is at its absolute maximum value which is equal to θ_1. When ramp 2 becomes segment "d", ramp 3 can only be segment "c", and when ramp 2 is segment "e", ramp 3 can only be segment "f". As X_1 is increased, the slopes of segments "d" and "e" will change, altering the allowable max and min values of θ_2. Similarly the max and min values of X_2 are dependent on X_1. X_2 can be equal to X_1 at the lower limit, and to $(\angle_{NOSE} - X_1)/2$ at the upper limit.

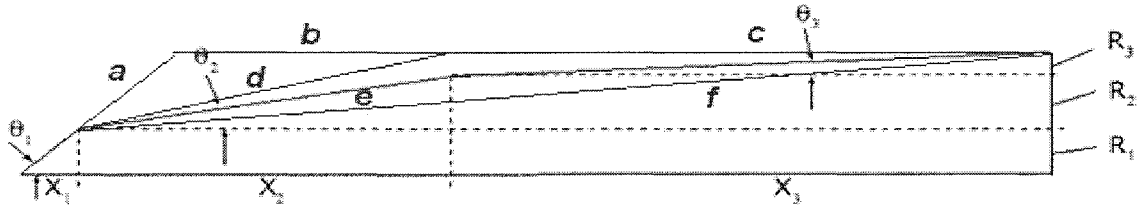

Figure 36: Constraints illustrated partially for 2nd and 3rd ramps on a 3-ramp configuration

The relationship of the range of a factor can be recursively related to the values of the factors of preceding ramps. These relationships are given by

$$X_i range = X_i high - X_i low = (L_{Nose} - \sum_{j=0}^{i-1} X_j)/(N_{RAMP} - i + 1) - X_{i-1} \tag{78}$$

where $X_0 = 0$ and i = 1, 2, …, $N_{RAMP} - 1$

$$\begin{aligned} \theta_i range &= \theta_i high - \theta_i low \\ \theta_i high &= \min\left(\theta_{i-1}, \tan^{-1}\left\{ \frac{1}{X_i}\left(R_B - \sum_{j=1}^{i-1} X_j \tan\theta_j \right) \right\} \right) \\ \theta_i low &= \tan^{-1}\left\{ \frac{R_B - \sum_{j=1}^{i-1} X_j \tan\theta_j}{L_{NOSE} - \sum_{j=1}^{i-1} X_j} \right\} \end{aligned} \tag{79}$$

where i = 2, 3, …, $N_{RAMP} - 1$. Instead of using X_i and θ_i as factors directly in the experimental design matrix, they can be defined in terms of a new set of factors **F** as

$$\begin{aligned} X_i &= X_i low + F_i X_i range \\ \theta_j &= \theta_j low + F_k \theta_j range \\ k &= j + N_{Ramp} - 2 \\ i &= 1, 2, \ldots, N_{Ramp} - 1 \\ j &= 2, 3, \ldots, N_{Ramp} - 1 \end{aligned} \tag{80}$$

where constraints on **F** are simply $\mathbf{0 < F < 1}$. Using this formulation the actual physical constraints are masked, and an orthogonal design matrix can be setup using factorial points. The formulation given in Eqs. (78) through (80) are easily implemented in a computer code which can generate the meridian profiles and computational grids for any desired number of ramps.

In some cases, it is desirable to limit the experiments to a sub-space in the entire design space, where the center of this sub-space can be different than the global center. For example, after running and analyzing a number of design points in the entire domain space, a finer analysis, using tightly spaced points, can be carried out in the vicinity of a local minimum. The formulation above is modified slightly to accommodate the user defined center and limits of the design sub-space.

$$X_i = X_i low + (X_i c + F_i B_i) X_i range$$
$$\theta_j = \theta_j low + (\theta_j c + F_k B_k) \theta_j range \quad (81)$$

where now **-1 < F < 1**. $X_i c$ and $\theta_j c$ take values between 0 and 1, designating the location of the center point with respect to $X_i low$ and $\theta_i low$ in terms of a fraction of $X_i range$ and $\theta_i range$. **B** is a user defined vector constant, setting the limits of the design sub-space as a fraction of the physical range of each factor. For convenience, let

$$X_i^* = X_i c + F_i B_i; \quad \theta_j^* = \theta_j c + F_k B_k \quad (82)$$

The following has to hold for a run not to exceed the design space.

$$0 < X_i^* < 1; \quad 0 < \theta_j^* < 1 \quad (83)$$

6.1.2 Solution Method

Meridian profiles are created and used for axisymmetric grid generation in the in-house developed software "SFGA" that aligns and adapts the structured grid for shocks. Earlier versions of this software have been used previously in Refs. [53, 58, 81]. The axisymmetric domain is created as a slice with only two meridian planes, 1 degree apart, providing savings in computational resources. CFL3D is used to solve Euler equations on the grids for near-field prediction. The solver is coupled iteratively with SFGA to improve shock fitting and grid generation. By providing initial grids that are already aligned in the direction of the Mach lines, sharp and accurate pressure signals are obtained at $r/L_{NOSE} = 7.5$ after only two CFL3D/SFGA iterations. The total number of grid points used in the final adapted grids is around 175,000 for all cases. Far-field analysis is done using the Thomas Waveform Parameter Code in the stratified atmosphere mode. The utilized atmospheric data corresponded to the conditions for flight 15 of SSBD in January 2004 over Edwards AFB, CA. Linear propagation is shown to be accurate for the axisymmetric geometries formed by linear surface geometries in the previous chapter with the starting altitude $r/L \geq 1$. In this case the linear extrapolation starting altitude is $r/L_{NOSE} = 7.5$ which is well beyond the $r/L = 1$ threshold. The solution process is fully automated where the

user enters the values for L_{NOSE}, R_B, Mach number, N_{RAMP}, **Xc**, **θc**, **B**, and a user-defined design matrix listing **F** for each run. The framework "RAMPSOLV" established for the analysis automatically generates all the near-field grids and submits batch jobs to a high performance cluster (HPC) to run CFL3D in parallel mode for each run. CFL3D/SFGA iterations are also sequenced in the framework, followed by near-field signal extraction and linear extrapolation to far-field. The average computational time for one run is about 4 minutes using 8 AMD Opteron 64 bit 2.0GHz. CPUs. Multiple design points in the design matrix can be solved simultaneously to speed up the process. Using 7 groups of 8-CPU computations, for example, reduced the average computational time of one run to 0.6 minutes. The RAMPSOLV suite lists all the runs in the design matrix in a batch job file, and spawns as many parallel jobs on the high performance cluster as specified by the user. These parallel jobs work through the batch file collectively, each solving a different run until the list is cleared. In this way hundreds of runs can be queued up easily with a few commands, and processed with no user involvement. The data are compiled by the end of the run to list ground level peak Δp, pressure impulse, and drag coefficients. The ground pressure signals from each run are gathered in ASCII Tecplot format for visual inspection. The optimization studies are carried out sequentially, starting with 2-ramp configurations and ending with 5-ramp configurations. The number of run cases increases exponentially with the number of ramps. The analysis is limited to a maximum of 5-ramp configurations to prove the concept. The design is improved with increasing numbers of ramps, especially in terms of drag.

Two approaches are followed in the optimization. One is to minimize the ground level impulse of the axisymmetric geometry, and the other is to minimize the ground level peak Δp. The ground level here is taken as the ground level of the SSBD aircraft, which is at about r = $600L_{SSBD}$ ($3000L_{NOSE}$). While the reason to minimize the peak Δp is obvious, the reasoning behind impulse minimization warrants an explanation.

Whitham's linear theory shows that in the far-field the leading shock strength is directly proportional to the pressure impulse, which is the integral of Δp where $\Delta p > 0$ (the leading part of the signal in general). This can be deduced from Eqs. (10) and (11), with the clue that $\Delta p(F(y_0))=0$. Unlike Gulfstream's approach to divide the bow shock into smaller shocks and avoid their coalescence, the current approach is to reduce the leading shock strength itself, without dividing it. This approach eliminates the need for a long nose boom which has to provide enough separation between frontal shocks so their coalescence is delayed. It is not clear at this point whether the leading shock coming off the tip of the nose geometry will coalesce with the rest of the frontal shocks of the SSBD. This may happen since no provisions are taken here to avoid shock coalescence. In case the remaining SSBD fore-body shocks coalesce with the new

bow shock coming from the nose attachment, the impulses are additive and simultaneously contribute to the strength of the bow shock on ground. Hence a minimum impulse nose can be more beneficial than a minimum peak Δp nose in this situation. Besides, while the peak Δp level is related closely to the outdoor loudness of the sonic boom through Eq. 1.1, the pressure impulse is related to its structural impact and indoor discomfort. While loudness can be quite irritating, structural damage can cause serious injuries (e.g. flying glass shards, Kelowna, Canada, Aug. 6th, 1969, 6 injured). It is possible to have signals with higher peak Δp but lower pressure impulse. The impulse minimization approach is covered in detail in the next part. The minimum peak Δp solution found following the same optimization strategy is provided at the end of this chapter, and compared to one of the well known minimum Δp solutions in the literature.

The reference benchmark meridian profile is chosen as a single ramp connecting the tip to the base. For Mach 1.414, the benchmark $C_D = 0.07386$, ground level peak $\Delta p = 0.32$ psf, and pressure impulse $I = 0.1$ psf·msec at $r = 600\ L_{SSBD}$. The drag is computed using the base area as reference. The drag in general increases while Δp is reduced, and drag minimization counters sonic boom mitigation efforts. However, increasing the number of ramps significantly reduces the increase in drag for optimum profiles. Therefore drag response is excluded from the optimization procedure as it naturally decreases with increasing number of ramps. This renders the current analysis a single response optimization study.

The optimization algorithm based on response surface methodology is outlined as follows.

1. Scan the entire design space using evenly distributed design points, with the center point $\mathbf{F} = \mathbf{0}$ placed at the center of the global design space via setting $\mathbf{Xc} = \mathbf{\theta c} = 0.5$. Avoid the absolute boundaries by 10% of the total range of each factor by setting $\mathbf{B} = 0.4$. This step is called the "grid search".
2. Select the design point with the minimum pressure impulse or Δp as the starting point of the optimization loop.
3. Setup a face centered design (CCD) for a 2nd order surface analysis, centering on the selected design point in step 2. Reduce the design space range to 1/10th of the grid search range in step 1, by setting $\mathbf{B} = 0.04$. Use the RAMPSOLV suite to carry out the computations.
4. Analyze and model the response using quadratic fitting in Design-Expert.
5. Use the optimization tool to predict an optimum in the current sub-design space.
6. Test the optimum.

7.

   a. If the actual response of the optimum is better than any other points in the recent design matrix, center here and run a new CCD keeping the same boundary limits (leaving **B** unchanged)
   b. If the response of any of the points in the recent design matrix is better than the optimum actual, center here instead and run a new CCD, keeping the same boundary limits.
   c. If the new center point is the same as the recent center point (no change in optimum from the previous loop), reduce the sub-design space by 50% and run a new CCD (to dig deeper around the optimum).

8. Repeat steps 4 – 7 until the location of the optimum is converged.

A non-linear design (CCD) with quadratic modeling is used instead of linear models and steepest descent search, primarily to decrease the number of iterations to reach the optimum. Quadratic modeling can show the stationary points in the design space. This is preferable to a steepest descent search which can start sending the center point back and forth instead of converging towards the stationary point. The penalty of using CCD instead of just factorial points becomes negligible when the number of design factors increase with increasing number of ramps. For example, the 3-ramp configuration which has 3 design factors needs 8 points (factorials, $\mathbf{F} = \pm\mathbf{1}$) for linear analysis, and 14 points for nonlinear analysis with CCD (8 factorials + 6 axials). On the other hand, the 5-ramp configuration which has 7 design factors requires 128 points for linear analysis and 142 points for CCD analysis. If half-fractional factorials are used, then these numbers are 4 and 10 for the 3-ramp configuration, and 64 and 78 for the 5-ramp configuration. Clearly the linear analysis does not provide significant savings in design matrix size for a high number of ramp configurations. The non-linear analysis on the other hand increases the accuracy of the predicted optimum and speeds up the convergence of the solution. This will be made clear with an example using the 3-ramp configuration in the next section.

6.1.3 Results and Discussion

As mentioned earlier, the following presents the impulse minimization in detail. To be concise, the peak Δp optimum, found using the same procedure, is provided without going through similar details. The simplest case is the 2-ramp case with only one design factor, X_1 being the free variable. For this case, the same 5 level design with F_1 = -1, -0.5, 0, 0.5, and 1 is used in the initial grid search (step 1) and with the subsequent nonlinear models. Table 2 shows the results of optimization iterations for this case. The 2nd row in the table shows the location of the center point ($F_1 = 0$) used in the design matrix at each iteration. $X_1c = 0.5$ means the center of the design matrix is at the global center of the entire design space. The 3rd row is the boundary range parameter which is set at 0.4 at the grid search step and then reduced to 0.04. The 4th row shows the factor level setting of the optimum configuration, determined at step 7 in terms of X_1^*. X_1^* is the fraction of the absolute range of this factor. The physical value X_1 for the optimum setting can be found by working through Eqs. (78), (81), and (82). The 5th row is the impulse, I, at ground level, the response being minimized, and the last column is the percentage decrease in I computed by $100(I_{benchmark}-I_{new})/I_{benchmark}$ where $I_{benchmark} = 0.1$. At iteration 5, the center and the optimum are reported at the same location ($X_1c = X^*_{1,\,opt}$). This indicates that the situation in step 7.c has occurred, and the sub-design space range is reduced by 50% for the next iteration. Note that the drag is increasing as the impulse is minimized. This is typical for sonic boom minimization. The optimum solution is not changing for the last 4 iterations, which shows that there is no need to go any further with the optimization. The optimum result shows a 20.7% decrease in the ground level pressure impulse, and an increase in the drag by a factor of 2.82 compared to the benchmark values. The drag increase is obviously too much with the 2-ramp design.

Table 2: 2-ramp optimization results

Iter.	0 (grid search)	1	2	3	4	5	6	7
X_1c	0.5000	0.5000	0.5400	0.5800	0.5705	0.5669	0.5669	0.5669
B	0.4	0.04	0.04	0.04	0.04	0.04	0.02	0.01
$X^*_{1,\,opt}$	0.5000	0.5400	0.5800	0.5705	0.5669	0.5669	0.5669	0.5719
I_{ground}	0.0836	0.0821	0.0806	0.0801	0.0801	0.0801	0.0801	0.0800
C_D	0.1646	0.1919	0.2167	0.2105	0.2080	0.2080	0.2080	0.2103
-%ΔI	17.1	18.6	20.2	20.6	20.7	20.7	20.7	20.7

Figure 37 shows the variation of ground level pressure impulse and drag responses with the parameter X_1^* defined by Eq. (82). $X_1^* = 0$ means the 1st ramp length setting is at its absolute minimum, which is zero. This would be equivalent to the benchmark case with a single ramp. The dots on the impulse curve are the actual data points obtained in the computations. The impulse response goes gradually through the minimum at about $X_1^* = 0.57$. The drag response on the other hand is monotonous and goes to a minimum towards $X_1^* = 0$, the benchmark case. The plot on the right of Figure 37 shows the variation of the predicted ground level pressure signal as X_1^* is changed between 0.5 and 0.62. The optimum is located about the center of this range at $X_1^* = 0.57$, shown with the dashed line. Two distinct changes in the signal are the increase of the leading shock strength, and the downstream movement of the intermediate shock. Increasing the leading shock strength has a positive effect on the impulse, the integral area under the positive Δp sections, which is countered by the downstream movement of the intermediate shock. Up to $X_1^* \approx 0.55$, the negative effect of the downstream movement of the intermediate shock is stronger than the positive effect of the increasing leading shock strength on the pressure impulse. Between $X_1^* \approx 0.55$ and 0.6, the leading and intermediate shock effects balance each other and the minimum impulse is obtained at $X_1^* = 0.57$. As soon as the intermediate shock goes under the $\Delta p = 0$ line, the positive effect of the leading shock becomes more pronounced. Hence, there is a steep increase in impulse for $X_1^* > 0.60$.

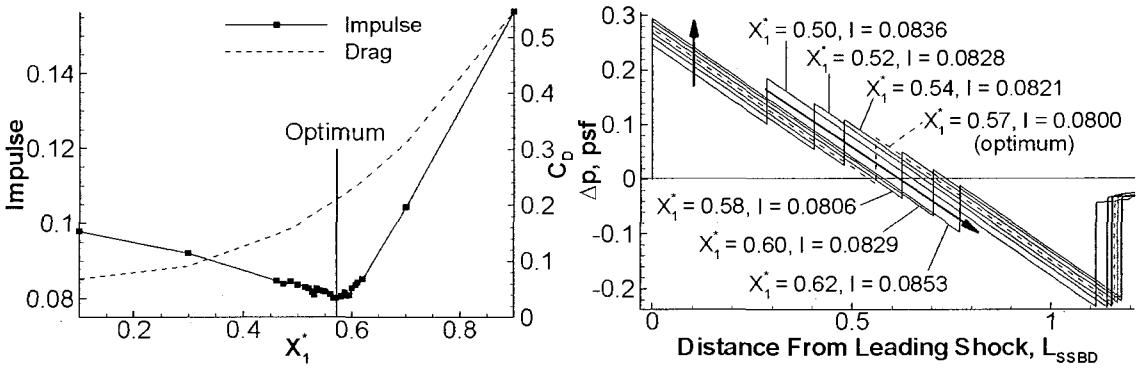

Figure 37: Ground impulse and drag (left), and ground signal shape (right) variation with X_1^*. Mach 1.41.

Next, the investigation is extended to the 3-ramp configuration. There are 3 design factors in this case, X_1, X_2, and θ_2.. The behavior of the response with respect to the ramp lengths is expected to be similar to the findings of the 2-ramp analysis. Again the first step of the grid search is performed using 5 factor levels at -1, -0.5, 0, 0.5, and 1 for all three factors, making 5^3 =

125 runs. A summarized version of the grid search design matrix is given in Table 3. The bold typeset refers to column vectors spanning through the runs indicated in the first column. The values in the brackets at each column indicate the rows being repeated for that factor. For example, to find the settings of run 62, the first column reads $F_1 = 0$, the second column points to the second row with $F_2 = -1$, and the third column points to $F_3 = -0.5$. Figure 38 shows the results of all 125 runs as a scatter plot with impulse and drag responses. The optimal points are located in the lower left corner of the plot. All the runs above run 75 are far from the optimal region. These runs have $F_1 = 0.5$ and $F_1 = 1$ settings in common. This observation suggests that $F_1 = 0.5$ and $F_1 = 1$ settings can be omitted in the grid search step for higher numbers of ramp cases, to save computational time. The Pareto-front shows the set of optimal points with low drag and low impulse. The points are labeled using run numbers. For the best compromise between impulse and drag, run 18 is a good choice. However, sonic boom reduction is the primary concern in the current study, therefore run 62 is selected as the starting point of the following optimization study of the 3-ramp configuration. Table 4 shows the best 12 runs from the grid search step having lowest impulses. This table can be used to determine which factor levels should have priority in the grid search step of a 4-ramp optimization. F_2 setting which is associated with the 2nd ramp length spans the -1 through 1, somewhat evenly, meaning that it should be tested at all levels. F_3 setting which is associated with the 2nd ramp angle goes above 0 only twice, at runs 9 and 29. The drag in these runs is high compared to the remainder of the list. Therefore it is concluded that 2nd ramp angle does not need to be tested beyond the center level at the grid search for 4-ramp optimization.

Table 3: Summarized design matrix for 3-ramp grid search step

Run	F_1	F_2	F_3	Run	F_1	F_2	F_3	Run	F_1	F_2	F_3
1	-1	-1	-1	6 - 10	**-1**	**-0.5**	**[1-5]**	26-50	**-0.5**	**[1-25]**	**[1-25]**
2	-1	-1	-0.5	11-15	**-1**	**0**	**[1-5]**	51-75	**0**	**[1-25]**	**[1-25]**
3	-1	-1	0	16-20	**-1**	**0.5**	**[1-5]**	76-100	**0.5**	**[1-25]**	**[1-25]**
4	-1	-1	0.5	21-25	**-1**	**1**	**[1-5]**	100-125	**1**	**[1-25]**	**[1-25]**
5	-1	-1	1								

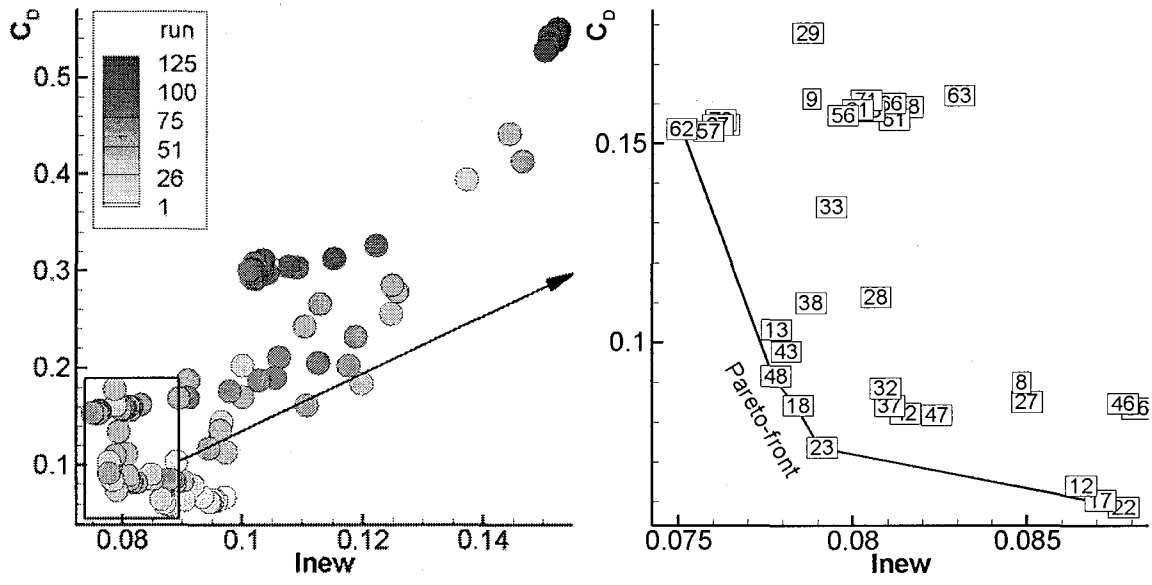

Figure 38: Scatter plot showing impulse and drag variation for the grid search step of 3-ramp configuration.

Table 4: Best 12 runs with lowest impulse in the 3-ramp grid search step.

Run	62	57	67	72	52	48	13	43	18	29	38	9
F_1	0.0	0.0	0.0	0.0	0.0	-0.5	-1.0	-0.5	-1.0	-0.5	-0.5	-1.0
F_2	0.0	-0.5	0.5	1.0	-1.0	1.0	0.0	0.5	0.5	-1.0	0.0	-0.5
F_3	-0.5	-0.5	-0.5	-0.5	-0.5	0.0	0.0	0.0	0.0	0.5	0.0	0.5
I_{ground}	.0751	.0758	.0761	.0762	.0763	.0778	.0778	.0781	.0785	.0787	.0788	.0788
C_D	.1537	.1531	.1547	.1560	.1549	.0915	.1032	.0977	.0841	.1780	.1100	.1613

The experimental design for the non-linear response analysis is selected as a full quadratic orthogonal CCD with axials at ±1.2154 factor settings. For the 3-ramp case having 3 design factors the full CCD has 8 factorials, 6 axials, and the center point, totaling 15 runs per iteration. The center points are already available from preceding iterations. Table 5 displays the results for 5 optimization iterations. There is no change in the location of the optimum for the last 3 iterations, and the process is terminated at iteration 5. The optimum for the 3-ramp configuration shows a 27.2% decrease in the ground impulse level, and 132.7% increase in drag. The 3-ramp configuration provides considerable improvement over the 2-ramp configuration regarding both responses.

To answer the question whether a steepest descent search would be more efficient as it requires almost half the number of runs per iteration, data in Table 6 is provided. This data shows the optimization iteration results using 8 point full factorial designs and steepest descent method

based on linear models. The steepest descent direction is calculated in the usual way as described in Ref. [102], with the step size set as 1 for the most rapidly varying factor. Steps 5 and 6 given in the previous section are combined here by running a few cases in the steepest descent direction. Looking at Table 6, one can see that the linear modeling approach does not really improve on the initial solution obtained from the grid search step. Ten iterations require a total of 80 runs with the linear method, whereas 5 iterations require a total of 70 runs with the non-linear method. Obviously non-linear modeling is the method of choice.

Table 5: 3-ramp optimization iteration results, using CCDs.

Iter.	0	1	2	3	4	5	6	7
X_1c	.5000	.5000	.5486	.5086	.5086	.5286	.5286	.5286
X_2c	.5000	.5000	.5000	.5400	.5400	.5200	.5443	.5443
θ_2c	.5000	.3000	.3000	.3400	.3400	.3600	.3600	.3600
B	.4000	.0400	.0400	.0400	.0200	.0200	.0200	.0100
$X^*_{1,\,opt}$	.5000	.5486	.5086	.5086	.5286	.5286	.5286	.5286
$X^*_{2,\,opt}$	.5000	.5000	.5400	.5400	.5200	.5443	.5443	.5443
$\theta^*_{2,\,opt}$	.3000	.3000	.3400	.3400	.3600	.3600	.3600	.3600
I_{ground}	.0751	.0749	.0746	.0746	.0734	.0728	.0728	.0728
C_D	.1537	.1838	.1612	.1612	.1718	.1719	.1719	.1719
-%ΔI	24.9	25.1	25.4	25.4	26.6	27.2	27.2	27.2

The 4-ramp configuration has 5 design factors, X_1, X_2, X_3, θ_2, and θ_3. To reduce the number of runs in the grid search step, specific levels of certain factors are eliminated in the initial design matrix. Based on the insight gained in the 3-ramp configuration grid search, the factors are tested at the following levels:

$$F_1 = -1, 0; \quad F_2 = -1, 0, 1; \quad F_3 = -1, 0, 1; \quad F_4 = -1, -0.5, 0; \quad F_5 = -1, -0.5, 0, 0.5, 1$$

This setup makes 2·3·3·3·5 = 270 runs, which is tabulated in Table 7 in summarized format. The results of the 270 runs are shown as scatter plot of impulse and drag in Figure 39, and the best 12 runs with lowest impulse are given in Table 8. Run 186 gives the lowest impulse, whereas run 132 gives the best compromise between low impulse and low drag. Again since the current research is primarily intended to reduce the sonic boom, run 186 is selected as the optimum of the grid search step. Again for the iteration steps, the non-linear experimental design used is a quadratic orthogonal CCD with axials at ±1.5467. A half-fractional factorial section is

used this time to save on computational time. This design is still adequate to obtain a full quadratic model. The number of design points per iteration is distributed as 16 factorials, 10 axials, and 1 center, totaling 27 points. The results of the optimization iterations are shown in Table 9. This time no significant improvement is achieved on the best run of the grid search step. Run 186 is obviously fortuitous where even the short range design matrix with **B** = 0.0025 does not provide a lower impulse than the center point. With the 4-ramp optimization, the impulse decrease is now 28.9% and drag increase is 108.1%. These values still show improvement over the 3-ramp design, however, the decrease in impulse seems to be converging.

Table 6: 3-ramp optimization iterations using full factorial linear modeling and steepest descent method.

Iter.	0	1	2	3	4	5	6	7	8	9	10
$X_1 c$	.5000	.5000	.5000	.5400	.5400	.5400	.5450	.5400	.5446	.5446	.5446
$X_2 c$	.5000	.1000	.1000	.0988	.0988	.0988	.1038	.1088	.1121	.1121	.1121
$\theta_2 c$	.5000	.3000	.3000	.3120	.3120	.3120	.3070	.3020	.2970	.2970	.2970
B	.4000	.0400	.0200	.0200	.0100	.0050	.0050	.0050	.0050	.0025	.0013
$X^*_{1,\,opt}$	.5000	.5000	.5400	.5400	.5400	.5450	.5400	.5446	.5446	.5446	.5446
$X^*_{2,\,opt}$	.1000	.1000	.0988	.0988	.0988	.1038	.1088	.1121	.1121	.1121	.1121
$\theta^*_{2,\,opt}$	.3000	.3000	.3120	.3120	.3120	.3070	.3020	.2970	.2970	.2970	.2970
I_{ground}	.0763	.0763	.0761	.0761	.0761	.0756	.0754	.0753	.0753	.0753	.0753
C_D	.1549	.1549	.1774	.1774	.1774	.1802	.1769	.1796	.1796	.1796	.1796
-%ΔI	23.7	23.7	23.9	23.9	23.9	24.4	24.6	24.7	24.7	24.7	24.7

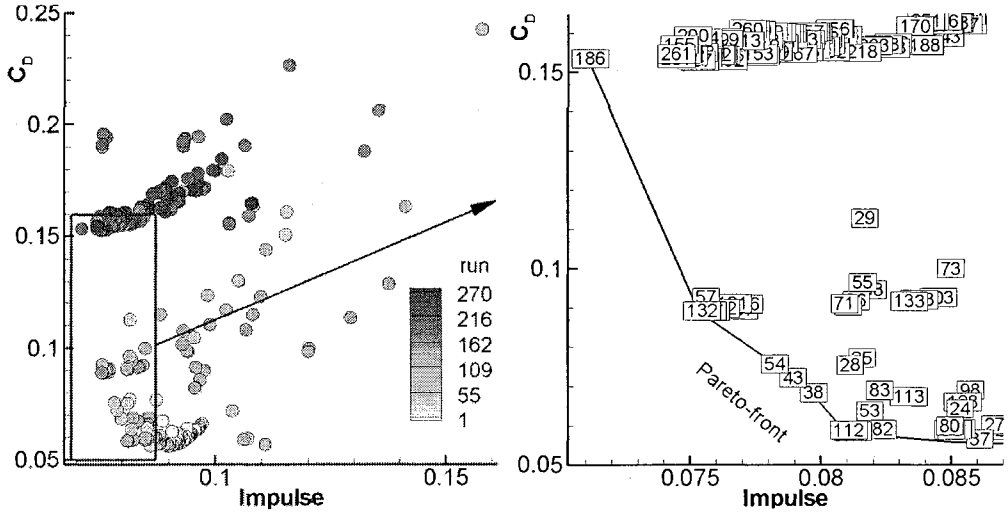

Figure 39: Scatter plot showing impulse and drag variation for the grid search step of 4-ramp configuration.

Table 7: Summarized design matrix for 4-ramp configuration grid search study.

Run	F_1	F_2	F_3	F_4	F_5	Run	F_1	F_2	F_3	F_4	F_5
1	-1	-1	-1	-1	-1	11-15	**-1**	**-1**	**-1**	**0**	**[1-5]**
2	-1	-1	-1	-1	-0.5	16-30	**-1**	**-1**	**0**	**[1-15]**	**[1-15]**
3	-1	-1	-1	-1	0	36-45	**-1**	**-1**	**1**	**[1-15]**	**[1-15]**
4	-1	-1	-1	-1	0.5	46-90	**-1**	**0**	**[1-45]**	**[1-45]**	**[1-45]**
5	-1	-1	-1	-1	1	91-135	**-1**	**1**	**[1-45]**	**[1-45]**	**[1-45]**
6 - 10	**-1**	**-1**	**-1**	**-0.5**	**[1-5]**	136-270	**0**	**[1-135]**	**[1-135]**	**[1-135]**	**[1-135]**

Table 8: Best 12 runs with lowest impulse in the 4-ramp grid search step.

Run	186	261	201	155	246	231	172	200	187	168	217	216
F_1	0	**0**	0	0	0	0	0	0	0	0	0	0
F_2	0	1	0	-1	1	1	-1	0	0	-1	0	0
F_3	-1	1	0	0	0	-1	1	0	-1	1	1	1
F_4	-0.5	-0.5	-0.5	-1	-0.5	-0.5	-0.5	-1	-0.5	-1	-0.5	-0.5
F_5	-1	-1	-1	1	-1	-1	-0.5	1	-0.5	0	-0.5	-1
I_{ground}	.0711	.0745	.0745	.0746	.0747	.0747	.0749	.0751	.0752	.0753	.0753	.0755
C_D	.1535	.1547	.1535	.1570	.1547	.1546	.1542	.1592	.1530	.1550	.1528	.1537

Table 9: 4-ramp optimization iteration results, using CCDs.

Iter.	0	1	2	3	4	5	6
X_1c	0.5	0.5	0.5	0.5	0.5	0.5	0.5
X_2c	0.5	0.5	0.5	0.5	0.5	0.5	.4975
X_3c	0.5	0.1	0.1	0.1	0.1	0.1	.1025
θ_2c	0.5	0.3	0.3	0.3	0.3	0.3	.2975
θ_3c	0.5	0.1	0.1	0.1	0.1	0.1	.0975
B	0.4	0.04	0.02	0.01	0.005	.0025	.0025
$X^*_{1,opt}$	0.5	0.5	0.5	0.5	0.5	.5008	.5008
$X^*_{2,opt}$	0.5	0.5	0.5	0.5	0.5	.4975	.4975
$X^*_{3,opt}$	0.1	0.1	0.1	0.1	0.1	.1025	.1025
$\theta^*_{2,opt}$	0.3	0.3	0.3	0.3	0.3	.2975	.2975
$\theta^*_{3,opt}$	0.1	0.1	0.1	0.1	0.1	.0975	.0975
I_{ground}	.0711	.0711	.0711	.0711	.0711	.0711	.0711
C_D	.1535	.1535	.1535	.1535	.1535	.1539	.1539
$-\%\Delta I$	28.9	28.9	28.9	28.9	28.9	28.9	28.9

The final set of results in this section is given for the 5-ramp configuration optimization. The design factors are now X_1, X_2, X_3, X_4, θ_2, θ_3, and θ_4. To reduce the number of runs in the grid search step, specific levels of certain factors are eliminated in the initial design matrix. Based on

the insight gained in 3-ramp and 4-ramp configuration grid search steps, the factors are tested at the following levels:

$$F_1 = -1, 0; \quad F_2 = -1, 0; \quad F_3 = -1, 0; \quad F_4 = -1, 0;$$
$$F_5 = -1, -0.5, 0; \quad F_6 = -1, -0.5, 0; \quad F_7 = -1, -0.5, 0$$

This setup makes a total of 432 runs, which is tabulated in Table 10 in summarized format. The results of the 432 runs are shown as a scatter plot of impulse and drag in Figure 40, and the best 12 runs with lowest impulse are given in Table 11. Run 364 gives the lowest impulse. For the optimization iteration steps, the non-linear experimental design is again a CCD, but this time with the axials set at ±1. The reason behind this is that a quadratic orthogonal setup requires axials to be around 1.8, which is almost twice the intended sub-design space size. For practical reasons the axials are now set at factorial levels, making this a Face Centered Design (FCD). A half-fractional factorial section is used this time to save on computational time. This design is still adequate to obtain a full quadratic model. The number of design points per iteration is distributed as 64 factorials, 14 axials, and 1 center, totaling 79 points. The results of the optimization iterations are shown in Table 12. The optimum is reached in 2 iterations. With the 5-ramp optimization, the impulse decrease is 27.6% and drag increase is 57.1%. The impulse decrease is no better than that obtained with the 4-ramp configuration, but it is very close. The improvement in drag however is significant. This concludes that the 5-ramp optimum is just as good as the 4-ramp optimum in terms of sonic boom reduction, and much better in terms of drag. The physical levels of the design factors of the optimum configuration with 5 ramps are found to be

$$X_1 = 0.01840 L_{SSBD} \quad \theta_1 = 28.000^o$$
$$X_2 = 0.03082 L_{SSBD} \quad \theta_2 = 12.095^o$$
$$X_3 = 0.03432 L_{SSBD} \quad \theta_3 = 5.5638^o$$
$$X_4 = 0.04627 L_{SSBD} \quad \theta_4 = 3.0067^o$$
$$X_5 = 0.07019 L_{SSBD} \quad \theta_5 = 2.3158^o$$

Table 10: Summarized design matrix for 5-ramp configuration grid search study

Run	F_1	F_2	F_3	F_4	F_5	F_6	F_7
1	-1	-1	-1	-1	-1	-1	-1
2	-1	-1	-1	-1	-1	-1	-0.5
3	-1	-1	-1	-1	-1	-1	0
4 - 6	**-1**	**-1**	**-1**	**-1**	**-1**	**-0.5**	**[1-3]**
7 - 9	**-1**	**-1**	**-1**	**-1**	**-1**	**0**	**[1-3]**
10 - 18	**-1**	**-1**	**-1**	**-1**	**-0.5**	**[1-9]**	**[1-9]**
19 - 27	**-1**	**-1**	**-1**	**-1**	**0**	**[1-9]**	**[1-9]**
28 - 54	**-1**	**-1**	**-1**	**0**	**[1-27]**	**[1-27]**	**[1-27]**
55 - 108	**-1**	**-1**	**0**	**[1-54]**	**[1-54]**	**[1-54]**	**[1-54]**
109 - 216	**-1**	**0**	**[1-108]**	**[1-108]**	**[1-108]**	**[1-108]**	**[1-108]**
217 - 432	**0**	**[1-216]**	**[1-216]**	**[1-216]**	**[1-216]**	**[1-216]**	**[1-216]**

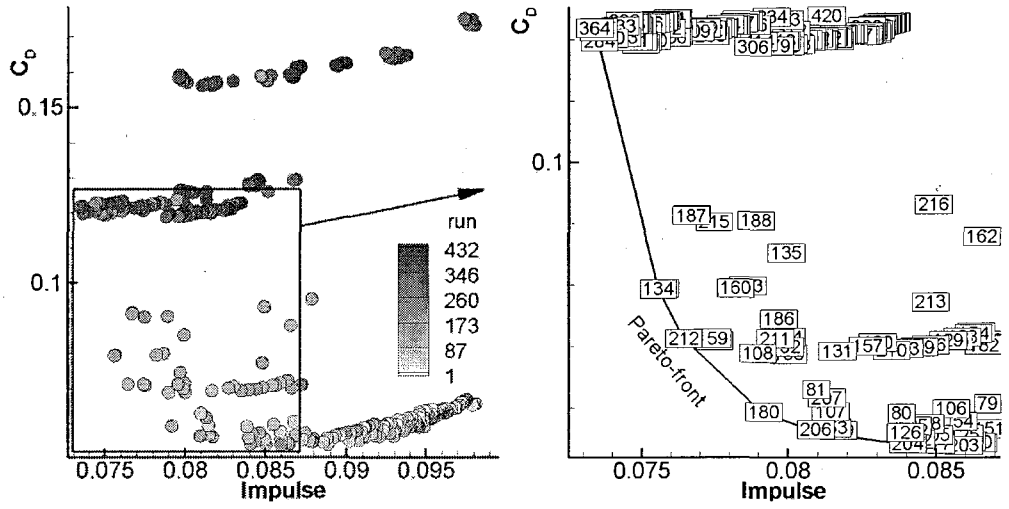

Figure 40: Scatter plot showing impulse and drag variation for the grid search step of 5-ramp optimization.

Table 11: Best 12 runs with lowest impulse in the 5-ramp grid search step.

Run	364	338	337	284	310	233	283	232	259	363	336	417
F_1	0	0	0	0	0	0	0	0	0	0	0	0
F_2	0	0	0	-1	-1	-1	-1	-1	-1	0	0	0
F_3	-1	-1	-1	0	0	-1	0	-1	-1	-1	-1	0
F_4	0	-1	-1	-1	0	-1	-1	-1	0	0	-1	0
F_5	-0.5	-0.5	-0.5	-0.5	-0.5	-0.5	-0.5	-0.5	-0.5	-0.5	-0.5	-0.5
F_6	-0.5	-0.5	-0.5	-0.5	-0.5	0	-0.5	0	0	-1	-1	-1
F_7	-1	-0.5	-1	-0.5	-1	-0.5	-1	-1	-1	0	0	0
I_{ground}	.0734	.0735	.0735	.0735	.0739	.0743	.0743	.0744	.0744	.0746	.0746	.0747
C_D	.1218	.1213	.1220	.1197	.1202	.1222	.1204	.1230	.1225	.1226	.1227	.1224

Table 12: 5-ramp optimization iteration results, using CCDs

Iter.	0	1	2	3	4	5	6	7	8
X_1c	0.5	0.5	0.5	0.46	0.46	0.46	0.46	0.46	0.46
X_2c	0.5	0.5	0.5	0.46	0.46	0.46	0.46	0.46	0.46
X_3c	0.5	0.1	0.14	0.18	0.18	0.18	0.18	0.18	0.18
X_4c	0.5	0.5	0.5	0.46	0.5	0.5	0.5	0.5	0.5
θ_2c	0.5	0.3	0.3	0.34	0.34	0.34	0.34	0.34	0.34
θ_3c	0.5	0.3	0.3	0.26	0.26	0.26	0.26	0.26	0.26
θ_4c	0.5	0.1	0.1	0.14	0.14	0.14	0.14	0.14	0.14
B	0.4	0.04	0.04	0.04	0.04	0.02	0.01	0.005	0.0025
$X^*_{1,\,opt}$	0.5	0.5	0.46	0.46	0.46	0.46	0.46	0.46	0.46
$X^*_{2,\,opt}$	0.5	0.5	0.46	0.46	0.46	0.46	0.46	0.46	0.46
$X^*_{3,\,opt}$	0.1	0.14	0.18	0.18	0.18	0.18	0.18	0.18	0.18
$X^*_{4,\,opt}$	0.5	0.5	0.46	0.5	0.5	0.5	0.5	0.5	0.5
$\theta^*_{2,\,opt}$	0.3	0.3	0.34	0.34	0.34	0.34	0.34	0.34	0.34
$\theta^*_{3,\,opt}$	0.3	0.3	0.26	0.26	0.26	0.26	0.26	0.26	0.26
$\theta^*_{4,\,opt}$	0.1	0.1	0.14	0.14	0.14	0.14	0.14	0.14	0.14
I_{ground}	.0734	.0727	.0724	.0724	.0724	.0724	.0724	.0724	.0724
C_D	.1218	.1218	.1160	.1160	.1160	.1160	.1160	.1160	.1160
$-\%\Delta I$	26.6	27.3	27.6	27.6	27.6	27.6	27.6	27.6	27.6

Table 13: Summary data for axisymmetric nose geometry optimization for sonic boom mitigation.

N_{RAMP}	Opt. Iters.	Total Runs	I_{ground}	C_D	$-\%\Delta I$	$\%\Delta C_D$
2	7	40	.0800	.2080	20.7	181.6
3	5	200	.0728	.1719	27.2	132.7
4	0	270	.0711	.1535	28.9	107.8
5	2	590	.0724	.1160	27.6	57.1

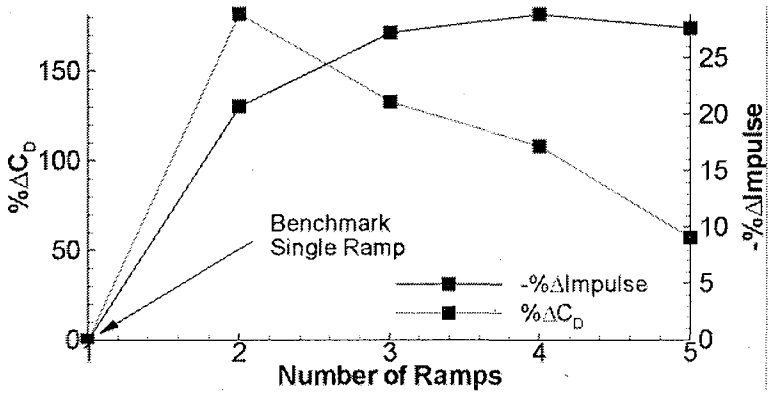

Figure 41: Variation of the drag increase and impulse decrease with the number of ramps.

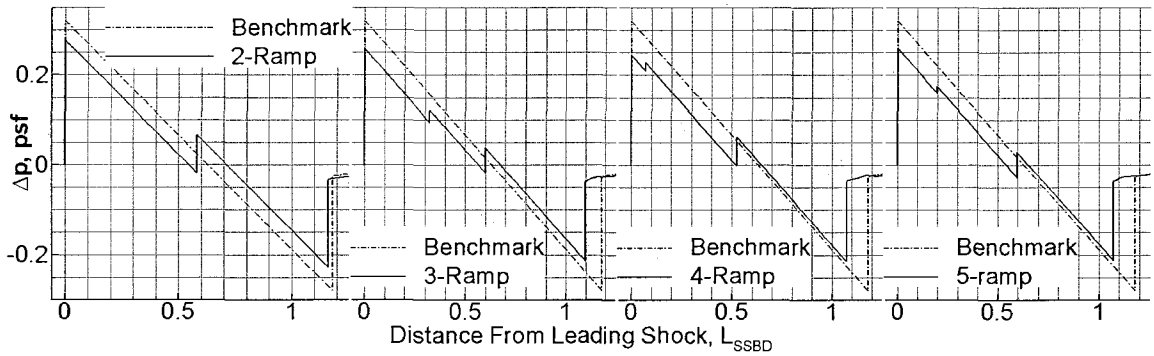

Figure 42: Pressure signatures of impulse minimized axisymmetric geometries at ground (r = 600 $\angle_{SSBD}$)

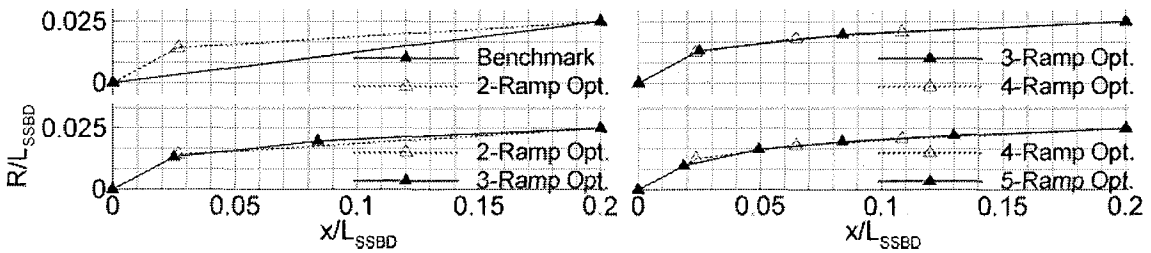

Figure 43: The meridian profiles of impulse-minimum configurations in Mach 1.414 axisymmetric flow.

A summary of the axisymmetric nose geometry sonic boom impulse optimization is tabulated in Table 13. The table shows the number of optimization iterations required to reach the reported optimum for each number of ramp settings, along with the total number of runs required by so many iterations. The last two columns in Table 13 are plotted in Figure 41. The decrease in the ground level pressure impulse asymptotes at about 28%, whereas the drag increase has a falling trend as the number of ramps is increased. The current optimization study is terminated at 5 ramps due to the process getting exponentially expensive as 2 more factors are introduced with every new ramp. The ground pressure signals of all four optimized configurations (2, 3, 4, and 5-ramp) are compared to the benchmark signal of the single ramp configuration in Figure 42. The decrease in the impulse can be observed as the area between the dashed (benchmark) and solid (optimized) lines at the $\Delta p>0$ regions. Figure 43 compares the impulse optimized meridian profiles. The profiles display convergence to a unique smooth shape that is obvious in the 5-ramp configuration. Increasing the number of ramps in the analysis will increase the smoothness of the meridian profile. In this case a new parametric setup with a smooth mathematical expression defining the profile can be a better alternative to increasing the number of ramps, as such an expression is likely to have fewer parameters to optimize.

A well-known set of solutions for optimized nose geometries with length and base radius constraints are given by Hague and Jones [15]. In that paper, the 1/4th power body shape given by

$$R(x) = R_{Base}\left(\frac{x}{L_{Nose}}\right)^{1/4} \tag{84}$$

is found to be the optimum shape for ground level minimum peak pressure, where the optimization parameter is the power of the term in parentheses. This geometry has a blunt tip which is known to reduce leading shock strength but increase drag considerably. Using the size constraints of the current analysis this shape produces $C_D = 0.1241$, and a peak Δp equal to 0.251 psf at $r = 600\ L_{SSBD}$. This is a 68% increase in drag compared to the benchmark geometry, and a 21.56% decrease in peak Δp. To compare to this solution, the 5-ramp optimization is repeated to minimize the ground level peak Δp this time. The physical levels of the design factors for minimum peak Δp is found to be

$$\begin{aligned} X_1 &= 0.00400 L_{SSBD} & \theta_1 &= 28.00000^o \\ X_2 &= 0.00850 L_{SSBD} & \theta_2 &= 17.32814^o \\ X_3 &= 0.01390 L_{SSBD} & \theta_3 &= 16.21086^o \\ X_4 &= 0.02119 L_{SSBD} & \theta_4 &= 15.12225^o \\ X_5 &= 0.15241 L_{SSBD} & \theta_5 &= 3.92370^o \end{aligned}$$

giving $C_D = 0.0865$, and a peak Δp equal to 0.236 psf at $r = 600\ L_{SSBD}$. This translates to only a 17.2% increase in drag and 26.25% decrease in peak Δp. The critical setting of the first ramp angle is mostly responsible for this improvement over the referenced 1/4th power-body solution. This 5-ramp optimum configuration for minimum peak Δp produces ground impulse equal to 0.0828 psf msec, which is even higher than the 2-ramp optimum solution for minimum ground impulse. This is a clear example of a situation where an aircraft can have the lowest peak pressure levels but high impulse. Thus focusing the optimization efforts to mitigate the pressure levels alone is not a safe route. It is imperative to consider the impulse as well. In Figure 44, the signals with minimum ground impulse and Δp are compared. A ground reflection factor of 1.9 is used to make the signals comparable to those presented in Section 6.4 where the nose shapes are attached to the SSBD. The minimum Δp occurs when the intermediate shock and the leading shock are at the same level.

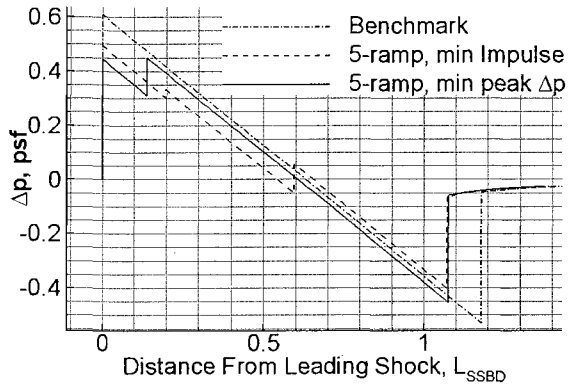

Figure 44: Pressure signals at ground level (r = 600 $\mathcal{L}_{SSBD}$) from the benchmark, 5-ramp minimum impulse, and 5-ramp minimum peak Δp configurations, with 1.9 reflection factor applied.

6.2 Delta Wing Optimization

In this section the delta wing geometry introduced in Section 5.4 is optimized for sonic boom mitigation. This reference geometry has a symmetric biconvex profile with a 5% thickness-to-chord ratio ($\mathcal{L}_c$), semi-vertex angle (90° - leading edge sweep) $\beta = 30°$, and the trailing edge set constant at x = L, where L is the wing root chord length. The half-span is then equal to tan(30°) L = 0.5774 L. The dihedral is zero for the benchmark configuration. The biconvex airfoil profile is generated by taking a cut on a circle with a chord such that the thickness of the smaller piece is 2.5% of the cutting chord length. This smaller piece is mirror-copied across the chord to form the symmetric biconvex profile with sharp leading and trailing edges. The 3D wing is generated by translating and resizing the root profile in the span-wise (y) direction linearly, making the chord length become zero at the tip at y = 0.5774L. Finally all span-wise sections are translated in the axial direction to have their trailing edges positioned at x = L. The flight conditions are Mach 2.0 and $\alpha = 2.24°$, producing $C_L = 0.0765$ and $C_D = 0.0102$ (without surface friction). The semi-vertex angle is set to match the Mach cone angle, which gives the largest span while barely avoiding the adverse wave drag effects of supersonic flow. These particular flow conditions and geometry settings have been used in numerous prior publications at ODU [30, 48, 49, 53, 57, 58, 60, 82, 93, 104], and are used here as the reference benchmark case.

Similar to the previous section with the axisymmetric nose shape optimization, the response being minimized in this section is the pressure impulse. The impulse is computed in the mid-field region this time on a vertical cut on the y = 0 symmetry plane, at x/L = 3.5 downstream of the nose. Doing so saves significant computational time on each run since far-field

propagation is not needed and the signal at x/L = 3.5 can be accurately obtained using the FUN3D/Optigrid adaptive unstructured Euler CFD method. The optimization for ground level boom minimization can safely be relied on the impulse response in the mid-field. This is because the percentage decreases in the impulse at both altitudes are the same order. This statement is supported first by the linear theory which relates the pressure attenuation only to the radial distance from the aircraft in Eq. 2.9 for r >> L, and second by the pilot comparative non-linear sonic boom prediction study carried out below using the optimum delta wing geometry reported in Ref. [93].

The primary constraint in the optimization is the volume of the delta wing. Basically the goal of the optimization is to have the same amount of material fly at the same velocity with weaker ground level sonic boom intensity. Conservation of the volume and hence the weight of the wing calls for conservation of lift as well. However, lift is not a design variable but is one of the responses. Therefore the study in this section is a multi-response optimization where the pressure impulse is being minimized while the lift is targeted at $C_L = 0.0765$. Allowing the volume to vary is pointless since the optimum solution in this case would be a zero-thickness wing flying at zero angle of attack with no lift and no sonic boom signal. Obviously the smaller the volume gets, the smaller the weight, thickness, disturbance, lift, and sonic boom intensity get. When the wing is optimized alone as a separate aerodynamic component, its volume should be conserved. If a wing-body configuration were being optimized on the other hand, reductions in wing volume could have been added to the fuselage or even ignored depending on the goal of the optimization. However, this is not the case in the current section where the wing is the only component being optimized.

The design variables for the optimization are selected as

- camber, κ_c,
- dihedral, θ_D
- tip twist, α_T
- angle of attack (or root twist), α,
- span-wise non-linear twist profile, $\alpha(y)$
- span-wise non-linear camber profile, $\kappa_c(y)$

The thickness ratio is not included in the variables list since it modifies the volume of the wing. All the other variables have negligible effects on the volume. Since volume of the wing is conserved in the current study, thickness ratio is set constant at 5% as in the benchmark configuration. Span-wise constant camber and dihedral angle have already been investigated in prior work (Ref. [93]), where the sonic boom response is computed using the linear waveform geometric acoustics method. These variables are reconsidered here for the non-linear analysis with unstructured grid adaptation and shock fitting. In addition to these two variables, the wing angle of attack and twist are included in the current design variables list. Since lift is now one of the constraints, the effects of camber and dihedral on lift need to be compensated by changing the angle of attack so that the original lift can be maintained. The wing twist is a new addition to the parameters investigated earlier in Ref. [93]. This parameter allows modification of the span-wise lift distribution which is very interesting in terms of sonic boom generation. The idea was inspired by the well known paper by Al George titled "*The Possibilities for Reducing Sonic Boom by Lateral Redistribution*" [9]. In this work George considers reorienting the sources and sinks in the cross-flow plane in such a way that off-centerline poles negate the sonic boom generating effects of the centerline sources below the aircraft. The simplest way to create such a span-wise lift variation is to play with the twist profile of the delta wing, which changes the local angle of attack at each span-wise location. In the current study the wing twist is investigated as three parameters, the root twist, the tip twist, and the span-wise twist profile. A non-linear twist profile determined by a single parameter is used. The twist is included among many other airframe design variables in Refs. [26, 31, 85] from Stanford and Georgia Tech., however, the twist profile is not tested. A linear twist profile is the general practice in aircraft design, which makes the optimization of the non-linear twist profile in the current study a new contribution. As will be shown shortly, the optimum camber producing the minimum pressure impulse is different for each angle of attack. Therefore the span-wise variance in the local angle of attack due to twist requires optimization of the span-wise camber profile as well. To the knowledge of the author, a study on the combined optimization of non-linear span-wise twist and camber profiles for sonic boom mitigation does not exist in the current literature.

The parametric delta wing optimization is done in sequential steps where the number of design factors involved is increased at each step. Initially two factor optimizations are carried out where factors are paired with each other in several combinations. Three and more factor optimizations are carried out in the following steps. This is a similar approach to the one carried out with the axisymmetric nose shape optimization in the previous section, where the number of factors increase as the number of ramps forming the meridian profile increases. The design

shows improvement as more factors are involved in the optimization. The sequential analysis starting with two factors is important to clearly understand and appreciate the effect of each factor on the response. In this way an educated multivariate optimization study can be carried out rather than throwing in all the variables and letting the algorithm produce a "magic set" of optimum parameters.

6.2.1 Sonic Boom Prediction for Low Boom Delta Wing

Before starting the optimization process for the delta wing, the response to be optimized and the parameters for the sonic boom prediction process should be established. As a pilot study, one of the optimal delta wing geometries reported in Ref. [93] is solved with the current non-linear sonic boom prediction technology. The design with the minimum leading shock strength from this reference work is chosen for analysis here. The airfoil profile is given in Figure 45. The flight conditions are Mach 2.0 and $\alpha = 2.24°$. The geometric parameters for this design are

- 2° nose angle,
- 3% thickness-to-chord ratio
- 1.5% camber at mid-chord
- 20° dihedral

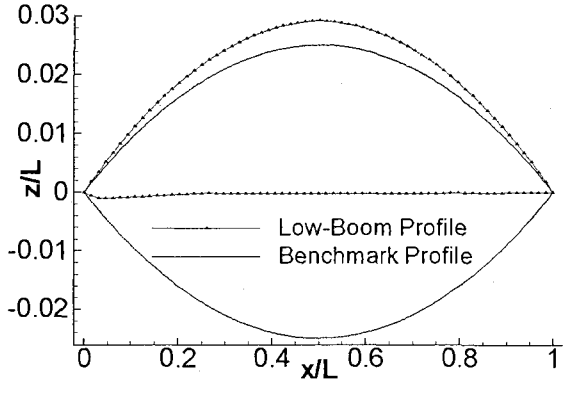

Figure 45: The optimum low-boom airfoil profile for minimum leading shock strength determined in Ref. [93], compared to the benchmark profile.

The near-field flow structure for low boom airframes is dominated primarily by isentropic compression regions and/or weak shocks. These flow features of low-boom aircraft develop into regular shock systems much farther downstream compared to standard high-boom aircraft. FPM3D requires that the leading and trailing shocks have developed prior to the Euler/FPE interface location so that shock detection, fitting, and grid generation can take place. The first test in this section is to determine a suitable axial distance downstream from the aircraft for the Euler/FPE interface. Using the Fun3D/Optigrid near-field unstructured shock fitted non-linear CFD based sonic boom prediction method, the flow is computed in the entire 3D domain down to x/L = 5. Figure 46 shows the adapted grid on the y = 0 symmetry plane, and the pressure signals at equidistant vertical data cuts downstream and below the aircraft. The solution/adaptation process has converged by cycle 10. The obvious observation from the grid is that the trailing shock does not form until about x/L = 2.5. Thus any optimization study based on pressure signals closer than 2.5 body lengths will produce unreliable results since almost half of the signal will be missing. The evolution of the pressure signal with the axial distance from the aircraft shows the development of the trailing shock in stages. By x/L = 3.5, both the leading and trailing shocks are acceptable shapes that are detectable by the shock fitting routines in FPM3D. With the formation of the two distinct shocks in the signal, x/L = 3.5 can be considered the start of the mid-field.

Although x/L = 3.5 is a suitable station for the Euler/FPE interface in terms of shock integrity, it is not far enough away to provide a safe distance between the inner boundary of the interface grid and the high vorticity region. The inner boundary needs to be far enough from the trailing shock that the pressure disturbance is flat, or else the $\Delta p = 0$ boundary condition enforced at this edge becomes problematic during full-potential marching. At x/L = 3.5, inner boundary placed at a radius where $\Delta p \approx 0$ passes through the high vorticity region with vorticity magnitude over 0.1. At x/L = 4.5 however, the inner boundary with $\Delta p \approx 0$ is at a safe distance from the high vorticity region. The vorticity magnitude distribution and the interface grid boundaries at two axial stations are shown in Figure 47. Figure 46 can be referenced for the leading and trailing shock locations at both stations. If vorticity > 0.1 (which is almost the same order as the free stream velocity) is included in the full potential propagation, the computational scheme first produces strong overshoots at the trailing shock and eventually diverges. To avoid such complications, the Euler/FPE interface is placed at x/L = 4.5, with inner boundary at r/L = 1.25 and outer boundary at r/L = 3.0. The grid contains 129 by 467 points in the circumferential and radial directions, respectively. The step size is set as 0.001.

Signal propagation is computed in an isothermal atmosphere since the reference results have been computed as such and there is no experimental in-flight data to compare with for the delta wing case. The FPM3D/Waveform Parameter changeover distance is found to be exactly 30 body lengths, with the ground signal impulse convergence threshold E_I (Eq. (5.6)) set at 0.001. This is 10 body lengths farther than that needed with the benchmark configuration to meet the E_I = 0.001 threshold. This clearly shows that non-linearities persist further downstream for lower boom signals. Obviously non-linear prediction is essential to compute accurate pressure responses that can be used in sonic boom minimization studies. Figure 48 shows a comparison of the signals from the benchmark and the Ref. [93] optimum delta wing geometries at x/L = 3.5 and at r/L = 600. The ground pressure levels are scaled with $(r/L)^{3/4}$ for convenient plotting. Although the low boom signal looks much weaker at x/L = 3.5, compared to the original signal, the peak Δp's are much closer at ground level. This is because the far field leading shock strength is directly proportional to the near-field pressure impulse, but not the near-field peak Δp. This is a very important statement and is the reason behind choosing the impulse as the response to be minimized rather than the peak Δp. Looking at the signals at x/L = 3.5, one can see that although there is a large gap between the peak Δp's, the pressure impulse (the area under the curve where $\Delta p > 0$) does not differ so much. A quantitative comparison of mid- and far-field sonic boom mitigation of the low boom geometry is provided in Table 14. The results show that the mid-field impulse decrease at x/L = 3.5 is perfectly correlated with the far-field peak Δp decrease. The peak Δp decrease in the mid-field is more than twice that of the far-field. Finally, the far-field impulse decrease is even greater than the mid-field impulse decrease. Obviously if a near- or mid-field response is to be used for sonic boom minimization to save computational time, it should be the pressure impulse. Relying on the mid-field peak Δp can be disastrous since the level of decrease observed in this response does not fully reflect the far-field behavior. However, by choosing the pressure impulse at x/L = 3.5 as the response for minimization, one guarantees at least the same level of reduction on both the impulse and peak Δp at r/L = 600. Some final statements can be made on the volume and lift of the wing analyzed in this section. The Ref. [93] optimum delta wing geometry has C_L = 0.0767, which is almost exactly the same as the benchmark geometry. However, there is a 40% volume loss due to the change in thickness from 5% to 3%. The goal of this chapter is to achieve at least the same level of sonic boom reduction while maintaining the volume by keeping the thickness constant at 5%.

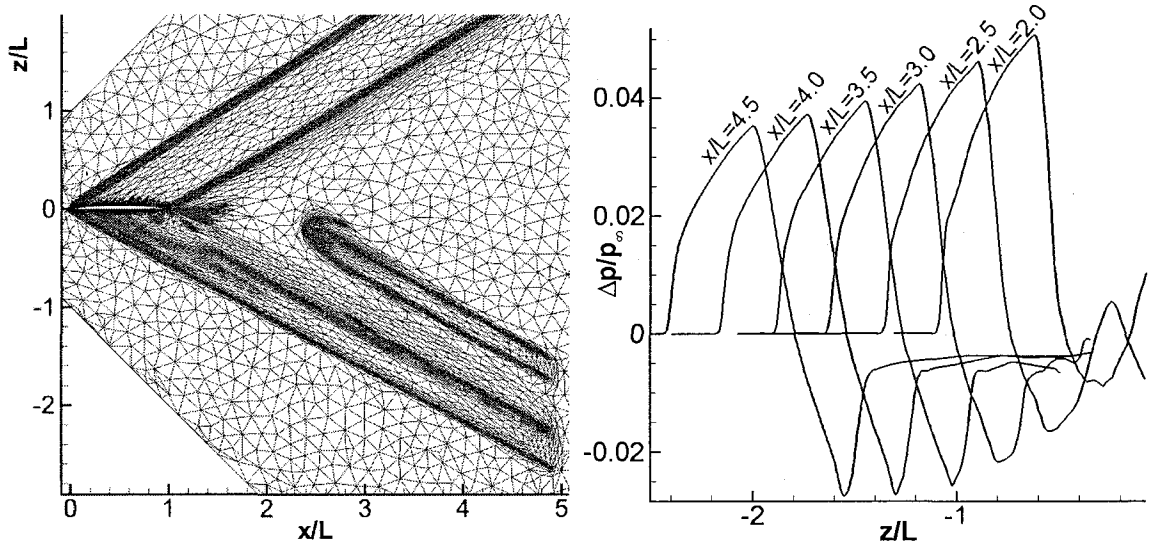

Figure 46: The optimized grid on the symmetry plane after 10 solution/adaptation cycles (left), and the pressure signals on several downstream vertical data cuts (right) for the optimum delta wing geometry listed in Ref. [93]. Mach 2.0, $\alpha = 2.24°$.

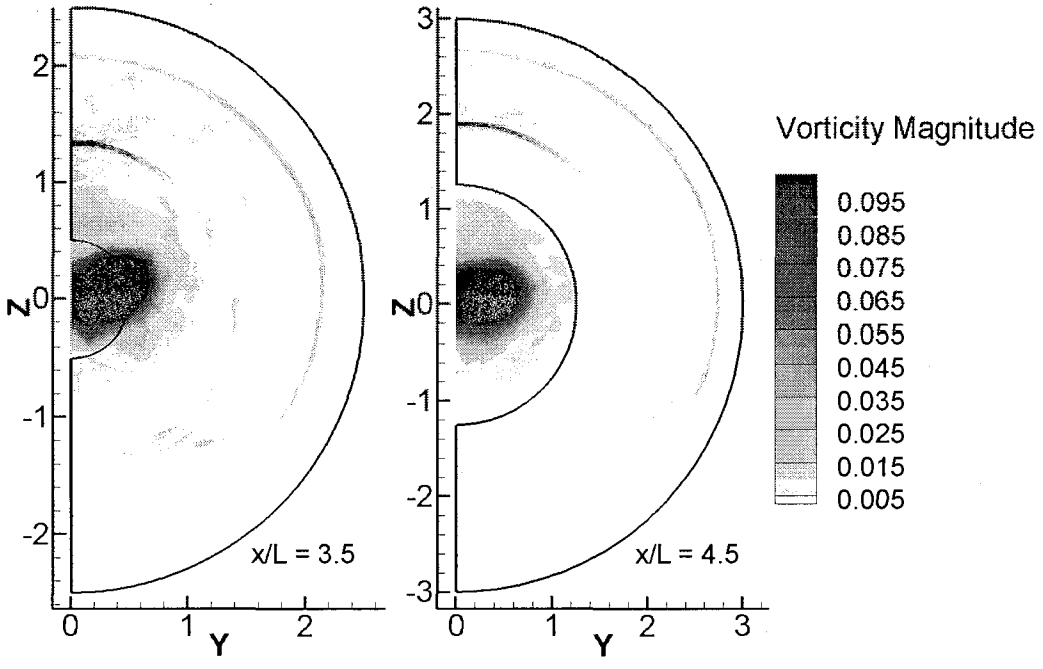

Figure 47: Vorticity distribution and the Euler/FPE interface grid boundaries at x/L = 3.5 and x/L = 4.5.

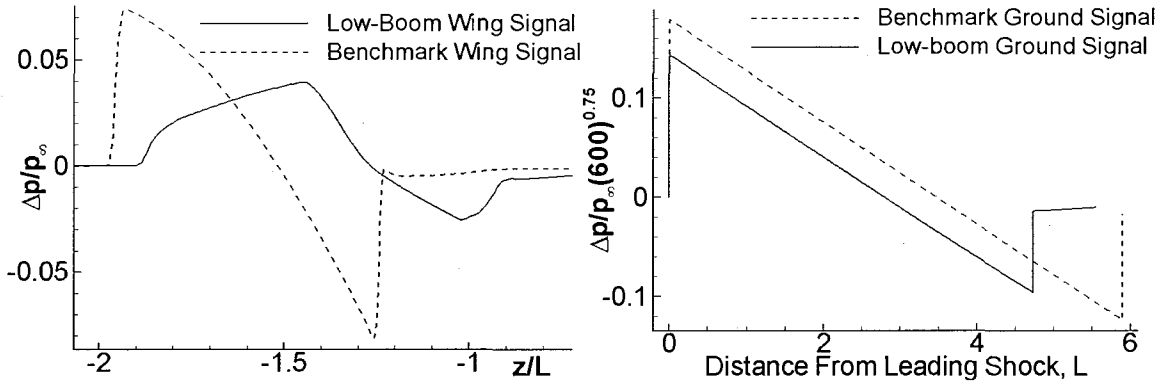

Figure 48: The pressure signals from the benchmark and the optimum geometry reported in Ref. [93] at x/L = 3.5 (left), and at r/L = 600 – ground level (right).

Table 14: Mid- and far-field sonic boom reduction comparison for the Ref. [93] optimum delta wing.

	Benchmark		Ref. [93] optimum			
Location	Impulse	Peak $\Delta p/p_\infty$	Impulse	Peak $\Delta p/p_\infty$	% Impulse reduction	% Peak $\Delta p/p_\infty$ reduction
x/L = 3.5	0.02	0.074	0.016	0.0394	20.0	46.8
r/L = 600	0.00256	0.001477	0.00165	0.001186	35.5	19.7

6.2.2 Angle of Attack – Camber Optimization

Perhaps the most obvious camber strategy is to set it such that the lower surface of the wing becomes flat. This way the flow is subjected to the lowest slope all along the lower surface and hopefully emits the lowest sonic boom disturbance towards ground. Unfortunately this is not the case. At each angle of attack there is a specific optimum camber setting that produces a particular curvature on the lower surface to minimize the sonic boom. This has already been shown on a much simpler configuration in the previous chapter, where the optimum meridian profile of an axisymmetric shape is curved towards the incoming flow (convex) rather than being flat with constant minimum slope. This statement can be generalized to all 3D geometries producing lift. Flat lower surfaces in lifting airframes do not produce minimum sonic boom pressure levels.

The benchmark configuration is at zero camber with $\alpha = 2.24^\circ$, producing $C_L = 0.0765$ in Mach 2.0 flow. The optimum camber producing minimum sonic boom at this angle of attack is not zero, and the configuration needs to be modified. Since camber has a positive effect on lift,

modifying camber requires for modification of the angle of attack if the original C_L is to be produced. This is a 2 factor optimization problem. The pilot study on low boom delta wing signal prediction already established that the response to be minimized is the pressure impulse on a vertical cut at x/L = 3.5. Optimizing the ground signal directly can work also, but since the near-field impulse decrease is at the same level as the ground peak Δp decrease, the extra computational time required for mid-field prediction with FPM3D from x/L = 4.5 to r/L = 30 for each run is not necessary.

Camber modification is accomplished through scaling a 1% camber profile with an input parameter – the camber design variable ℓ_c, and adding this data to the benchmark airfoil upper and lower surfaces. The 1% camber profile is generated by scaling the z-coordinate of the benchmark profile upper surface by 2/5. Doing so puts the maximum camber at the mid-chord location. The main reason for this particular camber profile selection is that a $\ell_c = 2.5$ setting creates a profile with a perfectly flat lower surface. In this way the obvious minimization idea mentioned in the first paragraph is included in the design space as well.

The lift at low α varies linearly with α. Therefore sonic boom due to lift is linearly dependent on α at this range, and 2 levels of α is adequate. Camber on the other hand modifies the non-linear curvature of the airfoil surfaces, and should be investigated in more than 2 levels so as not to overlook any non-linear relationships. The camber setting bounds are kept at $\ell_c = 0$ and $\ell_c = 2.5$. The lower bound here gives the original airfoil and the upper bound gives the flat lower surface profile. The camber is tested at 5 evenly spaced levels. Since positive camber increases lift, the upper bound of α does not need to exceed the original value of 2.24°. The lower bound for α is determined by using a linear relationship between α and C_L. Setting $\alpha = 2.0°$ as a reasonable value, the lift is predicted to be $C_L = 0.0683$. This is about 10% less than the original lift and a useful design space lower bound. Two levels for α and 5 levels for ℓ_c require a total of 10 runs. The results are tabulated in Table 15. Run 6 corresponds to the original benchmark configuration.

Table 15: Results of angle of attack and camber runs. Mach 2.0

Run	α	ℓ_c	Peak $\Delta p/p_\infty$ x/L=3.5	$\ell_{x/L=3.5}$	C_L	C_D	Run	α	ℓ_c	Peak $\Delta p/p_\infty$ x/L=3.5	$\ell_{x/L=3.5}$	C_L	C_D
1	2.0	0	.0690	.0191	.0685	.0096	6	2.24	0	.0761	.0203	.0765	.0102
2	2.0	0.625	.0625	.0178	.0703	.0099	7	2.24	0.625	.0655	.0190	.0786	.0105
3	2.0	1.25	.0544	.0169	.0727	.0110	8	2.24	1.25	.0595	.0185	.0806	.0115
4	2.0	1.875	.0483	.0177	.0743	.0127	9	2.24	1.875	.0511	.0197	.0823	.0133
5	2.0	2.5	.0497	.0197	.0751	.0139	10	2.24	2.5	.0607	.0236	.0842	.0158

The ANOVA tables for the impulse and lift response models are given in Table 16 and Table 17, respectively. The last column in the ANOVA table gives the significance (p-value) of the terms. Terms with $p < 0.05$ are considered significant. For the impulse response α, ℓ_c, $\alpha\,\ell_c$, and ℓ_c^2 are significant terms. The high R-squared value (>0.95) means that the model fits the available data exceptionally well. The two main reasons for this level of fit is that CFD computations are deterministic and no repeats are involved (pure error = 0), and the flow solution tools are accurate since there is no noise in that data. The lift model is linear in both angle of attack and camber, with no significant interaction of the two. The linear model is a perfect fit with R-squared > 0.99. The model equations for impulse and lift are given in Eqs. (85) and (86), respectively. The carrot (^) sign is used to indicate that these are model predicted responses. The actual response data and the model fits are displayed in Figure 49. The camber has strong non-linear non-monotonous influence on the pressure impulse with a stationary point available in the design space. The drag increases with camber and angle of attack as the values in the run table suggest. The optimum camber is not 2.5% which would make a flat lower surface, but is somewhere around 1%.

The optimization is carried out in Design-Expert by setting the goals as minimum impulse and target $C_L = 0.0765$. The predicted and actual results at the reported optimum point are given in Table 18. The optimum angle of attack is 2.131° and the optimum camber is 1.19%. The prediction shows a very close match with the actual computational results at this point, owing to the models being significant and with R-squared > 0.95. The impulse decrease with this optimum is 12.8%, and the drag increase is 9.8%.

Table 16: ANOVA for impulse reduced cubic model. Type III SS.

Source	*SS*	DoF	*MS*	F Value	p-value Prob. > F
Model	3.06E-05	5	6.13E-06	51.98	0.0010
α	2.13E-06	1	2.13E-06	18.04	0.0132
ℓ_c	3.53E-06	1	3.53E-06	29.93	0.0054
$\alpha\,\ell_c$	1.92E-06	1	1.92E-06	16.31	0.0156
ℓ_c^2	1.49E-05	1	1.49E-05	126.11	0.0004
$\alpha\,\ell_c^2$	5.16E-07	1	5.16E-07	4.38	0.1046
Residual	4.71E-07	4	1.18E-07		
Total (SS_T)	3.11E-05	9			
Std. Dev.	0.0003		R^2	0.985	
Mean	0.0192		$R^2_{Adj.}$	0.966	

Table 17: ANOVA for lift linear model. Type III SS.

Source	*SS*	DoF	*MS*	F Value	p-value Prob. > F
Model	2.36E-04	2	1.18E-04	814.96	< 0.0001
α	1.71E-04	1	1.71E-04	1175.76	< 0.0001
t_c	6.59E-05	1	6.59E-05	454.15	< 0.0001
Residual	1.02E-06	7	1.45E-07		
Total (SS_T)	2.37E-04	9			
Std. Dev.	0.000367		R^2	0.996	
Mean	0.076288		$R^2_{Adj.}$	0.995	

$$\hat{I}_{x/L=3.5} = 0.00852 + 0.00535\alpha + 0.00259 t_C - 0.003105\alpha t_C - 0.00427 t_C^2 + 0.00290\alpha t_C^2 \quad (85)$$

$$\hat{C}_L = -0.00030 + 0.03442\alpha + 0.00290 t_C \quad (86)$$

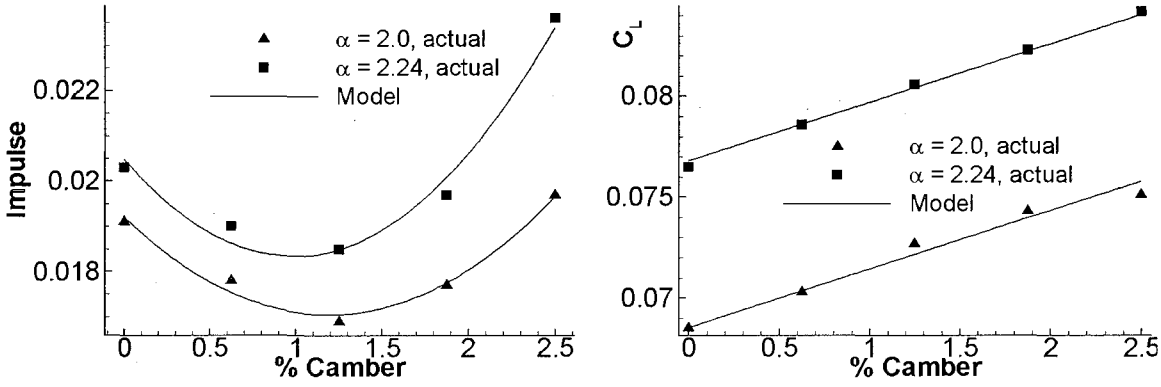

Figure 49: Model fits to actual computational data for impulse at x/L = 3.5 and lift. Mach 2.0.

Table 18: Angle of attack – camber optimum predicted and actual computed results.

α	t_c	Peak $\Delta p/p_\infty$ x/L=3.5	$I_{x/L=3.5}$	C_L	C_D	-%ΔI	%ΔC_D	
2.131	1.190		0.0178	0.0765				Prediction
		0.0549	0.0177	0.0769	0.0112	12.8	9.8	Actual

6.2.3 Angle of Attack – Dihedral Optimization

Dihedral has an attenuating effect on both lift and the sonic boom intensity, but the percentage decrease in sonic boom pressure is greater than the percent loss in lift. Therefore dihedral is a beneficial factor for sonic boom minimization. Using the Euler/FPE sonic boom prediction methodology, Ref. [30] shows that adding 15° dihedral to the same benchmark geometry used in the current study requires the angle of attack to be increased from 2.24° to 2.4° to match the original lift. This is approximately a 6.7% loss in lift due to dihedral at the original angle of attack. However, the ground level peak Δp decrease shown is about 11%. In this section the work in Ref. [30] is partially repeated using the unstructured near-field solution technology, and extended to a larger range of dihedral angles. Dihedral is denoted by θ_D.

There are two basic ways of adding dihedral to the wing. The first and most obvious way is to rotate the wing about the chord line, and the second way is to translate the span-wise sections in the vertical (positive z) direction. The two disadvantages of the first method are that such rotation changes (thickens) the root chord profile on the y = 0 symmetry plane, and the wing planform area parallel to the flow decreases. Changing the root chord profile complicates the multivariate optimization process since the effect of camber is now strongly coupled with the dihedral angle which also changes the airfoil profile. The loss in planform area comes as an additional dependent factor that affects the lift. The translation dihedral avoids these two problems, but brings a new one. As the dihedral angle increases, the height of the wing increases with it, and goes to infinity as $\theta_D \rightarrow 90°$. Fortunately high dihedral angles are of no interest since this causes excessive flight stability and the aircraft becomes unresponsive to controls. Around $\theta_D = 20°$, the heights of both the rotated and translated dihedral wings are close. In conclusion, the translated dihedral method is adapted in the current study for wing CAD generation. Just to rule out the question of rotated dihedral effect, this factor is investigated as well in this section, and the optimums are compared to those obtained using translated dihedral.

Table 19 shows the initial design set for the rotated dihedral analysis. The angle of attack is tested at two levels with the lower bound equal to the benchmark case since increasing dihedral decreases the lift. The upper bound of α is set at 2.6°. The dihedral angle is tested between 0° and 60° at 10 degree intervals. This set is more like a grid search rather than one of the "text-book" designs. It can provide a linear model in α and a high order non-linear model in θ_D. Although $\theta_D > 20°$ is not feasible, it is tested anyway to see how the responses behave at such extremes. The impulse and lift model equations created using the data in Table 19 are given in

Eqs. (87) and (88). Both models have $R^2_{Adj.} > 0.99$ with only significant terms included. There is significant interaction of the angle of attack and dihedral in this case for both the impulse and the lift. The quadratic dihedral term is also significant for both responses. Using these models, optimization is carried out to minimize the impulse while targeting the lift to the benchmark value. The predicted optimum angle of attack at several dihedral settings and the global optimum are given in Table 20. The first two predicted optimums are at preset dihedral angles of interest, and the last one is the predicted global optimum. The αs for the last two optimums exceed the current design space and are in the extrapolation zone. It is better to carry out an additional set of runs and optimization in this zone before testing these optimums. The second design set repeats the first for $\alpha = 3.3$ and $\alpha = 4.0$. The $\alpha = 2.6$ data set can be combined with these new runs for a 3-level orthogonal α variation in the design matrix. The results of the second set are given in Table 21. New response models are created using runs 8 through 28 to allow for testing the quadratic significance of the angle of attack term. The new models are given in Eqs. (89) and (90). Again these models have $R^2_{Adj.} > 0.99$. The α^2 terms is found to be insignificant. The optimums found using Eqs. (89) and (90) are given in Table 22. The global optimum is the second result, which has $\alpha \approx 10°$ and $\theta_D \approx 65°$. This is well outside of the already unfeasibly large design space limits. There seems to be no actual global optimum with the dihedral factor since the lift loss by dihedral can always be countered with angle of attack increase, and every new design set with higher angle of attack predicts a new global optimum above the design space limits. Therefore optimizing the angle of attack and other factors at preset dihedral angles seems to be the right way to continue the delta wing optimization study. The preset dihedral angles adapted in the current study are 15° and 20°, the same values used in Ref. [30]. Table 23 shows the actual results at predicted optimum α's for these two dihedral settings. The 15° dihedral has a 15.3% and the 20° dihedral has a 20.7% reduction in sonic boom impulse. The 20° dihedral optimum found here is already better than the nose angle, camber, thickness optimum geometry with the same dihedral angle and with 40% volume loss from Ref. [93], which is solved in section 6.2.1.

$$\hat{I}_{x/L=3.5} = 9.65 \cdot 10^{-3} + 4.78 \cdot 10^{-3}\alpha - 2.25 \cdot 10^{-4}\theta_D - 4.31 \cdot 10^{-5}\alpha\theta_D + 1.36 \cdot 10^{-6}\theta_D^2 \tag{87}$$

$$\hat{C}_L = -5.63 \cdot 10^{-3} + 3.70 \cdot 10^{-2}\alpha - 3.28 \cdot 10^{-4}\theta_D - 4.06 \cdot 10^{-4}\alpha\theta_D - 9.44 \cdot 10^{-6}\theta_D^2 \tag{88}$$

Table 19: Rotated dihedral design set 1.

Run	α	θ_D	Peak $\Delta p/p_\infty$ x/L=3.5	$I_{x/L=3.5}$	C_L	C_D	Run	A	θ_D	Peak $\Delta p/p_\infty$ x/L=3.5	$I_{x/L=3.5}$	C_L	C_D
1	2.24	0	.0761	.0203	.0765	.0102	8	2.6	0	.0777	.0220	.0891	.0112
2	2.24	10	.0603	.0173	.0715	.0100	9	2.6	10	.0659	.0191	.0835	.0109
3	2.24	20	.0511	.0147	.0627	.0097	10	2.6	20	.0561	.0158	.0736	.0105
4	2.24	30	.0437	.0119	.0510	.0093	11	2.6	30	.0459	.0133	.0605	.0100
5	2.24	40	.0367	.0097	.0377	.0090	12	2.6	40	.0399	.0105	.0453	.0095
6	2.24	50	.0316	.0075	.0235	.0088	13	2.6	50	.0327	.0087	.0296	.0092
7	2.24	60	.0273	.0060	.0098	.0089	14	2.6	60	.0302	.0069	.0137	.0091

Table 20: Predicted angle of attack – rotated dihedral optimums using Eqs. (87) and (88)

α	θ_D	Impulse (x/L = 3.5)	C_L
2.5667	15	0.0172	0.0765
2.7353	20	0.0164	0.0765
3.8631	38.89	0.0147	0.0765

Table 21: Rotated dihedral design set 2.

Run	α	θ_D	Peak $\Delta p/p_\infty$ x/L=3.5	$I_{x/L=3.5}$	C_L	C_D	Run	α	θ_D	Peak $\Delta p/p_\infty$ x/L=3.5	$I_{x/L=3.5}$	C_L	C_D
15	3.3	0	.0866	.0258	.1127	.0136	22	4	0	.1007	.0297	.1366	.0165
16	3.3	10	.0747	.0220	.1058	.0131	23	4	10	.0819	.0256	.1286	.0158
17	3.3	20	.0620	.0185	.0943	.0124	24	4	20	.0706	.0216	.1152	.0149
18	3.3	30	.0514	.0152	.0785	.0116	25	4	30	.0577	.0176	.0965	.0137
19	3.3	40	.0426	.0122	.0600	.0108	26	4	40	.0474	.0140	.0748	.0123
20	3.3	50	.0352	.0098	.0408	.0100	27	4	50	.0376	.0110	.0522	.0111
21	3.3	60	.0289	.0082	.0216	.0095	28	4	60	.0318	.0086	.0295	.0101

$$\hat{I}_{x/L=3.5} = 8.02\cdot 10^{-3} + 5.44\cdot 10^{-3}\alpha - 1.66\cdot 10^{-4}\theta_D - 7.32\cdot 10^{-5}\alpha\theta_D + 1.74\cdot 10^{-6}\theta_D^2 \tag{89}$$

$$\hat{C}_L = -4.49\cdot 10^{-3} + 3.59\cdot 10^{-2}\alpha + 4.68\cdot 10^{-4}\theta_D - 3.88\cdot 10^{-4}\alpha\theta_D - 1.25\cdot 10^{-5}\theta_D^2 \tag{90}$$

Table 22: Predicted angle of attack – rotated dihedral optimums using Eqs. (89) and (90).

α	θ_D	$\mathcal{I}_{x/L=3.5}$	C_L
2.7197	20	0.0162	0.0765
9.8173	65.33	0.01105	0.0765

Table 23: Actual results at predicted optimums for angle of attack – rotated dihedral study.

α	θ_D	Peak $\Delta p/p_\infty$ x/L=3.5	$\mathcal{I}_{x/L=3.5}$	C_L	C_D	-%Δ$\mathcal{I}$	%ΔC_D	
2.5667	15	0.0593	0.0172	0.0775	0.0106	15.3	3.9	Actual
2.7197	20	0.0565	0.0161	0.0769	0.0108	20.7	5.9	Actual

Next, the angle of attack – dihedral optimization is carried out using the translated dihedral method. Translated dihedral preserves the planform area of the wing, thus its impact on the lift is expected to be less than the rotated dihedral. To find optimum angle of attack settings at 15° and 20° dihedral angles, an experimental design matrix of 8 runs is executed. Angle of attack is tested at 2.24° (original) and 2.6° settings, and the dihedral is tested at 0, 10, 20, and 30°. The results of the 8 runs are tabulated in Table 24. A direct comparison with similar runs in Table 19 shows that lift coefficients are higher than those obtained with the rotated dihedral. The response models for the data in Table 24 are given in Eqs. (91) and (92). The data and the models are plotted in Figure 50. Again both models have $R^2_{Adj.} > 0.99$. In contrast to the rotated dihedral case, $\alpha\theta_D$ interaction term and the θ_D^2 quadratic term are found to be insignificant. Clearly the translated dihedral method uncouples the effects of angle of attack and dihedral on both responses. Rotation for dihedral causes thickening of the root chord profile at the y = 0 symmetry plane, along with shrinking the planform area. The first affects the sonic boom impulse and the second affects the lift. These parasitic interaction effects are eliminated using the translated dihedral method. Predicted and actual responses at the optimums found using Eqs. (91) and (92) are given in Table 25. The level of sonic boom reduction is about the same as that obtained with the rotated dihedral, but with less than half the drag increase. This is because of the lower α's required due to the conservation of the planform area. In conclusion, translated dihedral is preferable to rotated dihedral because the drag penalty is much less and the responses are simple with no 2-factor interactions or quadratic terms.

Table 24: Translated dihedral set.

Run	α	θ_D	Peak $\Delta p/p_\infty$ x/L=3.5	$I_{x/L=3.5}$	C_L	C_D
1	2.24	0	.0761	.0203	.0765	.0102
2	2.24	10	.0647	.0178	.0734	.0101
3	2.24	20	.0536	.0152	.0693	.0098
4	2.24	30	.0437	.0131	.0645	.0096
5	2.6	0	.0826	.0220	.0889	.0112
6	2.6	10	.0658	.0192	.0854	.0110
7	2.6	20	.0567	.0170	.0812	.0108
8	2.6	30	.0472	.0143	.0762	.0105

$$\hat{I}_{x/L=3.5} = 1.082 \cdot 10^{-2} + 4.236 \cdot 10^{-3}\alpha - 2.475 \cdot 10^{-4}\theta_D \tag{91}$$

$$\hat{C}_L = 2.438 \cdot 10^{-3} + 3.333 \cdot 10^{-2} - 4.120 \cdot 10^{-4}\theta_D \tag{92}$$

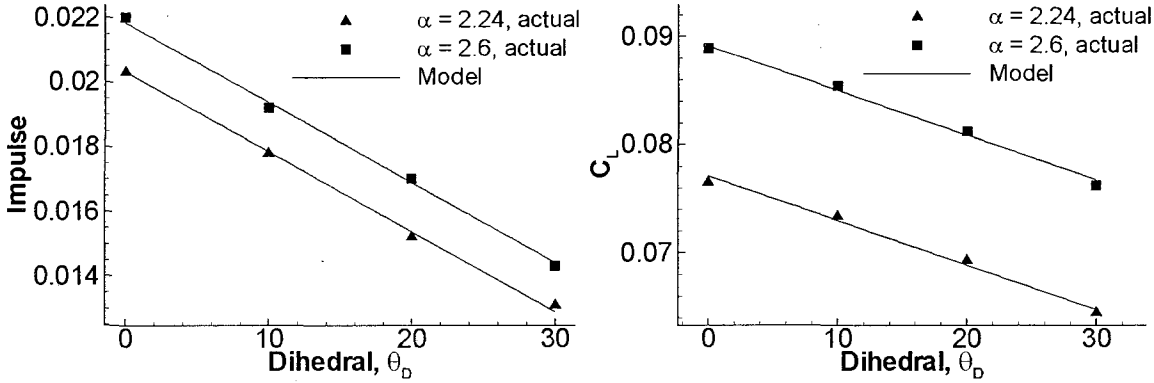

Figure 50: Actual data and model fits for impulse at x/L = 3.5 and lift responses for the $\alpha - \theta_D$ analysis.

Table 25: Translated dihedral optimum predicted and actual computed results.

α	θ_D	Peak $\Delta p/p_\infty$ x/L=3.5	$I_{x/L=3.5}$	C_L	C_D	-%ΔI	%ΔC_D	
2.4072	15		0.0173	0.0765				Prediction
		0.0587	0.0170	0.0769	0.01037	16.3	1.7	Actual
2.4690	20		0.0163	0.0765				Prediction
		0.0542	0.0161	0.0769	0.01041	20.7	2.1	Actual

6.2.4 Effect of Linear Twist

In this section, the effect of wing twist on sonic boom impulse is investigated. For simplicity, the twist from root to tip is modified linearly, and the root twist (or the wing angle of attack) is kept at zero. By applying positive twist towards the tip of the wing, the lift is redistributed away from the centerline. The tip twist setting α_T is optimized to match the original lift. Two sets of results are presented in this section where linear twist is separately coupled with constant span-wise camber, ℓ_c, and dihedral θ_D. Camber is tested at 0% (original) and 2.5% settings. A camber of 2.5% makes the lower surface flat and minimizes the sonic boom when the wing is at zero angle of attack. Section 6.1.2 shows that optimum camber changes with the angle of attack, which suggests that camber should vary along the span as the twist increases. However, an initial effort is given here with constant span-wise camber which is set to minimize the effect of the largest section of the wing. Combining twist with dihedral is expected to help move the lift disturbance further away from the centerline where the sonic boom is strongest.

Table 26 shows the results for the tip twist – camber coupling runs. Five levels of tip twist are tested to provide sufficient DoF for Lack-of-Fit (LoF) testing for quadratic and cubic models. The dihedral is kept at zero. The response model terms are given in Table 27. The interaction terms are found to be significant. Figure 51 shows the computed data points from Table 26 and the model fits. For low twist angles, setting camber at 2.5% does decrease the impulse, but this advantage is lost for $\alpha_T > 3°$. The optimums predicted at 0% and 2.5% camber are given in Table 28 with their actual computed responses. With the 0% camber optimum, the decrease in pressure impulse at x/L = 3.5 is only 4.1% with a very large increase in drag. Positive tip twist of over 7° is not feasible since it can easily induce flutter at supersonic speeds and cause early stall of the wing tip during take-off and landing. This is opposite of what twist is used for in general aviation. With 2.5% camber, the pressure impulse and drag increase significantly. The optimum twist which provides the target lift ends up increasing the sonic boom impulse by 15% and drag by 64%. Obviously setting the camber to minimize the effect of the root chord has back-fired causing the rest of the wing (with high twist) to produce very strong sonic boom signals. Considering the impulse increase is quadratic with camber as shown in Section 6.1.2, having inappropriate camber at high local angles of attack along the span drastically increases the sonic boom impulse. Therefore, providing the optimum camber at each span-wise location is crucial.

Table 26: Linear twist and camber coupling at zero dihedral.

Run	ℓ_c	α_T	Peak $\Delta p/p_\infty$ x/L=3.5	$\ell_{x/L=3.5}$	C_L	C_D	Run	ℓ_c	α_T	Peak $\Delta p/p_\infty$ x/L=3.5	$\ell_{x/L=3.5}$	C_L	C_D
1	0	0	.0452	.0103	.0000	.0074	6	2.5	0	.0106	.0044	.0058	.0134
2	0	2.5	.0462	.0127	.0272	.0080	7	2.5	2.5	.0363	.0122	.0335	.0138
3	0	5	.0507	.0157	.0542	.0097	8	2.5	5	.0721	.0194	.0615	.0153
4	0	7.5	.0560	.0201	.0805	.0125	9	2.5	7.5	.1122	.0275	.0891	.0181
5	0	10	.0636	.0242	.1060	.0163	10	2.5	10	.1552	.0342	.1156	.0217

Table 27: Response model terms for linear twist – camber analysis.

Response	I		CL	
Term	coefficient	p-value	coefficient	p-value
Mean	1.033E-02		3.429E-05	
α_T	-2.349E-03	< 0.0001	2.290E-03	< 0.0001
ℓ_c	6.158E-04	< 0.0001	1.079E-02	< 0.0001
$\alpha_T\ell_c$	9.141E-04	< 0.0001	9.897E-05	< 0.0001
α_T^2	1.229E-04	0.0007	3.314E-05	< 0.0001
$\alpha_T^2\ell_c$	-2.789E-05	< 0.0001	5.943E-06	0.0004
α_T^3	-4.533E-06	0.0257	-5.333E-06	< 0.0001

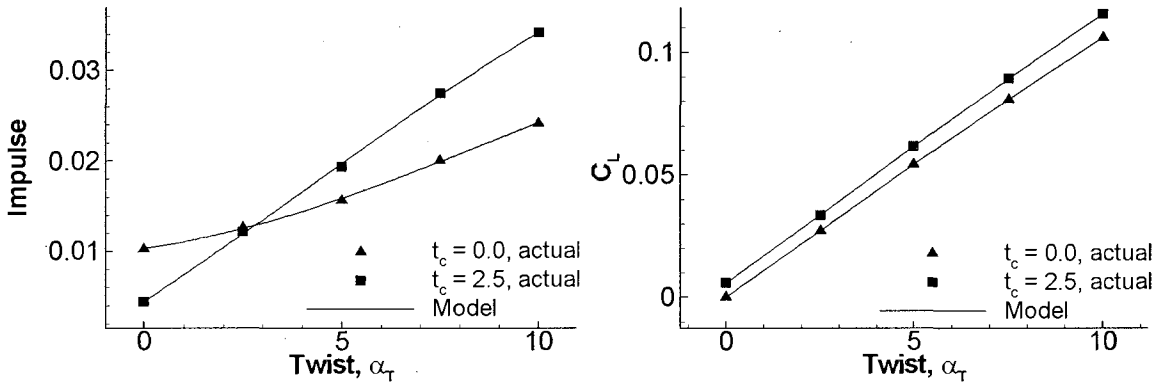

Figure 51: Actual data and model fits for impulse at x/L = 3.5 and lift responses for linear twist – camber analysis.

Table 28: Predicted and actual results for linear twist optimums at 0% and 2.5% camber.

ℓ_c	α_T	Peak $\Delta p/p_\infty$ x/L=3.5	$\ell_{x/L=3.5}$	C_L	C_D	-%$\Delta\ell$	%ΔC_D	
0	7.1170		0.0191	0.0765				Predicted
		0.0550	0.0195	0.0765	0.0121	4.1	18.6	Actual
2.5	6.3529		0.0236	0.0765				Predicted
		0.0922	0.0234	0.0764	0.0167	-15.3	63.7	Actual

The second set of experiments is carried out where positive linear twist is coupled with dihedral angle, at a 0% camber setting. Projections using the already available data on dihedral from the previous section and the linear twist just discussed suggest that α_T = 7, 8, 9 and θ_D = 10, 20, 30 level settings make up a suitable face centered design (FCD) matrix to locate optimums at 15° and 20° dihedral. The FCD results are tabulated in Table 29. The model terms for impulse and lift responses are given in Table 30. Figure 52 shows the computed data points and the model fits. The impulse increases with twist at the same rate for all dihedral angles. If the rate of increase in impulse with twist decreased with increasing dihedral, it would indicate that dihedral improves the effect of twist on sonic boom mitigation. However, this is not the case. The predicted optimums and their actual responses are given in Table 31. The reductions in the sonic boom impulse are practically the same as the dihedral-only optimization, with the drag penalty increased considerably. The optimum tip twist angles found are impractical.

Table 29: Linear twist – dihedral FCD set results.

Run	θ_D	α_T	Peak $\Delta p/p_\infty$ x/L=3.5	$\mathcal{I}_{x/L=3.5}$	C_L	C_D
1	10	7	0.0447	0.0167	0.0716	0.0117
2	10	8	0.0463	0.0183	0.0818	0.013
3	10	9	0.0483	0.0199	0.0918	0.0144
4	20	7	0.0369	0.0144	0.0669	0.0115
5	20	8	0.038	0.0159	0.0768	0.0127
6	20	9	0.0393	0.0172	0.0866	0.0141
7	30	7	0.029	0.0127	0.0612	0.0112
8	30	8	0.0309	0.0135	0.0707	0.0124
9	30	9	0.0315	0.0147	0.0802	0.0137

Table 30: Response model terms for linear twist – dihedral analysis.

Response	I		CL	
Term	coefficient	p-value	coefficient	p-value
Mean	-1.09E-03		-5.46E-03	
α_T	4.09E-03	< 0.0001	1.25E-02	< 0.0001
θ_D	2.04E-04	< 0.0001	-6.30E-06	< 0.0001
$\alpha_T\theta_D$	-1.53E-04	< 0.0001	-6.89E-05	< 0.0001
α_T^2	-1.65E-04	0.0605	-1.35E-04	< 0.0001
θ_D^2	1.31E-05	0.0012	-1.74E-06	< 0.0001
$\alpha_T^2\theta_D$	1.14E-05	0.0109	3.55E-06	< 0.0001
$\alpha_T\theta_D^2$	-1.47E-06	0.0024	-4.80E-07	< 0.0001

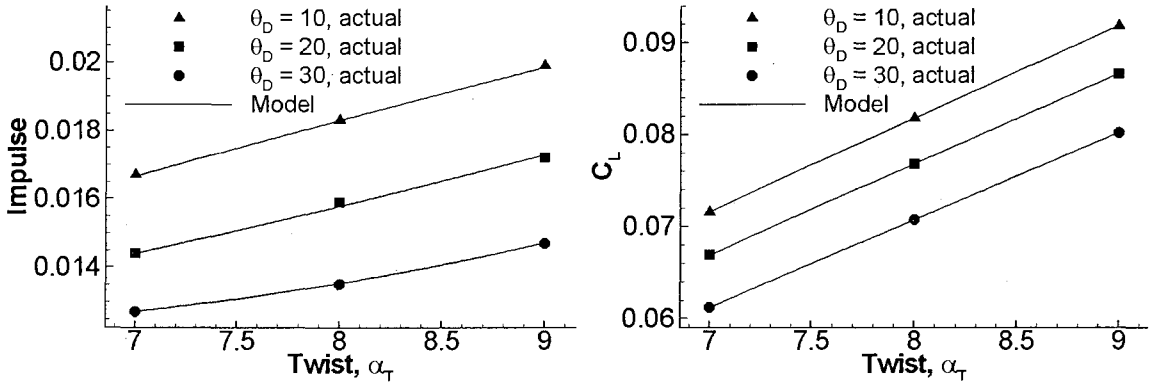

Figure 52: Actual data and model fits for impulse at x/L = 3.5 and lift responses for linear twist – dihedral analysis.

Table 31: Linear twist – dihedral optimum predicted and actual computed results.

α_T	θ_D	Peak $\Delta p/p_\infty$ x/L=3.5	$I_{x/L=3.5}$	C_L	C_D	-%ΔI	%ΔC_D	
7.7066	15		0.0165	0.0765				Prediction
		0.0413	0.0166	0.0764	0.0125	18.2	22.5	Actual
7.9677	20		0.0157	0.0765				Prediction
		0.0379	0.0161	0.0766	0.0127	20.7	24.5	Actual

Obviously there is not much that can be done with positive twist separately. Although it redistributes most of the lift towards the tip, this does not help reduce the under-track sonic boom impulse. Moreover, the drag is increased considerably. The structural implications of such high tip twist angles make its application impractical. However, lateral redistribution of sonic boom should be possible, and using span-wise twist should improve the sonic boom mitigation performance. The twist factor is not discarded, but is investigated more rigorously in the following sections by including root twist, negative tip twist with respect to the root chord ($\alpha_T < \alpha$), non-linear span-wise twist profile, and span-wise camber profile optimized for local twist angles.

6.2.5 Angle of Attack – Dihedral – Camber Optimization

In this section a three-factor optimization is carried out using angle of attack, dihedral, and span-wise constant camber. Effects of angle of attack and dihedral on impulse and lift were shown to be linear in the previous sections. Therefore a general factorial experimental design with 2 levels on α and θ_D and 5 levels on t_C is setup to analyze the responses. Camber effect on impulse is strongly quadratic, and 5-level setup for this variable leaves sufficient DoF for LoF testing. Since the dihedral angles of interest are 15° and 20°, the lower and upper bounds for this factor are set as 10° and 20°. This setup leaves 15° in the center, and 20° still inside the design space. The bounds on angle of attack are chosen as 2.1° and 2.6° in light of the findings in the previous sections, which sets $\alpha = 2.35°$ as the center. Camber bounds are set as 0.4% and 2.0%, centering the design at 1.2% camber. The design matrix with 20 runs is given in Table 32, and the response model terms are given in Table 33. For the impulse, all of the interaction terms are found to be significant whereas only a few of them are significant for the lift. The data points and the model fits are shown in Figure 53. The interactions of camber with angle of attack and dihedral seem to move the stationary point on the impulse vs. camber curves. While dihedral – camber interaction modifies the slope of the lift vs. camber lines slightly, angle of attack – camber interaction has little influence on lift. This is the least significant term in the lift model. Finally, the predicted optimums and their actual computed results are given in Table 34. The 20° dihedral optimum shows a 27.6% decrease in sonic boom pressure impulse. This is a significant improvement over the 2 factor α - t_C and α - θ_D optimizations. The drag penalty is 11.8%, mostly due to the camber.

Table 32: Angle of attack – dihedral – camber test results.

Run	α	θ_D	t_C	$\Delta p/p_\infty$ x/L=3.5	$I_{x/L=3.5}$	C_L	C_D	Run	α	θ_D	t_C	$\Delta p/p_\infty$ x/L=3.5	$I_{x/L=3.5}$	C_L	C_D
1	2.1	10	0.4	.0567	.0160	.0696	.0099	11	2.6	10	0.4	.0608	.0186	.0865	.0111
2	2.1	10	0.8	.0514	.0155	.0711	.0103	12	2.6	10	0.8	.0565	.0182	.0877	.0116
3	2.1	10	1.2	.0477	.0152	.0721	.0111	13	2.6	10	1.2	.0523	.0181	.0889	.0124
4	2.1	10	1.6	.0431	.0157	.0732	.0122	14	2.6	10	1.6	.0486	.0189	.0901	.0134
5	2.1	10	2	.0404	.0169	.0741	.0136	15	2.6	10	2	.0478	.0204	.0910	.0147
6	2.1	20	0.4	.0473	.0139	.0655	.0097	16	2.6	20	0.4	.0522	.0161	.0821	.0109
7	2.1	20	0.8	.0431	.0136	.0663	.0102	17	2.6	20	0.8	.0483	.0158	.0829	.0114
8	2.1	20	1.2	.0390	.0134	.0668	.0111	18	2.6	20	1.2	.0460	.0156	.0837	.0122
9	2.1	20	1.6	.0359	.0136	.0675	.0122	19	2.6	20	1.6	.0416	.0166	.0844	.0133
10	2.1	20	2	.0335	.0144	.0678	.0136	20	2.6	20	2	.0394	.0178	.0846	.0147

Table 33: Response model terms for angle of attack – dihedral – camber analysis.

Response	I		C_L	
Term	coefficient	p-value	coefficient	p-value
Mean	4.677E-03		1.964E-03	
α	7.095E-03	< 0.0001	3.333E-02	< 0.0001
θ_D	4.660E-05	< 0.0001	-3.711E-04	< 0.0001
ℓ_C	-1.114E-03	< 0.0001	4.565E-03	< 0.0001
$\alpha\theta_D$	-1.350E-04	< 0.0001	0	
$\alpha\,\ell_C$	-1.740E-03	< 0.0001	2.293E-04	0.0152
$\theta_D\,\ell_C$	3.230E-06	0.0249	-1.304E-04	< 0.0001
ℓ_C^2	2.249E-04	< 0.0001	-4.068E-04	< 0.0001
$\alpha\theta_D\,\ell_C$	4.753E-05	0.0504	0	
$\alpha\,\ell_C^2$	9.938E-04	0.0004	0	
$\theta_D\ell_C^2$	-5.362E-05	0.0001	0	

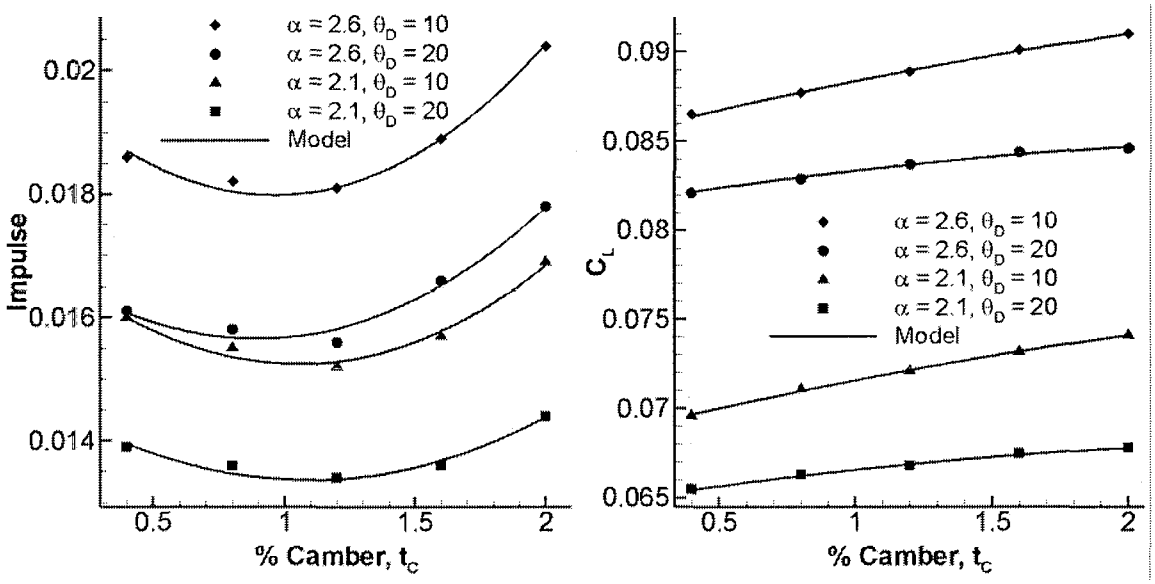

Figure 53: Actual data and model fits for impulse at x/L = 3.5 and lift responses for angle of attack – dihedral – camber analysis.

Table 34: Angle of attack – dihedral – camber optimum predicted and actual computed results.

α	θ_D	ℓ_C	Peak $\Delta p/p_\infty$ x/L=3.5	$\ell_{x/L=3.5}$	C_L	C_D	-%$\Delta\ell$	%ΔC_D	
2.3144	15	1.0996		0.0154	0.0765				Prediction
			0.0445	0.0154	0.0766	0.0114	24.1	11.8	Actual
2.3942	20	1.0336		0.0147	0.0765				Prediction
			0.0429	0.0147	0.0763	0.0114	27.6	11.8	Actual

6.2.6 Root/Tip Twist, Span-wise Twist and Camber Profile, and Dihedral Optimization

This section presents the final optimization study for delta wing sonic boom mitigation with preserved wing volume and lift. As the last step, wing twist is included with angle of attack, dihedral, and camber optimization. In section 6.2.4 the analysis show the required tip twist is about 7° to match the target lift. This is considered to be impractical due to possible flutter and early stall of the wing tip during take-off and landing. Besides the structural and aerodynamic concerns, the optimums found with such high wing tip twist are very poor designs in terms of sonic boom reduction and drag. To avoid the high tip twist for matching the target lift, the root chord should also originate at some angle of attack. In this section the wing angle of attack which is the angle of attack of the root chord at the same time is referred to as the root twist, and is denoted by the symbol α_R. In addition to the root twist, the span-wise twist profile is changed from a simple linear distribution to an adjustable (new factor) non-linear profile which can control how soon the root twist changes to tip twist. For example, it may be desirable to start with a low root twist and quickly increase the twist along the span and asymptote towards the tip twist. In that way, a larger portion of the wing will be at the high twist setting, reducing the value of tip twist required to match the target lift. The span-wise twist profile is formulated as

$$\alpha(y) = (\alpha_T - \alpha_R)\left(\frac{y}{b}\right)^{N_\alpha} + \alpha_R \tag{93}$$

where b is the span of the delta wing. In this case it is equal to tan(30°)L = 0.5774L. The quantity y/b is zero at the root and 1 at the tip. This makes $\alpha(y = 0) = \alpha_R$ and $\alpha(y = b) = \alpha_T$. The variable N_α controls the non-linearity where $N_\alpha = 1$ gives a linear change, $N_\alpha < 1$ accelerates the change, and $N_\alpha > 1$ delays the change from root twist to tip twist. This is displayed in Figure 54. This particular twist profile formulation is inspired by the meridian profile used in the axisymmetric geometry optimization study of Hague and Jones [15]. The advantage of this formulation is that the span-wise twist variation is smooth, and controlled with only one parameter, N_α. The more obvious brute force approach would be to select several sections along the span and include their local angles of attack as new factors in the optimization. This would seriously complicate the optimization process as additional design factors will exponentially increase the required number of runs.

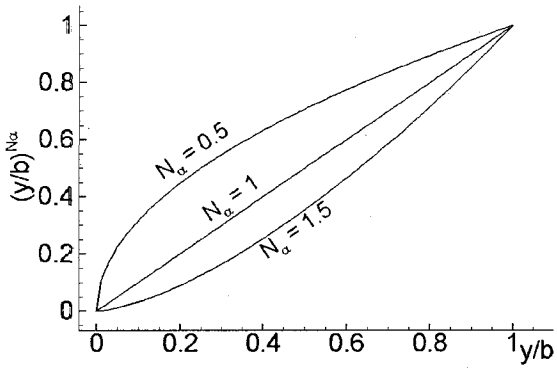

Figure 54: Plot of the exponential term in span-wise twist profile expression, Eq. (93).

Section 6.2.4 concludes that camber should also vary along the span due to changing local angle of attack when the wing is twisted. This is because the optimum camber giving the minimum impulse changes with angle of attack. Clearly the span-wise camber profile must be optimized to match the local angle of attack along the span when the wing is twisted. Trying to optimize camber at several sections along the span is not a very practical approach since many sections would require optimization in order to have a smooth camber profile that helps the entire wing, not just those sections being optimized. An alternative shortcut method is devised here, where a model equation for the optimum camber giving minimum impulse is generated in terms of angle of attack and dihedral. In that way the optimum camber for minimum impulse is readily known for any combination of angle of attack and dihedral. This model equation is then used during the CAD generation process where the span-wise camber profile is automatically set in terms of the span-wise twist profile and dihedral angle. Not only does this make the whole span-wise camber optimization much simpler and robust, it also takes camber out of the design matrix as one of the design factors. The only catch is that a rich set of runs are needed initially in order to provide adequate data to create the optimum camber model. The dihedral angles of interest are 15° and 20°, and the maximum twist at any section should stay below 5°. Cases are run for $\theta_D = 0, 10, 20, 30$ and $0 \leq \alpha \leq 5$ with at least 3 levels of camber for each α - θ_D combination. The optimum camber found at each α - θ_D setting is listed in Table 35. The quadratic model equation fitted to these data is given in Eq. (94). The data points and the model are shown in Figure 55. The grid lines at $\theta_D = 0, 10, 20, 30$ are highlighted to help assess the model fit accuracy. The model has $R^2_{Adj.} > 0.99$. The optimum camber decreases with increasing angle of attack and shows a weak quadratic behavior with dihedral.

Table 35: Optimum camber giving minimum impulse at various α - θ_D combinations.

θ_D	α	$\ell_{C,Opt.}$	θ_D	α	$\ell_{C,Opt.}$	θ_D	α	$\ell_{C,Opt.}$	θ_D	α	$\ell_{C,Opt.}$
0	0	2.3176	10	0	2.2947	20	0	2.3192	30	0	2.3936
0	1	1.8703	10	1	1.677	20	1	1.6932	30	1	1.8416
0	2	1.4235	10	2	1.1466	20	2	1.2058	30	2	1.3151
0	2.5	1.2003	10	2.5	0.8481	20	2.5	0.9156	30	2.5	1.0365
0	3	0.9772	10	3	0.5474	20	3	0.6232	30	3	0.7558
0	4	0.5314	10	4	0.30885	20	4	0.2349	30	4	0.1847
0	5	0.0861	10	5	-0.099	20	5	-0.2781	30	5	-0.129

$$\ell_{C,Opt.}(\gamma) = 2.390 - 0.0234\theta_D - 0.544\alpha(\gamma) - 2.526 \cdot 10^{-3}\theta_D\alpha(\gamma) + 8.454 \cdot 10^{-4}\theta_D^2 + 0.0186\alpha(\gamma)^2 \quad (94)$$

With dihedral preset and the camber profile given by the model in Eq. (94), the only factors involved in the optimization are root twist α_R, tip twist α_T, and twist profile power N_α. Global design space limits for this section are set as $0.5 \leq \alpha_R \leq 4$, $0 \leq \alpha_T \leq 5$, and $0.25 \leq N_\alpha \leq 1.25$. The optimization search algorithm is started by analyzing smaller sub-spaces (zones) in this range. The objective of matching the lift to the target benchmark value is exploited here to set the direction of the design space exploration route. Using the lift model on a 3D block domain with dimensions equal to the current zone limits, iso-surfaces of $C_L = 0.0765$ are plotted in Tecplot. One of the objectives is completed in this manner. Next, the impulse response is computed on this iso-surface and the minimum impulse location is sought either graphically or by searching for the 3D grid point with minimum impulse on this surface. If there is no impulse minima (stationary point) located on the iso-surface, the analysis is continued on an adjacent zone following the $C_L = 0.0765$ iso-surface direction. In this way the entire global design space need not be tested and the analysis progresses while satisfying the lift requirement at all times. A total of 11 zones are investigated for the 20° dihedral case, using a total of 130 runs. The zones are placed such that they overlap and share several data points. This way a smooth continuous iso-surface is created through all zones, and 50% savings in total number of runs is achieved by economically making use of runs from a previous zone. The design factor bounds for the 11 zones are listed in Table 36, and $C_L = 0.0765$ iso-surfaces found in these zones are plotted in Figure 56. Both impulse and lift responses are modeled as full-quadratic on all zones. The plot on the left in Figure 56 shows the numbers of the zones as labels attached at their lower left corners. The boundaries of the iso-surfaces are displayed to indicate the overlapping regions. Zones 1 through 9 cover 1° root twist and 2° tip twist intervals, whereas the last two zones cover

smaller volumes. The plot on the right of the figure shows the shaded iso-surface at a different angle to display the warping of this surface as N_α changes. Optimization for 15° is done similarly using the same zones since 5° dihedral variation has only a small effect on lift. The global optimum inside the entire design space is found in zone 11, and a close local optimum is found in zone 8. The optimums for both dihedral angles are listed in Table 37. Contours in Figure 56 shows that the impulse is decreasing in the increasing root twist direction. This is a very interesting discovery since with higher root twist a stronger under-track signal is expected. Moreover, the tip twist is less than root twist for the optimal locations, meaning that the twist is actually negative. This is great since it complies with the conventional intent of twist on wings which is to delay the tip stall at high angles of attack. Negative twist alleviates the concerns on flutter and bending due to intense tip loads as well. The optimums found with this combined optimization study are gratifying on all counts including aerodynamics, structural feasibility, and sonic boom mitigation. Optimums found here with non-linear span-wise twist and camber profile are much better than the optimums found in the linear twist analysis in Section 6.2.4. This is mainly because the camber now matches the local angle of attack everywhere along the span to give minimum impulse. The addition of non-linear twist and camber profile improves the impulse reduction by 3% for 15° dihedral and by 1.5% for 20° dihedral compared to the angle of attack – dihedral – camber optimums found in the previous section, with no increase in drag penalty.

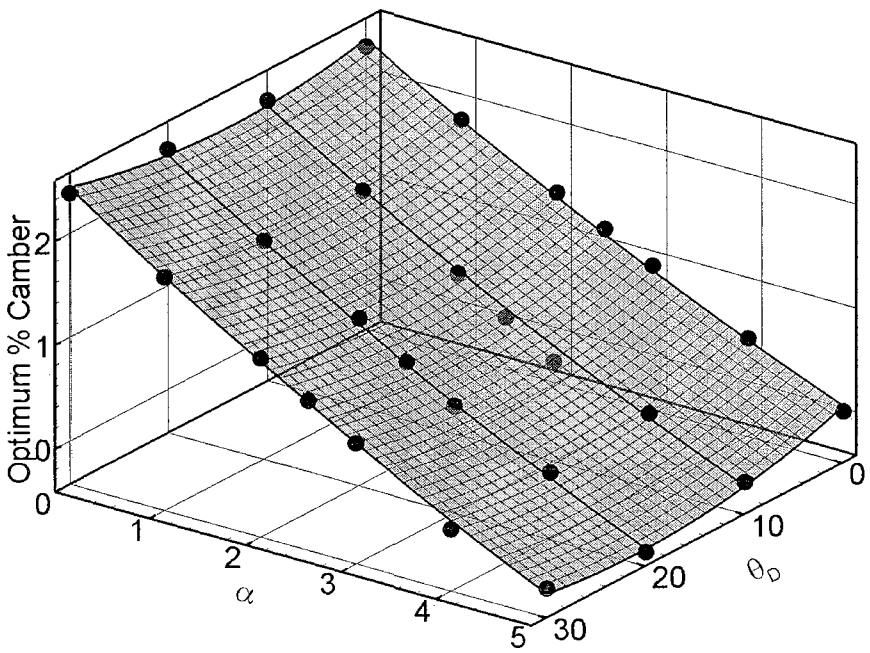

Figure 55: Optimum camber data points from Table 35 and the fitted model surface, Eq. (94).

Table 36: Factor limits for root/tip twist, twist and camber span-wise profile optimization at 20° dihedral.

Zone	α_R low	α_R high	α_T low	α_T high	N_α low	N_α high	Design	Runs
1	0.5	1.5	3	5	0.25	0.75	FCD	15
2	1.5	2.5	2	4	0.25	0.75	FCD	15
3	1.5	2.5	2	4	0.75	1.25	FCD	15
4	2	3	1	3	0.25	0.75	full 3^3	27
5	2	3	1	3	0.5	1	full 3^3	27
6	2	3	1	3	0.75	1.25	full 3^3	27
7	2.5	3.5	1	3	0.25	0.75	full 3^3	27
8	2.5	3.5	1	3	0.5	1	full 3^3	27
9	2.5	3.5	1	3	0.75	1.25	full 3^3	27
10	3	3.5	1.75	2.25	0.25	0.5	full 3^3	27
11	3.25	3.75	1.5	2	0.25	0.5	full 3^3	27

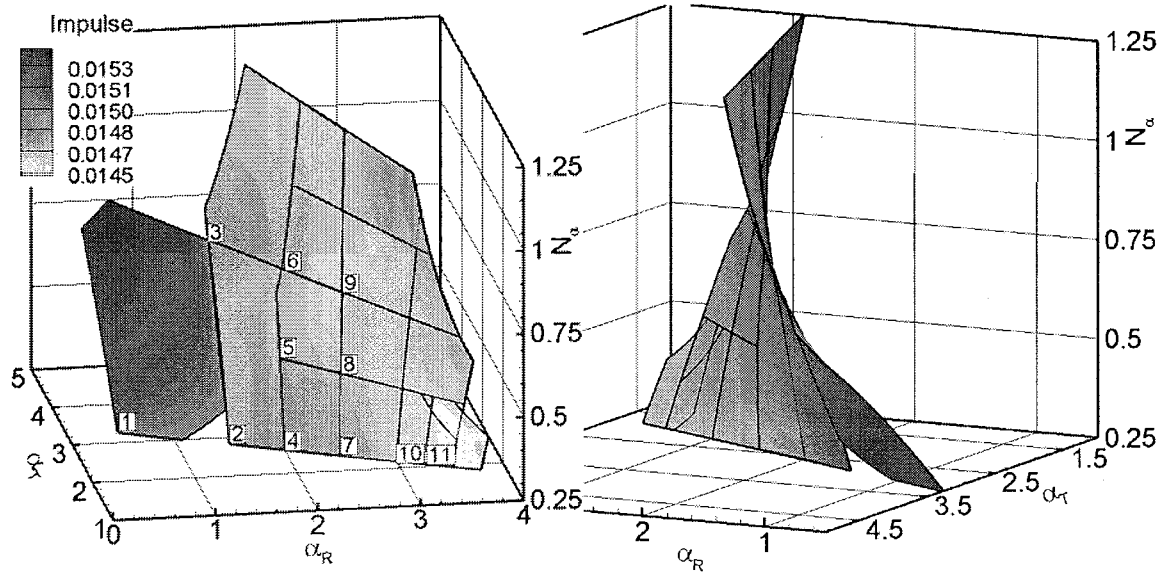

Figure 56: $C_L = 0.0765$ iso-surfaces on 11 zones tested for root/tip twist, twist and camber span-wise profile optimization at 20° dihedral.

Table 37: Root/tip twist, span-wise twist and camber profile predicted and actual computed optimums.

θ_D	α_R	α_T	N_α	Peak $\Delta p/p_\infty$ x/L=3.5	$\ell_{x/L=3.5}$	C_L	C_D	-%$\Delta\ell$	%ΔC_D	
15	2.736	1.779	.7075		0.0152	0.0765				Prediction
				0.0469	0.0148	0.0769	0.0114	27.1	11.8	Actual
15	3.778	1.721	0.25		0.0150	0.765				Prediction
				0.0454	0.0150	0.0764	0.0113	26.1	10.8	Actual
20	2.844	1.854	.6931		0.0146	0.0765				Prediction
				0.0434	0.0146	0.0765	0.0114	28.1	11.8	Actual
20	3.341	1.751	.4078		0.0145	0.0765				Prediction
				0.0441	0.0144	0.0765	0.0114	29.1	11.8	Actual

6.2.7 Concluding Remarks on Delta Wing Parametric Optimization

Figure 57 displays the pressure signals at x/L = 3.5 from the optimums of angle of attack – camber, angle of attack – dihedral, angle of attack – camber – dihedral, and finally root/tip twist, non-linear span-wise twist and camber profile at 20° dihedral. The camber and dihedral do not have a strong influence on the signal when they are applied alone, however, their combined effect is significant. Addition of lateral redistribution with wing twist (4th signal) does not change the signal shape much compared to angle of attack – camber – dihedral (3rd signal) optimum. Addition of camber significantly weakens the trailing shock. The mitigation of the mid-field signal at x/L = 3.5 is clear in these plots. Figure 58 shows the pressure signals from the optimum and benchmark delta wings at r/L = 600. Signal propagation is through a uniform atmosphere. The optimized signal belongs to the final configuration listed in Table 37 having a 29.1% reduction in the impulse at x/L = 3.5. The trailing shock of the optimum geometry is much weaker than the leading shock. The leading shock strength is $\Delta p/p_\infty = 0.001076$, and the impulse is 0.001503. These numbers correspond to 27.1% decrease in peak Δp, and 41.29% decrease in the pressure impulse compared to the original delta wing. As predicted by the linear theory (Eqs. 2.8 and 2.9), the percentage decrease in the far-field leading shock strength is about the same as the percentage decrease in the mid-field pressure impulse. Hence the decision to use the mid-field pressure impulse for ground level sonic boom minimization is justified.

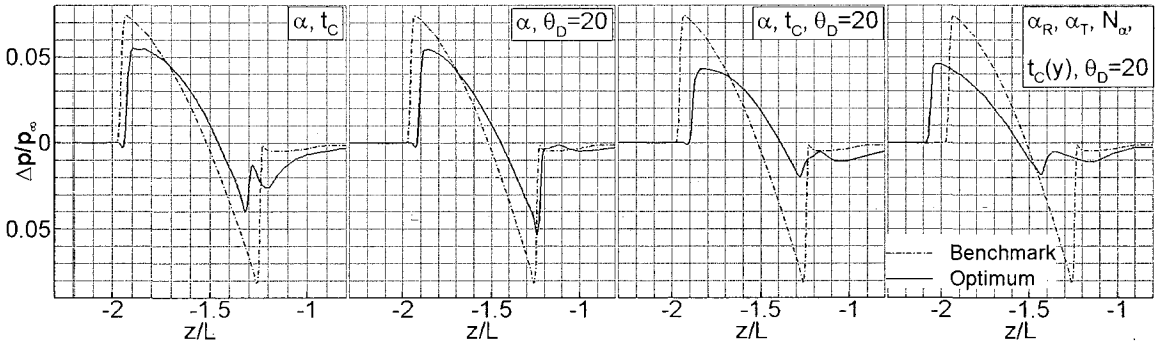

Figure 57: Comparison of pressure signals at x/L = 3.5 (vertical cut) from optimized delta wings and the benchmark wing. Mach 2.0, $C_L = 0.0765$.

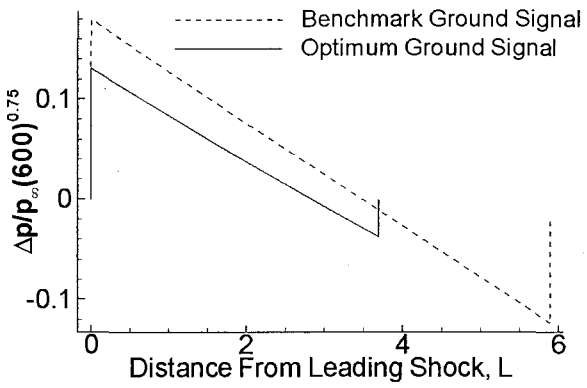

Figure 58: Pressure signal comparison at r/L = 600 (ground level) for the optimum delta wing with twist and 20° dihedral, and the benchmark wing.

The sequential analysis and optimization approach where design factors are first analyzed in pairs allows one to clearly understand and appreciate the effects of each parameter alone on the lift and sonic boom impulse responses. The latter part of the optimization study with root twist, tip twist, non-linear twist profile, non-linear camber profile optimized for local angle of attack, etc., is setup in light of the findings of the 2-factor analyses. The key findings in these analyses are:

- Dihedral does not provide a global optimum. Increasing dihedral decreases sonic boom impulse in the test region covered, up to 60° dihedral. Loss in lift can always be matched with increase in angle of attack. Therefore the dihedral factor should be used as a preset constant.
- Impulse varies in a strongly quadratic manner with camber. There is an optimum camber for minimum impulse, but its value varies with angle of attack. Linear twist cases show that incorrect camber variation along the span with local angle of attack severely increases the under-track sonic boom impulse. Therefore camber needs to vary along the span when the wing has twist.
- A linearly varying positive twist span-wise profile does not help reduce sonic boom, and increases drag considerably. Root twist should be included as a factor, and non-linear span-wise twist profiles should be considered.
- Negative twist variation where tip twist is less than root twist should be considered.

In light of these findings, dihedral is removed as a variable in the optimization, and a non-linear span-wise twist profile is formulated based on a single parameter as design factor, while the span-wise camber is tied to local angle of attack by a model equation that gives the optimum camber for minimum pressure impulse as a function of angle of attack. Doing so, a 3D wing geometry with very complex and non-linear axial and span-wise geometric features is optimized using ultimately only 3 design factors. If all the factors were to be considered at the same time with no prior insight, the number of design factors would be much higher. Considering the span-wise distributions, camber and twist would have to be modified on at least 3 sections along the span to get a non-linear span-wise profile for both. This would mean at least four more design factors (three for camber, one for the additional twist on the third section). Including dihedral, this would be at least 7 factors to optimize. Considering that a full three-level experimental design matrix would need $3^7 = 2187$ runs, an 11-zone RSM analysis and search, as demonstrated in the previous section, would require more than 20,000 runs! In short, the 2-factor analyses in the beginning of the study saved considerable time and resources in approaching the optimum design.

Redistributing the lift towards the tip along the span does not necessarily reduce the under-track sonic boom impulse on the $y = 0$ symmetry plane. For the particular wing geometry investigated in this section, negative twist which draws the lift closer to the symmetry plane decreases the sonic boom on the symmetry plane. This is a surprising result from the analysis which is counter intuitive. Actually twist not only changes the lateral distribution of lift, but the axial distribution as well due to the triangular wing planform. When lift is distributed towards the tip, it is distributed downstream on the axial coordinate as well, since span-wise section aerodynamic centers move towards $x = L$ as $y \rightarrow b$. On a rectangular wing, twist would not alter the axial lift distribution. Since low-boom supersonic aircraft designs employ delta wings or swept wings in general, a generalization can be made by saying that lateral distribution of the lift towards the wing tips is not beneficial for sonic boom mitigation. Lateral distribution of lift towards the centerline however is found to be beneficial in the current study, as it mediates the axial lift distribution. Similar to cross-sectional area distribution, axial lift distribution is of first order importance to sonic boom generation. This means that the sonic boom signal is more sensitive to changes in the axial lift distribution than to those in the lateral distribution. These two effects cannot be uncoupled using a swept or delta wing.

RSM model predictions and actual data points match exceptionally well in general for both lift and impulse responses. Lift response is relatively simpler to calculate given that the flow is inviscid, and does not require significant grid manipulation. Computation of shock waves to

the downstream end of the body should provide accurate lift computations reliably. Computing sonic boom impulse of a 3D lifting wing at x/L = 3.5 however requires significant grid adaptation and shock fitting. The exceptional accuracy and predictive capability of the RSM models show that the CFD tools and methods used in getting the impulse response are highly accurate and reliable. There is no noise in the data provided to the least-square fitting routine. Noise could occur due to random grid problems, dissipated shocks, inappropriate solver settings, convergence issues, etc. The unstructured grid adaptation methodology for sonic boom prediction pays off quite well in this case.

6.3 SSBD Optimization

In this section the original SSBD aircraft is equipped with an optimized axisymmetric nose geometry, and its wing is replaced with a delta wing optimized for sonic boom mitigation. While the optimum axisymmetric nose shapes found in Section 6.2 can be used directly on the aircraft, the optimum delta wing found in Section 6.3 cannot. To replace the original wing of the SSBD, the new wing needs to have about the same volume, center of gravity, and aerodynamic center. The delta wing optimized in the previous section does not adhere to these additional constraints. Moreover, the flight Mach number and the lift requirement are different for the SSBD case, and there are significant interference effects on lift caused by the existence of the fuselage. Therefore wing parameter optimization for matching target lift needs to be carried out while the wing is attached to the aircraft. In short, a new (shorter) optimization study is carried out for the SSBD wing modification for sonic boom mitigation.

This section is laid out in four parts. First, a replacement baseline delta wing is designed to fit the SSBD, having exactly the same volume, root thickness ratio, and aerodynamic center as the original wing. Next, this baseline wing is optimized for sonic boom minimization while it is attached to the SSBD to make sure lift interference is included while matching the target lift of the aircraft. Third, the optimum nose shapes found in Section 6.1, one with the minimum ground peak Δp and the other with minimum ground impulse are attached to the SSBD with the original wing. Both optimized nose shapes are tested since at this point it is not obvious how the shock system will be modified and which of the two will actually give the minimum ground level bow shock strength when attached to the SSBD. Finally, the optimum nose shape chosen in the previous step is attached to the SSBD with the optimized delta wing, and the current work is

concluded. The following information should be noted as a reminder. The SSBD aircraft original length is 50 ft., flight altitude is 32,140 ft., flight speed is Mach 1.414, angle of attack is 1.922°, the nominal pressure at flight altitude is 589.23 psf, and the ground pressure at 2,372 ft asl is 1967 psf.

6.3.1 Baseline Delta Wing Design for the SSBD

The replacement delta wing for the SSBD needs to match the original wing characteristics in order to avoid significant changes in the aircraft weight, balance and trimming requirements. The new wing needs to have the same weight which is approximated here by setting the volume equal to the original wing volume. The center of gravity (CG) of the new wing needs to be close to the original, and the aerodynamic center (AC) should exactly match the original locations. Any small mismatch in the CG can virtually be accommodated by internal adjustments inside the fuselage, however, changes in AC would require aerodynamic trimming. Trimming can only be done with modifications on the elevators which will likely change the trailing shock signal and the drag force. In order not to get side-tracked with trim adjustments in the wing optimization for sonic boom mitigation, the wing AC is secured at its original location. The root chord length, root chord thickness ratio, and the mount location of the wing should match the original wing as well in order not to require any virtual adjustments on the internal structural frame and mount points of the fuselage.

Figure 59 shows the SSBD original wing. The wing is detached from the fuselage at y = 0.065L as shown in the figure, where the wing meets the inlet cowling. The cut is made planar to simplify delta wing CAD generation and fuselage integration processes. The wing alone, when separated from the fuselage at y = 0.065, is shown on the right of the figure. The leading edge extension (LEX) is also included in the parted wing. The parameters of the original wing with LEX are:

- root chord length, $C_R = 0.267L$ ($L = L_{SSBD}$),
- Maximum thickness-to-chord ratio at root, $t_C = 3.34\%$
- volume = $0.006\ C_R^3 = 0.000114\ L^3$
- incidence angle of the root chord with respect to SSBD centerline, $\alpha_i = -0.450°$

- wing angle of attack: $\alpha_w = 1.922° - 0.450° = 1.472°$
- Aerodynamic center axial location at $\alpha_w = 1.472°$, $AC_x = 0.751C_R$

To generate a delta wing with fixed root chord and maximum root thickness, the only parameter left to adjust the volume is the semi-vertex angle, β. The volume (and span) decreases with decreasing β. Setting $\beta = 38.95°$ gives the required volume of $0.006\ C_R^3$. This setting of β puts the leading edge well inside the Mach cone which has a 45° half-cone angle for Mach 1.414. To adjust AC_x, wing sweep is modified. A delta wing already has a leading edge sweep, which is equal to 90 - β. An additional sweep parameter that applies to the trailing edge is designated by λ. After the delta wing is created with a certain β, the entire wing is swept back (or forward) by λ to translate the aerodynamic center in the axial direction. While doing so, the span is kept the same so as not to change the volume. This is illustrated in Figure 60. The aerodynamic center of wings in supersonic flow is approximately at the 50% chord location. However, this information is not sufficient unless the y-coordinate of the aerodynamic center (AC_y) is known. Thus flow solutions at several λ's are needed to model the AC_x change with λ, and pinpoint the correct λ setting. Upon carrying out such tests, the required trailing edge sweep is found to be $\lambda = 15.24°$ to have $AC_x = 0.751\ C_R$. The delta wing α_w is kept equal to the original wing α_w while adjusting AC_x.

Next, the correct incidence angle for the new wing needs to be adjusted to produce the original lift of the SSBD aircraft. To do this, first the baseline delta wing is attached to the fuselage by placing the mid root chord point at x = 0.6L, y = 0.065L, and z = -0.014L. This is the same location where the mid root chord center of the original wing shown in Figure 59 is found. The incidence angle of the root chord is then adjusted by pivoting the new wing about this mount point. To achieve a water-tight connection with the fuselage, the portion of the original wing between the fuselage and the y = 0.065L plane is removed, and filled with surfaces created by extruding the root profile of the new wing in the –y direction. The incidence angle is tested starting from $\alpha_i = -1°$, and the correct setting producing $C_L = 0.0936$ is found to be $\alpha_i = -0.668°$ ($\alpha_w = 1.254°$). To be consistent, the same reference area is used in calculating lift for both the original and the new wing attached to the fuselage. Figure 61 compares the original and the baseline delta wing attached to the SSBD, showing top and bottom surface pressure distributions. The new wing has a larger planform, and lower pressure difference between the upper and lower surfaces. This in turn decreases the sonic boom impulse shed from the wing itself. The leading edge sweep of the new wing is considerably larger than the original wing, yielding a much

smaller drag coefficient. Furthermore, the original wing airfoil has a round leading edge whereas the delta wing has a sharp leading edge. This brings additional savings in the drag component. The overall inviscid C_D of SSBD with the original wing is 0.0370 whereas with the new baseline wing it is 0.0301. This is an 18.65% decrease in drag caused solely by a wing replacement. However, due to increased surface area the viscous drag component would be higher than the original value. This is not computed in the current study. The new wing is a "dedicated" supersonic wing that would perform poorly in subsonic flight due its sharp leading edge with high sweep.

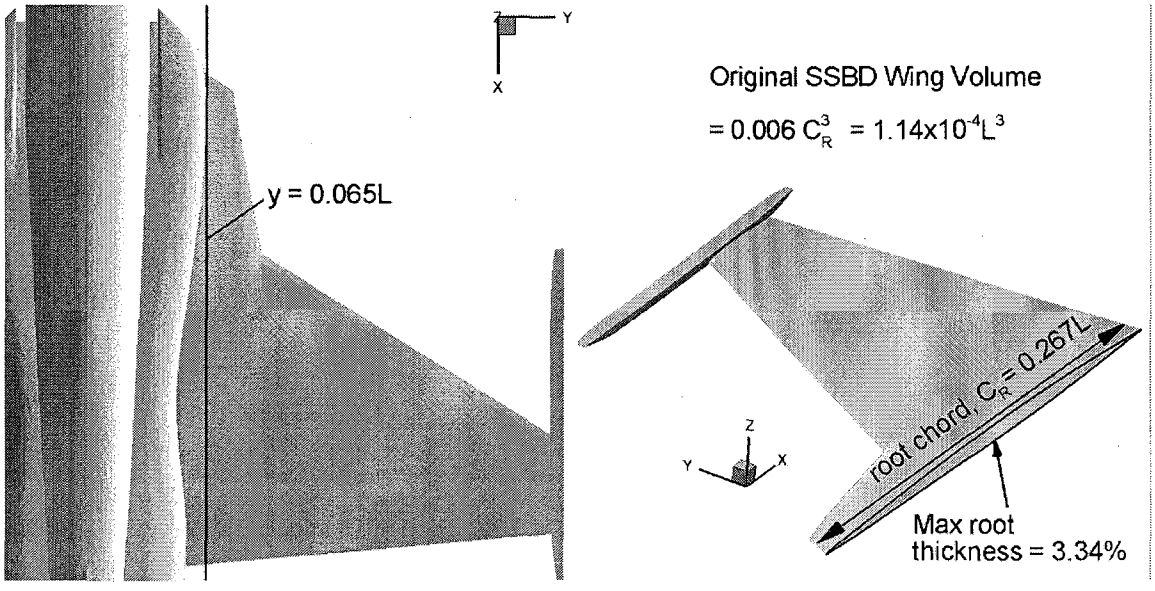

Figure 59: SSBD original wing parameters.

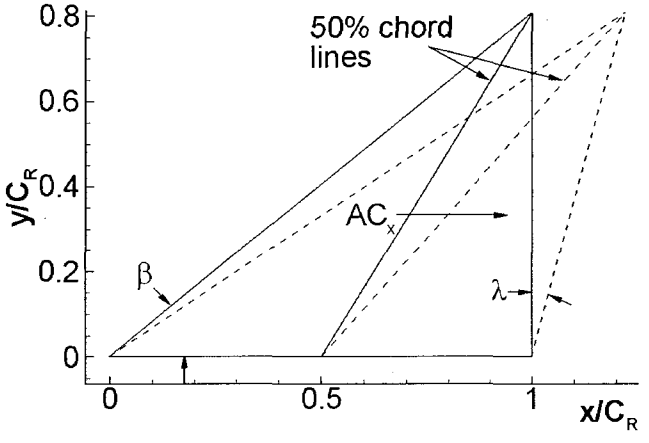

Figure 60: Trailing edge sweep λ effect on the aerodynamic center axial location.

The pressure signals on a vertical cut at x/L = 1.5 from SSBD with the original wing, SSBD fuselage only, and SSBD with the new baseline delta wing are given in Figure 62. This figure shows the effect of the wing on the near-field pressure signal. The signal distance of x/L = 1.5 is about 5.6 root-chord lengths for the wing, and is a decent mid-field range to observe the wing effect on the signal. Considering that the pressure impulse is computed as the integral of pressure above the $\Delta p = 0$ line, the difference of the original and the new baseline delta wing can be observed as the shaded areas under the solid and dashed curves, shown in the figure. The pressure impulse of the shaded area for the original wing is 60.45 psf·ft, and the for the baseline delta wing it is 23.71 psf·ft. This is a significant decrease already prior to carrying out an optimization study. The optimization of the baseline delta wing further decreases the sonic boom impulse due to the wing. The signal of the fuselage alone sets a virtual limit on the pressure signal shape obtainable if the wing impulse were to be minimized to zero. The following optimization study places the near-field signal between the dashed and dash-dotted curves in Figure 62.

Before concluding this section, a final word should be said on the interference lift caused by having a fuselage beside the wing. The lift coefficient for the wing alone and the fuselage alone are 0.0575 and -0.01176 respectively, while the combined lift is 0.0936. This means that the interference lift coefficient is 0.04786, which is almost half of the total lift. This is a significant contribution, thus for the optimization to match, the total lift should be predicted using a CAD model including the fuselage as well as the wing.

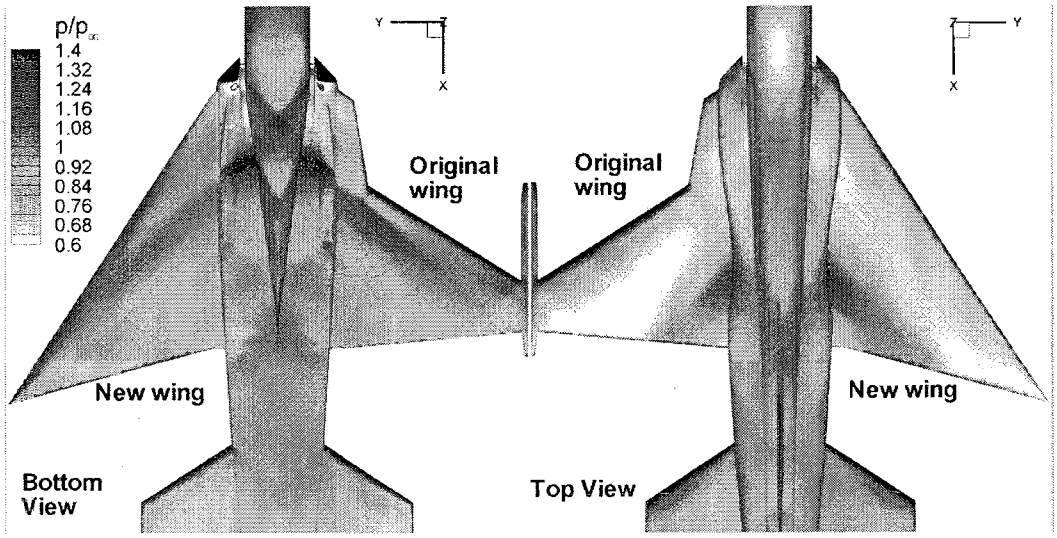

Figure 61: Planform and surface pressure comparison of the original and the baseline delta wing attached to the SSBD, at same overall lift.

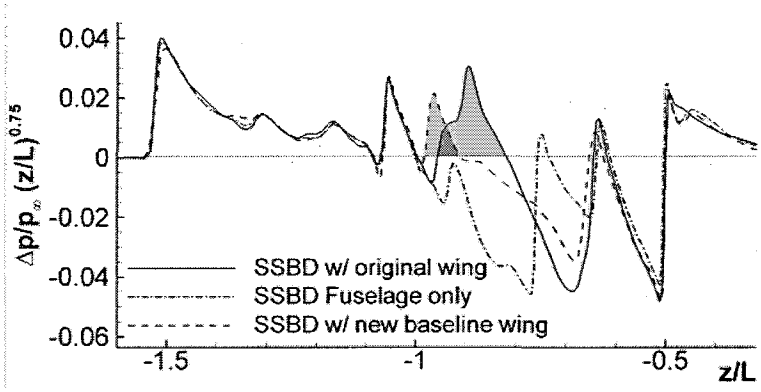

Figure 62: Pressure signals at x/L = 1.5 from the SSBD with original wing, fuselage only, and with new baseline delta wing.

6.3.2 SSBD Wing Optimization

In this section, the baseline delta wing for SSBD determined above is optimized to reduce its impulse, while maintaining the target lift. Similar to the delta wing optimization, the volume needs to be conserved so as not to require any changes in lift. There is no straight-forward way to calculate the weight of the wing as its volume changes unless the composition of the materials inside the wing is known. Since this work is primarily a demonstration of the sonic boom prediction tools in sonic boom mitigation studies, detailed internal structural design is omitted. By keeping the wing volume, total lift, wing mount point and the aerodynamic center the same as the original aircraft, uncertainties related to these parameters are avoided.

During the optimization process, the lift response needs to be computed while the wing is attached to the fuselage to account for the interference lift. However, the wing pressure impulse response is not easily identified on the pressure signal of the entire aircraft. The impulse specific to the wing is easily picked out if the wing is analyzed alone. Doing both at the same time is at first challenging, but a short-cut is found in the current work. First, optimization is limited to angle of attack – dihedral – camber combination only since addition of twist is found to improve the sonic boom mitigation only slightly (1.5%) in Section 6.3.6. Next, the optimum camber giving minimum impulse is modeled by testing the wing alone at various dihedral and angle of attack settings, as done similarly in Section 6.3.6. Provided that the wing CAD is created with the proper camber found through this model for any angle of attack setting, the only thing left to do is to find the correct incidence angle to give the target lift at preset dihedral angles. To create the optimum camber for the minimum impulse model, camber is tested at 5 levels at

combinations of $\theta_D = 0°, 20°$ and $\alpha_w = 0.5°, 0.75°, 1.0°, 1.5°, 2.0°$. The optimum camber settings found for each combination is tabulated in Table 38. The response model fit to this data is given in Eq. (95). Next, the delta wing is attached to the fuselage and the flow around the whole aircraft is computed for various dihedral and wing incidence angles. The camber is set automatically depending on the wing angle of attack and dihedral utilizing Eq. (95) during CAD generation. The configuration is tested at $\theta_D = 0°, 15°$, and $20°$ for $\alpha_i = -1.3°, -1.2°, -1.1°$, and $-1°$. The incidence angle is kept lower than the baseline value of -0.668 for this delta wing replacement since camber notably increases lift. The results for the dihedral and incidence angle tests are shown in Figure 63. The lift and drag responses are linear with the incidence angle at all dihedral settings. The results show that overall lift increases and drag decreases with increasing dihedral in the SSBD case with the new delta wing. This is exactly the opposite of the findings in the delta wing alone optimization in Section 6.3. This unanticipated reversal of the behavior of both responses can only be explained as a favorable interference effect of the fuselage and the wing. The supersonic area shaping applied on the F5 fuselage seems to be responsible for this favorable interference effect, as tests conducted using a straight cone-cylinder-cone fuselage with the same wing (not included in the text) did not produce the same favorable effect when dihedral was increased. This interference effect is not investigated any further and taken for granted in the current study. The increase of lift with dihedral allows the wing angle of attack to be reduced, which in turn decreases the wing impulse significantly, in addition to the reduction obtained by the dihedral itself. A similar result is true for the drag force where increased dihedral and decreased wing angle of attack separately decrease the wing drag. The optimum wing incidence angles found for $\theta_D = 0°, 15°$, and $20°$ are listed in Table 39. The pressure signals at $x/L = 1.5$ from the SSBD with the baseline delta wing and optimized delta wings at these dihedral angles are shown in Figure 64. The regions labeled "a", "b", and "c" in this figure are the parts in the signal that change after the optimization. Camber further decreases the peak pressure caused by the wing in part "a", and flattens the signal in part "c". These are both favorable changes for a quieter sonic boom signal. Dihedral only affects region "b" where it also flattens the signal. The signal at $x/L = 1.5$ is not far enough to place a clear judgment on how the optimized wings affect the far-field signal. Therefore the far-field signal is computed using FPM3D for mid-field and Thomas Waveform Parameter Method for far-field. Figure 65 shows the comparison of predicted ground signals with the new wing (left), and comparison of experimental and computational signals of the original SSBD with the predicted signal of SSBD with the optimized delta wing at $\theta_D = 20°$ (right). For the cases with the new wing, mid-field full-potential propagation is carried out down to $r/L = 50$, and then switched to linear propagation for ground signal prediction.

Comparing the solid and dashed curves in the plot on the left in Figure 65 shows that camber addition decreases the pressure impulse as well as the foot print size. Addition of dihedral reduces further small intermediate shock and decreases the impulse slightly. The ground signals for the 15° and 20° dihedral are practically the same. Foot print size remains about the same with changing dihedral. Comparing the computational signals only on the right plot shows that the new wing optimized at $\theta_D = 20°$ has a significantly lower impulse, foot print size, and peak Δp compared to the original wing. The bow shock of the SSBD is the same in both cases since the modifications in the wing impulse do not reach the upstream bow shock. Decrease of the foot print size is a favorable change since the frequency of the wave increases. Low frequency sonic boom signals have a greater impact on structures. The experimental results for the original SSBD is included in the plot only for reference purposes. Quantitative comparison of the impulse, pressure levels, and the foot print size is among the computational results only, since the original SSBD computational signal is a proper reference point to judge any other computational signal. Ground level signal quantitative comparison between the original and modified SSBD is given in Table 40. The new wing provides a 14.8% reduction in peak ground Δp, and a 22.5% reduction in ground impulse. These values are on the same order as the original peak Δp reduction (25%) achieved by Northrop Grumman by transforming the F-5E into SSBD. The current reduction of the sonic boom signal comes with no loss in lift or aircraft volume, and a substantial 21.6% decrease in drag. The drag decrease is caused by the sharp and highly swept leading edge of the new wing that is now inside the Mach cone. Due to the increase in surface area of the wing, the viscous drag will definitely increase. This drag component is not computed in the current analysis.

Table 38: Optimum camber giving minimum impulse at various α_w - θ_D combinations.

θ_D	α_w	$\ell_{C,Opt.}$	θ_D	α	$\ell_{C,Opt.}$
0	0.5	0.9783	20	0.5	0.9785
0	0.75	0.8564	20	0.75	0.8569
0	1	0.8125	20	1	0.8127
0	1.5	0.6955	20	1.5	0.5180
0	2	0.2323	20	2	0.1255

$$\ell_{C,Opt.} = 0.8736 + 7.492 \cdot 10^{-3}\theta_D + 0.2606\alpha_w - 1.363 \cdot 10^{-2}\theta_D\alpha_w - 0.2842\alpha_w^2 + 3.313 \cdot 10^{-3}\alpha_w^2\theta_D \quad (95)$$

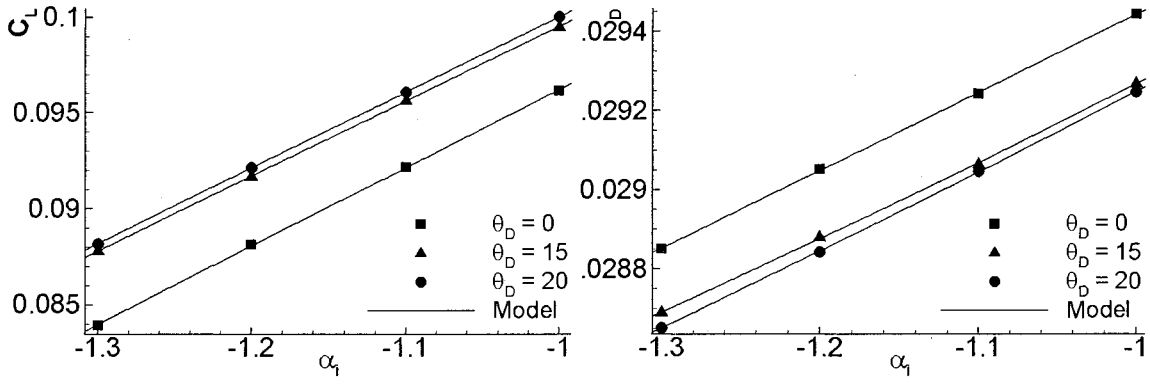

Figure 63: Changes in overall lift and drag of SSBD with the dihedral and incidence angles of the new wing.

Table 39: Optimum wing dihedral, incidence and camber settings for the new wing on SSBD.

θ_D	α_i	f_C	C_L	C_D
0	-1.064	0.8880	0.0937	0.0293
15	-1.151	0.8899	0.0937	0.0290
20	-1.163	0.8885	0.0938	0.0289

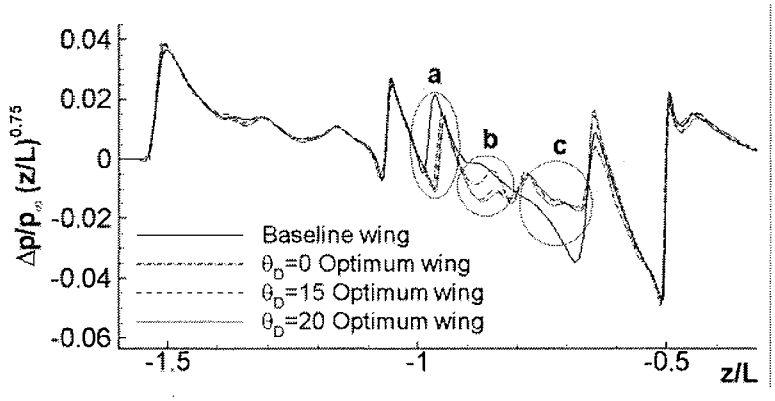

Figure 64: Pressure signals at x/L = 1.5 from the SSBD with new baseline delta wing and $\alpha_i - t_C$ optimized wings at various dihedral angles.

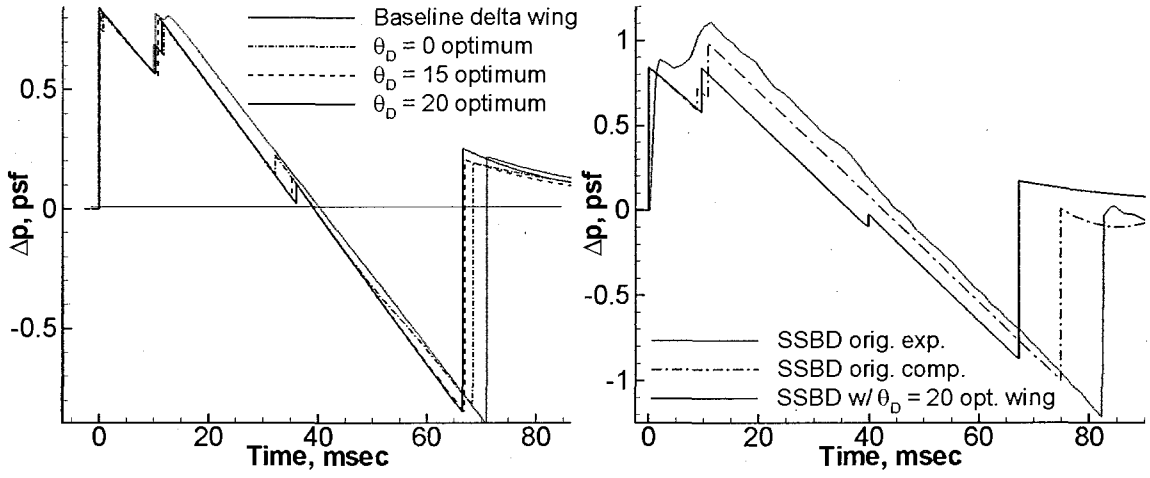

Figure 65: Pressure signals at ground level (2372 ft asl, r/L = 595.36) for the SSBD with original wing (experimental and computational) and optimized delta wings (computational).

Table 40: Comparison of drag and ground level pressure signal parameters for SSBD with original and the optimized wing.

	SSBD with original wing	SSBD with optimum delta wing at $\theta_D = 20°$	Percent decrease
Peak Δp, psf	0.988	0.842	14.8%
Impulse, psf·msec	23.34	18.10	22.5%
Foot print, msec	74.8	67.1	10.3%
C_D (inviscid)	0.0370	0.0289	21.6%

6.3.3 SSBD with Optimized Nose Attachment

In this section, the 5-ramp optimum axisymmetric nose shapes for minimum ground pressure impulse and minimum ground peak Δp, found in Section 6.2, are attached to the SSBD with the original wing. The benchmark conical nose is also tested to place a fair judgment on the optimization efforts of Section 6.2. The nose attachments are placed at the tip of the aircraft at the x = 0 station, with a negative 1.922° inclination to the aircraft centerline. By doing so the nose attachments, which are optimized for axisymmetric flow, are placed parallel to the flow path while the rest of the aircraft is still at the original angle of attack. The nose attachments are $0.2L_{SSBD}$ long and have base radii equal to $0.025L_{SSBD}$. To create a non-intrusive water-tight connection between the base of the nose attachment and the original fore-body of the aircraft, the base perimeter of the nose attachment is extruded in the axial direction (parallel to the flow)

creating a cylindrical fairing. SSBD with the optimized nose attachment (for minimum pressure impulse) is shown in Figure 66 using various view angles. The z-axis position of the nose attachment is carefully set to minimize the jump in the slope of the lower airframe contour where the fairing and the fore-body intersect. Doing so avoids a high compression corner on the lower surface which can generate a strong shock and high drag. Since the axisymmetric nose attachment is placed parallel to the flight path, it will not create any lift force or induce a moment. However, the fairing changes the fore-body profile and will alter the lift and moment slightly. Moreover, the nose attachment adds an unknown amount of weight to the aircraft, which needs to be compensated with some increase in lift. Implications of the nose attachment on the lift and moment are ignored in the current section since there is no relevant data available to estimate the weight distribution of the added components.

Figure 67 shows the pressure signals at x/L = 1.5 and at ground level for the SSBD with the original nose, the conical nose used as benchmark in Section 6.2, and the 5-ramp nose shapes optimized for minimum ground impulse and minimum ground peak Δp. The length, L, used for non-dimensionalization is equal to the original SSBD length L_{SSBD} (50 ft.), and not equal to the new length increased by the nose attachment. In this way, the signal foot print sizes of the original and the modified SSBD are non-dimensionalized with the same value for direct comparison purposes. The near-field signatures show the upstream displacement of the bow shock due to the nose attachments. The original bow shock can be said to be divided into two main shocks, one due to the nose attachment (the new weaker bow shock) and the other due to the remainder of the original fore-body airframe aft of the cylindrical fairing (the shock at z/L = -1.4). The peak Δp upstream of z/L = -1.4 is the same for all nose attachment configurations. All signals can be considered to be identical downstream from z/L = -1.2. The computational signals at ground level are shown on the right in Figure 67, where a reflection factor of 1.9 is used. The mid-field marching with full-potential formulation is carried out down to 50 body lengths for the modified nose configurations. All ground signals have about the same peak Δp around 1 psf. The main difference is in the bow shock strengths. Without any optimization, addition of the benchmark conical nose already decreases the bow shock strength significantly (by 26.6%). As expected, the optimized nose geometries result in weaker bow shocks than that of the benchmark nose. The nose optimized for minimum peak Δp produces a weaker bow shock than the nose optimized for minimum impulse. This means that the original bow shocks coming off from these nose shapes are not much affected by the rest of the signal, and they present the same behavior as when they are computed alone as axisymmetric bodies in Section 6.2. In fact, a direct comparison of the ground signals in Figure 67 and Figure 44 shows that bow shock strengths are

about the same for the nose shapes when they are computed alone or attached to the SSBD. Obviously the new displaced bow shocks from the nose attachments do not coalesce with the rest of the signal and amplify. If the opposite was the case, the nose with larger impulse would have provided a larger contribution to the formation of the bow shock. The nose with the minimum impulse reduces the total impulse of the aircraft slightly compared to the minimum peak Δp nose, where the impulse reduction is insignificant compared to the bow shock strength reduction. A quantitative comparison of the four SSBD configurations is given in Table 41. The changes in responses with respect to the original SSBD are shown in parentheses as percentage values. The lift increases about 1% when the nose shape is attached. This can be explained as the result of the cambered geometry formation when the nose shape is inclined at a negative angle to the SSBD centerline. The increase in lift is favorable since the addition of the nose geometry increases the volume and weight of the aircraft. The lift is increased in the front of the aircraft which moves the aerodynamic center forward. Since the center of gravity is also moved forward with the nose attachment, the need to rebalance the aircraft may be minimal. Drag is reduced with the benchmark and minimum peak Δp noses and increased with the minimum impulse nose. Again this is comparable to the solutions where the nose shapes are analyzed alone. The benchmark nose has the lowest drag ($C_D = 0.0739$), the minimum impulse nose has the highest drag ($C_D = 0.116$), and the minimum peak Δp nose is in between these two ($C_D = 0.0865$). These values have been computed in Section 6.2 using the base area of the nose shape as the reference area for C_D computation. The reduction in the wave drag will most probably be undone by the increase in viscous drag due to increased surface area. The deviations in the total ground impulse are small compared to the changes in the bow shock strength. This is because the nose geometry is a small portion of the entire aircraft volume.

In conclusion, the "best" configuration is selected as the one with the minimum peak Δp nose which results in a 42.1% reduction in the bow shock strength. In the next section, the optimum wings found in the previous part are used on this configuration to bring down the ground level peak Δp which is currently around 1 psf.

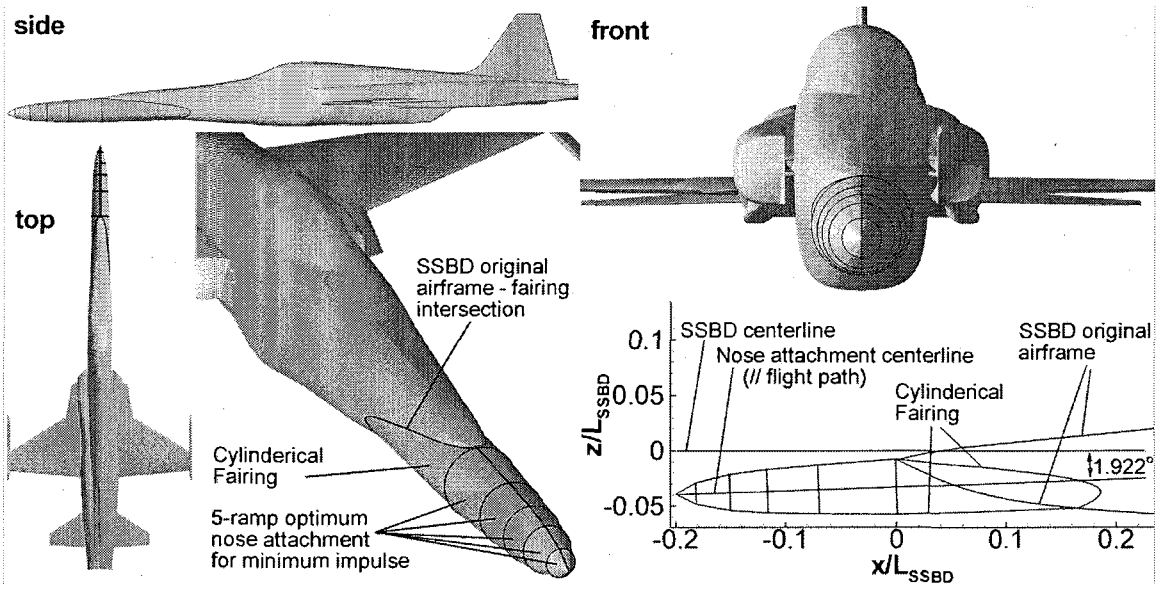

Figure 66: Axisymmetric nose attachment to SSBD.

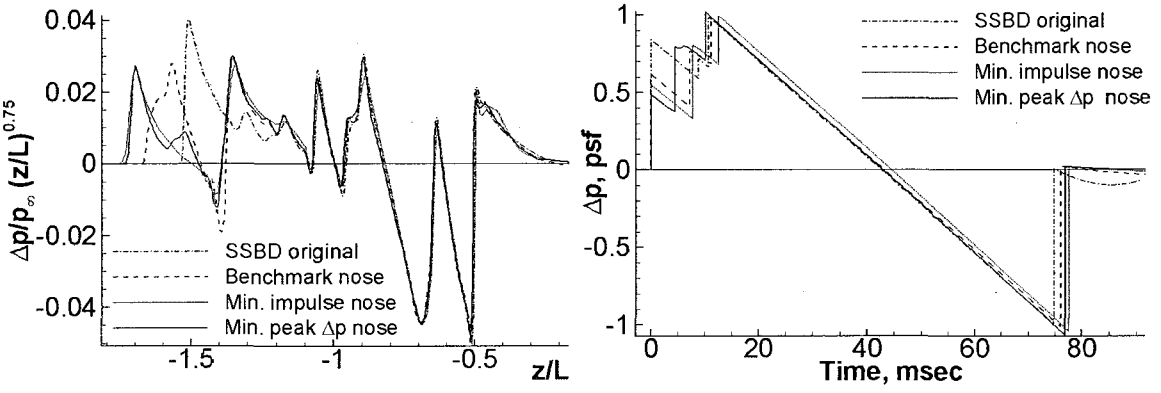

Figure 67: Computational pressure signatures at x/L = 1.5 (left), and at 2,372 ft asl –ground level (right) from the SSBD with original nose, benchmark conical, and 5-ramp optimum nose attachments.

Table 41: Lift, drag, volume, ground level bow shock strength and pressure impulse for the SSBD with original and modified noses.

	Original SSBD	Benchmark Nose	Min Impulse Nose	Min Δp Nose
C_L	0.0936	0.0947 (+1.2%)	0.0945 (+1.0%)	0.0944 (+1.0%)
Inviscid C_D	0.0370	0.0363 (-1.9%)	0.0375 (+1.4%)	0.0366 (-1.1%)
Volume, ft^3	683.2	683.2 + 36.4 (+5.3%)	683.2 + 50.0 (+7.3%)	683.2 + 46.0 (+6.7%)
Bow Shock, psf	0.836	0.614 (-26.6%)	0.544 (-34.9%)	0.484 (-42.1%)
Impulse, psf·msec	23.34	22.31 (-4.4%)	22.88 (-2.0%)	22.93 (-1.8%)

6.3.4 SSBD with Optimized Nose and Wing

In this final result sub-section, the optimum nose and the wing are applied simultaneously to the SSBD aircraft, for a combined reduction of sonic boom signal parameters at ground level. The optimum nose is chosen as the one giving the minimum peak Δp when modeled alone, which gives the minimum bow shock strength when attached to the SSBD. The wing chosen is the $\alpha - t_c$ optimum having $\theta_D = 20°$, which produces the minimum impulse in mid-field and in far-field, and reduces the peak Δp of the entire SSBD signal in the far-field. As Figure 65 shows, there is no difference in peak Δp at the ground between the 0° and 20° dihedral. The increased dihedral creates a small reduction in impulse only. If increased roll stability and Dutch-roll threat are of concern, $\theta_D = 0°$ is a better design, with its minor impulse penalty. In any case, the following results show the analysis carried out with the $\theta_D = 20°$ wing for maximum sonic boom reduction in general. The optimum configuration is shown in Figure 68.

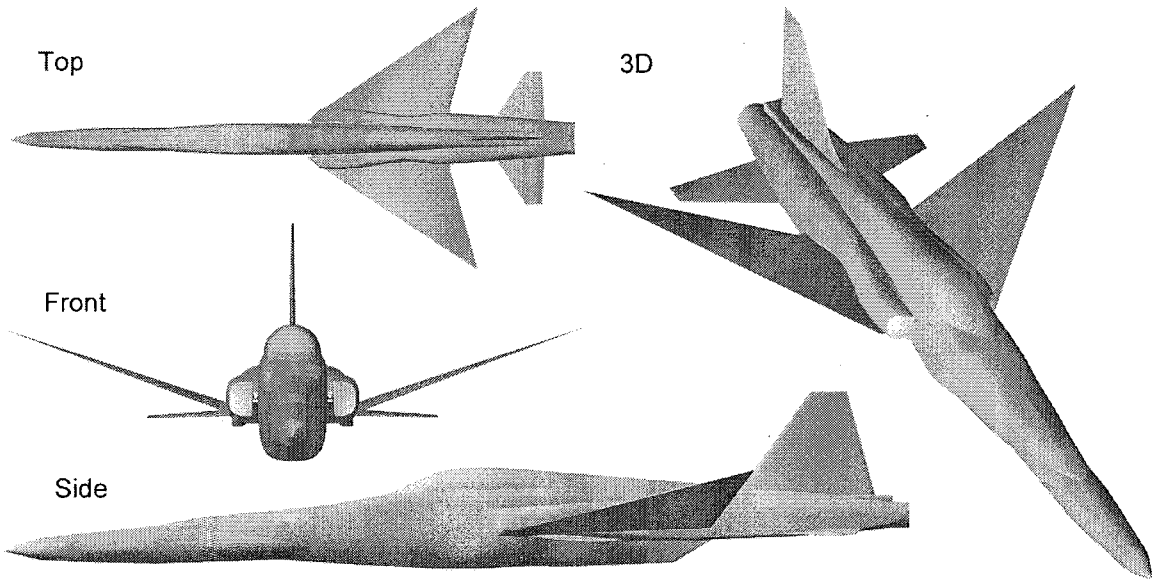

Figure 68: SSBD with minimum peak Δp nose attachment and minimum impulse wing at $\theta_D = 20°$.

The computed pressure signatures in the near-field and at ground level are shown in Figure 69 for the original SSBD, SSBD with optimum nose, and SSBD with optimum nose and wing. In the near-field plot, the optimum nose (dotted) and the optimum nose/wing (solid) curves overlap exactly, up to about z/L = -1. That is where the optimized wing starts being effective and

dramatically reduces the pressure disturbance between z/L = -1 and z/L = -0.65. The signals for the original SSBD and the optimum nose alone match exactly after about z/L = -1.15. The near-field plot displays distinctly the changes in the signal due to the addition of the nose attachment, and modification of the wing. The fact that signals match for the aircraft parts that are the same can be considered as a cross-validation of the CAD generation and flow solution through unstructured grid adaptation methodology, developed in this dissertation. The ground level signal plot shows the final product of the entire flow solution and optimization study carried out in the current work. The reductions in bow shock strength, peak pressure level, signal duration (foot print size), and the pressure impulse are obvious. The results are summarized in Table 42 for a quantitative comparison of the original and the optimized SSBD configurations. Compared to the original SSBD, the final optimum aircraft with the 5-ramp minimum peak Δp nose attachment and the angle of attack – camber optimized wing at 20° dihedral show 42% reduction in bow shock strength, 17% reduction in peak Δp, 22% reduction in pressure impulse, 10% reduction in foot print size, and 24% reduction in inviscid drag along with a slight increase in lift, volume, and weight (unknown small amount). The reduction in drag is mainly due to the high leading edge sweep of the new wing that is inside the Mach cone. The foot print size decrease (thus frequency increase) is also a direct effect of the wing optimization. Lower frequency waves are more destructive for structures, windows, etc.

Before finalizing this section, some direct results from the full-potential marching part of the sonic boom prediction process are given in Figure 70 for the final optimum aircraft. The figure shows the mid-field signal computed with the full-potential method at five different altitudes. The shocks are computed very sharp, clean, and free of oscillations which is the result of the automated shock fitted grid generation scheme embedded in the code. The pressure curve for r/L = 50 is input to the Thomas Waveform Parameter code as is to produce the ground signal shown with a solid line in Figure 69. The mid-field signal plot shows the upstream and downstream moving parts of the signal. The "dividing characteristic" that separates the leading and trailing parts of the signal (indicated as "y_0" in the linear theory, see. Eq. 2.9) is around 40 ft. from the bow shock for the range of altitude shown. Both the leading and the trailing shocks continue to move away from this dividing characteristic as the signal propagates towards the ground.

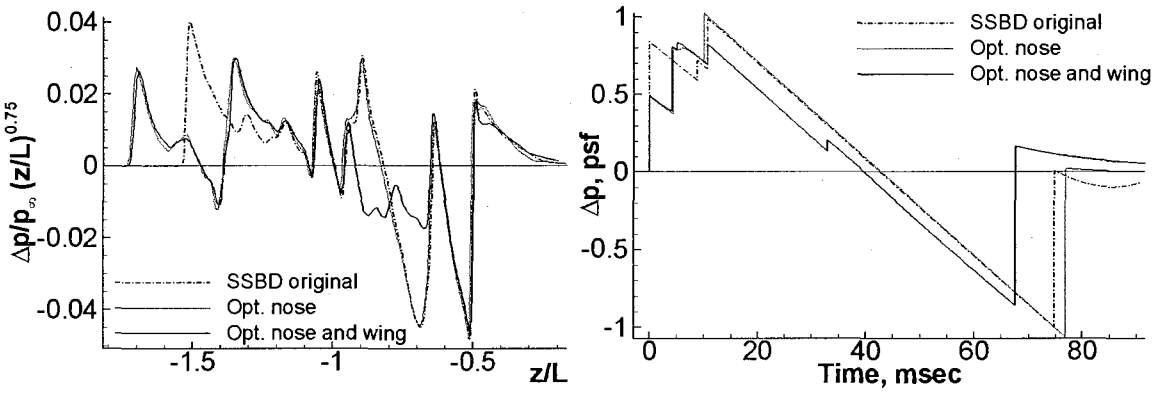

Figure 69: Computational pressure signals at x/L = 1.5 (left) and at ground altitude of 2,372 ft. asl (right) from the original SSBD, SSBD with optimized nose attachment, and SSBD with optimized nose and wing at $\theta_D = 20°$.

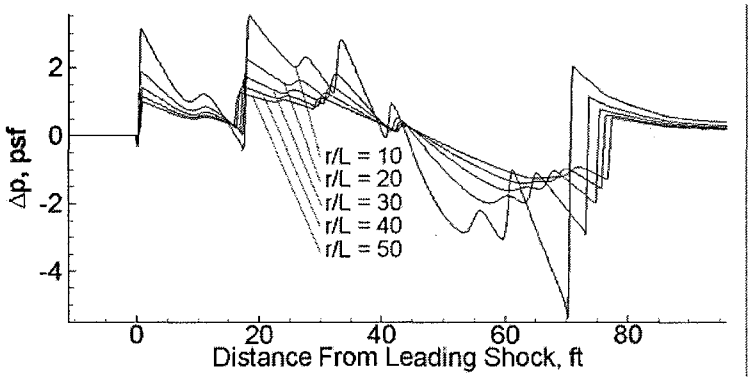

Figure 70: Mid-field pressure signals computed by FPM3D using full-potential propagation method up to r/L = 50 for the SSBD with optimized nose and wing at $\theta_D = 20°$.

Table 42: Computational responses of interest from four SSBD configurations.

	Original SSBD	Optimized Nose	Optimized Wing, $\theta_D = 20°$	Optimized Nose and Wing, $\theta_D = 20°$
C_L	0.0936	0.0944 (+1.0%)	No change	0.0943 (+0.7%)
Inviscid C_D	0.0370	0.0366 (-1.1%)	0.0289 (-21.9%)	0.0283 (-23.5%)
Volume, ft^3	683.2	683.2 + 46.0 (+6.7%)	No change	683.2 + 46.0 (+6.7%)
Length, ft	50	60	No change	60
Bow Shock, psf	0.836	0.484 (-42.1%)	No change	0.488 (-41.6%)
Peak Δp, psf	1.0	No change	0.84 (bow shock)	0.83 (-17.0%)
Impulse, psf·msec	23.34	22.93 (-1.8%)	18.1	18.2 (-22.0%)
Foot Print Size, msec	74.8	76.8 (+2.7%)	66.5 (-11.1%)	67.7 (-9.5%)

7. CONCLUSION

This dissertation presents a complete automated sonic boom analysis methodology for steady state flow with high accuracy and 3D and non-linear computations extended to a greater distance than what is used in industry today. The efficiency and applicability of this sonic boom prediction methodology in optimization design loops are demonstrated through aerodynamic shape optimization for sonic boom mitigation of a real aircraft, namely, the Shaped Sonic Boom Demonstrator. The SSBD is a modified F-5E built by Northrop Grumman to demonstrate the shaping of the sonic boom signal by careful tailoring of the fore-body of the aircraft to modify the standard N-wave type sonic boom signal to something more like a "flat-top" shape. In this dissertation, conceptual modifications are done on the nose and wings of this particular aircraft to further decrease its ground level sonic boom signal properties like bow shock strength, peak pressure, pressure impulse, and foot print size.

The highlights of the sonic boom prediction methodology are the unstructured grid adaptation technique in the near-field computations, and the full-potential mid-field sonic boom marching program. The full-potential sonic boom prediction code has been under development with Dr. Kandil's team since 2000, and is currently the one and the only CFD software that can compute the sonic boom signal non-linearly in 3D all the way from the aircraft to the ground with changing atmospheric temperature and pressure conditions with altitude. The unstructured grid adaptation technique developed in this work is a major improvement on the available feature-based (Hessian-based) adaptation technique, where the scalar field used for the error computation is specialized in shock detection and shock strength normalization across the entire flow domain. The scalar field formulation is derived upon the fact that the normal Mach number across shocks changes from supersonic to subsonic. Consequently it is equal to 1 right on the shock. Hence the shocks can be found by looking at places where the normal Mach number is around 1. This technique has been used previously for shock visualization in software like Plot3D from NASA, but has never been used to drive grid adaptation for shocks. The adaptation scalar derived in the current work embeds this technique to detect the shocks, and uses it to control/reduce/eliminate the presence of the non-shock phenomena that are not of interest, e.g. strong gradients on the surface of a complex aircraft. Doing so avoids excessive adaptation on such regions while trying to refine the shocks, which is a common problem of feature-based adaptation techniques. Having the feature-based adaptation routines focusing on shocks alone provides huge savings in the grid size, and this is the main reason behind the development of the particular scalar field formulation

used in the Hessian based adaptation here. The entire 3D domain around a real aircraft is solved using only 500,000 grid nodes up to 1.5 body lengths downstream the nose, with shocks in the entire cross-flow adapted for and captured equally fine. Similar examples from the literature show final adapted grids that only solve the under-track portion of the aircraft using 3 to 7 million nodes. Furthermore the shocks captured with such grid are still rounded (dissipated). This brings the subject to the second advantage of the current grid adaptation methodology, which is shock fitting. Hessian based adaptation provides anisotropic grid formation where the grid elements can be stretched along shock surfaces to align their largest face with the shock. This is achieved by using the eigenvectors of the Hessian matrix as directions to move the nodes of the element to reduce the error metric. The alternative is to divide the cell into 4 smaller cells to reduce the error metric. The Hessian based adaptation saves grid size by not increasing the number of cells, and by moving the available nodes towards the high gradients instead. When the grid element is aligned with the shock surface, the fluxes are computed normal across the shock. If the computational scheme is a Riemann type scheme like Roe's FDS, the one dimensional Riemann problem is numerically replicated across the grid surface which naturally satisfies the conservation laws across the shock. When these conditions are satisfied, the dissipation and dispersion errors that occur across the shock are eliminated and the sonic boom signal is computed accurately. In short, the newly developed adaptation scalar used in the current study provides an efficient small size grid that also provides shock fitting.

One other major problem of feature based grid adaptation is that the initial grid has to be fine enough to resolve the features (shocks in this case) at least to some level so the adaptation routines can find them and start working on them. This means the initial grid has to be created with some prior knowledge of the shock structure (which is impractical for complex 3D geometries), and using a lot of grid nodes. This totally abolishes automation and user-friendliness of the grid generation and flow solution techniques. A third great advantage of the adaptation scalar devised herein is that it does not require a fine initial grid. The initial grids used in the current study are all created very coarse and with no prior knowledge of the shock structure. The adaptation scalar involves a distance based factor multiplying the disturbance which amplifies the error in the distant locations in the domain and literally lures the adaptation towards coarse regions, but following the shocks only. This also provides great savings in the total number of solution/adaptation iterations. The cases solved require a maximum of 11 solution/adaptation cycles to complete, and most of them require only about 6-7 cycles. The cycles terminate upon meeting a special criterion indicating signal shape convergence at a preset target distance from the aircraft.

A fourth advantage of the adaptation scalar developed here is that it uses a predefined set of constants and parameter values that work for all aircraft configurations simple or complex, and domains small or large. An axisymmetric body signal up to 20 body lengths and a complex 3D real aircraft signal up to 4 body lengths can be computed using exactly the same grid adaptation parameters. This in turn makes the grid adaptation method extremely user-friendly and automated. These are necessary properties for a method to be included in rapid design optimization loops. When coupled with automatic CAD and initial grid generation, sonic boom signal computation for any geometry becomes a trivial command-line operation.

Unlike prior studies involving the full-potential sonic boom prediction software, the far-field computations are finalized using the linear waveform parameter method in this work. This is mainly because the non-linearities and 3D cross-flow effects clearly disappear after some distance from the source, and non-linear computations become overkill. A methodology is devised in the current work to determine when to switch from the non-linear full-potential computations to the linear geometric acoustics method. This distance is different for each aircraft shape, and cannot be determined before the start of the signal propagation. The method developed in this work uses a convergence criterion on the ground signal computed by the linear method, starting at increasing distances from the source. The results show that for a simple axisymmetric geometry the linear propagations can start as close as one body length to the centerline, whereas for the SSBD it has to be around 40 body lengths. The waveform parameter method works only for the far-field, where the input signal is at an asymptotic state. This is crucial to obtain reliable results from the Thomas waveform method. Input signals that are not yet at an asymptotic state are strongly non-linear and do not carry the full effect of lift generated off-centerline. Use of such signals will result in severe under-prediction of the ground signal pressure levels, and will lead to over-estimated success for a particular sonic boom mitigating aircraft.

Automated parametric surface definition generation and non-linear 3D sonic boom computation methodology is used in three design optimization studies to demonstrate its applicability as a design tool. First an axisymmetric shape is optimized, second a delta wing, and third the nose and the wing of the SSBD. These studies switch from simplest to most complex to show the methodology works for all levels of complexity. Hundreds of cases are rapidly set up submitted to a parallel high performance cluster queue using a rich set of Unix scripts that couple all stages of preprocessing, analysis, and postprocessing. Optimization strategy is based on DoE and RSM, where 2^{nd} order orthogonal experimental designs are used to model responses like drag, lift, pressure impulse, and peak pressures in the sonic boom signal. The response models

are used to find optimum points using the Design-Expert software which employs gradient based search algorithms starting from randomly distributed locations to avoid getting stuck at local minima. RSM also helps to find erroneous computed cases which stand out as outliers in the statistical analyses. This in turn ensures that the results are checked and corrected and the predictions and actual computations match. RSM also shows the individual and combined effects of factors on the responses, helping a designer to employ new design factors or adjust the bounds of the factors better. Carrying out optimization with closed box methods like genetic algorithms and like can lead to a good design after tens of thousands of runs, but do not give significant insight to the problem and promote further development.

The axisymmetric optimization study resulted in low boom design with low drag as well. Sonic boom mitigation studies that are based on the F-function optimization method generally end up increasing the drag while reducing the boom. The optimum shape found in the current study has lower peak pressure and much lower drag than the optimum found by Hague and Jones [15] using similar geometric constraints and linear prediction methods. The key point for low drag in the current axisymmetric optimization study that is not found in the literature is the particular setting of the starting half cone angle of the nose of the piece which is set equal to the critical shock detachment angle for that Mach number. This way the boom reduction effect of bluntness is used up to the point where drag is still low by keeping the bow shock attached.

The sonic boom mitigation study for the delta wing features wing twist as an addition to the parameters investigated earlier. Furthermore, the wing twist and camber are allowed to vary non-linearly along the span, and these non-linear profiles for both parameters are optimized as well. The literature shows root/tip twist optimization with standard linear span wise distribution, and camber optimization at several span wise locations at the most. The current optimization study optimizes the expression that defines the twist and camber along the span to create a continuous twist and camber variation along the span. For the twist, a non-linear parametric equation is devised to define the span wise twist variation, and the three parameters involved in this equation are used as design factors in the optimization. The span wise camber variation is tied to the local angle of attack, or the twist profile. The optimum camber for any angle of attack is first found, and a model equation relating the angle of attack and optimum camber is generated. This model equation is then used with the twist equation where first the twist at a span wise location is computed and then the optimum camber is found for that local angle of attack. To the knowledge of the author, non-linear span wise twist and camber profile optimization has not been carried out prior to the current dissertation for sonic boom mitigation of lifting bodies. Up to

30% reduction in ground level peak pressure is obtained while conserving the volume and lift of the delta wing.

The axisymmetric nose found in the first of the optimization studies is used as a nose extension to the SSBD aircraft to reduce its bow shock strength. Unlike Gulfstream's Quiet Spike design, the nose attachment in the current study is not targeted to divide the bow shock into several consecutive smaller shocks. Instead, the bow shock is mitigated as a whole on its own without being divided. This allows to have a shorter nose since the cylindrical extensions on the nose piece to delay the shock coalesce are not needed in this case. This makes the current design stiffer and less prone to aeroelastic problems. Gulfstream's Quiet Spike can be used as a further extension to this particular optimized nose shape to take advantage of its shock dividing characteristic. The nose is designed axisymmetric and attached to the SSBD with a negative angle to make it parallel to the flight path. This way the nose extension does not induce any lift or moment when added to the aircraft. If the moment center of the SSBD changes, the center of gravity and trimming settings have to change as well. Not to complicate and lose focus on the problem, parasitic effects like aerodynamic center change are eliminated. The wing optimization of the SSBD is done using a delta wing similar to the one optimized prior. However, a brand new wing needs to be designed for the SSBD to match its root chord length, thickness, mount points, aerodynamic center, and volume. Furthermore the interference lift between the wing and the fuselage needs to be accounted for, which can only be done by solving the wing while it is attached to the SSBD fuselage. Therefore a second delta wing parametric optimization is carried out for the SSBD, and reported in a concise manner. The final results show that the SSBD aircraft with the optimized nose and the wing has 42% reduction in bow shock strength, 17% reduction in peak Δp, 22% reduction in pressure impulse, 10% reduction in foot print size, and 24% reduction in inviscid drag along with slight increase in lift, volume, and weight (unknown small amount).

In short, the current dissertation study introduces an efficient non-linear sonic boom prediction methodology and successfully demonstrates its use in aircraft design loops for sonic boom mitigation. The current study is not intended to propose a low boom aircraft that meets the required FAA terms, but only demonstrates the available design tools for the development of such aircraft. Actual aircraft require many other levels of design including fuel space, engine specifications, mission parameters, etc., which are not covered in the current work. For future recommendation, the prediction and optimization methods shown here can be used in more general optimization of realistic business jet designs that include mission and engine optimization as well. Fuselage optimization can be carried out in addition to the nose and wing optimization

demonstrated here. Gulfstream's Quiet Spike could be added to the optimized nose found in the current study for further mitigation of the bow shock signal. Unsteady design problems where the axial lift and volume distribution is varied in time can be undertaken to break the N-wave tendency of the sonic boom signal, however, care must be taken not to induce jerk and excessive accelerations on passengers and delicate equipment. The development of the non-linear CFD sonic boom prediction methods to the level that they can be utilized in rapid design optimization loops is a great benefit to the sonic boom mitigation research as more complex interacting flow structures can be exploited to mitigate the undertrack signal, and concepts like external energy deposition to the flow can easily be modeled using simple boundary conditions in the CFD grid. The shape optimization methodology in steady state flows gives out designs that are only good at the design conditions in general. Off-design situations can easily produce higher level sonic booms. Unsteady optimization and active sonic boom control by movable surface or by energy deposition should achieve better results for a large envelope of flight conditions, however, implementation of such systems on aircraft will definitely increase the design, manufacturing, and operating costs.

REFERENCES

1. Pawlowski, J.W., Graham, D. H., *Origins and Overview of the Shaped Sonic Boom Demonstration Program*, in *43rd AIAA Aerospace Sciences Meeting*. 2005: Reno, NV.

2. *Environmental Impact Analysis Process. Environmental Assessment for U.S. Air Force Atmospheric Interceptor Technology Program*. 1997, SPACE AND MISSILE SYSTEMS CENTER LOS ANGELES AFB CA.

3. Plotkin, K.J., *Sonic Boom Focal Zones from Tactical Aircraft Maneuvers*. Journal of Aircraft, 1993. **30**(1).

4. Henne, P.A., *The Case For Small Supersonic Civil Aircraft*, in *AIAA/ICAS International Air and Space Symposium and Exposition*. 2003: Dayton, OH.

5. Haering, E., A., Ehernberger, L., J., Whitmore, S., A., *Preliminary Airborne Measurements for the SR-71 Sonic Boom Propagation Experiment*. 1995, NASA.

6. Haering, E.A.J., Murray, J. E., Purifoy, D. D., Graham, D. H., Meredith, K. B., Ashburn, C. E., and Lt. Col. Stucky, M., *Airborne Shaped Sonic Boom Demonstration Pressure Measurements with Computational Fluid Dynamics Comparisons*, in *43rd AIAA Aerospace Sciences Meeting and Exhibit*. 2005, AIAA Reno, Nevada.

7. Carlson, H.W., Mack, R. J., Morris, O. A., *A WIND-TUNNEL INVESTIGATION OF THE EFFECT OF BODY SHAPE ON SONIC-BOOM PRESSURE DISTRIBUTIONS*, L.R. Center., Editor. 1965.

8. Busemann, A., *Sonic Boom Reduction*, in *Sonic Boom Research*. 1967, NASA: Washington, D.C.

9. George, A.R., *The Possibilities for Reducing Sonic Boom by Lateral Redistribution*, in *Sonic Boom Research*. 1967, NASA: Washington, D.C.

10. Howes, W.L., *On Supersonic Vehicle Shapes for Reducing Auditory Response to Sonic Booms*, in *Sonic Boom Research*. 1967, NASA: Washington, D.C.

11. Koegler, R.K., *Possible Means of Reducing Sonic Booms and Effects Through Shock Decay Phenomena and Some Comments on Aural Response*, in *Sonic Boom Research*. 1967, NASA: Washington, D.C.

12. Resler, E.L., *A Boomless Wing Configuration*, in *Sonic Boom Research*. 1967, NASA: Washington, D.C.

13. Barger, R.L., Jordan, F. L., *Investigation of a class of bodies that generate far-field sonic-boom shock strength and impulse independent of body length and volume*. 1969, Langley Research Center: Hampton.

14. Ferri, A. *Airplane Configurations for Low Sonic Boom*. in *Third Conference on Sonic Boom Research*. 1971. Washington, DC: NASA.

15. Hague, D.S., Jones, R. T. *Application of Multivariable Search Techniques to the Design of Low Sonic Boom Overpressure Body Shapes*. in *Third Conference on Sonic Boom Research*. 1971. Washington, DC: NASA.

16. Maglieri, D.J., Hilton, D. A., Huckel, V., Henderson, H. R., McLeod, N. J. *Measurements of Sonic Boom Signatures From Flights at Cutoff Mach Number.* in *Third Conference on Sonic Boom Research.* 1971. Washington, DC: NASA.

17. Miller, D.S. *Status of Research on Boom Minimization Through Airstream Alteration.* in *Third Conference on Sonic Boom Research.* 1971. Washington, DC: NASA.

18. Schwartz, I.R., *Third Conference on Sonic Boom Research*, D. NASA Headquarters, Editor. 1971, NASA.

19. Seebass, R., George, A. R., *Sonic-Boom Minimization.* The Journal of the Acoustical Society of America, 1972. **51**(2).

20. Darden, C.M., *Sonic-Boom Minimization With Nose-Bluntness Relaxation* L.R. Center, Editor. 1979, NASA.

21. Crow, S.C., Bergmeier, G. G., *Active Sonic Boom Control.* Journal of Fluid Mechanics, 1996. **325**: p. 1-28.

22. Tam, T., Ruffin, S., Yates, L., Gage, P., Bogdanoff, D., Morgenstern, J., *Sonic Boom Testing of Artificially Blunted Leading Edge (ABLE) Concepts in the NASA Ames Aeroballistic Range*, in *38th AIAA Aerospace Sciences Meeting and Exhibit.* 2000, AIAA: Reno, NV.

23. Miles, R.B., Macheret, S. O., Martinelli, L., Murray, R., Shneider, M., Ionikh, Y. Z., Kline, J., Fox, J., *Plasma Control of Shock Waves in Aerodynamics and Sonic Boom Mitigation*, in *32nd AIAA Plasmadynamics and Lasers Conference and 4th Weakly Ionized Gases Workshop Conference and Exhibit.* 2001, AIAA: Anaheim, CA.

24. Alonso, J.J., Kroo, I. M., Jameson, A., *Advanced Algorithms for Design and Optimization of Quiet Supersonic Platforms*, in *40th AIAA Aerospace Sciences Meeting and Exhibit.* 2002, AIAA: Reno, NV.

25. Bivolaru, D., Kuo, S. P., *Observation of Supersonic Shock Wave Mitigation by a plasma aero-spike.* Physics of Plasmas, 2002. **9**(2).

26. Briceno, S.I., Buonanno, M. A., Fernandez, I., Mavris, D. N., *A Parametric Exploration of Supersonic Business Jet Concepts Utilizing Response Surfaces*, in *AIAA's Aircraft Technology, Integration, and Operations (ATIO) 2002 Technical Forum.* 2002, AIAA: Los Angeles, CA.

27. Howe, D.C., *Engine Placement for Sonic Boom Mitigation*, in *40th AIAA Aerospace Sciences Meeting and Exhibit.* 2002, AIAA: Reno, NV.

28. Miles, R.B., Martinelli, L., Macheret, S. O., Shneider, M., Girgis, I. G., Zaidi, S. H., Mansfield, D. K., Siclari, M., Smereczniak, P., Kashuba, R., Vogel, P., *Supression of Sonic Boom by Dynamic Off-Body Energy Addition And Shape Optimization*, in *40th AIAA Aerospace Sciences Meeting and Exhibit.* 2002, AIAA: Reno, NV.

29. Adelgren, R.G., Yan, H., Elliott, G. S., Knight, D. D., Zheltovodov, A. A., Ivanov, M., *Localized Flow Control by Laser Energy Deposition Applied to Edney IV Shock Impingement and Intersecting Shocks*, in *41st AIAA Aerospace Sciences Meeting and Exhibit.* 2003, AIAA: Reno, NV.

30. Bobbitt, P., Kandil, O. A. and Yang, Z., *The Beneficial Effects of Wing Dihedral on Sonic Boom*, in *Aeroacoustics Conf.* 2003: HiltonHead, SC.

31. Bucovsky, A., Eyer, J., Mavris, D., *Design Space Exploration for Boom Mitigation on a Quiet Supersonic Business Jet*, in *AIAA's 3rd Annual Aviation Technology, Integration, and Operations Forum*. 2003: Denver, CO.

32. Howe, D.C., *Sonic Boom Reduction Through the Use Of Non-Axisymmetric Configuration Shaping*, in *41st Aerospace Sciences Meeting and Exhibit*. 2003, AIAA: Reno, NV.

33. Karr, C.L., Bowersox, R., Singh, V. *Minimization of Sonic Boom on Supersonic Aircraft Using an Evolutionary Algorithm*. in *Genetic and Evolutionary Computation Conference, GECCO 2003*. 2003. Chicago.

34. Macheret, S.O., Shneider, M. N., Zaidi, S. H., Miles, R. B., Van Wie, D. M., *Plasma and MHD Control of Oblique Shocks*. 2003, Princeton University, Johns Hopkins University Applied Physics Laboratory.

35. Mack, R.J., *A Quick Method for Evaluating the Merits of a Proposed Low Sonic Boom Concept*, L.R. Center., Editor. 2003, NASA.

36. Mack, R.J., *A Supersonic Business-Jet Concept Designed for Low Sonic Boom*, L.R. Center., Editor. 2003, NASA.

37. Phan, L.L., Yamaoka, Y., Mavris, D. N., *Implementation and Benefits of Variable Geometry Wings for a Supersonic Business Jet*, in *AIAA 3rd Annual Aviation Technology, Integration, and Operations Forum*. 2003, AIAA: Denver, CO.

38. Henne, P.A., Howe, D. C., Wolz, R. R., Hancock, J. L., *Supersonic Aircraft With Spike For Controlling and Reducing Sonic Boom*. 2004, Gulfstream Aerospace Corporation: USA.

39. Lyman, V., Morgenstern, J. M., *Calculated and Measured Pressure Fields for an Aircraft Designed for Sonic Boom Alleviation*, in *22nd Applied Aerodynamics Conference and Exhibit*. 2004: Providence, Rhode Island.

40. Howe, D.C., *Improved Sonic Boom Minimization with Extendable Nose Spike*, in *43rd AIAA Aerospace Sciences Meeting and Exhibit*. 2005, AIAA: Reno, NV.

41. Mack, R.J., *Method for Estimating the Sonic-Boom Characteristics of Lifting Canard-Wing Aircraft Concepts*. 2005, Langley Research Center: Hampton, VA.

42. Darden, C.M., *Affordable/Acceptable Supersonic Flight: Is it near?*, in *40th Aircraft Symposium*. 2002, JSASS: Yokohoma, Japan.

43. Hayes, W.D., Haefeli, C. R., Kulsrud, H. E., *Sonic Boom Propagation In A Stratified Atmosphere, With Computer Program*, L.R. Center., Editor. 1969.

44. Thomas, C.L., *Extrapolation of Sonic Boom Pressure Signatures by the Waveform Parameter Method*, A.R. Center, Editor. 1972.

45. Whitham, G.B., *The Flow Pattern of a Supersonic Projectile*. Communications on Pure and Applied Mathematics, 1952. **5**: p. 48.

46. Shepherd, K.P., Sullivan, B. M., *A Loudness Calculation Procedure Applied to Shaped Sonic Booms*. 1991, NASA.

47. Morgenstern, J.M., Arslan, A., Lyman, V., Vadyak, J., *F-5 Shaped Sonic Boom Demonstrator's Persistence of Boom Shaping Reduction through Turbulence*, in *43rd AIAA Aerospace Sciences Meeting and Exhibit.* 2005, AIAA: Reno, NV.

48. Kandil, O., A., Yang, Z., Bobbitt, P., J., *Prediction of Sonic Boom Signature Using Euler-Full Potential CFD With Grid Adaptation and Shock Fitting*, in *8th AIAA/CEAS Aeroacoustics Conference* 2002, AIAA: Breckenridge, CO.

49. Kandil, O.A., Yang, Z., *Codes and Applications for the Full-Potential Equation Methodology of Three-Dimensional Sonic Boom Propagation.* 2004, Aerospace Engineering Department, Old Dominion University: Norfolk.

50. Baize, D.G., Coen, Peter G. *A Mach 2.0/1.6 Low Sonic Boom High-Speed Civil Transport Concept.* in *High Speed Research: Sonic Boom.* 1993. Ames Research Center: NASA.

51. Cliff, S., E., Thomas, S., D., *Euler/Experiment Correlations of Sonic Boom Pressure Signatures.* Journal of Aircraft, 1993. **30**(5).

52. Kandil, O.A., Ozcer, I. A., Zheng, X., Bobbitt, P. J., *Comparison of Full-Potential Propagation-Code Computations with the F-5E "Shaped Sonic Boom Experiment" Program*, in *43rd AIAA AEROSPACE SCIENCES MEETING AND EXHIBIT.* 2005: Reno, NV.

53. Ozcer, I.A. and Old Dominion University. Dept. of Aerospace Engineering., *Sonic Boom Prediction Using Euler/Full Potential Methodology.* 2005, Old Dominion University, 2005. p. xvi, 202 leaves.

54. Kandil, O.A., Zheng, X., *Computational Solution of Nonlinear Tricomi Equation for Sonic Boom Focusing and Applications*, in *International Sonic Boom Forum.* 2005: Penn State, PA.

55. Kandil, O.A., Zheng, X., *Prediction of Superboom Problem Using Computational Solution of Nonlinear Tricomi Equation*, in *AIAA Atmospheric Flight Mechanics Conference and Exhibit.* 2005, AIAA: San Francicso, California.

56. Kandil, O.A., Khasdeo, N., *Parametric Investigation of Sonic Boom Focusing using Solution of Nonlinear Tricomi Equation*, in *44th AIAA Aerospace Sciences Meeting and Exhibit.* 2006, AIAA: Reno, NV.

57. Kandil, O.A., Khasdeo, N., Ozcer, I. A., *Sonic Boom Mitigation Through Thickness, Camber, and Nose Angle Optimizations for a Delta Wing*, in *AIAA Atmospheric Flight Mechanics Conference and Exhibit.* 2006, AIAA: Colorado, Keystone.

58. Ozcer, I.A., Kandil, O. A., Yagiz, B. , *Parametric Study and Effect of Nose-Piece Attachment on Sonic Boom Mitigation*, in *45th AIAA Aerospace Sciences Meeting and Exhibit.* 2007: Reno, NV.

59. Kandil, O.A., Khasdeo, N., Ozcer, I. A., *Optimization of Delta Wing Geometry Parameters for Sonic Boom Mitigation*, in *37th AIAA Fluid Dynamics Conference and Exhibit.* 2007, AIAA: Miami, FL.

60. Ozcer, I.A., Kandil, O. A., *FUN3D / OptiGRID Coupling for Unstructured Grid Adaptation for Sonic Boom Problems*, in *46th AIAA Aerospace Sciences Meeting and Exhibit.* 2008, AIAA: Reno, NV.

61. Anderson, J.D., *Modern compressible flow : with historical perspective.* 3rd ed. McGraw-Hill series in aeronautical and aerospace engineering. 2003, Boston: McGraw-Hill. xvi, 760 p.

62. Liepmann, H.W., Roshko, A., *Elements of Gas Dynamics.* 1957, Mineola, NY: Dover.

63. Lighthill, M.J., *Supersonic Flow Past Slender Bodies of Revolution the Slope of Whose Meridian Section is Discontinuous.* Quarterly Journal of Mechanics and Applied Mathematics, 1948. **1**(1): p. 13.

64. Gottlieb, J.J., Ritzel, D. V., *Analytical Study of Sonic Boom From Supersonic Projectiles.* Progress in Aerospace Sciences, 1988. **25**(2): p. 58.

65. Walkden, F., *The Shock Pattern of a Wing-Body Combination, Far From the Flight Path.* The Aeronautical Quarterly, 1958. **9**: p. 164-194.

66. Plotkin, K.J., *State of the art of sonic boom modeling.* Journal of Acoustical Society of America, 2002. **111**(1): p. 530-536.

67. Page, J., A., Plotkin, K., J., *An Efficient Method for Incorporating Computational Fluid Dynamics Into Sonic Boom Prediction*, in *AIAA 9th Applied Aerodynamics Conference.* 1991, AIAA: Baltimore, MD.

68. Siclari, M.J., Darden, C. M., *Euler Code Prediction of Near-Field to Midfield Sonic Boom Pressure Signatures.* Journal of Aircraft, 1993. **30**(6).

69. Ma, K.L., Rosendale, J. V., Vermeer, W. *3D Shock Wave Visualization on Unstructured Grids.* in *Symposium on Volume Visualization.* 1996. San Francisco, CA: IEEE.

70. Trepanier, J., Y., Paraschivoiu, M., Reggio, M., Camarero, R., *A Conservative Shock Fitting Method on Unstructured Grids.* Journal of Computational Physics, 1996. **126**.

71. Chung, H.S., Choi, S., Alonso, J. J., *Supersonic Business Jet Design using a Knowledge-Based Genetic Algorithm with an Adaptive, Unstructured Grid Methodology*, in *21st Applied Aerodynamics Conference.* 2003, AIAA: Orlando, Florida.

72. Choi, S., Alonso, J. J., Weide, E. V., *Numerical and Mesh Resolution Requirements for Accurate Sonic Boom Prediction of Complete Aircraft Configurations*, in *42nd Aerospace Sciences Meeting and Exhibit.* 2004, AIAA: Reno, NV.

73. Choi, S., Alonso, J. J., Chung, H. S., *Design of a Low-Boom Supersonic Business Jet Using Evolutionary Algorithms and an Adaptive Unstructured Mesh Method*, in *45th AIAA/ASME/ASCE/AHS/ASC Structures, Structural Dynamics and Materials Conference.* 2004, AIAA: Reno, NV.

74. Park, M.A., *Adjoint-Based, Three-Dimensional Error Prediction and Grid Adaptation*, in *32nd Fluid Dynamics Conference* 2002, AIAA: St. Louis, MO.

75. Park, M.A., *Three-Dimensional Turbulent RANS Adjoint-Based Error Correction*, in *16th AIAA Computational Fluid Dynamics Conference.* 2003, AIAA.

76. Gnoffo, P.A., *Computational Fluid Dynamics Technology for Hypersonic Applications.* 2003, Langley Research Center.

77. Gnoffo, P.A., White, J. A., *Computational Aerothermodynamic Simulation Issues on Unstructured Grids*, in *37th AIAA Thermophysics Conference.* 2004.

78. Bibb, K.L., Gnoffo, P. A., Park, M. A., Jones, W. T., *Parallel, Gradient-Based Anisotropic Mesh Adaptation for Re-entry Vehicle Configurations*, in *9th AIAA/ASME Joint Thermophysics and Heat Transfer Conference*. 2006, AIAA: San Francisco, CA.

79. Jones, W.T., Nielsen, E. J., Park, M. A., *Validation of 3D Adjoint Based Error Estimation and Mesh Adaptation for Sonic Boom Prediction*, in *44th AIAA Aerospace Sciences Meeting and Exhibit*. 2006, AIAA: Reno, NV.

80. Remaki, L., Lepage, C., Habashi, W. G., *Efficient Anisotropic Mesh Adaptation on Weak and Multiple Shocks*, in *42nd Aerospace Sciences Meeting and Exhibit*. 2004, AIAA: Reno, NV.

81. Kandil, O.A., Ozcer, I. A., *Sonic Boom Computations for Double-Cone Configuration using CFL3D, FUN3D and Full Potential Codes*, in *44th AIAA Aerospace Sciences Meeting and Exhibit*. 2006, AIAA: Reno, NV.

82. Ozcer, I.A., *Sonic Boom Prediction Using Euler / Full Potential Methodology*, in *45th AIAA Aerospace Sciences Meeting and Exhibit*. 2007, AIAA: Reno, NV.

83. Yamashita, H., Obayashi, S., *Numerical Investigation on Sonic Boom Reduction with Non-axisymmetric Body Shapes*, in *46th AIAA Aerospace Sciences Meeting and Exhibit*. 2008, AIAA: Reno, NV.

84. Yamaguchi, H., Nakamura, Y., *Optimization of Low Boom Configuration of SST by Genetic Algorithm*, in *29th AIAA Fluid Dynamics Conference*. 1998, AIAA: Albuquerque, NM.

85. Chung, H.S., Alonso, J. J., *Multiobjective Optimization Using Approximation Model-Based Genetic Algorithms*, in *10th AIAA/ISSMP Symposium on Multidisciplinary Analysis and Optimization*. 2004, AIAA: Albany, NY.

86. Rallabandi, S., *Sonic Boom Minimization through Vehicle Shape Optimization and Probabilistic Acoustic Propagation*, in *School of Aerospace Engineering*. 2005, Georgia Institute of Technology.

87. Simmons, F., Freund, D., *Morphing Concept for Quiet Supersonic Jet Boom Mitigation*, in *43rd AIAA Aerospace Sciences Meeting and Exhibit*. 2005, AIAA: Reno, NV.

88. Wintzer, M., Sturdza, P., *Conceptual Design of Conventional and Oblique Wing Configurations for Small Supersonic Aircraft*, in *44th AIAA Aerospace Sciences Meeting and Exhibit*. 2006: Reno, NV.

89. Farhat, C., Maute, K., Argrow, B., Nikbay, M., *Shape Optimization Methodology for Reducing the Sonic Boom Initial Pressure Rise*. AIAA Journal, 2007. **45**(5).

90. Farhat, C., Argrow, B., Nikbay, M., Maute, K., *Shape Optimization with F-function balancing for reducing the sonic boom initial shock pressure rise*. International Journal of Aeroacoustics, 2005. **3**(4).

91. Maute, K., Farhat, C., Argrow, B., Nikbay, M., *Sonic Boom Mitigation Via Shape Optimization Using an Adjoint Method and Application to a Supersonic Fighter Aircraft*. European Journal of Computational Mechanics, 2008. **17**.

92. Nadarajah, S., K., Jameson, A., Alonso, J., J., *Adjoint-Based Sonic Boom Reduction for Wing-Body Configurations in Supersonic Flow*. Canadian Aeronautics and Space Journal, 2005. **51**(4).

93. Kandil, O.A., Khasdeo, N., and Ozcer, I. A., *Optimization of Delta Wing Geometry Parameters for Sonic-Boom Mitigation* in *37th AIAA Fluid Dynamics Conference and Exhibit.* 2007: Miami, FL.

94. Krist, S.L., Biedron, R. T., Rumsey, C. L., *CFL3D User's Manual.* 1998, Langley Research Center: Hampton.

95. Shankar, V., *Conservative Full Potential, Implicit Marching Scheme for Supersonic Flows.* AIAA J, 1982. **20**(11).

96. Shankar, V., Szema, K.-Y., Osher, S., *A Conservative Type-Dependent Full Potential Method For The Treatment Of Supersonic Flows With Embedded Subsonic Regions*, in *6th Computational Fluid Dynamics Conference.* 1983, AIAA: Danvers, MA.

97. Shankar, V., Osher, S., *An Efficient, Full-Potential Implicit Method Based on Characteristics for Supersonic Flows.* AIAA J 1983. **21**(9).

98. Moretti, G., *Thirty-six years of shock fitting.* Computers and Fluids, 2002. **31**: p. 719-723.

99. Lee-Rausch, E.M., Park, M. A., Jones, W. T., Hammond, D. P., Nielsen, E. J., *Application of Parallel Adjoint-Based Error Estimation and Anisotropic Grid Adaptation for Three-Dimensional Aerospace Configurations*, in *23rd AIAA Applied Aerodynamics Conference.* 2005, AIAA: Toronto, Ontario.

100. Newmerical Technologies, I., *NTI Solutions User's Guide.* 2005: Montreal.

101. Montgomery, D.C., *Design and Analysis of Experiments.* 6 ed. 2005, New York: Wiley.

102. Myers, R.H., Montgomery, D. C., *Response Surface Methodology.* 2 ed. 2002, New York: Wiley & Sons.

103. Plotkin, K.J., Hearing, E. A., Murray, J. E., Maglieri, D. J., Salamone, J., Sullivan, B. M., Schein, D., *Ground Data Collection of Shaped Sonic Boom Experiment Aircraft Pressure Signatures*, in *43rd Aerospace Sciences Meeting and Exhibit.* 2005, AIAA: Reno, NV.

104. Kandil, O.A., Ozcer, I. A. and Khasdeo, N., *Sonic Boom Prediction, Focusing, and Mitigation*, in *25 Congress of the Aeronautical Sciences.* 2006: Hamburg, Germany.

VITA

Isik Ali Ozcer

Aerospace Engineering Department

Old Dominion University

Norfolk, VA 23529

Educational Background

M.S.: December 2005, Old Dominion University, Norfolk, VA, USA

Major: Aerospace Engineering

Thesis: Sonic Boom Prediction Using Euler / Full Potential Methodology

B.Sc.: June 2003, Istanbul Technical University, Istanbul, Turkey

Major: Aeronautical Engineering

Thesis: CFD Modelling of a 2-D Compressor Stage in Unsteady Flow

Sample Publications

1. Comparison of Full-Potential Propagation-Code Computations with the F-5E "Shaped Sonic Boom Experiment" Program, Kandil, O.A., Ozcer, I. A., Zheng, X., Bobbitt, P. J., 43rd AIAA ASM. 2005: Reno, NV.

2. Sonic Boom Computations for Double-Cone Configuration Using CFL3D, FUN3D and Full-Potential Codes, Kandil, O. A. and Ozcer, I. A., 44th AIAA ASM, Jan. 2006, Reno, NV

3. Sonic Boom Prediction Using Euler / Full Potential Methodology, Ozcer, I. A., 45th AIAA ASM, Jan. 2007, Reno, NV.

4. Parametric Study and Effect of Nose-Piece Attachment on Sonic Boom Mitigation, Ozcer, I.A., Kandil, O. A., Yagiz, B. , 45th AIAA ASM, Jan. 2007, Reno, NV.

5. FUN3D / OptiGRID Coupling For Unstructured Grid Adaptation to Solve Sonic Boom Problems, Ozcer, I. A., Kandil, O. A., 46th AIAA ASM, Jan. 2008, Reno, NV.

6. Design Optimization of Nose Geometry of F-5E Aircraft for Sonic Boom Mitigation, Ozcer, I. A., Kandil, O. A., 47th AIAA ASM, Jan. 2009, Orlando, FL.